学位論文

Redox states of shergottites and HED meteorites as inferred from iron micro-XANES measurements of maskelynite and plagioclase

(マスケリナイトおよび斜長石を対象とした鉄マイクロ XANES 分析による シャーゴッタイトおよび HED 隕石の酸化還元状態の比較)

平成 25 年　11 月　博士（理学）申請

東京大学大学院　理学系研究科

地球惑星科学専攻

佐竹　渉

Abstract

Oxygen fugacity (fO_2) is one of the most important factors which determine mineral assemblages and their chemical compositions. The data of oxygen fugacity for other planetary bodies are still limited, although there are some estimates by using several different techniques. This is simply because it is difficult to obtain the samples of other planetary bodies, and also because mineral phases used to estimate oxygen fugacity such as Fe-Ti oxides are absent or not in equilibrium. Thus, I focused on analyzing the iron valence states of plagioclase and maskelynite (shocked plagioclase glass) in samples from two planetary bodies, Mars and Vesta with synchrotron radiation (SR) Fe micro XANES (X-ray Absorption Near Edge Structure) technique. These two bodies are important examples in comparison with the earth in terms of the evolution of planetary materials. I attempt to make relative comparison of oxygen fugacity of these two bodies.

In the case of Mars, I focused on shergottites which is the largest group of Martian meteorites, in order to study the origin of shergottite source. I analyzed two geochemically (light rare earth elements: LREE) depleted (Dar al Gani 476 and Dhofar 019), four LREE intermediate (EETA 79001 lithology A, ALH 77005, LEW 88516, and NWA 5029), and eight LREE enriched (Dhofar 378, NWA 856, Zagami, Shergotty, RBT 04262, NWA 4468, NWA 1068, and LAR 06319) shergottites. The obtained Fe^{3+}-Fe^{2+} peak-intensity ratios for maskelynite in the depleted, intermediate, and enriched shergottites were 0.39–0.49, 0.13–0.66, and 0.40–0.81, respectively. I revealed that the Fe^{3+}-Fe^{2+} peak-intensity ratios for maskelynite in intermediate shergottites show a very wide range (0.13–0.66), exceeding the ratios obtained for maskelynite in depleted and enriched shergottites. This result suggests that a mantle reservoir distinct from the depleted and enriched reservoirs is required to form intermediate shergottites.

For HED meteorites, I focused on eucrites with variable grain sizes that were formed by different cooling histories due to different formation depths, in order to discuss the obtained redox states and the formation model of Vesta. I analyzed five surface eucrites (Padvarninkai, ALH 76005, Piplia Kalan, Petersburg and Y-75011), three cumulate eucrites (EETA 87520, Moore County and Y 980433), and a diogenite (Y-75032). The Fe^{3+}-Fe^{2+} peak-intensity ratios for plagioclase and maskelynite in the surface eucrites, cumulate eucrites and a diogenite were 0.14–0.43, 0.49–0.70, and 0.52, respectively. This result suggested that there was a heterogeneous redox environment in the Vesta's crust and deep areas were more oxidized than the surface. The oxidized lower crust could be formed when the surface of Vesta temporarily formed a thin layer in early differentiation and / or by the presence of water in the lower crust.

Furthermore, I created a calibration curve in order to estimate the oxygen fugacity from the Fe^{3+}-Fe^{2+} peak-intensity ratios of plagioclase. I synthesized plagioclase specimens using an electric furnace under two different oxygen fugacities, and analyzed the specimens by the same XANES technique. In addition, I analyzed plagioclase in the terrestrial sample whose fO_2 has been measured. From the Fe^{3+}-Fe^{2+} peak-intensity ratio obtained, log fO_2 (⊿QFM) is defined by the following equation:

log fO_2 (⊿QFM) = 0.39 × exp (2.1 × Fe^{3+}-Fe^{2+} peak-intensity ratio) – 3

The estimated redox states of shergottites obtained from the calibration curve are between the estimates by Ol-Px-Sp and Fe-Ti oxides oxybarometers. This is consistent with the suggestion that fO_2 changed during the crystallization in parent magma of shergottites. The redox states of HED meteorites obtained from the equation showed that they crystallized at log fO_2 = QFM –2.4 to –2.0 at near the surface of Vesta and QFM -1.9 to -1.3 at near the bottom of the Vesta's crust, respectively. This is the first report estimating the oxygen fugacity of Vesta's crust.

Accordingly, this study revealed that iron micro-XANES analyses of the maskelynite and plagioclase phases in Martian and HED meteorite is a useful method to compare the redox states of different samples whose redox states cannot be estimated using regular oxybarometers such as Fe-Ti oxides and Ol-Px-Sp.

Contents

1. Introduction

1.1 Oxygen Fugacity

Oxygen fugacity (fO_2) is one of the most important factors which determines mineral assemblages and their chemical compositions. Oxygen fugacity takes the common logarithm, as a relative value from the fugacity with the buffer, which is expressed by the following formula:

$$\triangle \log fO_2 \text{ (buffer)} = \log fO_2 \text{ (P, T)} - \log fO_2 \text{ (buffer, P, T)} = \log \frac{fO_2\,(P,T)}{fO_2(buffer,P,T)}$$

The quartz-fayalite-magnetite (QFM) buffer is often used to discuss redox states of terrestrial minerals and it is defined by chemical equilibrium of quartz, fayalite and magnetite represented by the chemical equilibrium shown below:

$$\underset{\text{(Fayalite)}}{3Fe_2SiO_4} + O_2 = \underset{\text{(Magnetite)}}{2Fe_3O_4} + \underset{\text{(Quartz)}}{3\,SiO_2}$$

Similarly, the iron-wüstite (IW) buffer is often used and it is defined by chemical equilibrium of iron metal and wüstite represented by the chemical equilibrium shown below:

$$\underset{\text{(Iron metal)}}{Fe} + (1/2)\,O_2 = \underset{\text{(Wüstite)}}{FeO}$$

There are several methods to determine the oxygen fugacity of rocks. The most widely used methods for mafic igneous rocks are oxybarometers using the mineral equilibria of Fe-Ti oxides and olivine-spinel-orthopyroxene (Ol-Sp-Opx). A lot of studies have estimated the oxygen fugacity of terrestrial rocks and revealed that it is complicated. Oxygen fugacity of continental crust is log fO_2 = QFM –2 to log fO_2 = QFM +5, upper mantle is log fO_2 = QFM –4 to log fO_2 = QFM +2, lower mantle is less or equal to log fO_2 = QFM –5 (Fig. 1.1) (e.g., McCammon 2005). Thus, terrestrial crust and mantle show wide variations in oxygen fugacity and the deeper Earth's interior is more reduced.

Focusing on other planetary materials, their oxygen fugacities have been estimated and discussed for some samples. For example, oxygen fugacity of Mars has been estimated by the europium valances of pyroxene (Wadhwa 2001, 2008; McCanta et al. 2004) and Fe-Ti oxides and Ol-Sp-Px oxybarometers (e.g., Herd et al. 2002) of Martian meteorites.

In the case of asteroid Vesta, oxygen fugacity has been measured by using the meteorites that are believed to have originated from Vesta. Diogenite (Johnstown and Tatahouine), a putative Vestan meteorite group, was measured with the double ZrO_2 cell technique between 800 ^{o}C and 1150 ^{o}C by Hewins (1984). In addition, the redox state during the core formation of Vesta was estimated by moderately siderophile element partitioning (Righter and Drake, 1997) and the Si isotopic composition of the bulk silicate Vesta (Pringle et al. 2013).

In this way, although there are some estimates by using several different techniques, the data of oxygen fugacity for other planetary bodies are still limited. This is simply because it is difficult to obtain the samples of other planetary bodies, and also because mineral phases used to estimate oxygen fugacity such as Fe-Ti oxides oxybarometer are absent or not in equilibrium.

Accordingly, non-destructive methods that can analyze a mineral which is included in a number of meteorites are needed. Thus, I focused on analyzing the iron valence states of plagioclase and maskelynite (shocked plagioclase glass) with synchrotron radiation (SR) Fe micro XANES (X-ray Absorption Near Edge Structure) technique.

Delaney et al. (1998) first proposed XANES analysis may be an important technique to determine the iron valence of plagioclase by comparing terrestrial samples (Stillwater and Lake County), lunar samples (lunar rocks: 15415 and 60035), Martian meteorites (ALH 77005 and EETA 79001), and achondrites (EETA 87520 and Vaca Muerta). They found some variations in Fe^{3+}/Fe^{2+} ratios (Delaney et al. 1998). Similarly, Polyak et al. (2001) reported the $Fe^{3+}/\Sigma Fe$ ratio of one HED meteorite (EET 90020), two lunar samples (60025 and 15555), seven Martian meteorites (ALH 77005, QUE 94201, Chassigny, LEW 88516, EETA 79001, Shergotty and Zagami), four terrestrial samples (Palisades, Marcy, Whiteface and Skaergaard) by Fe XANES analysis of plagioclase and maskelynite to understand the processes that constrain and control plagioclase crystallization on the bodies of interest. Since then, there is no report on the XANES analysis of extraterrestrial and terrestrial plagioclase samples.

However, this method can analyze and evaluate oxygen fugacity of almost all the planetary materials, because plagioclase (and/or maskelynite) is commonly present in these samples. Also, I found that the valence states of iron are variable in these samples possibly due to the variable redox states during their formation. Furthermore, this method can analyze a small mineral and area because ~5 μm beam size can be obtained by SR beam, and thus I found that it is a very effective technique for the analysis of planetary materials.

I tried to make relative comparison of oxygen fugacity by analyzing the iron valence

states of plagioclase and maskelynite with SR Fe micro XANES technique.

I selected samples from two planetary bodies, Mars: the size of about half of the Earth and Vesta: the third largest asteroid in the asteroid belt. I consider that these two bodies are important examples in comparison with the earth in terms of the evolution of planetary materials. I tried to make relative comparison of oxygen fugacity of these two bodies.

In addition, I attempted XANES analysis to estimate redox state of various plagioclase samples recovered from shock-loading experiments. Because all shergottites and most of HED meteorites have experienced heavy shock and one may be concerned that there is a possibility that the Fe^{3+}-Fe^{2+} peak intensity ratios of plagioclase was changed by the impact.

To determine the oxygen fugacity from the results of this XANES analysis, I created a calibration curve by synthetic experiment of plagioclase using the electric furnace under the conditions of controlled oxygen fugacities, and analyzed the specimens by the same XANES technique. By applying this result to the measured Fe^{2+}/Fe^{3+} ratios of maskelynite and plagioclase from Martian and HED meteorites, with the XANES analysis, I discussed the redox states of Mars and Vesta.

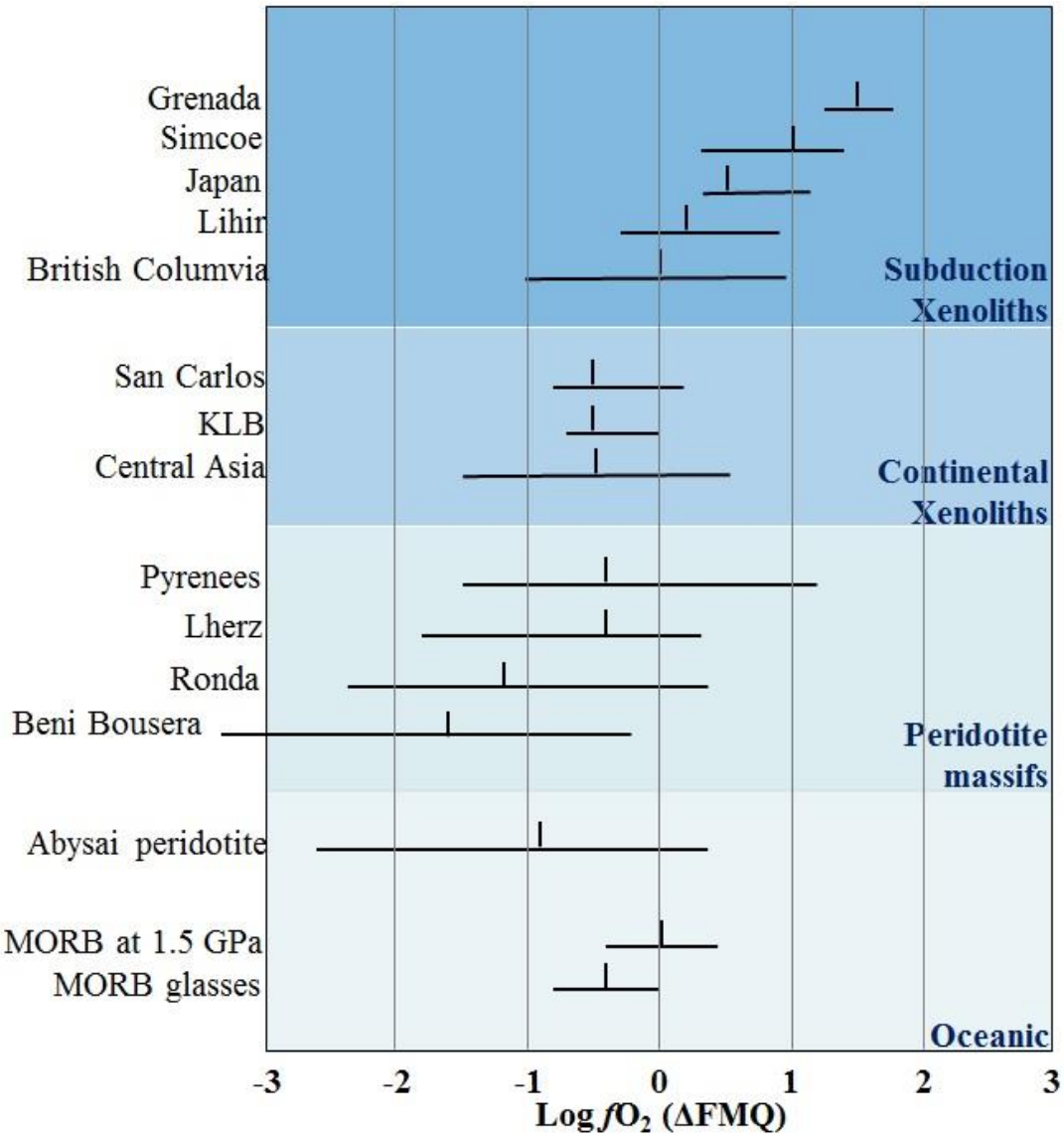

Fig. 1.1 Oxygen fugacities (range and median value) calculated for spinel peridotite assemblages from a number of tectonic settings from Frost and McCammon (2008). Measurements from the same setting are grouped within the shaded regions, which are, from the bottom up, oceanic (Bryndzia and Wood 1990), peridotite massifs (Woodland et al. 1992; Woodland et al. 1996 and 2006), xenoliths from the continental lithosphere (Ionov and Wood 1992), and xenoliths from subduction settings (Wood and Virgo 1989, Canil et al. 1990, Brandon and Draper 1996, McInnes et al. 2001, Parkinson et al. 2003). Included within the oceanic group are fO_2 measurements of MORB glasses (Bézos and Humler 2005) and the same samples corrected to source region conditions of 1.5 GPa (Kress and Carmichael 1991).

1.2 Mars and Martian Meteorites

Recently, several spacecrafts explored Mars, and they have provided new information about the red planet. One of their main purposes is to study the materials present on/in Mars to understand their evolution in relation with its environment. In spite of the addition of tons of remote sensing data by spacecrafts, at present the only available samples from Mars are Martian meteorites.

All known Martian meteorites are igneous rocks and important to understand the evolution of Martian igneous history (e.g., McSween 2002). Martian meteorites have been largely classified into four groups (shergottites, nakhlites, chassignites and orthopyroxenite) based upon petrological features. Shergottite is the largest group and is mainly composed of olivine, pyroxene and plagioclase (now shock transformed to "maskelynite"), which I focus on in this thesis. Furthermore, shergottites have been classified into three subgroups by light rare earth element (REE) abundances: depleted, intermediate and enriched shergottites. Depleted shergottites are low in light REEs while enriched shergottites are high in these elements. Intermediate shergottites are intermediate between the two (e.g., Symes et al. 2008). Recent petrological and isotopic studies have indicated that shergottites show obvious correlations between oxidation states and geochemical characteristics, and such a correlation must have important information about their mantle sources and are directly relevant to the Martian evolution (e.g., Borg and Draper 2003). Combining this result with the results from the estimate of oxygen fugacity by Herd et al. (2002), Borg and Draper (2003) also suggested the correlations of Sm/Nd, $^{87}Sr/^{86}Sr$, and La/Yb ratios with estimated oxygen fugacity. These correlations suggest that the source melt of shergottites (e.g., Shergotty, Zagami, and Los Angeles) that crystallized under relatively oxidized environment and those (e.g., Dar al Gani 476, Yamato 980459, and QUE 94201) crystallized under relatively reduced environment. Thus, the source melt of shergottites was separated into two groups (oxidized shergottites and reduced shergottites), by the large scale fractionation when magma ocean was cooled at around 4.5 Ga (Borg et al. 1997; Debaille et al. 2007). After that, most of them have never been mixed or assimilated over the groups. This geochemical classification of shergottites is independent from petrological classification described above, and they are called depleted shergottites and enriched shergottites, respectively. In this relationship, it has been thus known that depleted shergottites crystallized under reduced environment and in contrast, enriched shergottites crystallized under oxidized environment. The presence of intermediate subgroup has been proposed based on trace element abundance and isotopic ratios (Fig. 1.2) (e.g., Symes et al. 2008).

Such studies showed that there are two models regarding the two geochemical source reservoirs for the shergottites. One model proposes assimilation of oxidized crust by mantle-derived, reduced magmas (Fig. 1.3) (Herd et al. 2002; Wadhwa et al. 2001). In this model, the assimilated enriched reservoir occurs as domains in the crust, which must be traversed by ascending mantle magmas. In contrast, Herd et al. (2006) proposed that the assimilation is not a viable mechanism for oxidation of Martian basalts. They suggested that the results of oxygen fugacity measurement and textural observations are strongly indicative of a xenocrystic origin for the olivine megacrysts and associated chromite of NWA 1068/1110, and lend support to a model in which oxygen fugacity of Martian basalt is determined by mantle-source redox conditions as opposed to assimilation of oxidized crustal material. However, Papike et al. (2013) lately proposed a model that the source of enriched shergottites is at the crust-mantle boundary where heavy volcanic edifices cause crustal down-warping and basalt ponding by the experiments focusing upon mineralogical and crystal chemical aspects of the basalt-eclogite transformation on Mars. This model is similar to the previous assimilation model.

The other model proposes mixing of two distinct mantle reservoirs during melting as stated above (Fig. 1.4) (Symes et al. 2008; Borg and Draper 2003; Treiman et al. 2003). In this model, both geochemical reservoirs resided in the mantle and were formed as a result of either crystallization of a magma ocean to produce geochemically-depleted and enriched domains (Borg and Draper 2003), or fluid-induced metasomatism that produced mantle heterogeneity (Treiman et al. 2003). Furthermore, Herd et al. (2006) proposed that the heterogeneous mantle model in which the oxygen fugacity of Martian basalts is a function of the redox conditions of their mantle source.

Based on the application of some oxybarometers, it is inferred that the Martian mantle records significant redox variations from log fO_2 = QFM –3 to log fO_2 = QFM. Although there are few data of oxygen fugacity in shergottites, the relationship between the results of the oxygen fugacity and the isotopic characteristics (Fig. 1.5) suggested that intermediate mantle source formed by mixing of depleted and enriched mantle sources.

According to the result of two oxybarometers (Ol-Sp-Opx and Fe-Ti oxides), Peslier et al. (2010) found that the increase of redox states by ~2 log units likely occurred during fractional crystallization and ascent of magma by analysis of LAR 06319 shergottite. The cause for the wide range of oxygen fugacity of the mantle instead may be features acquired early in the planet's history during the magma ocean solidification and it is more readily explained by a process such as planet-wide slow crystallization and stratification (Peslier et al. 2010). Furthermore, Shearer et al. (2013) reconstructed the

crystallization history of two shergottites (NWA 1183 and Y 980459) using phosphorus zoning and placed trace element variation of olivine megacrysts. This study suggested that enriched and depleted sources for the shergottites reside in the mantle, and that magmas produced in these sources have different capabilities for changing their redox state during crystallization.

Therefore, it is important to estimate redox states and compare geochemical characteristics of much more shergottite samples for revealing the evolution of Martian mantle and crust.

Although Fe-Ti oxides and/or Ol-Sp-Opx oxybarometers are used to estimate redox states of shergottites, these minerals are not always in equilibrium in rapidly cooled samples, and therefore, these methods cannot be used to estimate redox states of all shergottites. In such a circumstance, it is important to focus on a mineral that is commonly present in all samples and thus I paid attention to iron valences of plagioclase (maskelynite). Delaney et al. (1998) and Polyak et al. (2001) briefly reported the Fe-XANES analysis of maskelynite in six shergottites as already stated, but the relationship between oxygen fugacity and geochemical characteristics were not known at the time and the number of the known shergottites was much smaller.

Since then, a number of shergottites have been recovered especially from African/Arabian deserts and Antarctica, and at present we can make a better comparison of many shergottite samples. Thus, it is a good timing to explore the redox state of Mars by using the Fe micro-XANES analysis of maskelynite and plagioclase in shergottites. Especially, recent finding of an intermediate mantle source is a key to understand the evolution of Martian mantle and it is proposed to be formed by mixing of depleted and enriched mantle sources (e.g., Symes et al. 2008). Therefore, analyzing many intermediate shergottites is a point of this study to confirm the origin of intermediate mantle source, and the discussion of the intermediate mantle source is important to verify the two basic models proposed for the Martian mantle.

Thus, Fe micro-XANES analysis of maskelynite and plagioclase is significant because it can provide useful information about the evolution of the inner structure of the Martian crust. As described above, I focus on the formation of intermediate mantle source to verify whether it can be formed by simple mixing of depleted and enriched mantle sources in terms of their distinct redox states. In this study, I analyzed fourteen shergottites and tried to interpret the obtained redox data by verifying which mantle model is better supporting the results.

Furthermore, as I wrote in the section “Oxygen fugacity”, this method can be applied to not only for all shergottites, but also for other planetary materials. In fact, I analyzed

meteorites from Vesta as shown in the following chapter.

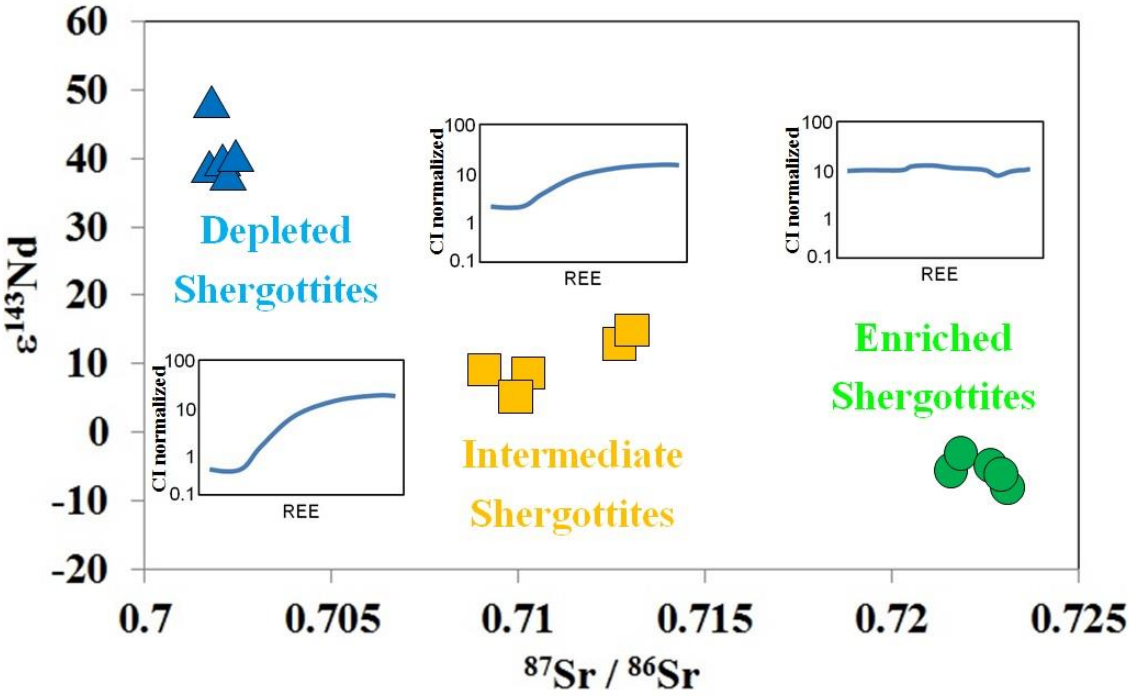

Fig. 1.2 Relation between ε^{143}Nd and Sr-Nd isotopic ratios of shergottites (after Symes et al. 2008). They proposed that shergottites can be classified into three subgroups by geochemistry.

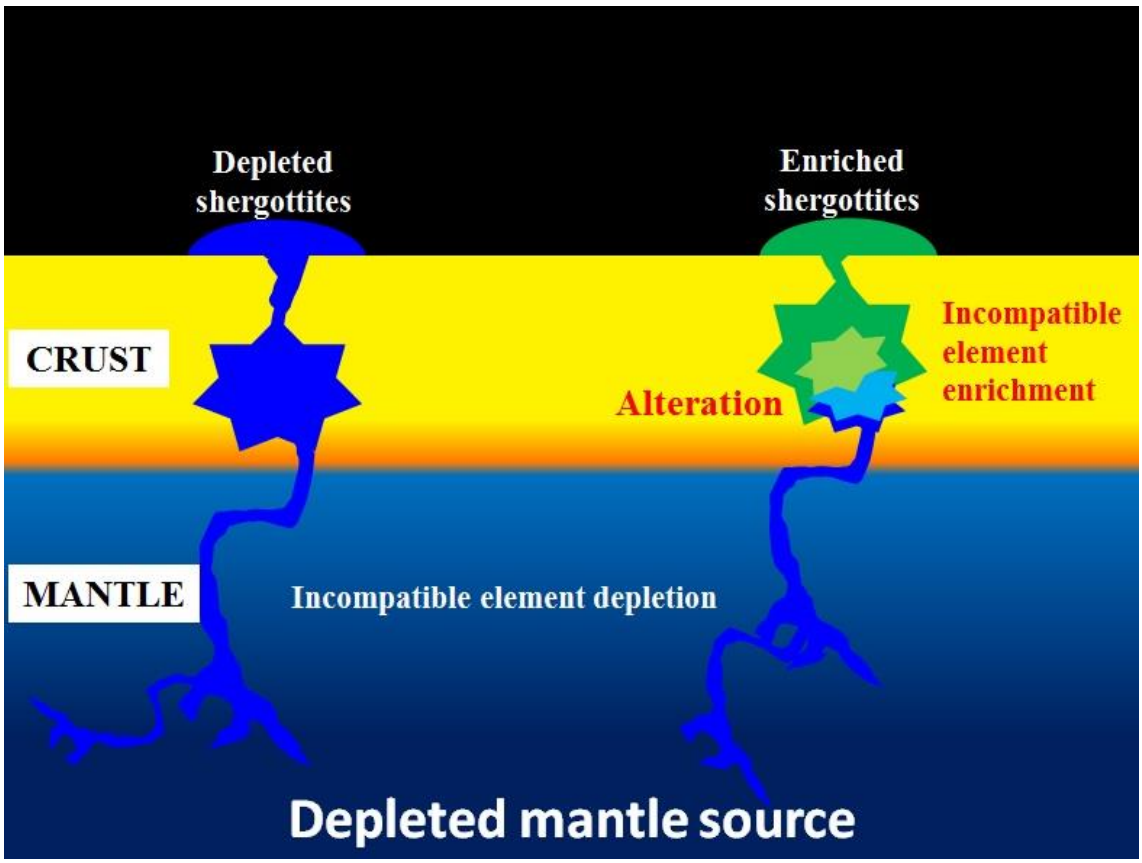

Fig. 1.3 Schematic illustration of the Martian interior showing two geochemical sources (after Wadhwa et al. 2001). This illustration shows that magma interacts with altered (weathered or chemically reacted with hot water) basalt to various extents.

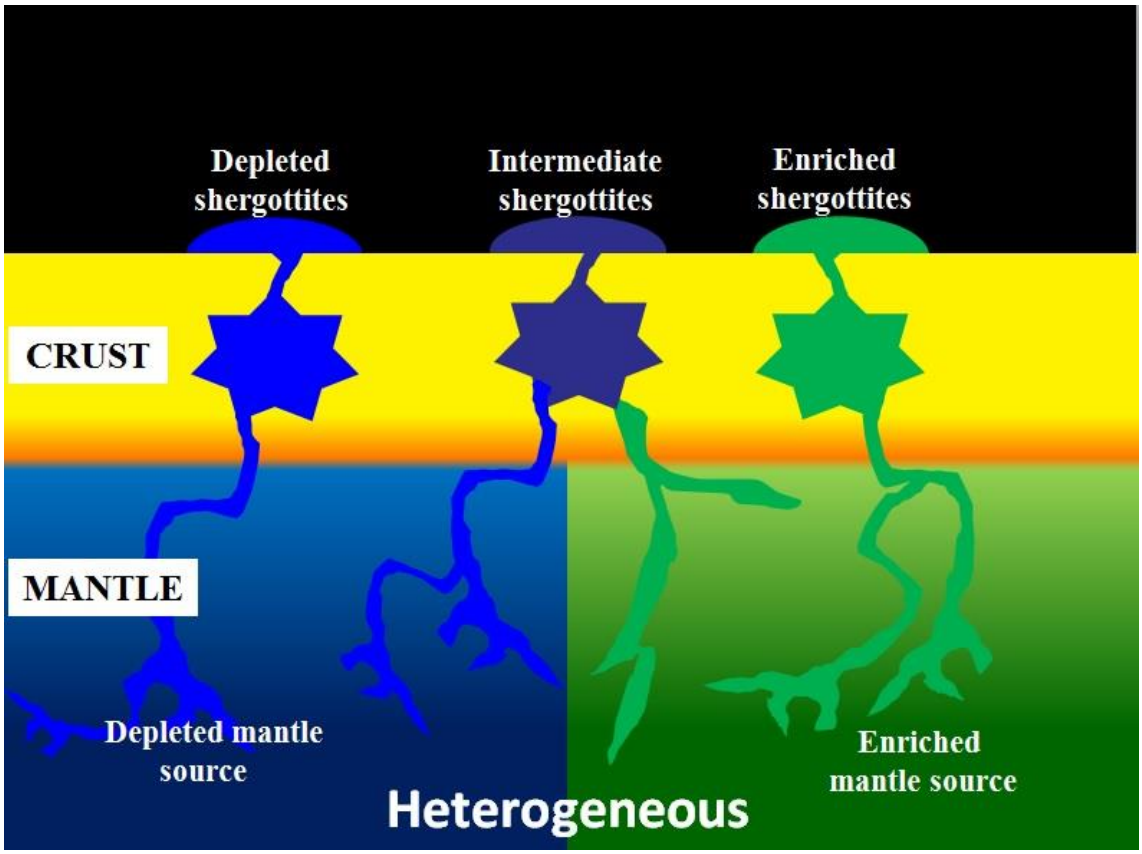

Fig. 1.4 Schematic illustration of the Martian interior showing the two geochemical sources (after Borg and Draper 2003). This model shows that two distinct reservoirs were produced early in Martian history. One is depleted in trace elements and is highly reducing. The other is enriched in trace elements and oxidized.

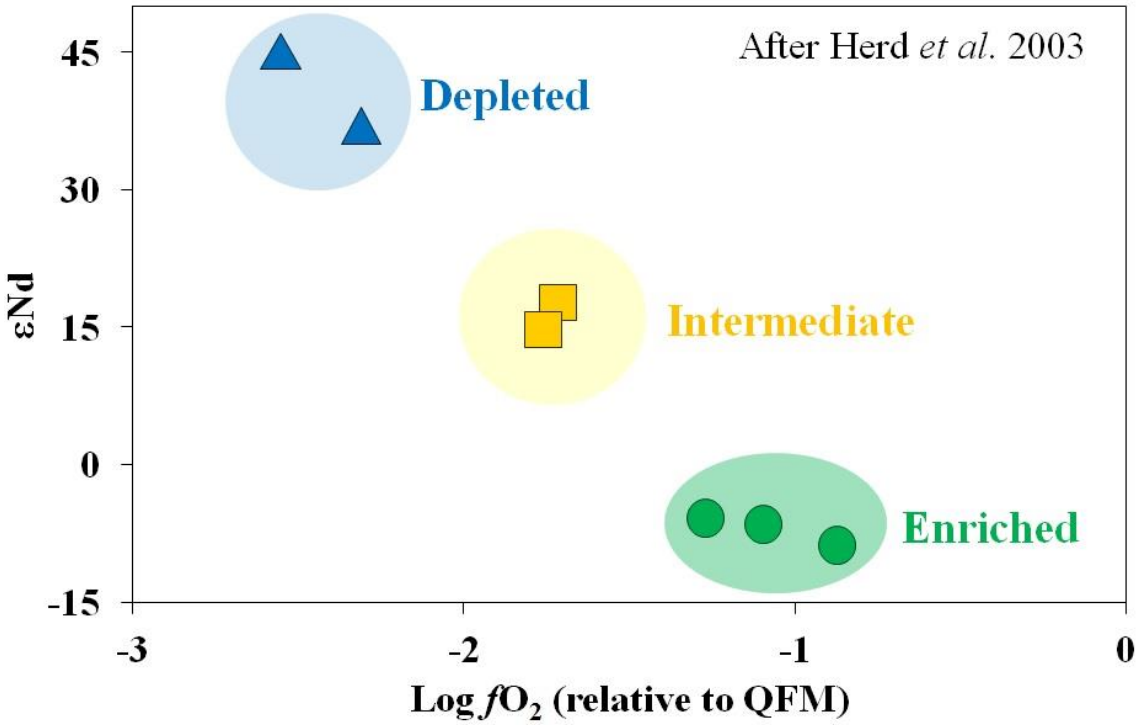

Fig. 1.5 The relationship between the oxygen fugacity estimated by Fe-Ti oxides oxybarometer and the Nd isotopic ratios of shergottites (after Herd et al. 2003). This diagram indicates that an intermediate mantle source formed by mixing of depleted and enriched mantle sources.

1.3 HED Meteorites

The HED (Howardites, Eucrites and Diogenites) meteorites are the largest group of achondrites and are considered to have originated on Vesta (e.g., McCord et al. 1970). Recently, the Dawn spacecraft has observed from the orbit and has revealed the existence of a metallic core in Vesta (Russel et al. 2012). This strongly indicates that Vesta has experienced early differentiation in the solar system (e.g., Russel et al. 2012). Furthermore, the mineral data obtained by the Dawn's visible and infrared spectrometer is consistent with the mineralogical information of HED meteorites (Sanctis et al. 2012). In this way, Vesta is an important example of early planetary differentiation in the solar system, and thus, HED meteorites may offer substantial information to understand igneous differentiation on Vesta (e.g., Takeda et al. 1997). In addition, HED meteroites are among the oldest differentiated materials in the solar system, with crystallization ages of only ~3 Myr after the CAI formation (Trinquier et al. 2008).

Eucrite is pyroxene-plagioclase achondrite and it originated from Vesta's crust. Diogenite is monomict or unbrecciated achondrite with major orthopyroxene and it is considered that most samples originated from Vesta's mantle. Howardites are polymict breccias of diogenites and eucrites, and contain over 10% of orthopyroxene (e.g., Takeda et al. 1997) (Fig. 1.6).

Eucrites are generally divided into three subgroups by texture: surface eucrites, ordinary eucrites and cumulate eucrites (Fig. 1.6) (McCarthy et al. 1973). All eucrites are mainly composed of pyroxene and calcic plagioclase with accessory ilmenite, chromite, troilite, Fe metal, apatite, zircon and silica mineral, and have a basaltic composition, although texture is different from one group to another. The chemical composition, extent of chemical zoning and the abundance ratio of constituent minerals also varies among these groups (e.g., Takeda et al. 1997).

Surface eucrites crystallized near the surface of Vesta. Pyroxene included in surface eucrites shows needle shape and strong chemical zoning, suggesting that they had undergone very rapid cooling near the surface (Takeda et al. 1978). Augite exsolution lamellae in pyroxene are rare or very fine which can be found only by using transmission electron microscope (TEM) analysis (Takeda et al. 1978). The grain size of both pyroxene and plagioclase is thus small (Takeda et al. 1978).

Ordinary eucrites crystallized below the surface eucrites on the Vesta. Plagioclase shows a lath shape and weak chemical zoning at the rim. Takeda et al. (1997) reported that pyroxene is subhedral to anhedral pierced by euhedral plagioclase laths and has fine to medium augite exsolution lamellae (5-20 μm) due to moderate cooling. The grain size of constituent minerals of ordinary eucrites is medium to large (>~300 μm).

Cumulate eucrites are considered to have crystallized below the ordinary eucrite layer. It is composed of coarse-grained gabbros and shows a cumulate texture of subhedral pyroxene and euhedral plagioclase. Ca-poor pyroxene and Ca-rich plagioclase are dominant. Pyroxene is more Mg-rich than ordinary and surface eucrites, and has thick augite exsolution lamellae (Miyamoto and Takeda, 1977). Chemical zoning of plagioclase and pyroxene is not clear and they are homogenized. These explain that pyroxene in cumulate eucrites crystallized and accumulated on the diogenite layer with Ca-rich plagioclase before the formation of pyroxene in ordinary eucrites, and underwent slow cooling (Takeda 1979).

The earliest petrogenetic model showed that the lithologies in the HED group plausibly represent a fractional crystallization sequence from early orthopyroxenites, through increasing plagioclase content to the basaltic eucrite (Mason 1962). The chondritic body depleted in Na was totally melted, a metallic core segregated, and the silicate melt solidified via fractional crystallization. In this model, the crust of the asteroid from top down was composed of eucrites, howardites and diogenites. The characteristics of this model are that howardite is a brecciated igneous rock type, not a mixture of lithologies.

Then, Stolper (1977) suggested that an alternative model for eucrite petrogenesis in which the basaltic eucrites represent primary partial melts of their parent body. This model is based on the results of melting experiments on basaltic eucrites in which he found conditions of temperature and oxygen fugacity at which the eucrites are multiply saturated with pyroxene, plagioclase, olivine, metal and spinel. In this model, the parent body undergoes minimal heating as total melting is not envisioned.

These two models represent end member models, and several intermediate or hybrid models have been developed.

Ikeda and Takeda (1985) proposed a magma ocean model for the HED petrogenesis. This model showed an accretional energy source to cause total melting of the outer portion of the parent asteroid, producing a thin magma ocean. The magma ocean undergoes fractional crystallization and volatile loss, producing first dunites and then orthopyroxenites (diogenites). The important point of this model is that at some point during crystallization, the surface of the magma ocean became a stable, crystalline “scum” layer composed of volatile-poor eucrites. The lower region was occasionally extruded and became volatile-rich.

Jones et al. (1996) reported that five eucrites (Bouvante, Stannern, Cachari and Sioux County) are primary partial melts. On the other hand, Ruzicka et al. (1997) reported basaltic eucrites (without Bouvante and Stannern) formed form a magma ocean that first

fractionally crystallized. In this way, the partial melt vs. residual melt origin for main-group eucrites remains an unsettled problem.

In addition, Barrat et al. (2010) reported that the anomalies of diogenite are the first firm indication that parental melts of diogenites have intruded into the eucritic crust, and consequently are younger than eucrites.

Recently, Mandler et al. (2013) proposed a model to produce all the igneous HED lithologies by invoking 60–70% equilibrium crystallization of a magma ocean followed by continuous extraction of the residual melt into shallow magma chambers.

Thus, as shown by these previous studies, the interior of Vesta is complex.

As described in the chapter 1.1, oxygen fugacity during the core formation of Vesta has been estimated. Pringle et al. (2013) suggested that Vesta accreted from reduced volatile-poor materials much closer to the Sun and later moved outwards to its present location. In addition, oxygen fugacity of diogenite was estimated in order to compare diogenites and mesosiderites. The oxygen fugacity of two diogenites (Johnstown and Tatahouine) is log fO_2 = IW (Hewins 1984). This result is higher than the redox states during the core formation (Pringle et al. 2013). However, redox states of eucrites have not been estimated and it is not possible to discuss the transition of the redox states during the formation of Vesta. Moreover, there is a room for the improvement of the partial melt and residual melt models. Thus, I reconsider these formation models from the point of view of oxygen fugacity in order to better understand the early differentiation of Vesta. In particular, I focused on the period of the later stage during the Vesta's crust formation.

In this way, I focused on eucrites with variable grain sizes that were formed by different cooling histories due to different formation depths in the crust, and analyzed plagioclase in these samples by SR Fe XANES to discuss their redox states during the crust crystallization.

My literature search showed that there is only one report studying XANES analysis on HED meteorites (Delaney et al. 1998). They reported that plagioclase in EETA 87520 eucrite has high energy side of Fe^{3+} Kα absorption edge peak position. However, Delaney et al. (1998) analyzed only this sample and did not discuss the redox state of eucrites in general.

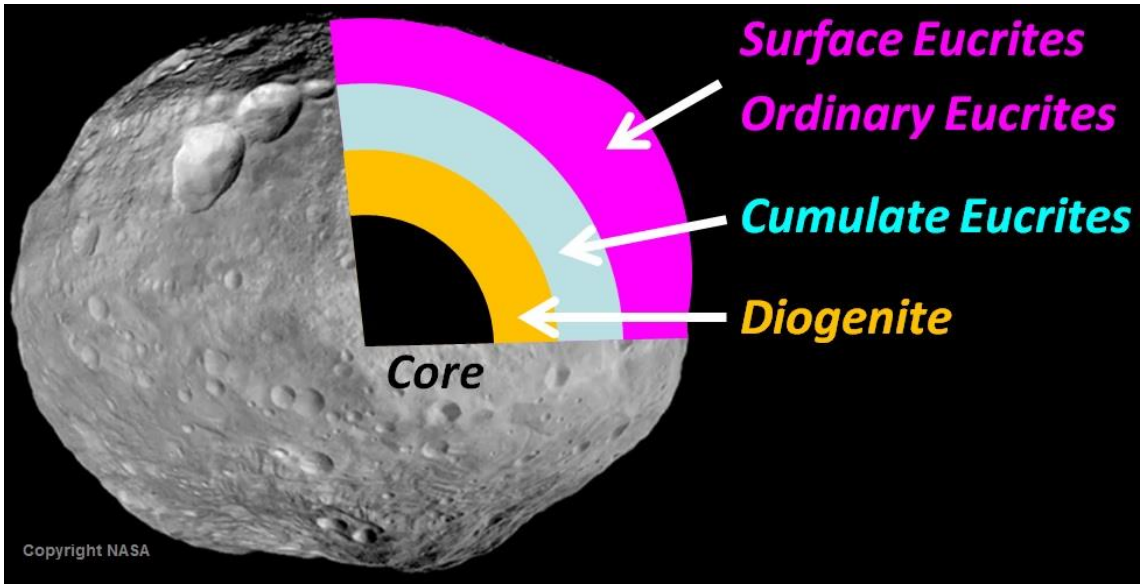

Fig. 1.6 An early model of the layered crust of the HED parent body Vesta.

2 Samples

2.1. Shergottites

I studied polished thin sections of two geochemically-depleted (Dar al Gani 476 and Dhofar 019), four geochemically-intermediate (ALH 77005, EETA 79001 lithology A, LEW 88516 and NWA 5029) and eight geochemically-enriched (Dhofar 378, LAR 06319, NWA 856, NWA 1068, NWA 4468, Zagami, RBT 04262 and Shergotty) shergottites. One polished thin section of each shergottite was analyzed in this study. The sizes of thin sections are Dar al Gani 476: 10x6 mm, Dhofar 019: 7x3 mm, ALH 77005: 7x5 mm, EETA 79001 lithology A: 4x3 mm, LEW 88516: 6x4 mm, NWA 5029: 12x9 mm, Dhofar 378: 6x3 mm, LAR 06319: 9x7 mm, NWA 856: 8x6 mm, NWA 1068: 4x3 mm, NWA 4468: 9x7 mm, Zagami: 5x5 mm, RBT 04262: 12x10 mm and Shergotty: 13x2 mm, respectively.

The thin sections of LEW 88516, EETA79001 lithology A, LAR 06318 and RBT 04262 were supplied by The Meteorite Working Group, USA. The ALH77005 thin section was supplied by National Institute of Polar Research, Japan.

2.1.1. Dar al Gani 476

This meteorite was found in 1998, in the Dar al Gani region of the Libyan Sahara (Zipfel et al. 2000). Dar al Gani 476 is mainly composed of olivine, pyroxene and maskelynite with accessory Ca phosphates (Fig. 2.1) and mineralogical mode of this sample was 25% olivine, 60 % pyroxene, 10% maskelynite and Ca phosphates. This meteorite shows a porphyritic texture with large olivine phenocrysts set in the groundmass of smaller pyroxene and maskelynite grains. Dar al Gani 476 is classified as an olivine-phyric shergottite. Olivine grains are euhedral to subhedral and their sizes are over 1 mm and sometimes embayed by the groundmass minerals, suggesting reaction with the groundmass magma (Mikouchi et al. 2001). Olivine shows extensive chemical zoning from the Fo_{76} cores to the Fo_{58} rims. In the groundmass the pyroxenes (about 500μm) are larger than the maskelynites (200 μm). Pyroxenes are elongated in shape and maskelynites are subhedral.

Low-Ca pyroxene is zoned from En_{76} Fs_{21} Wo_3 to En_{58} Fs_{30} Wo_{12} (Zipfel et al. 2000, Folco et al. 2000, Mikouchi et al. 2001). All plagioclase grains in this sample are changed to maskelynite by shock metamorphism. The maskelynite composition in Dar al Gani 476 is An_{70-62} and the FeO abundance is 0.3 to 0.6 wt% (Table 2.1 and Fig. 2.2). The light rare earth element abundance is low, the value of La/Yb is about 0.13 (Barrat et al. 2001) and it is classified as a depleted shergottite.

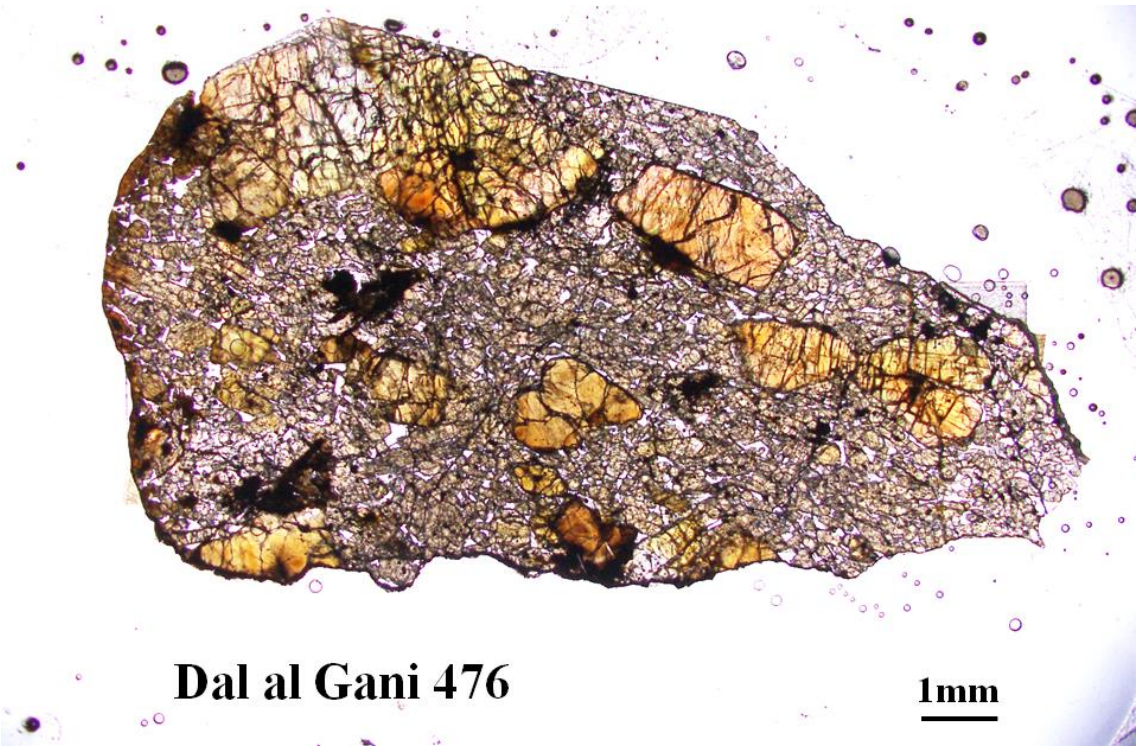

Fig. 2.1 Optical photomicrograph of Dar al Gani 476 (plane-polarized light).

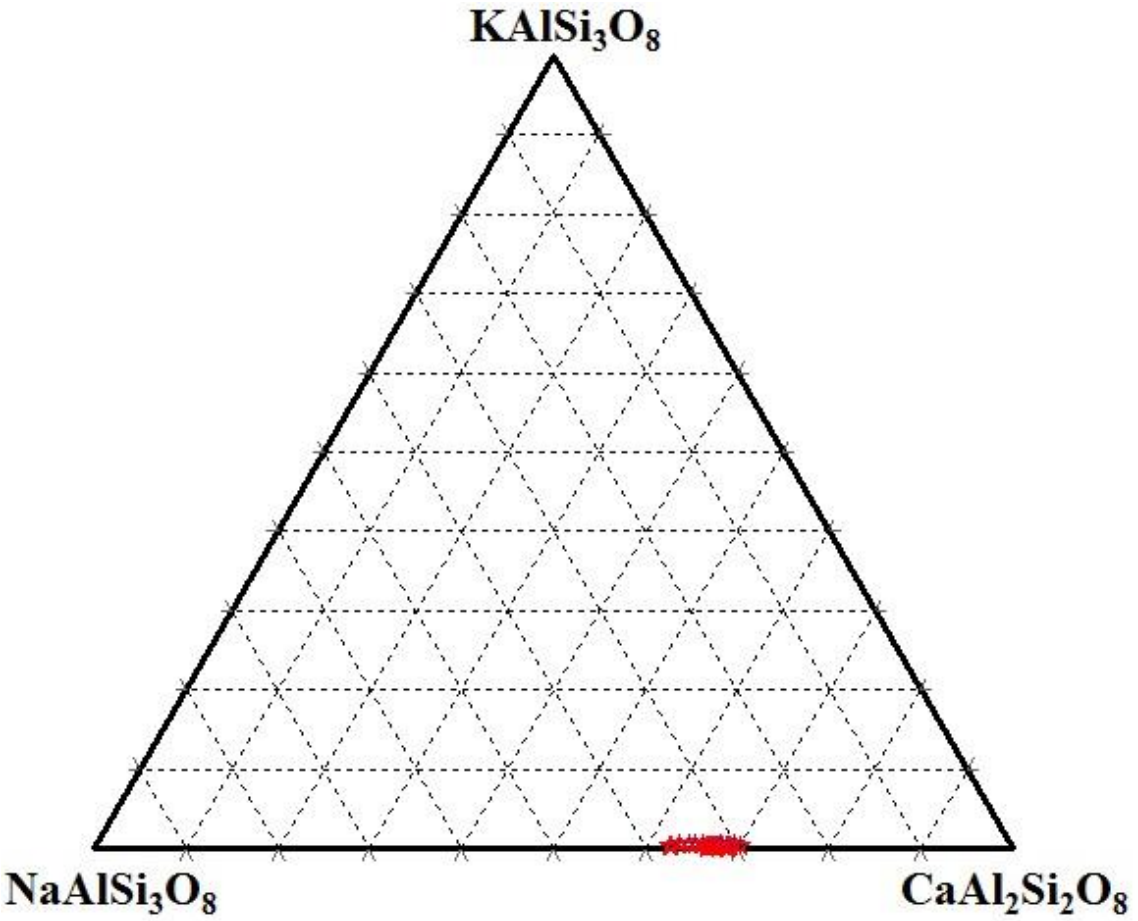

Fig. 2.2 Chemical composition of maskelynite in Dal al Gani 476.

2.1.2. Dhofar 019

Dhofar 019 was found in Oman in January 2000 (Grossman 2000). Borg et al. (2001) reported a Sm-Nd age of 575±7 m.y. for Dhofar 019 and this age is older than those of other shergottites. The texture of this sample shows the presence of large olivine phenocrysts with smaller pyroxene and maskelynite grains in the groundmass (Fig. 2.3). According to this characteristic, it is classified as an olivine-phyric shergottite. The modal abundances of minerals are 25% olivine, 60% pyroxene, 20% maskelynite with some accessory minerals such as Ca phosphates. Olivine grains are subhedral and their sizes are about 500 μm. Mikouchi and Miyamoto (2001) reported the olivine composition of Fo_{73-25}. Pigeonite ($En_{40-70}Wo_{5-9}$) is commonly rimmed with augite ($En_{40-50}Wo_{30-40}$). All of plagioclase are converted to maskelynite by shock metamorphism and their sizes are about 300 μm. Mikouchi and Miyamoto (2001) pointed out that Dhofar 019 showed a close mineralogical relationship to EETA 79001

and Dar al Gani 476. The maskelynite composition in Dhofar 019 is An_{59-49} and the FeO abundance is 0.2 to 0.5 wt% (Table 2.1 and Fig. 2.4). Neal et al. (2001) reported that Dhofar 019 is interpreted as a melt product derived from a source already depleted in incompatible elements and Platinum Group Elements (PGEs). The La/Yb ratio is 0.282 and it is classified as a depleted shergottite.

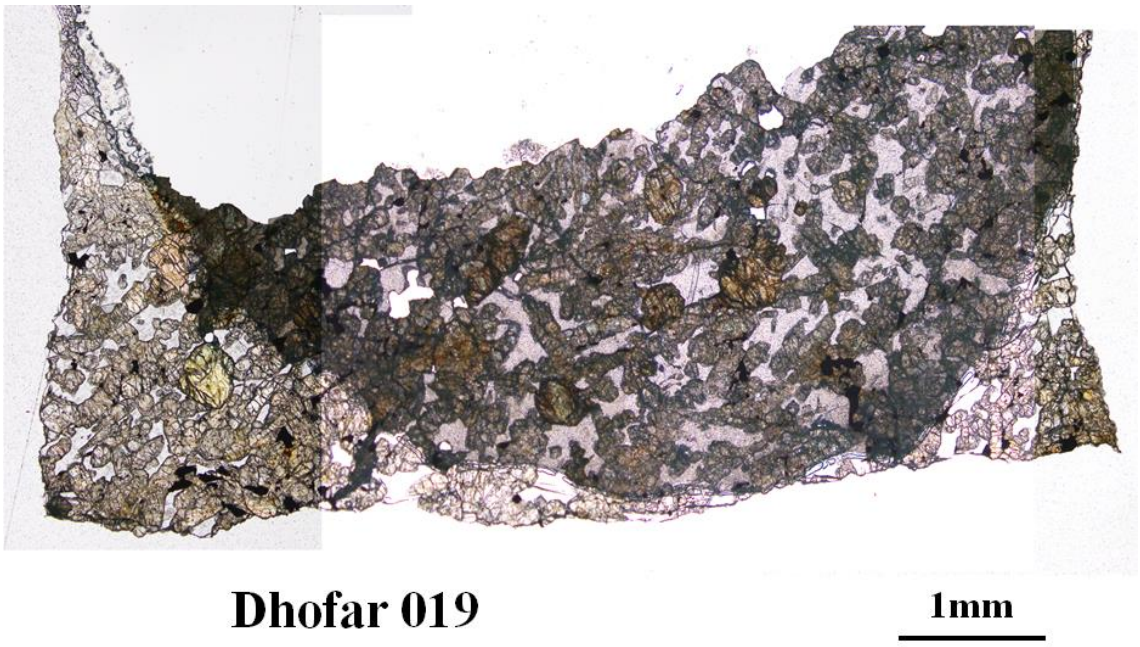

Fig. 2.3 Optical photomicrograph of Dhofar 019 (plane-polarized light).

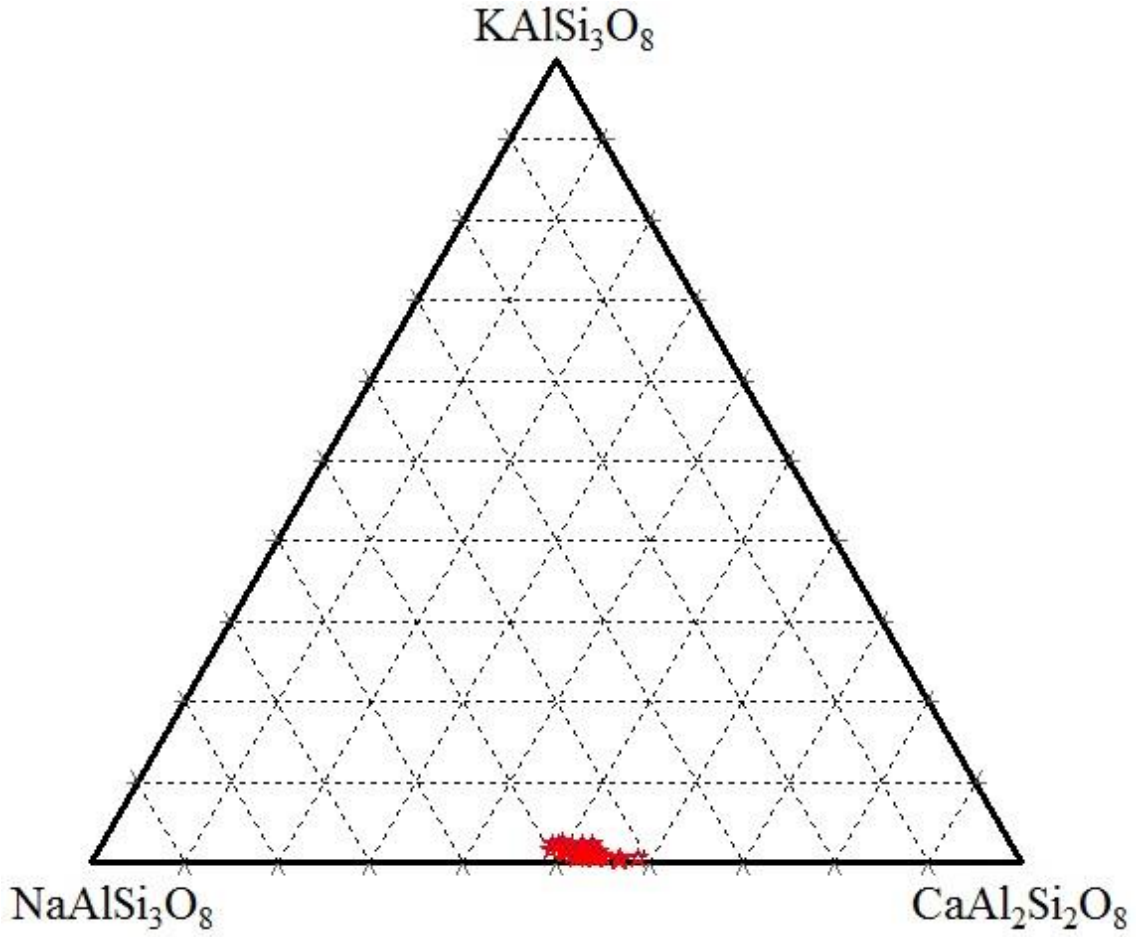

Fig. 2.4 Chemical composition of maskelynite in Dhofar 019.

2.1.3. ALH 77005

ALH 77005 is an Antarctic meteorite and it was found partially imbedded in the ice at the Allan Hills site (Yanai et al. 1978). ALH 77005 has been more heavily shocked than the other Martian meteorites. ALH 77005 mainly contains olivine, pyroxene, maskelynite and shock melt. Mineralogical modes of ALH 77005 are 35% olivine, 40% pyroxene, 10% maskelynite and 15% melt. The texture is characterized by large pyroxene oikocrysts enclosing olivine (Fig. 2.5). For this characteristic texture, it is classified as a lherzolitic shergottite. Mikouchi and Miyamoto (1997) reported that the large pyroxene in the poikilitic portion of ALH 77005 show chemical zoning from high-Mg, low-Ca orthopyroxene cores to Mg-rich pigeonite rims of ferroan pigeonite. Olivine has an unusual, distinctive pale brown color. Olivine shows subhedral shapes and their grain sizes reach up to 1 mm. ALH77005 contains small areas showing partial recrystallization of plagioclase as described by Ikeda (1994). There are variable sizes of

maskelynite and the size of the largest grain is about 1 mm. Maskelynite is found to have refractive indices lower than that in other shergottites (McSween and Stöffler 1980; Stöffler et al. 1986). Stöffler et al. (1986) reported that ALH 77005 reached equilibrium shock pressure of 43±2 GPa and post-shock temperature of 400-800 ^{o}C. The maskeynite composition in ALH 77005 is An_{53-40} and the FeO abundance is 0.4 to 1.0 wt% (Table 2.1 and Fig. 2.6). The light rare earth element abundance is low. The value of La/Yb is about 0.58 (Lodder et al. 1998) and it is classified as an intermediate shergottite.

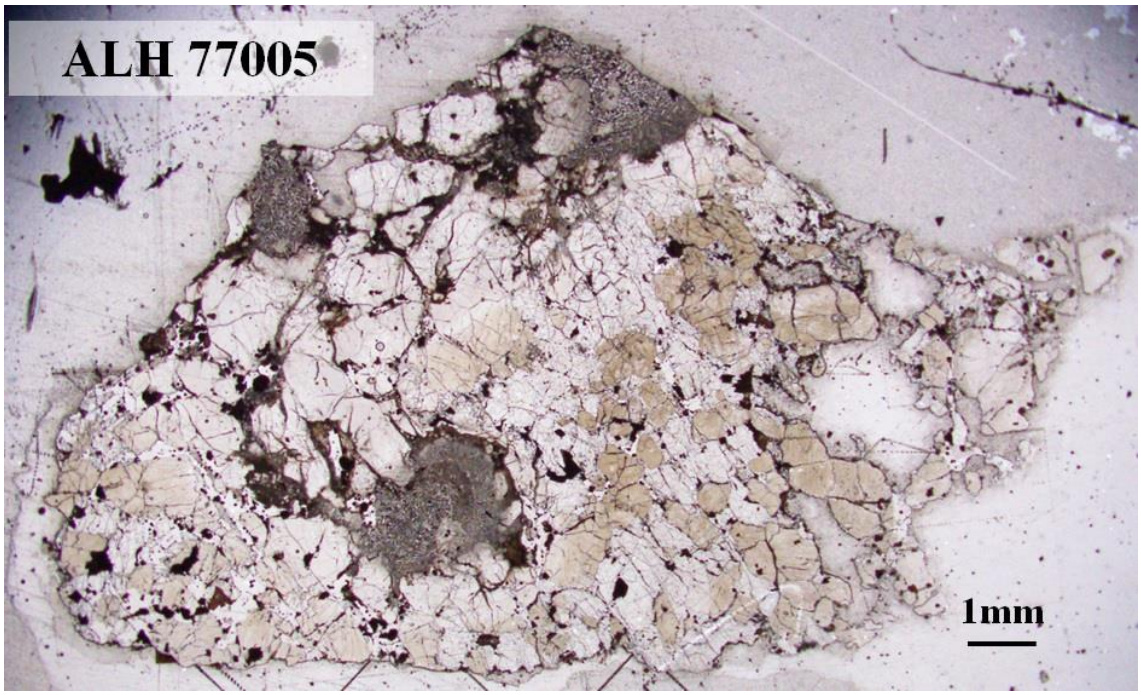

Fig. 2.5 Optical photomicrograph of ALH 77005 (plane-polarized light).

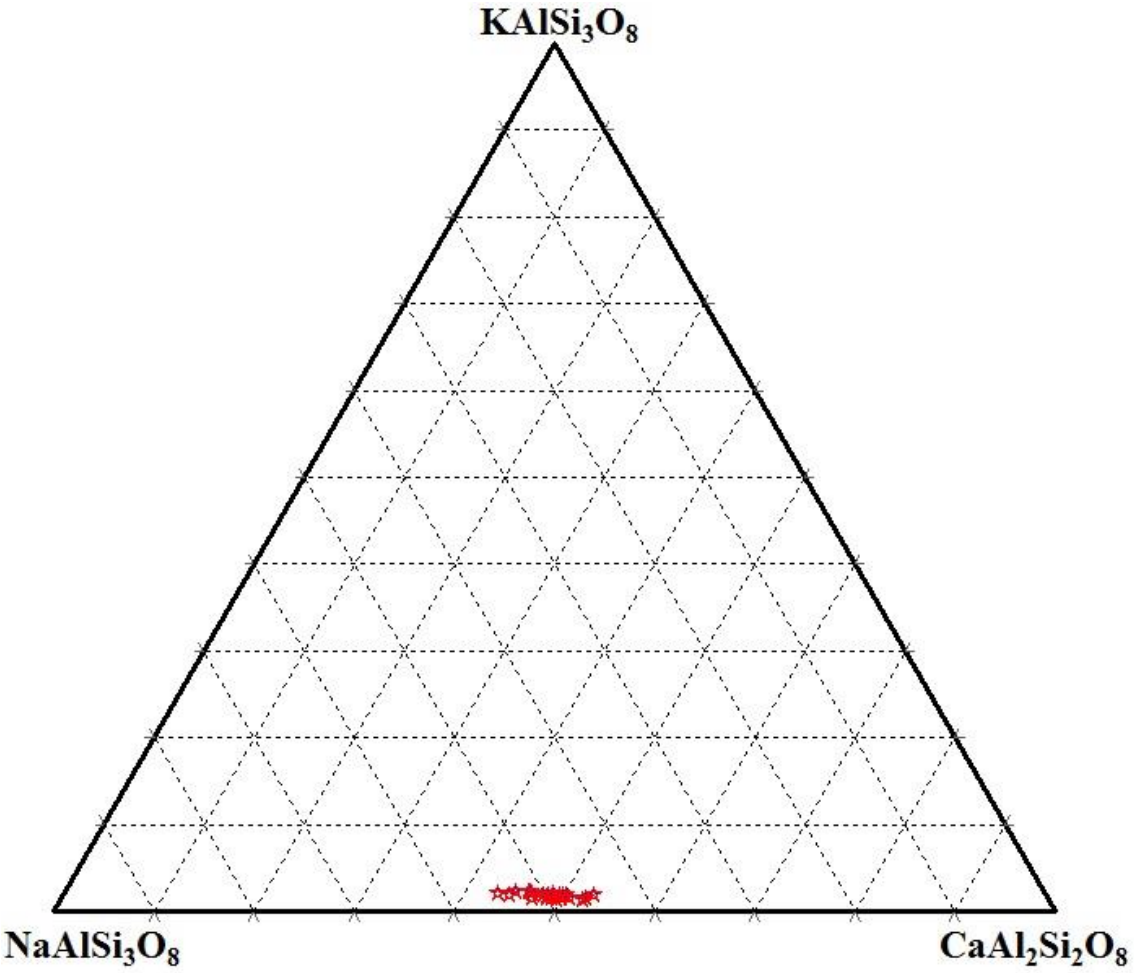

Fig. 2.6 Chemical composition of maskelynite in ALH 77005.

2.1.4. EETA 79001 (lithology A)

EETA 79001 was found on the ice at the Elephant Moraine location near Reckling Peak, Victoria Land, Antarctica. It is the largest stony meteorite returned by the 1979-1980 ANSMET expedition (Cassidy and Rancitelli 1982). Glass inclusions in EETA 79001 were found to contain gas and its noble gas composition is consistent with the Martian atmosphere as determined by the Viking spacecraft (Bogard and Johnson 1983; Becker and Pepin 1984; Ott and Begemann 1985). EETA 79001 contains two different igneous lithologies (A and B). Lithology B is a basalt composed of only pyroxene and maskelynite, while lithology A is more Mg-rich and contains olivine. This sample (lithology A) shows large olivine phenocrysts with smaller pyroxene and maskelynite grains in the groundmass. According to this texture, the lithology A of EETA 79001 is now termed as an olivine-phyric shergottite (Fig. 2.7). It is mainly

composed of pyroxene, olivine megacrysts, maskelynite and accessory phases. Olivine has a compositional range of Fo_{81-55} (Steele and Smith 1982). Pyroxene also shows chemical zoning. The xenocryst clusters in EETA 79001 lithology A were composed of Mg-rich orthopyroxene coexisting with olivine. The groundmass consists of zoned pigeonite and sub-calcic augite. Plagioclase has been converted to maskelynite by shock as is the case for other shergottites. Maskelynites show subhedral shapes and their grain sizes are about 300 to 500 μm. The maskelynite composition of EETA 79001 lithology A is An_{59-56} and the FeO abundance is 0.5-0.8 wt% (Table 2.1 and Fig. 2.8). The La/Yb ratio is 0.37 (Warren et al. 1997), indicating that it is an intermediate shergottite.

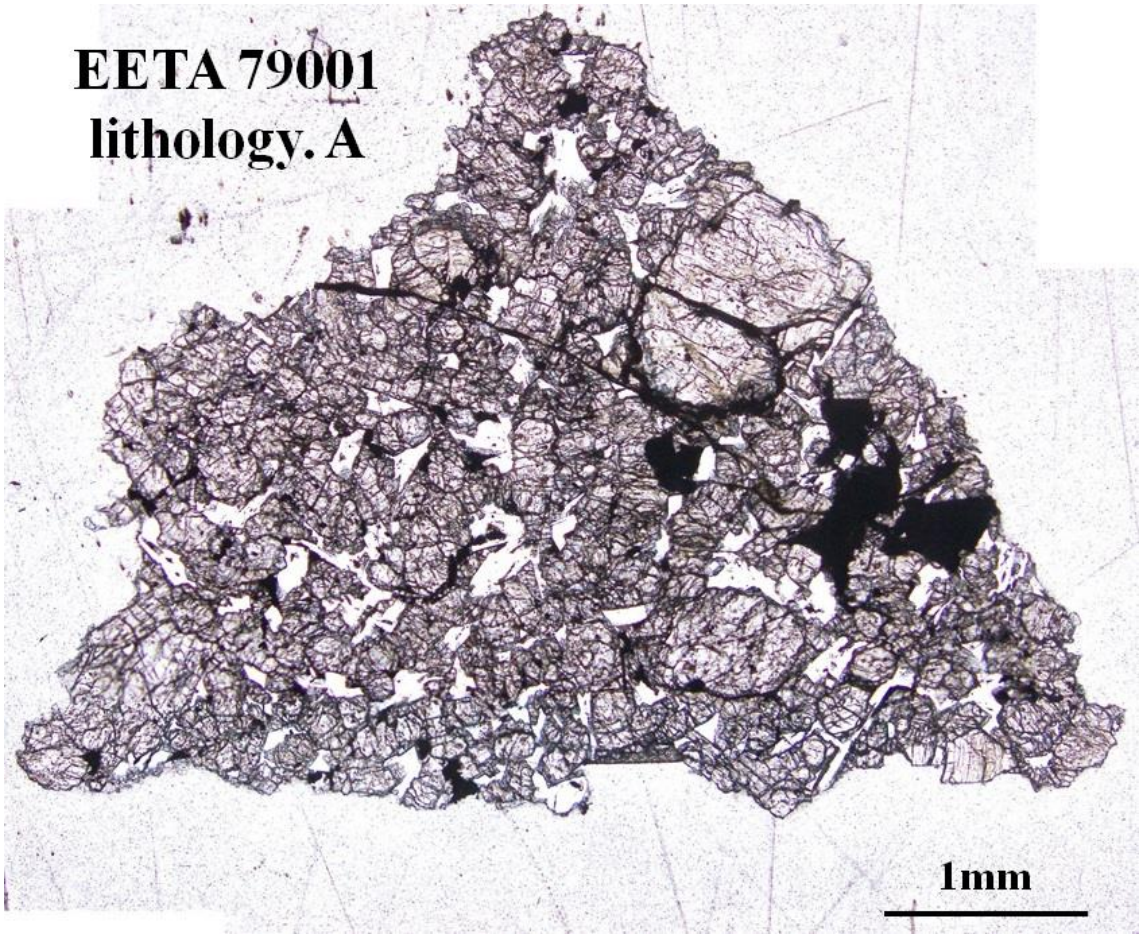

Fig. 2.7 Optical photomicrograph of EETA 79001 (lithology A) (plane-polarized light).

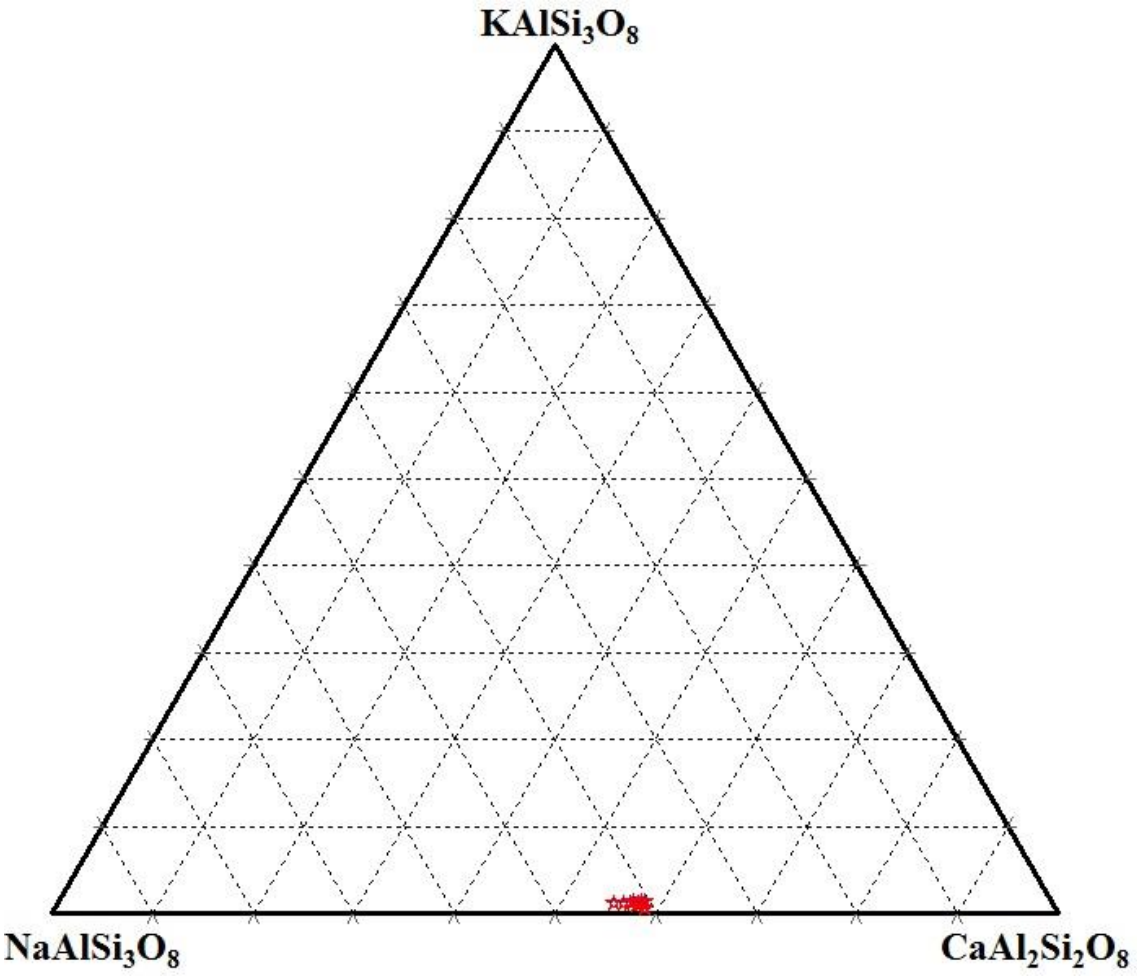

Fig. 2.8 Chemical composition of maskelynite in EETA 79001 (lithology A).

2.1.5. LEW 88516

LEW 88516 was found in Lewis Cliff, Antarctica and it is petrologically similar to ALH 77005 (Treiman et al. 1994). Because of their distinct terrestrial exposure ages (Eugster et al. 1996), they are not paired. Satterwhite and Masson (1997) reported that LEW 88516 had a pitted and mostly shiny fusion crust over 80% of the surface. It is mainly composed of olivine, pyroxene and maskelynite with accessory Ca phosphates and chromite (Fig. 2.9). Mineralogical mode of LEW 88516 is 40 % olivine, 40% pyroxene, 15% maskelynite and other minerals. Chromite is the most abundant accessory mineral in this sample. Mikouchi and Miyamoto (2000) and Monkawa et al. (2001) found kaersutite amphibole in melt inclusions in orthopyorxene and reported its unusually high Ti content. LEW 88516 is dominated by large pyroxene oikocrysts enclosing olivine chadacrysts (Fig 2.9). For this reason, it is classified as a lherzolitic

shergottite. Olivine is a major component of the non-poikilitic portion of this sample and is compositionally zoned from Fo_{70-64} (Treiman et al. 1994). Their sizes are up to 1 mm. There are two types of pyroxene in LEW 88516. One is low-Ca pyroxene and the other is high-Ca pyroxene. The size of pyroxenes is about 2 mm. Plagioclase in LEW 88516 is completely transformed to isotropic glass and it is maskelynite. Maskelynite grains are about 700 μm. The maskelynite composition in LEW 88516 is An_{58-55} and the FeO abundance is 0.3-0.6 wt% (Table 2.1 and Fig. 2.10). The La/Yb ratio is 0.62 (Gleason et al. 1997) and it is classified as an intermediate shergottite.

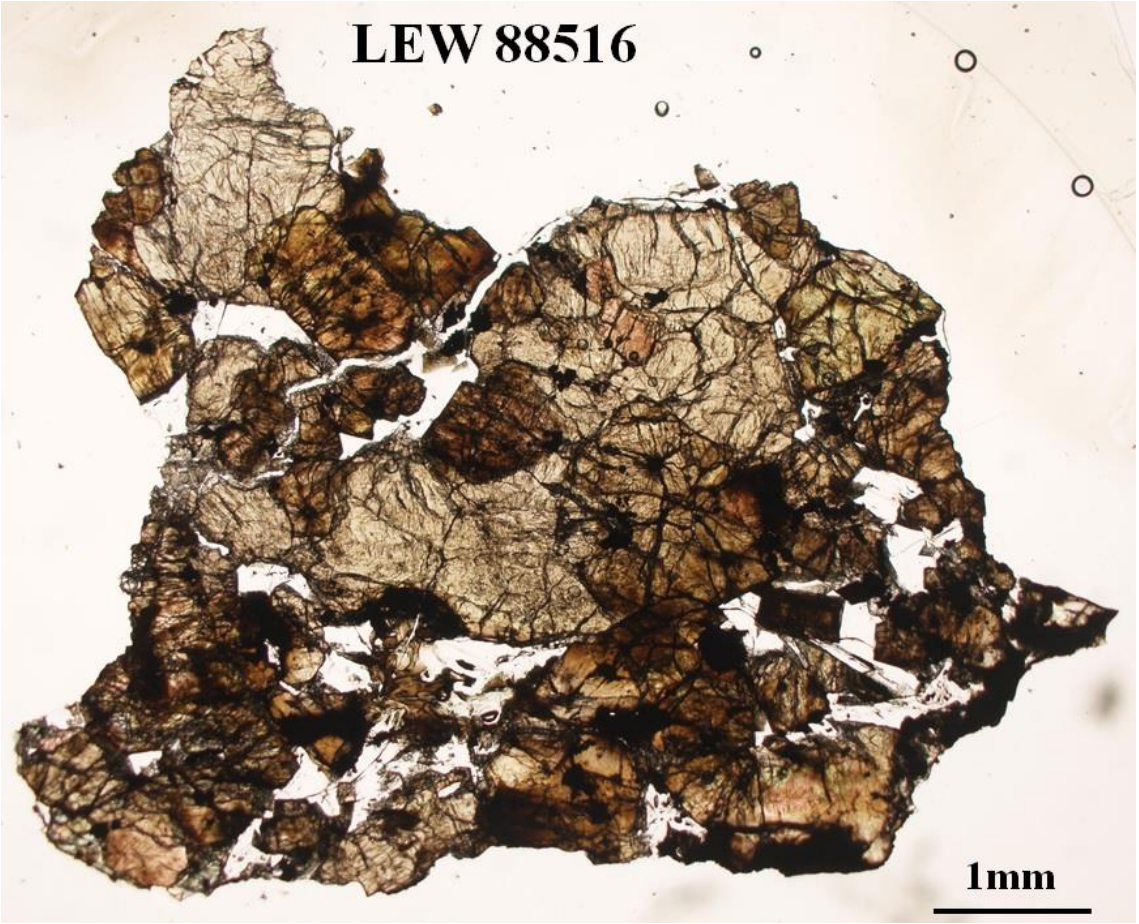

Fig. 2.9 Optical photomicrograph of LEW 88516 (plane-polarized light).

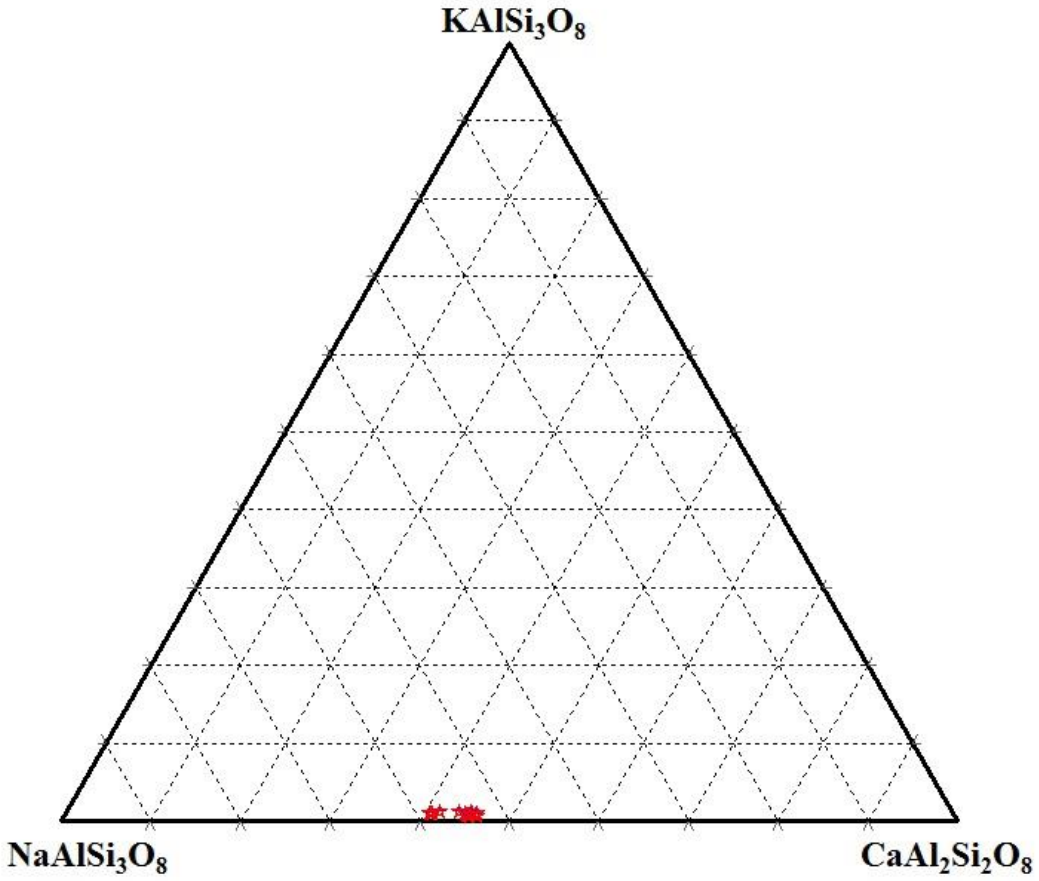

Fig. 2.10 Chemical composition of maskelynite in LEW 88516.

2.1.6. NWA 5029

NWA 5029 was found in Morocco in 2003. It is covered with ~60% fusion crust. NWA 5029 mainly contains pyroxene and maskelynite (Fig. 2.11). Modal abundances of minerals are 80% pyroxene and 15% maskelynite, and it is classified as a basaltic shergottite. Pyroxene is usually elongated and euhedral to subhedral. Mg-rich pigeonite cores are mantled by thin ragged augite (Mikouchi and Barrat 2009). Most of the plagioclase grains are elongated and have been converted to maskelynite by shock. The maskelynite composition in NWA 5029 is An_{56-47} and the FeO abundance is 0.6-1.3 wt% (Table 2.1 and Fig. 2.12). Rare earth element abundance of this sample is intermediate between those of depleted and enriched ones, indicating that it is an intermediate shergottite.

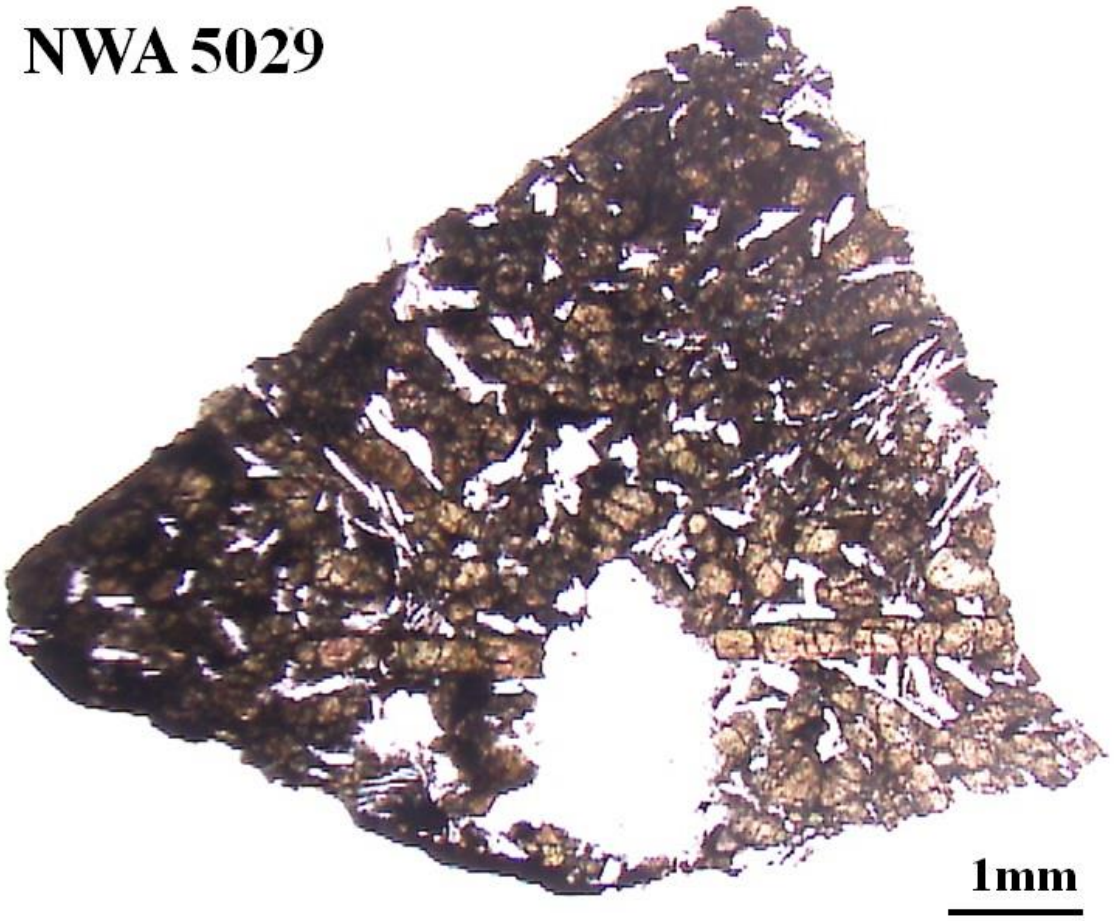

Fig. 2.11 Optical photomicrograph of NWA 5029 (plane-polarized light).

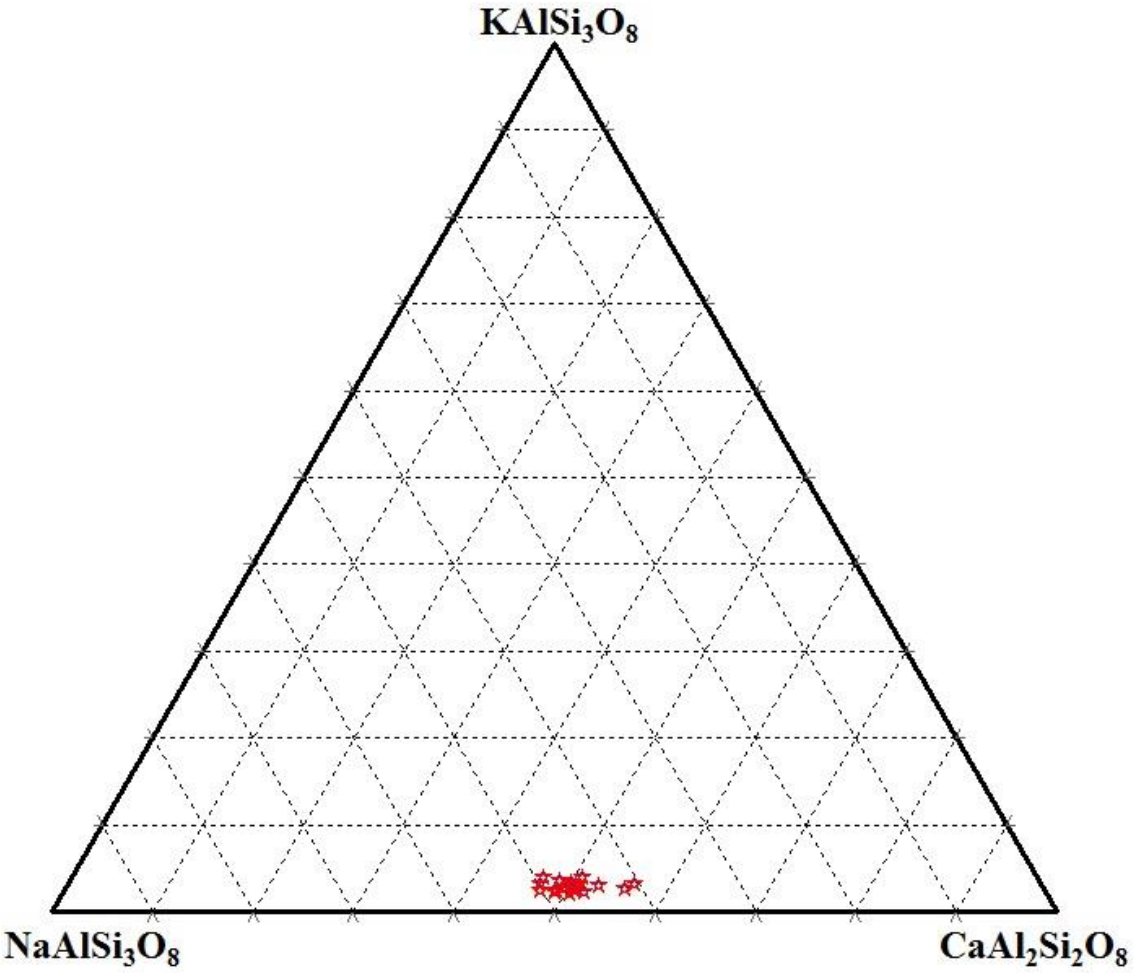

Fig. 2.12 Chemical composition of maskelynite in NWA 5029.

2.1.7. Dhofar 378

Dhofar 378 was found in Oman. Dhofar 378 is composed of subequal amounts of pyroxene and plagioclase (Fig. 2.13). Mineralogical mode of the studied section is 40% pyroxene and 50% plagioclase, suggesting that it is classified as a basaltic shergottite. Dhofar 378 has a fresh black fusion crust on and has been highly shocked (Ikeda et al. 2002). Pyroxene shows undulatory extinction and mosaicism due to strong shock (Mikouchi and McKay 2006). Ikeda et al. (2002) reported that subcalcic clinopyroxene is exsolved and chemically zoned. Dhofar 378 is different from other samples because plagioclase is crystalline and no maskelynite was present (Park et al. 2008). The plagioclase grains are fibrous and fine-grained (~20 μm), suggesting that they were formed by recrystallization from shocked plagioclase melt. The plagioclase composition in Dhofar 378 is An_{58-50} and the FeO abundance is 0.5-2.0 wt% (Table 2.1 and Fig.

2.14). The La/Yb ratio is about 1.28 (Dreibus et al 2002) and it is classified as an enriched shergottite.

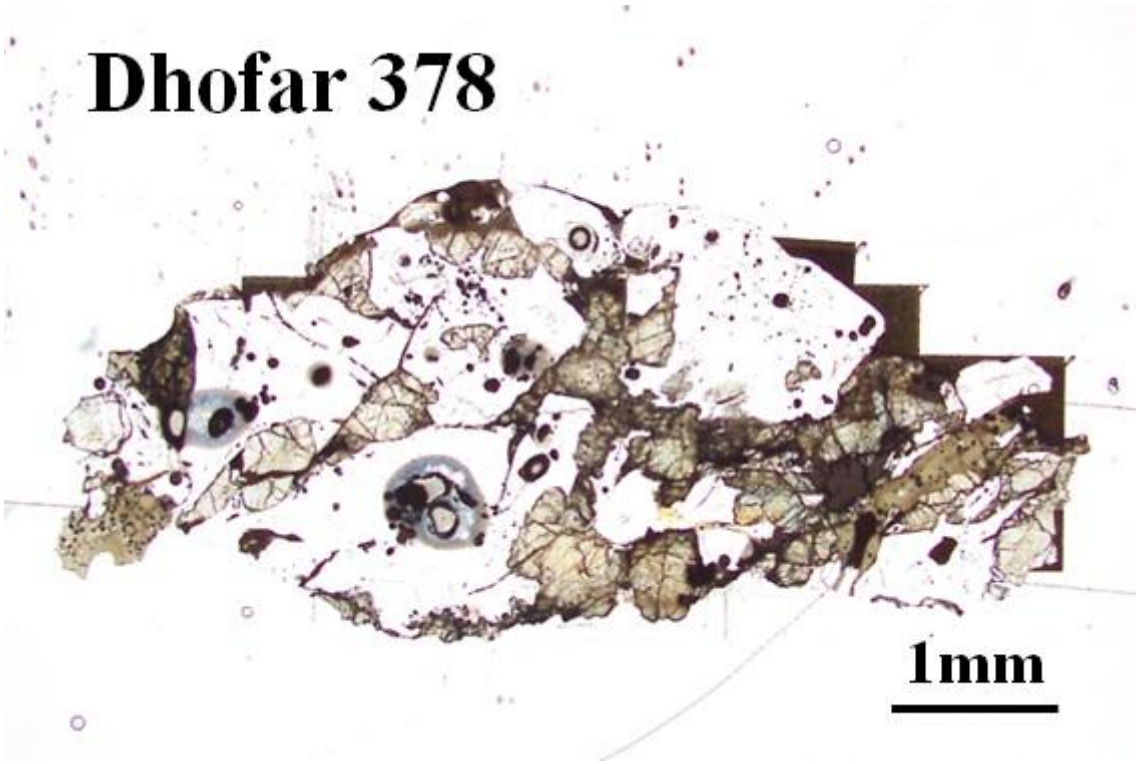

Fig. 2.13 Optical photomicrograph of Dhofar 378 (plane-polarized light).

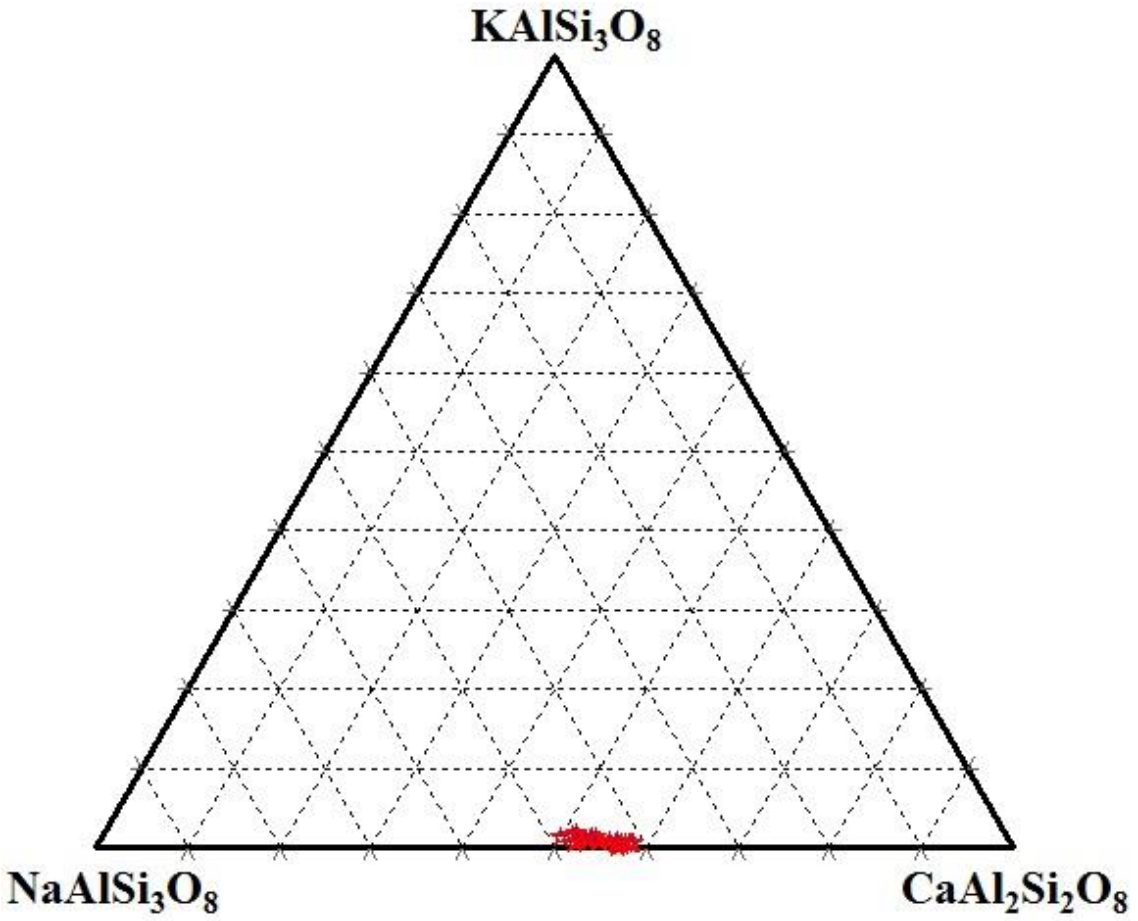

Fig. 2.14 Chemical composition of plagioclase in Dhofar 378.

2.1.8. LAR 06319

LAR 06319 is an Antarctic meteorite found near Larkman Nunatak in 2006. LAR 06319 mostly contains olivine, pyroxene and maskelynite with accessory Ca phosphates, oxides and sulfides. The modal abundances of minerals are 30% olivine, 30% pyroxene, 30% maskelynite and 10% other minerals. Large olivine phenocrysts are present in the groundmass of smaller pyroxene and maskelynite grains with shock melt veins (Fig. 2.15). This characteristic texture shows that it is classified as an olivine-phyric shergottite. Large olivine phenocrysts show euhedral to subhedral shapes and their grain sizes reach up to 1 mm and they are chemically zoned (Fig. 2.16). Peslier et al. (2010) reported that the olivine phonocrysts in this meteorite have very pronounced zonation of phosphorous. Pyroxene is classified into three subgroups; orthopyroxene, pigeonite and augite. Their shapes are subhedral. Because olivine and pyroxene exhibit strong mosaicism and this sample contains abundant shock melt veins, LAR 06319 has been

heavily shocked. Furthermore, plagioclase is shocked to maskelynite. Maskelynites are fine-grained showing needle shapes. The maskelynite composition in LAR 06319 is An_{60-51} and the FeO abundance is 0.6-1.0 wt% (Table 2.1 and Fig. 2.17). The La/Yb ratio is about 1.5 (Basu et al 2009) and this result is close to those of enriched shergottites.

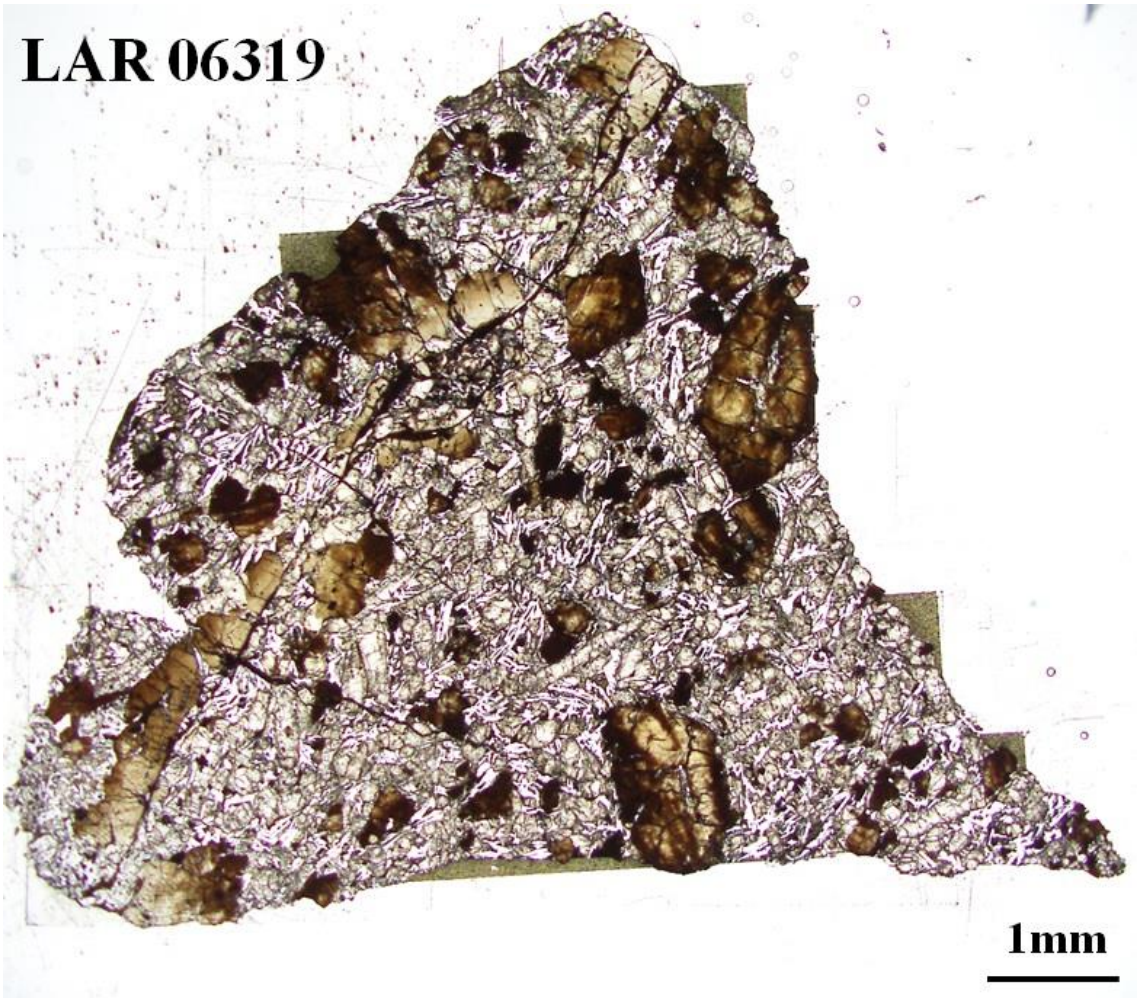

Fig. 2.15 Optical photomicrograph of LAR 06319 (plane-polarized light).

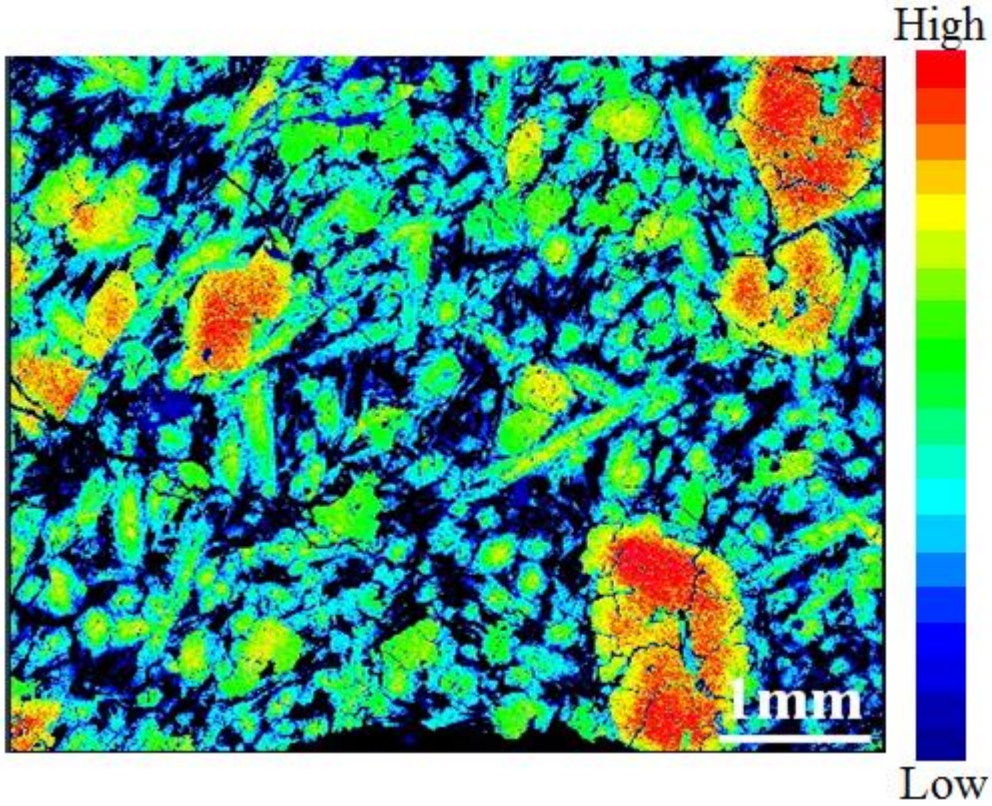

Fig. 2.16 Mg X-ray map of LAR 06319. Red-to-yellow part shows the high-Mg area and blue-colored part shows the low-Mg area. Note the presence of large olivine phenocrysts with extensive chemical zoning.

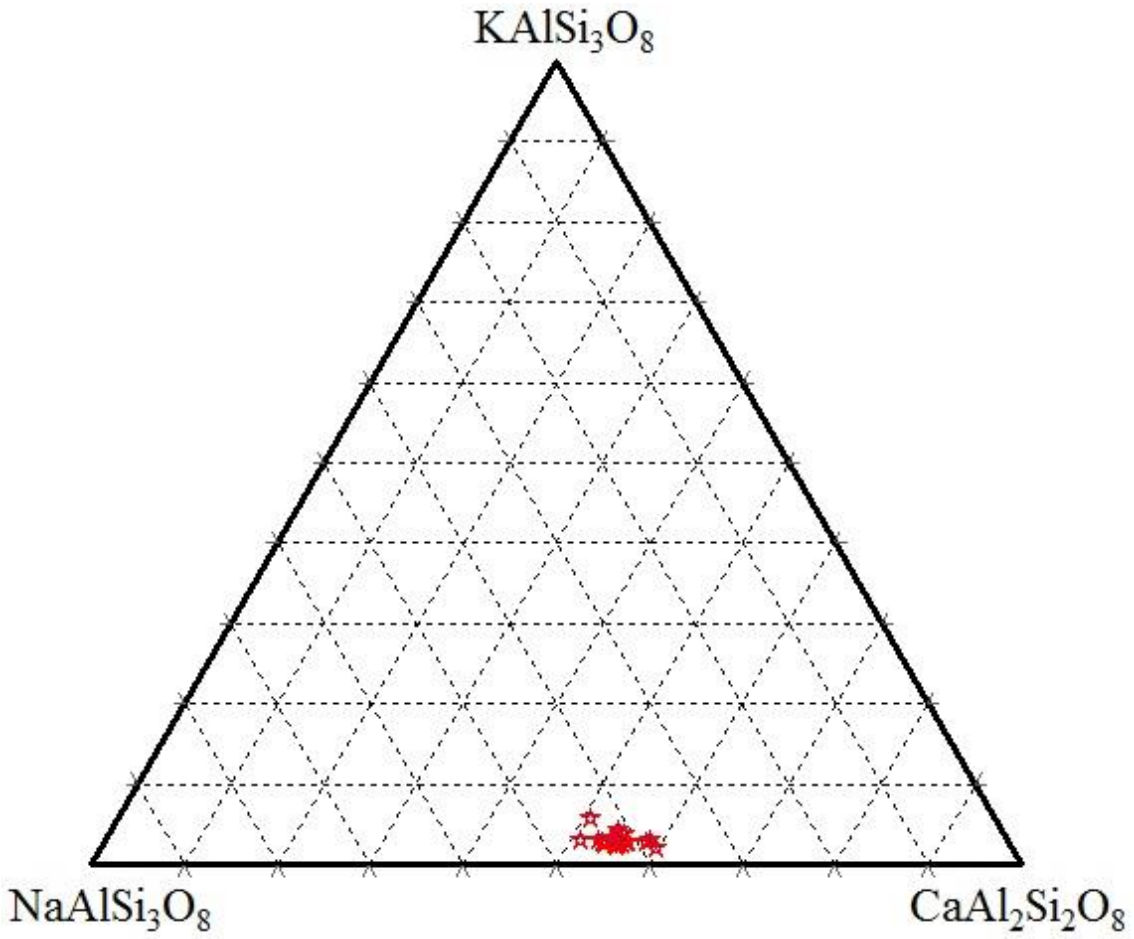

Fig. 2.17 Chemical composition of maskelynite in LAR 06319.

2.1.9. NWA 856

Jambon et al. (2002) reported that NWA 856 was found in Morocco in 2001 and the original piece had a thin black fusion crust that was well preserved. NWA 856 contains pyroxene and maskelynite, and does not contain olivine (Fig. 2.18) and mineral abundances are 70% pyroxene and 20% maskelynite with 10% other minerals. NWA 856 is a fine-grained basalt with pyroxene phenocrysts of over 1 mm in size. It is classified as a basaltic shergottite. Pyroxenes are chemically zoned; pigeonite ranges from $En_{59}Wo_{12}$ to $En_{26}Wo_{15}$ and augite from $En_{36}Wo_{32}$ to $En_{48}Wo_{13}$ (Jambon et al. 2002). Plagioclases have been shocked to maskelynite and they are euhedral to subhedral. The maskelynite composition in NWA 856 is $An_{58\text{-}47}$ and the FeO abundance is 0.5-1.0 wt% (Table 2.1 and Fig. 2.19). NWA 856 is classified as an enriched shergottite because the La/Yb ratio is 1.32 (Jambon et al. 2002).

Fig. 2.18 Optical photomicrograph of NWA 856 (plane-polarized light).

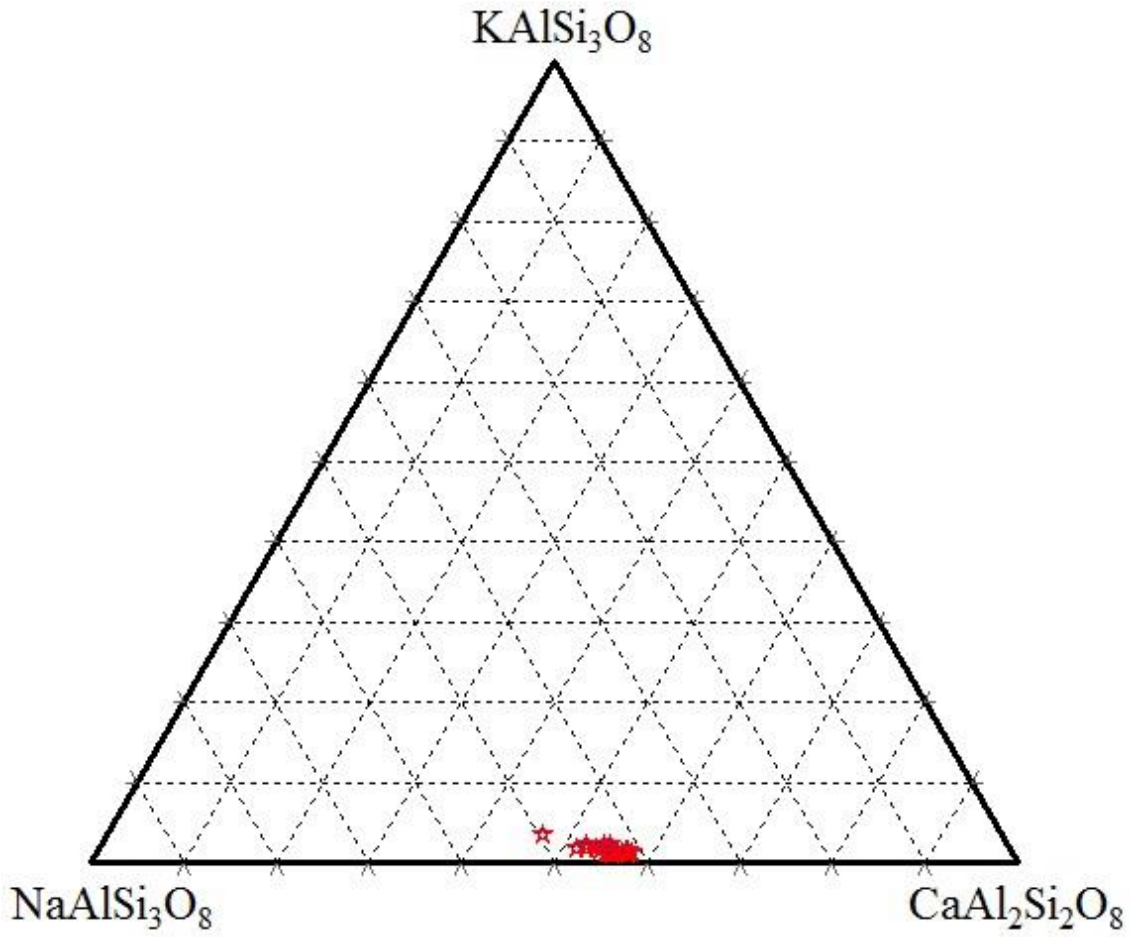

Fig. 2.19 Chemical composition of maskelynite in NWA 856.

2.1.10. NWA 1068

NWA 1068 was found in the Moroccan Sahara in April 2001. It has no fusion crust and is greenish-brown. NWA 1068 is mainly composed of olivine, pyroxene and maskelynite with accessory Ca phosphates. The polished thin section studied contains one big olivine grain with a size of about 1 mm. There are smaller olivine grains, and pyroxene in a fine-grained groundmass is about ~100 μm. The groundmass mainly consists of pyroxene and maskelynite (Fig. 2.20). This texture indicates that it is an olivine-phyric shergottite. The modal abundances of minerals are 25% olivine, 50% pyroxene, 15% maskelynite and some minor minerals such Ca phosphates. The largest olivine grain is extensively zoned in chemical composition (Fig. 2.21). Barrat et al. (2002) observed that pyroxenes are normally zoned from $En_{57}Wo_5$ to $En_{40}Wo_{13}$. Plagioclase has been converted to maskelynite by strong shock. The maskelynite composition in NWA 1068 is An_{52-42} and the FeO abundance is 0.4-0.7 wt% (Table. 2.1

and Fig. 2.22). Although mineralogy of NWA 1068 appears similar to other olivine-phyric shergottites such as Dar al Gani 476 and Dhofar 019, but the REE pattern of NWA 1068 shows no depletion in light REE (La/Yb=~1.64) (Barrat et al. 2002) and it is classified as an enriched shergottite.

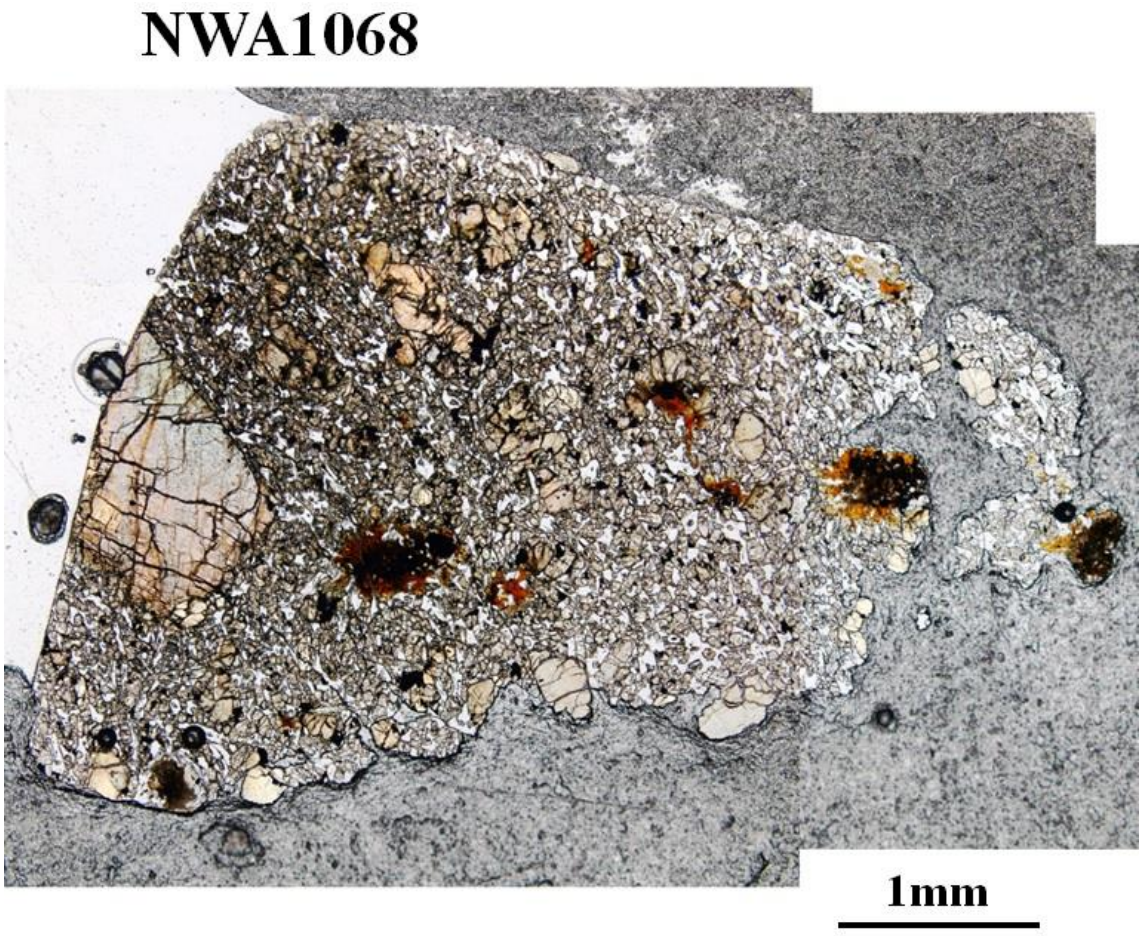

Fig. 2.20 Optical photomicrograph of NWA 1068 (plane-polarized light).

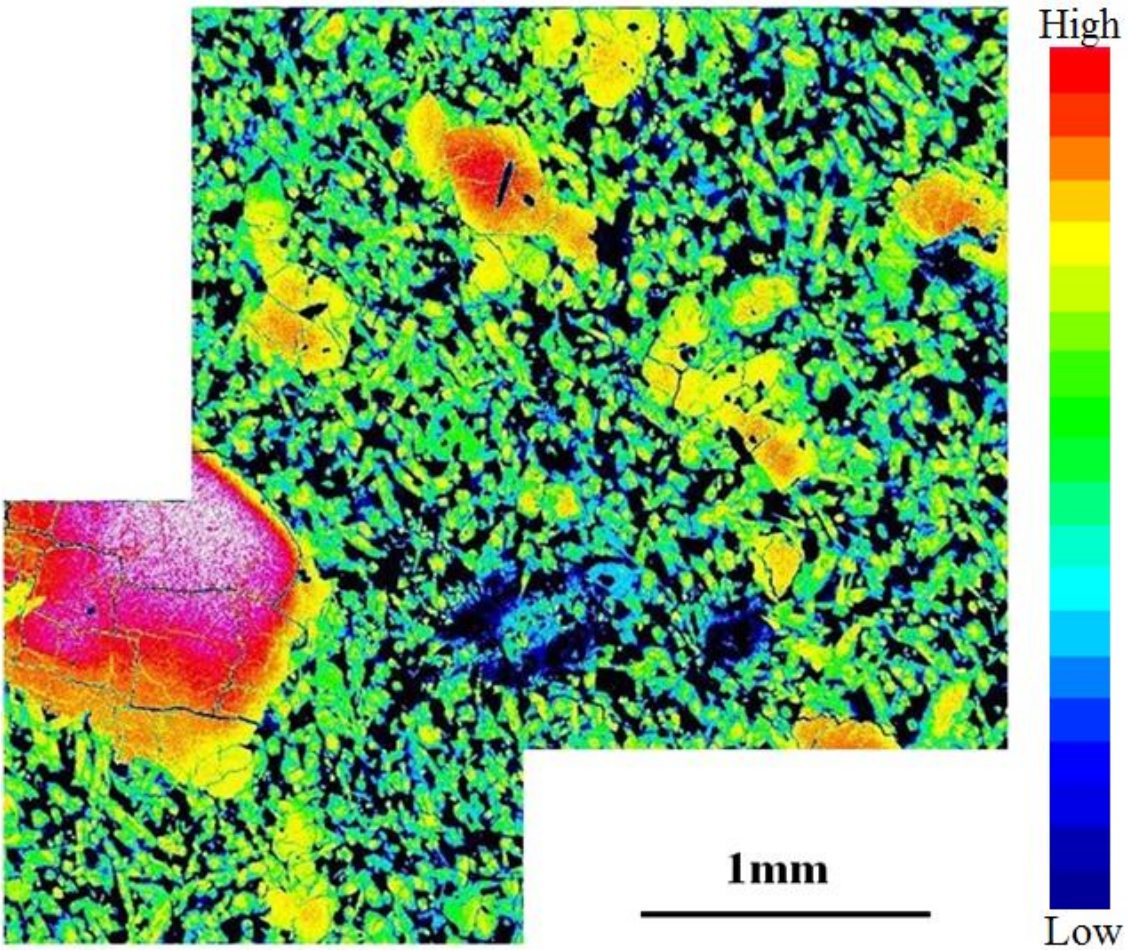

Fig. 2.21 Mg X-ray map of NWA 1068. Red-to-yellow parts show the high-Mg area and blue-colored parts show the low-Mg area.

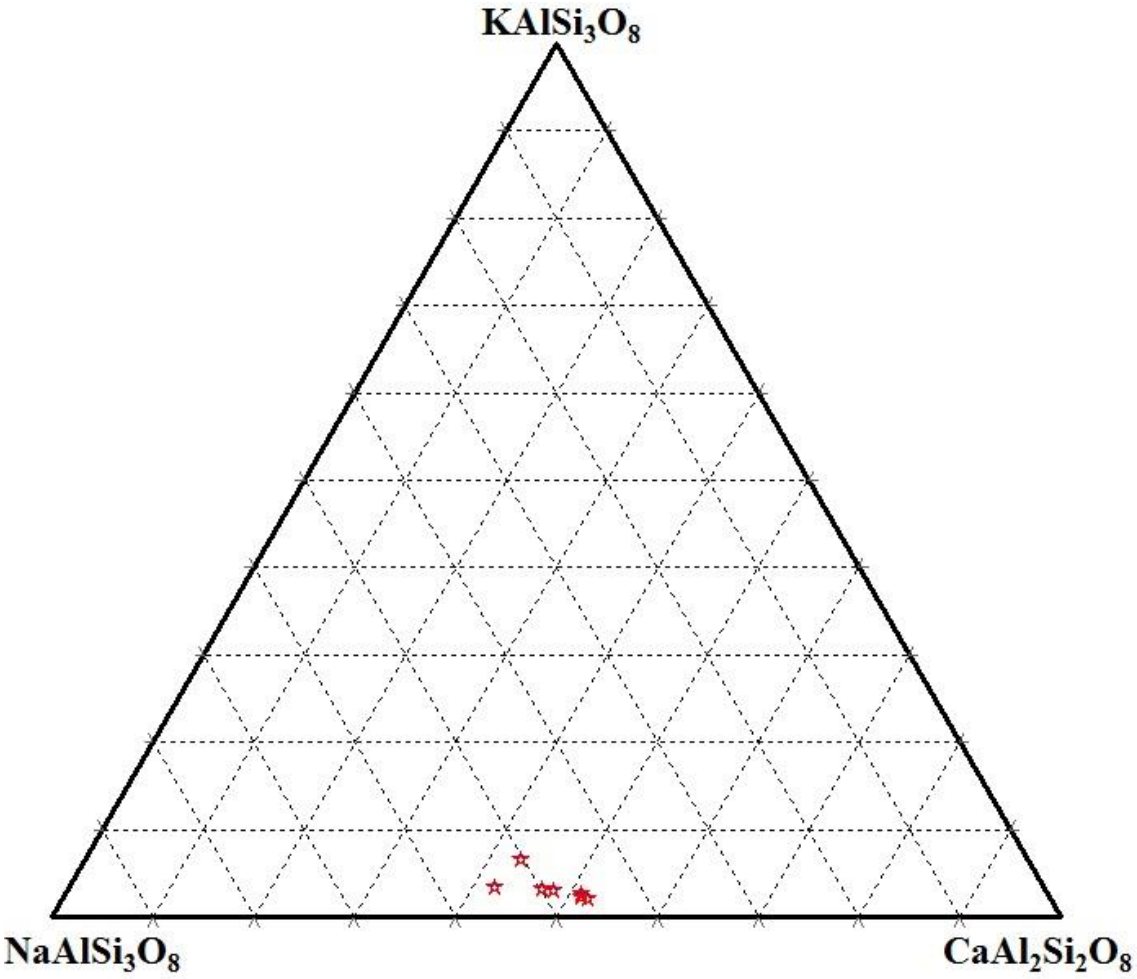

Fig. 2.22 Chemical composition of maskelynite in NWA 1068.

2.1.11. NWA 4468

NWA 4468 was found in Layoune, Morroco. NWA 4468 is mainly composed of olivine, pyroxene, maskelynite and some accessory minerals. This sample has 30% olivine, 40% pyroxene, 20% maskelynite with some other minerals. It is classified as a lherzolitic shergottite, because it contains large pyroxene oikocrysts enclosing olivine (Fig. 2.23). The sizes of pigonite oikorysts are large up to 1 mm in size and chemically zoned (Fig. 2.24). Some olivine grains are euhedral and their sizes are about 1 mm. Some of these olivine grains contain magmatic inclusions. Spray and Boonsue (2011) reported that NWA 4468 is considered to be highly shocked because of the presence of stishovite in magmatic inclusions. The presence of maskelynite is consistent with this report. Most maskelynite grains are subhedral and they are over 500 μm in size. The maskelynite composition in NWA 4468 is An_{57-39} and the FeO abundance is 0.3-0.6

wt% (Table. 2.1 and Fig. 2.25). It is an enriched shergottite because the La/Yb ratio is about 1.70 (Irving et al. 2007).

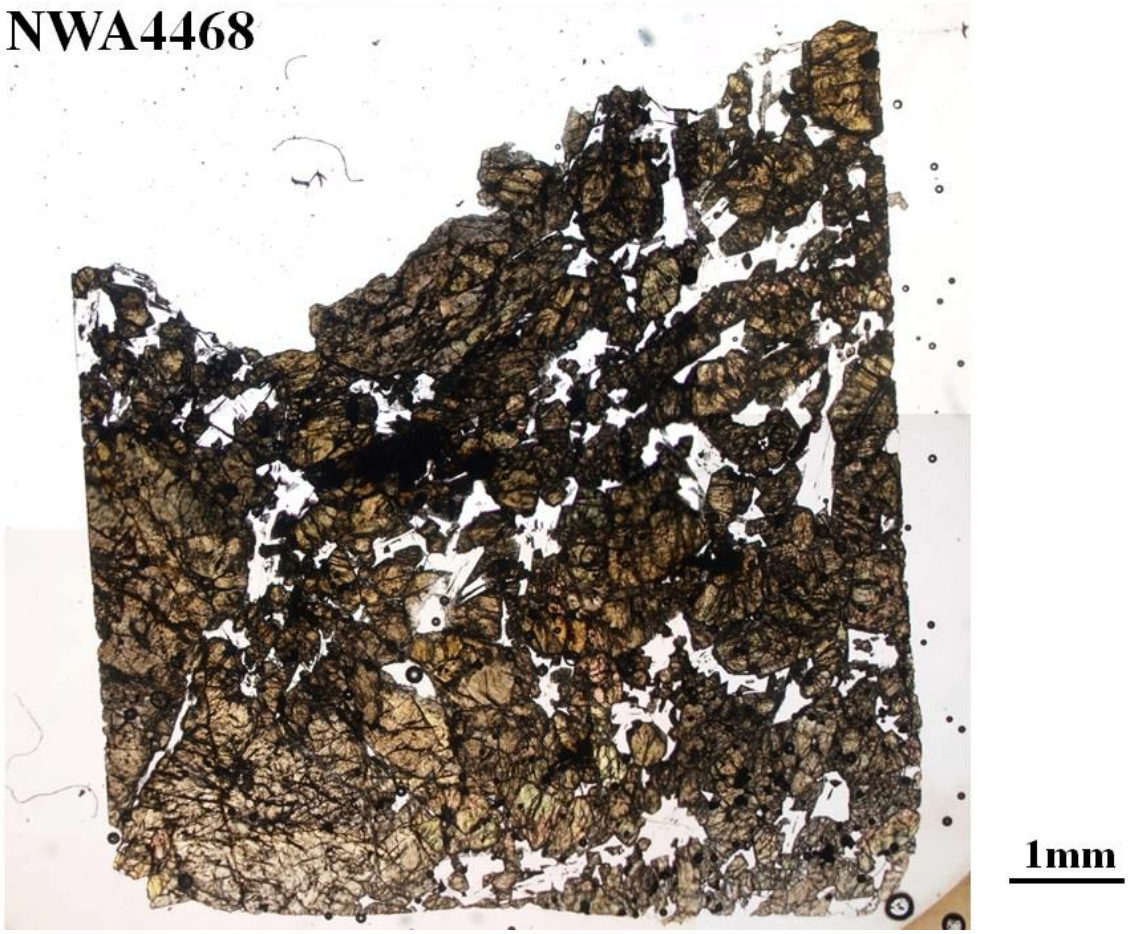

Fig. 2.23 Optical photomicrograph of NWA 4468 (plane-polarized light).

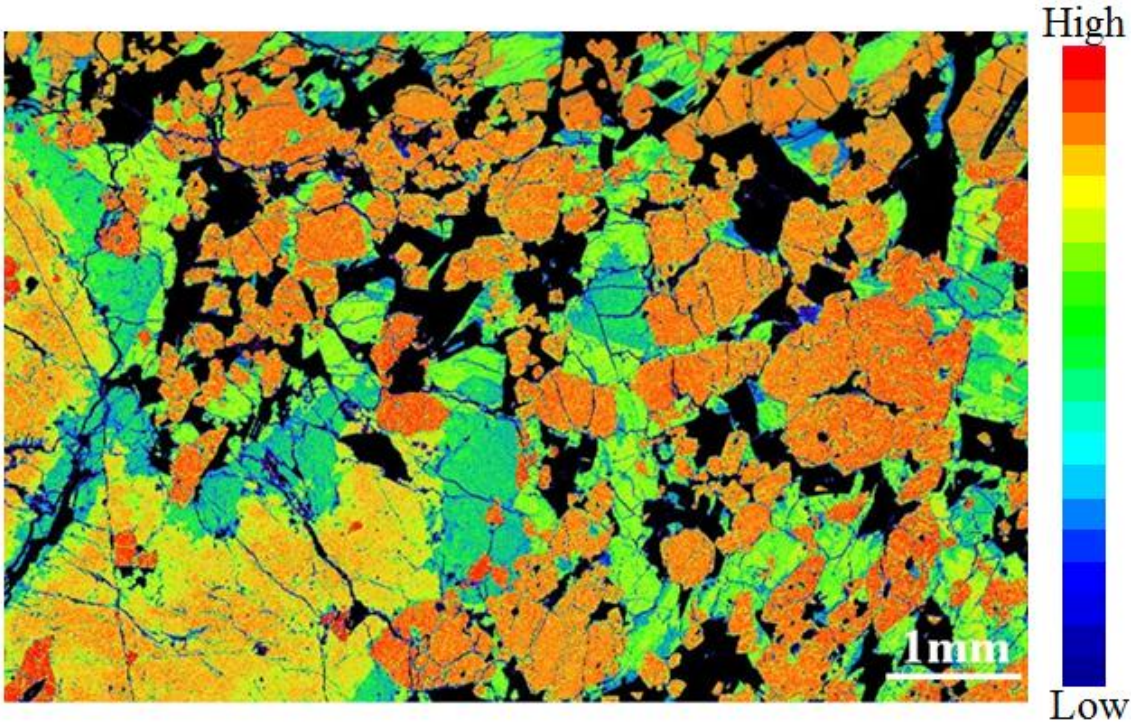

Fig. 2.24 Mg X-ray map of NEW 4468. Orange-to-yellow part shows the high-Mg area and blue-colored part shows the low-Mg area.

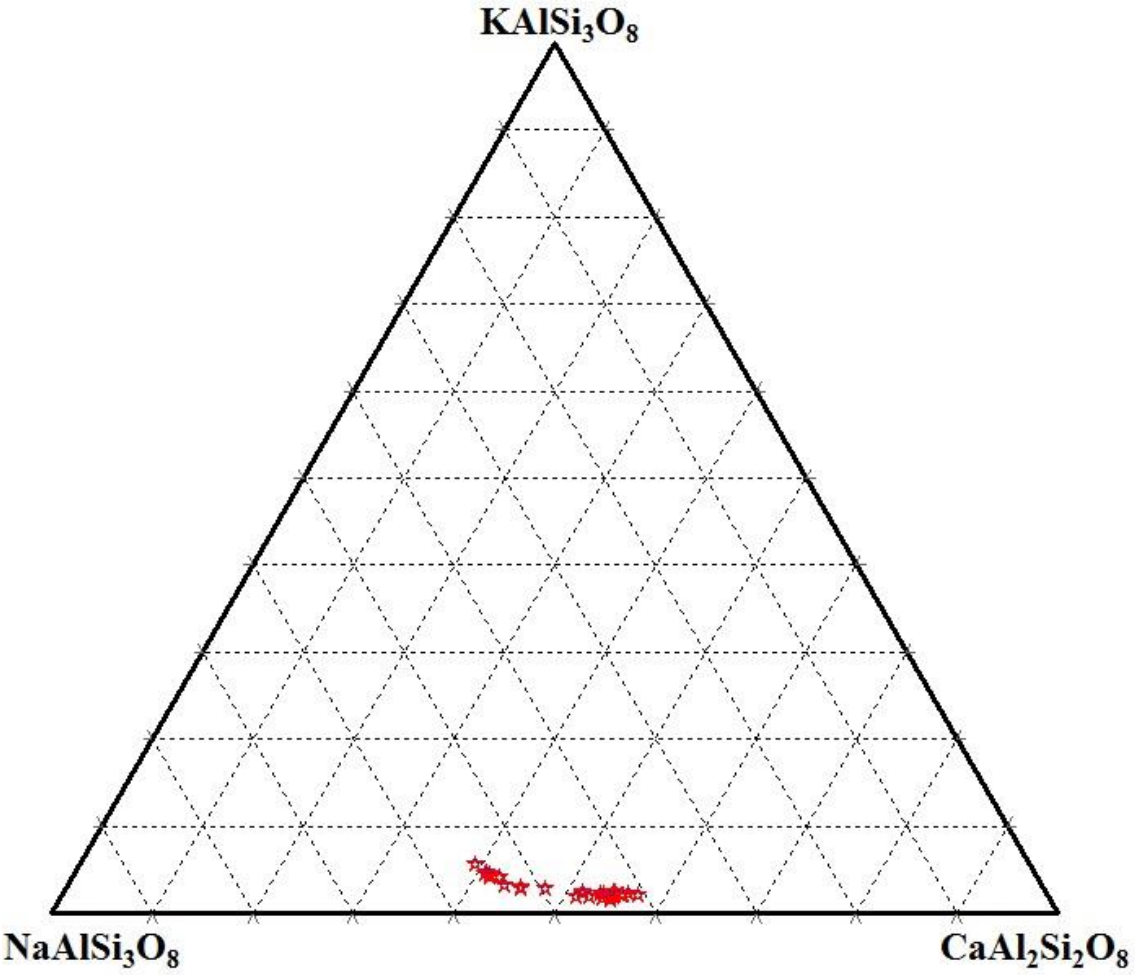

Fig. 2.25 Chemical composition of maskelynite in NWA 4468.

2.1.12. Zagami

Zagami is an observed meteorite fall on October 3, 1962 in Zagami Rock, Katsina Province, Nigeria (Graham et al. 1985). Zagami was the second meteorite found to contain a significant amount of trapped gas which was derived from Mars (Marti et al. 1995). It is known that Zagami is apparently heterogeneous containing several different lithologies (Stolper and McSween 1979). The sample used in this study is mainly composed of pyroxene and maskelynite, and does not contain olivine (Fig. 2.26). The modal abundances of minerals are 75% pyroxene and 20% maskelynite. This texture shows that it is a basaltic shergottite. Pyroxenes show subhedral shapes and their grain sizes are over 1 mm in longer dimension. Mikouchi et al. (1999) and McCoy et al. (1999) have studied the pyroxene zoning and found it nearly identical to that of pyroxene in Shergotty. Plagioclase in Zagami is completely transformed to maskelynite.

Mikouchi et al. (1998) and McCoy et al. (1999) reported that maskelynite in Zagami was not a diaplectic glass, but was a melt glass. Maskelynites show subhedral shapes and their grain sizes are up to about 1 mm. The maskelynite composition in Zagami is An_{51-46} and the FeO abundance is 0.5-0.8 wt% (Table 2.l and Fig. 2.27). The La/Yb ratio is 1.18 (Barret et al. 2001), showing that it is classified as an enriched shergottite.

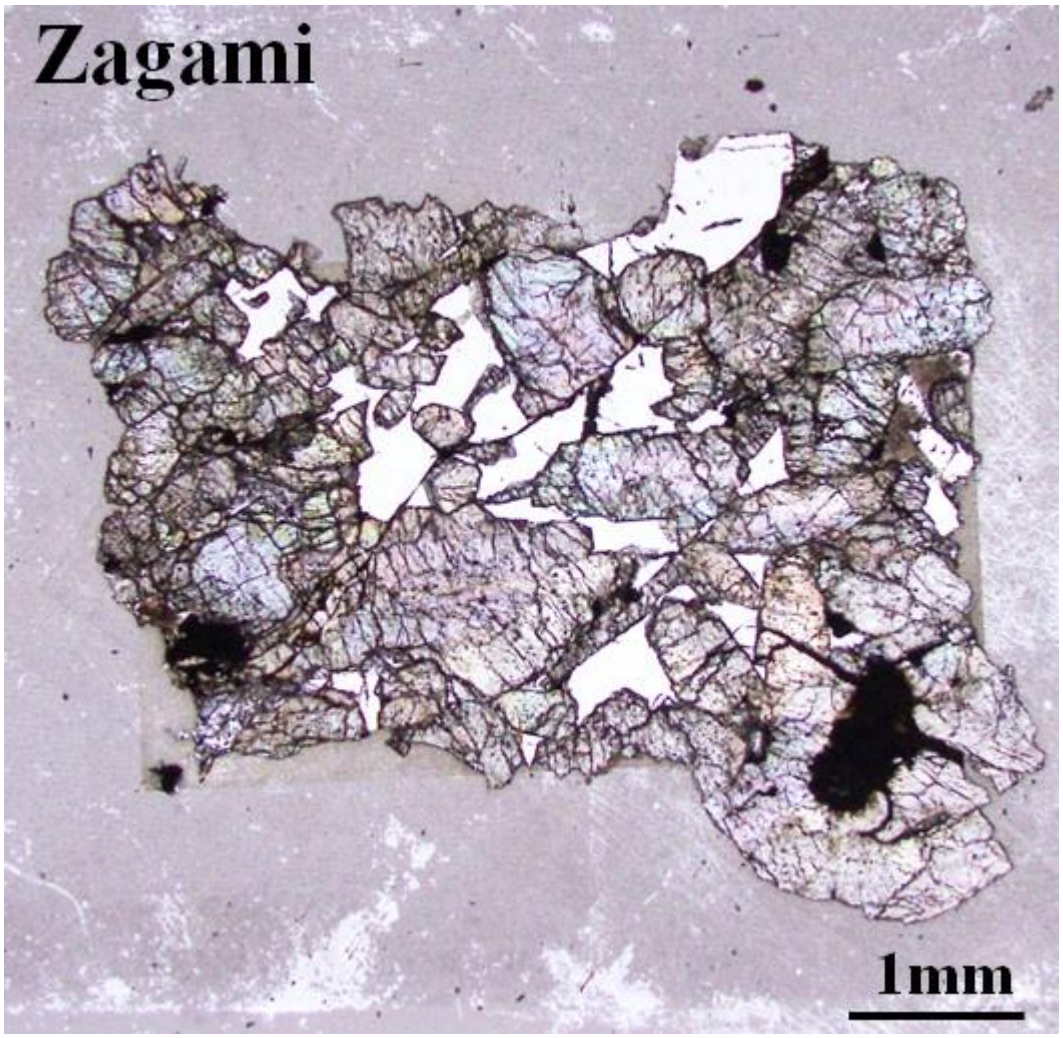

Fig. 2.26 Optical photomicrograph of Zagami (plane-polarized light).

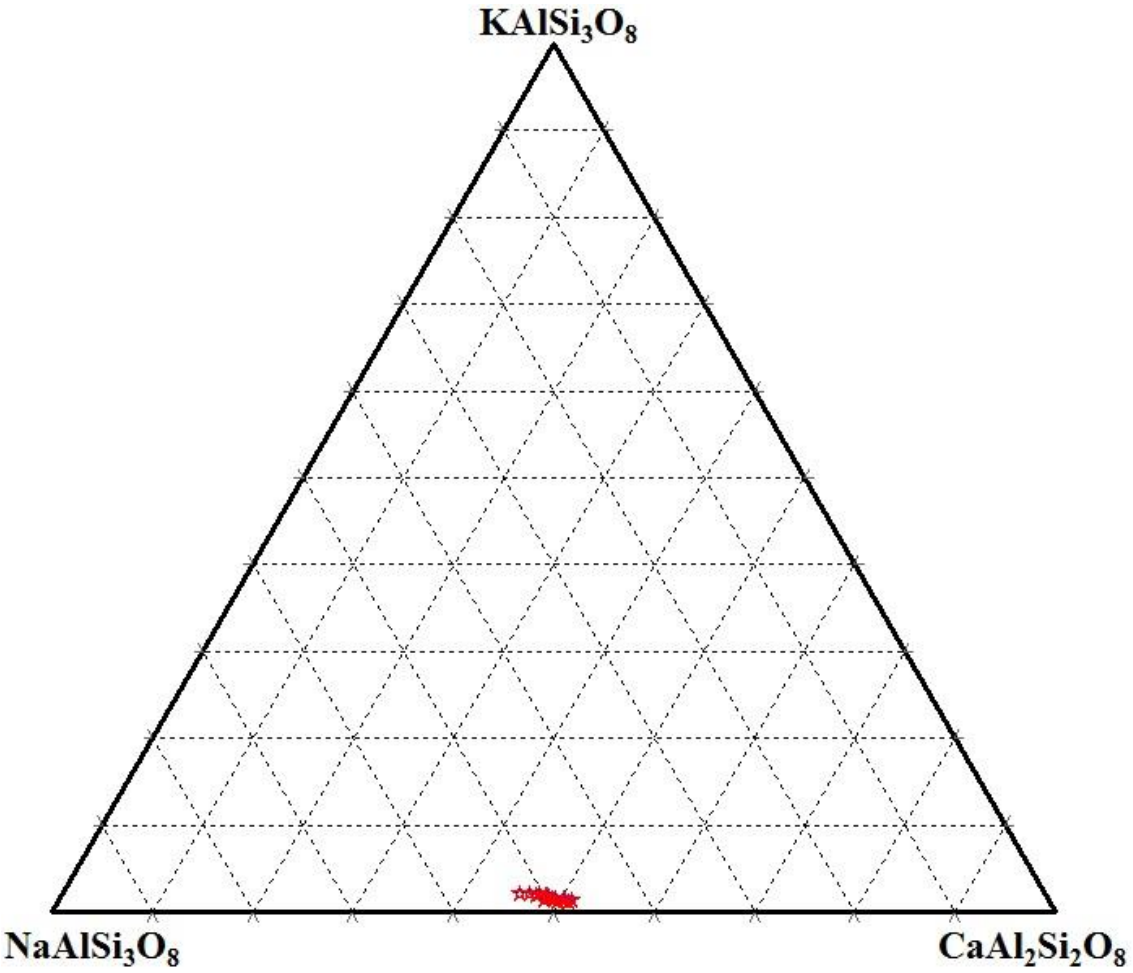

Fig. 2.27 Chemical composition of maskelynite in Zagami.

2.1.13. RBT 04262

RBT 04262 was found at Robert Massif, Antarctica, in 2004. RBT 04262 is mainly composed of olivine, pyroxene, and maskelynite. This sample shows a coarse-grained assemblage of 50% pyroxene, 30% olivine and 10% maskelynite, and is classified as a lherzolitic shergottite because it contains large pyroxene oikocrysts (over 3 mm) enclosing olivine chadacrysts (Fig. 2.28). Olivine grains are euhedral to subhedral, and their sizes are up to 1 mm. Usui et al. (2010) reported that the poikilitic areas had olivine that was distinctly higher in forsterite content (Fo_{60-70}) than the olivine in the non-poikilitic areas (Fo_{57-62}). Low-calcium pyroxene oikocrysts are abundant and they are rimmed by augite (Mikouchi et al. 2008; Anand et al. 2008; Usui et al. 2010). Plagioclase is shocked to maskelynite. The maskelynite composition in RBT 04262 is An_{55-50} and the FeO abundance is 0.1-0.6 wt% (Table 2.1 and Fig. 2.29). RBT 04262 is

classified as an enriched shergottite because its REE pattern is essentially flat, like that of Shergotty, but slightly lower. The La/Yb ratio is about 1.20 (Anand et al 2008).

Fig. 2.28 Optical photomicrograph of RBT 04262 (plane-polarized light).

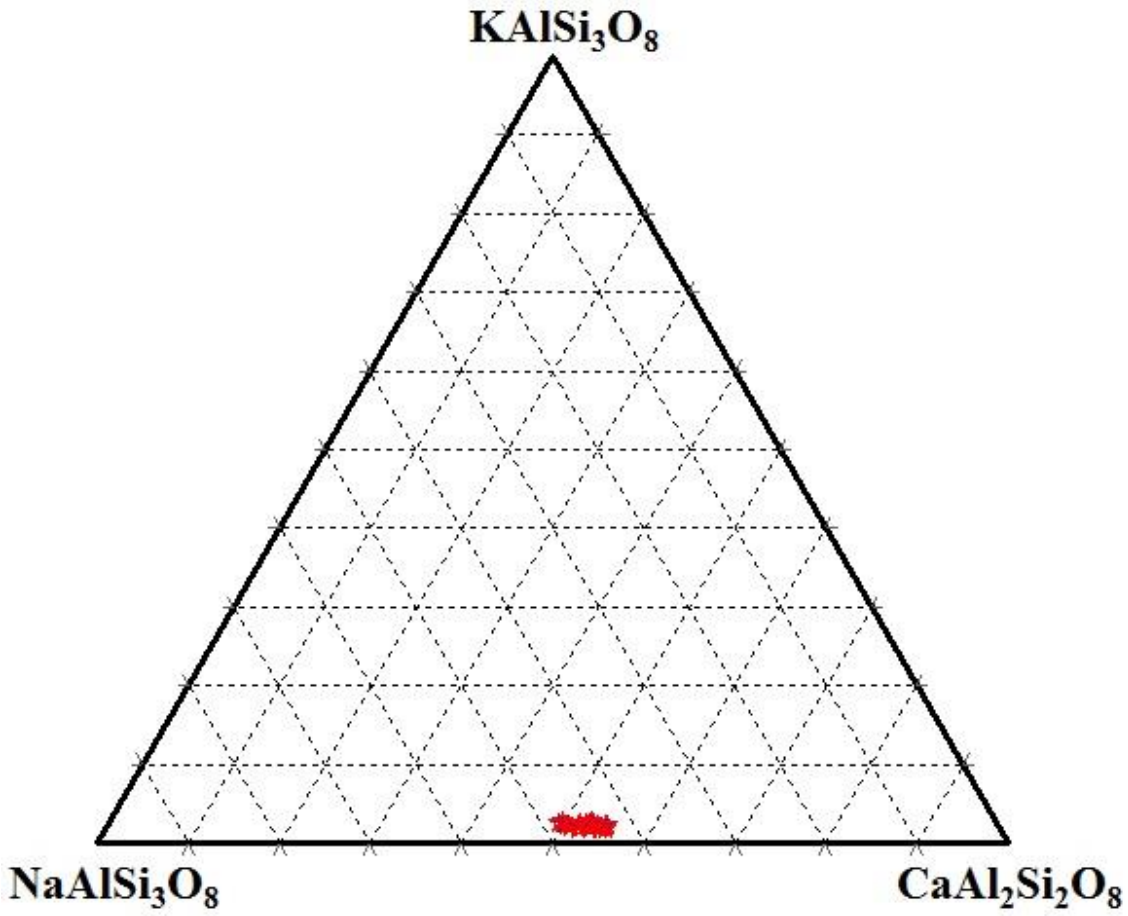

Fig. 2.29 Chemical composition of maskelynite in RBT 04262.

2.1.14. Shergotty

Shergotty fell on August 25, 1865 at 9:00 A.M. in Bihar State, India. Major minerals in Shergotty are subhedral grains of pyroxene and maskelynite (Fig. 2.30). The grain sizes of most pyroxene and maskelynite grains are almost over 1 mm, slightly larger than those of Zagami. The modal abundances of minerals are 70% pyroxene, 25% maskelynite with accessory Ca phosphates. It is classified as a basaltic shergottite. Pyroxenes show two trends in chemical zoning ($En_{48}Wo_{33}$ to $En_{25}Wo_{28}$ and $En_{61}Wo_{13}$ to $En_{21}Wo_{18}$) (e.g., Papike et al. 2009). Plagioclase has been converted to maskelynite by shock and the estimated shock pressure is ~30 GPa (Smith and Hervig 1979) or 29 GPa (Stoffler et al. 1986). The maskelynite composition in Shergotty is An_{53-39} and the FeO abundance is 0.5-0.8 wt% (Table 2.1 and Fig. 2.31). Most of the trace elements in Shergotty are located in Ca phosphates and the La/Yb of ~1.34 shows that it is classified as an enriched shergottite.

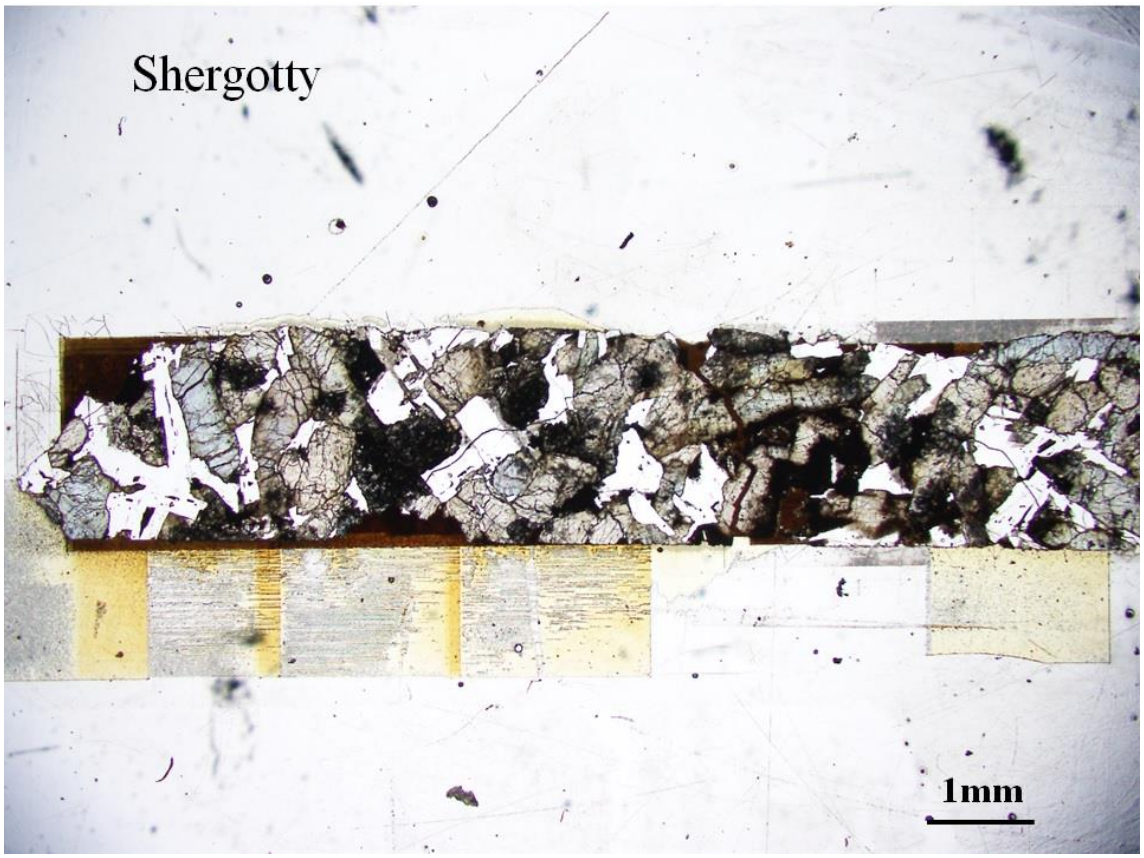

Fig. 2.30 Optical photomicrograph of Shergotty (plane-polarized light).

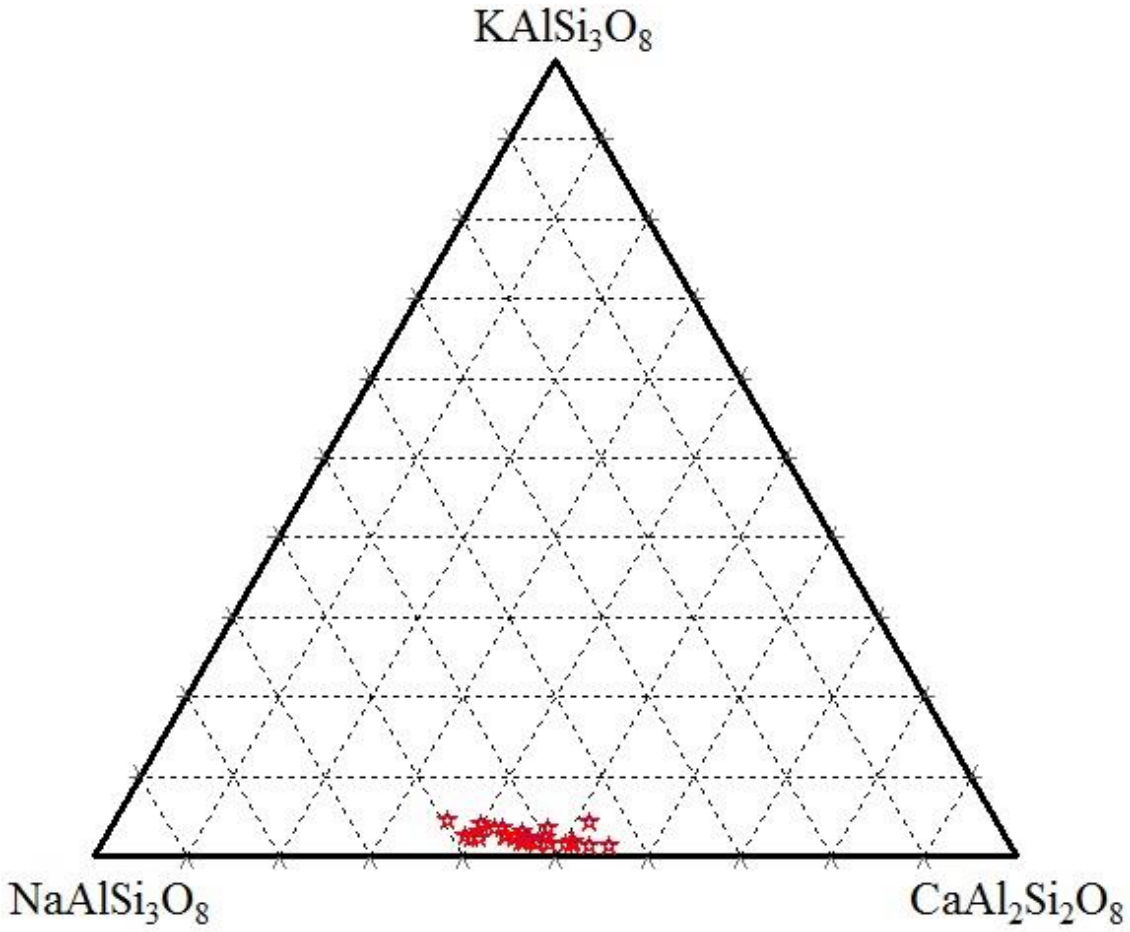

Fig. 2.31 Chemical composition of maskelynite in Shergotty.

Table 2.1

Average maskelynite and plagioclase group, compositions and FeO* abundance for studied shergottites. D: depleted shergottite, I: intermediate shergottite, and E: enriched shergottite.

Sample	Group	An	Or	FeO* (FeO* = FeO + Fe_2O_3) (wt%)
Dar al Gani 476	D	70–62	–1	0.3–0.6
Dhofar 019	D	59–49	–1	0.2–0.5
ALH 77005	I	53–40	1–2	0.4–1.0
EETA 79001 lithology A	I	59–56	–1	0.5–0.8
LEW 88516	I	58–55	–0.5	0.3–0.6
NWA 5029	I	56–47	2–4	0.6–1.3
Dhofar 378	E	58–50	–1	0.5-2.0
LAR 06319	E	60–51	–1	0.6–1.0
NWA 856	E	58–47	1–3	0.5–1.0
NWA 1068	E	52–42	2–7	0.4–0.7
NWA 4468	E	57–39	2–7	0.3–0.6
Zagami	E	51–46	1–2	0.5–0.8
RBT 04262	E	55–50	4–9	0.1–0.6
Shergotty	E	53–39	1–4	0.5–0.8

2.2. HED Meteorites

Polished thin sections of ten HED (Howardites-Eucrites-Diogenites) meteorites (ALH 76005, Piplia Kalan, Petersburg, Padvarninkai, Y-75011, EETA 87520, Moama, Moore County, Y980433 and Y-75032) were also studied. One polished thin section of each sample was analyzed as done for shergottites. The thin section sizes are ALH 76005: 10x20 mm, Piplia Kalan: 16x9 mm, Petersburg: 3x4 mm, Padvarninkai: 18x16 mm, Y-75011: 10x6 mm, EETA 87520: 16x11 mm, Moama 8 x 6 mm, Moore County: 19x19 mm, Y980433: 7x9 mm and Y-75032: 7x13 mm, respectively.

The thin sections of ALH 76005 and EETA 87520 were supplied by The Meteorite Working Group. Y-75011 and Y 980433 were supplied by National Institute of Polar Research. Moore County, Piplia Kalan, and Petersburg were supplied by Smithsonian Institution, The National Museum of Natural History. Padvarninkai was supplied from Dr. L. Nyquist at NASA Johnson Space Center.

2.2.1. ALH 76005

ALH 76005 is an Antarctic meteorite found at the Allan Hills site. It is a polymict eucrite that contains significant proportions of unequilibrated clasts along with a few coarse-grained eucrite clasts (Fig. 2.32). There are a couple of small clasts with fine-grained textures that appear to be unequilibrated in the thin section. ALH 76005 is classified as a surface eucrite. This sample mainly contains pyroxene, maskelynite and groundmass of smaller pyroxene and plagioclase grains with shock melt.

There is a variation of the pyroxene composition and it has been classified into four distinct groups (Miyamoto et al. 1979). Some plagioclase grains show subhedral shapes and their grain sizes are about 500 μm. In addition, lathy plagioclase grains are found and their sizes are 200 x 50 μm. Chemical composition of plagioclase is An_{92-80} and the FeO abundance is 0.2-0.4 wt% (Table 2.2 and Fig. 2.33).

Fig. 2.32 Optical photomicrograph of ALH 76005 (plane-polarized light).

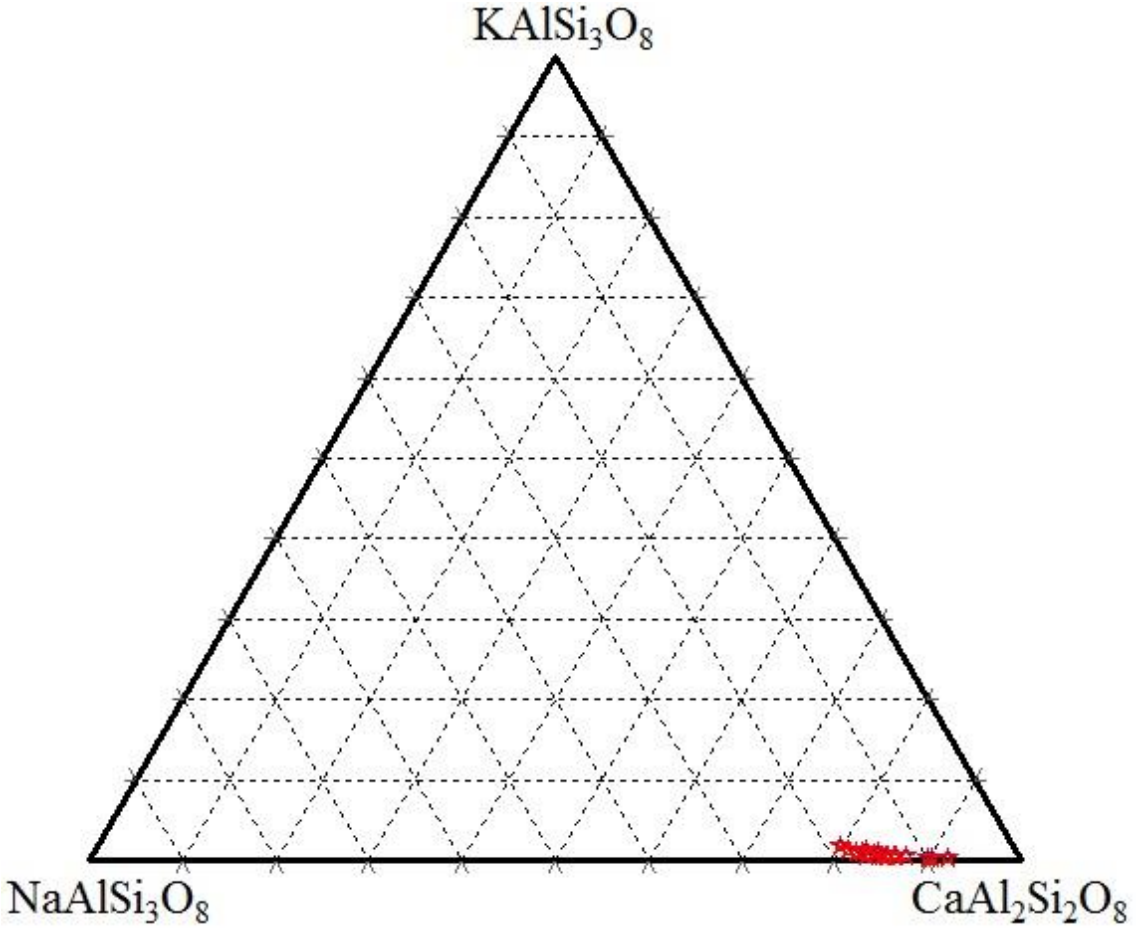

Fig. 2.33 Chemical composition of plagioclase in ALH 76005.

2.2.2. Petersburg

Petersburg fell on August 5, 1855 in Tennessee, USA and this meteorite is a polymict eucrite. Buchanan et al. (1996) reported that after final accretion, Petersburg apparently was exposed to a minor episode of thermal metamorphism causing ~30 μm wide alteration rims around larger pyroxene fragments and causing alteration of pyroxenes at the edges of eucritic clasts (Fig. 2.34).

Petersburg is classified as a surface eucrite, however the studied sample is mainly composed of pyroxene and plagioclase showing a coarse-grained texture. Pyroxene grains are subhedral in shape and their grain sizes reach up to 1 mm. Plagioclase grains show a subhedral shape and their sizes are larger than 500 μm, although the largest grain is over 1 mm.

The plagioclase composition in Petersburg is An_{89-86} and the FeO abundance is 0.2-0.4 wt% (Table 2.2 and Fig. 2.35).

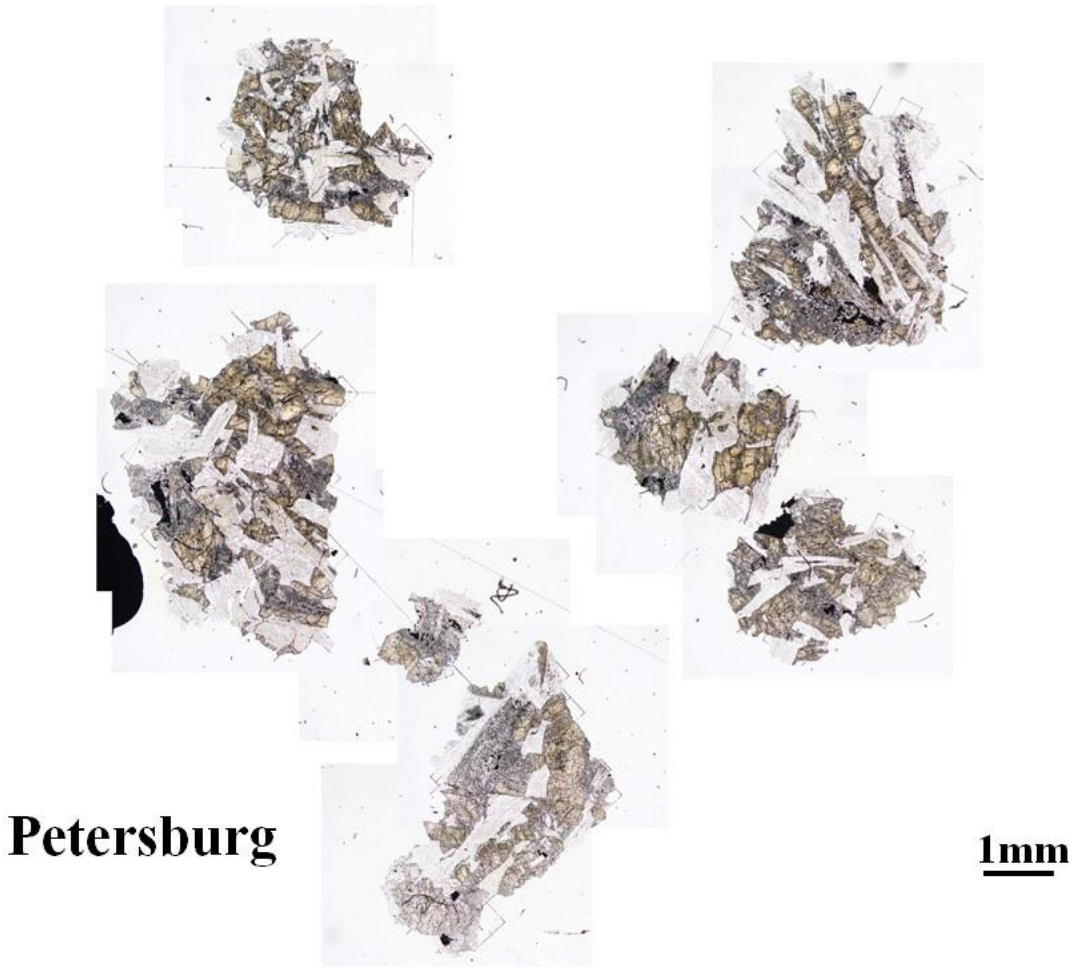

Fig. 2.34 Optical photomicrograph of Petersburg (plane-polarized light).

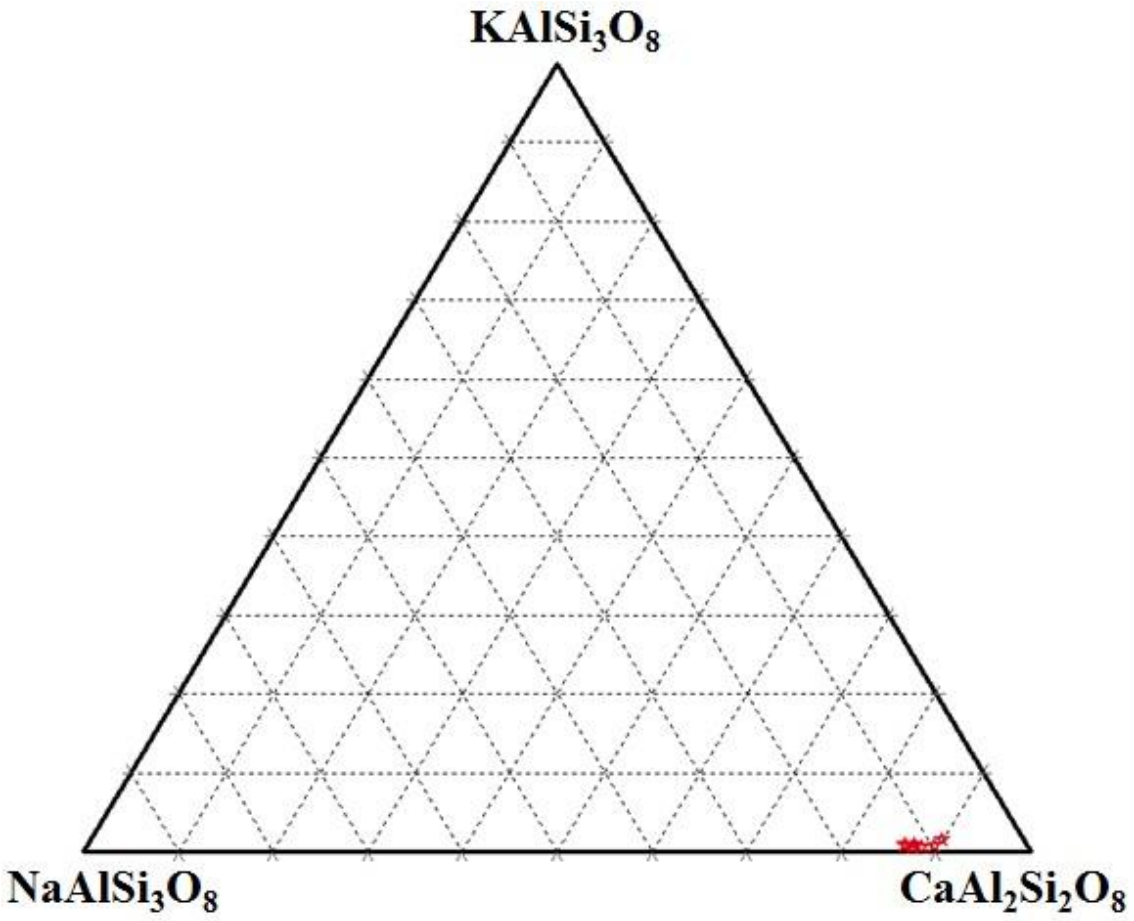

Fig. 2.35 Chemical composition of plagioclase in Petersburg.

2.2.3. Piplia Kalan

Piplia Kalan fell near the Pali district of Rajasthan, India on June 20, 1996. This meteorite fragment was covered with a thin, shining fusion crust (Shukla et al. 1997). Piplia Kalan is a genomict brecciated eucrite and the crack due to shock is present.

Piplia Kalan shows a fine-grained texture and it consists of pyroxene, plagioclase and some accessory minerals such as opaque minerals (Fig. 2.36). The size of pyroxene is about 50 μm. Plagioclase grains show a needle-like shape and its size is 200 x 50 μm. According to these characteristics, this is classified as a surface eucrite.

The mineral compositions in the coarse-grained texture are the same as those in the fine-grained texture. The abundance of plagioclase in the coarse-grained texture is larger than that of fine-grained texture. Pyroxene grains are in subhedral shape and their sizes are about 500 μm. Plagioclase megacryst grains are subhedral to euhedral and their sizes are about 1000 x 250 μm. Pyroxene in the both fine-grained and

coarse-grained textures shows extinction mosaicism by shock. Shukla et al. (1997) reported that the chemical composition of orthopyroxene is $En_{34}Wo_2$ and few pyroxenes show $En_{32}Wo_5$. In addition, exsolution lamellae of augite are $En_{28}Wo_{44}$.

The plagioclase composition in Piplia Kalan is $An_{89\text{-}87}$ and the FeO abundance is 0.2-0.3 wt% (Table 2.2 and Fig. 2.37).

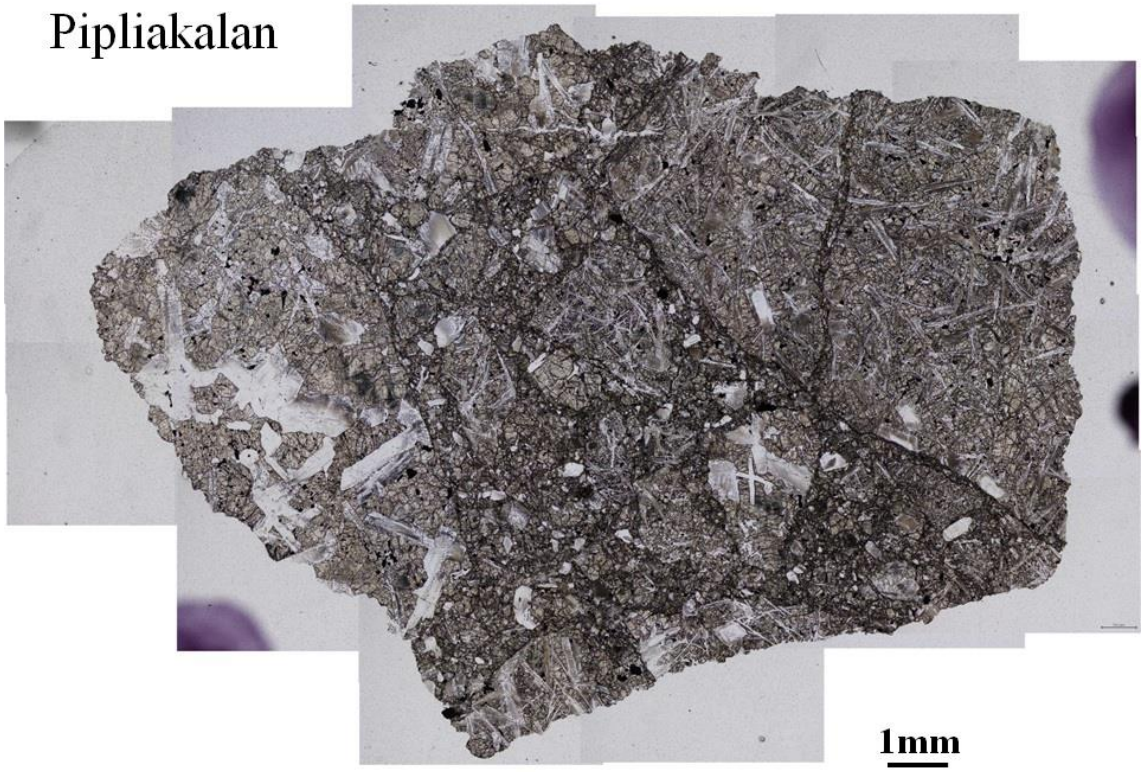

Fig. 2.36 Optical photomicrograph of Piplia Kalan (plane-polarized light).

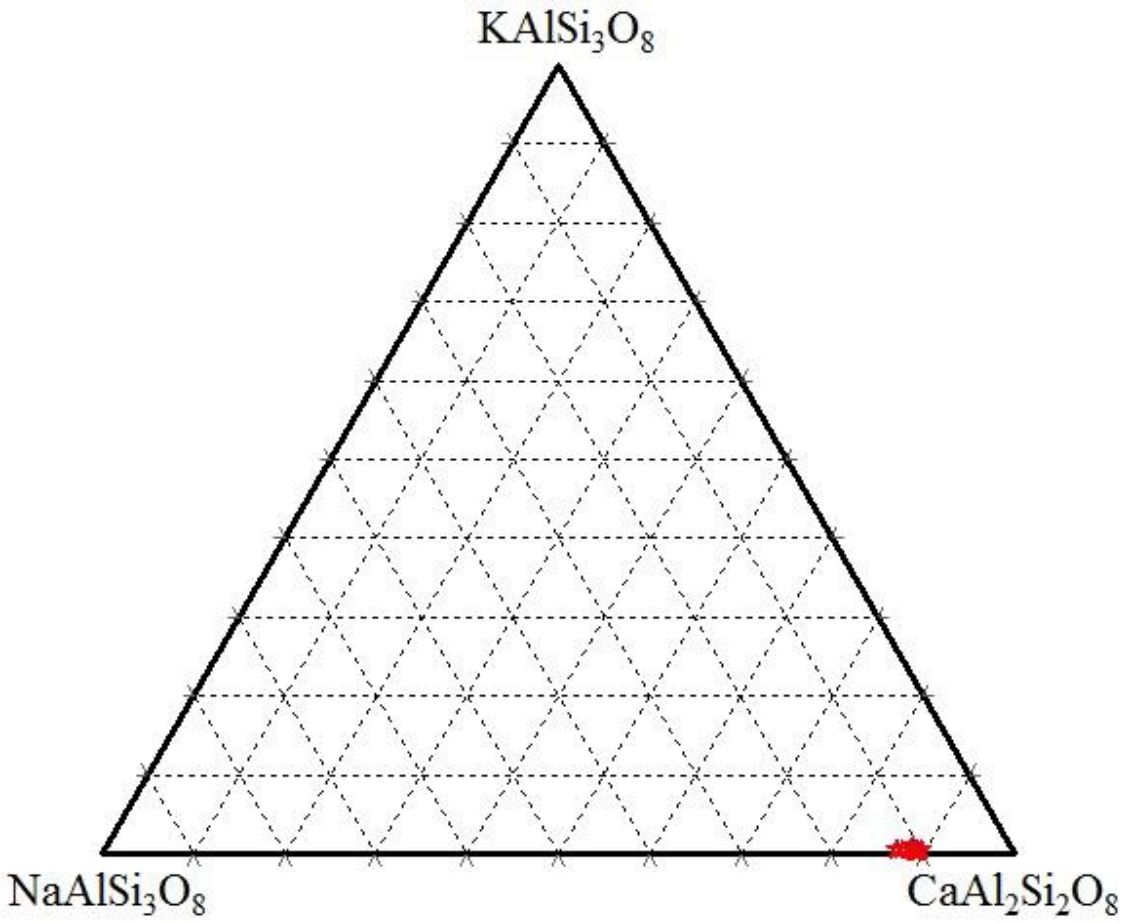

Fig. 2.37 Chemical composition of plagioclase in Piplia Kalan.

2.2.4. Padvarninkai

Padvarninkai fell in Androniski, Lithuania in 1929. This meteorite shows an ophitic texture and is heavily shocked. Padvarninkai is classified as a surface eucrite and mineral assemblage of Padvarninkai includes pyroxene, plagioclase, impact melt veins and some accessory minerals such as ilmenite and chromite (Fig. 2.38). This eucrite is highly shocked and some plagioclase grains are completely transformed to maskelynite. Padvarninkai is one the most highly shocked eucrites and the estimated shock pressure is over 42 GPa (Bischoff and Stoffler 1992).

Pyroxene has exsolution lamellae and pigonite is severely fractured and mosaicized. The studied maskelynite grains show subhedral or needle-like shape whose sizes are about 500 x 300 and 500 x 50 μm, respectively. The chemical composition of Padvarninkai maskelynite is An_{92-87} and the FeO abundance is about 0.4 wt% (Table 2.2 and Fig. 2.39).

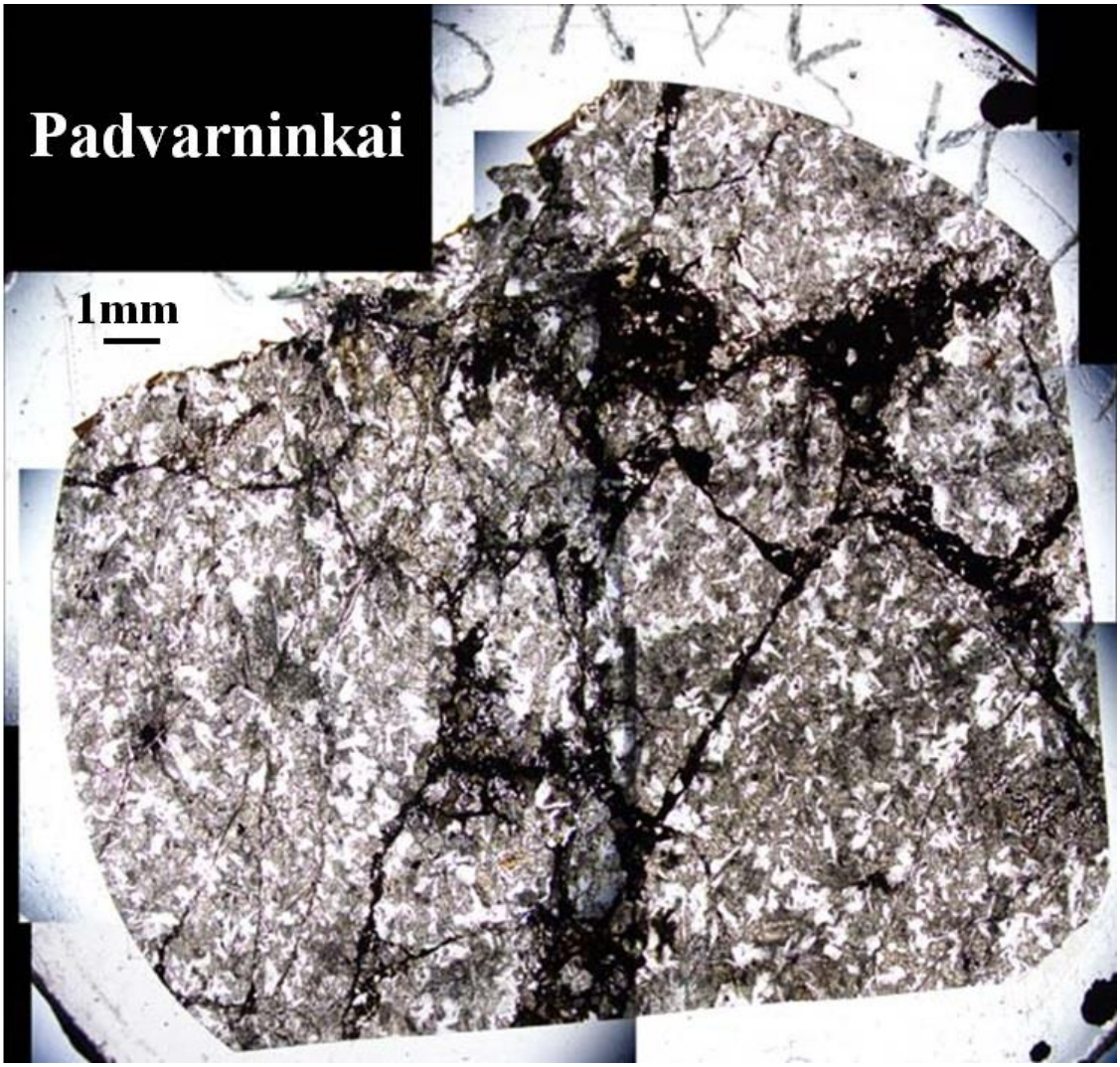

Fig. 2.38 Optical photomicrograph of Padvarninkai (plane-polarized light). Note the presence of dark shock melt veins forming network structures.

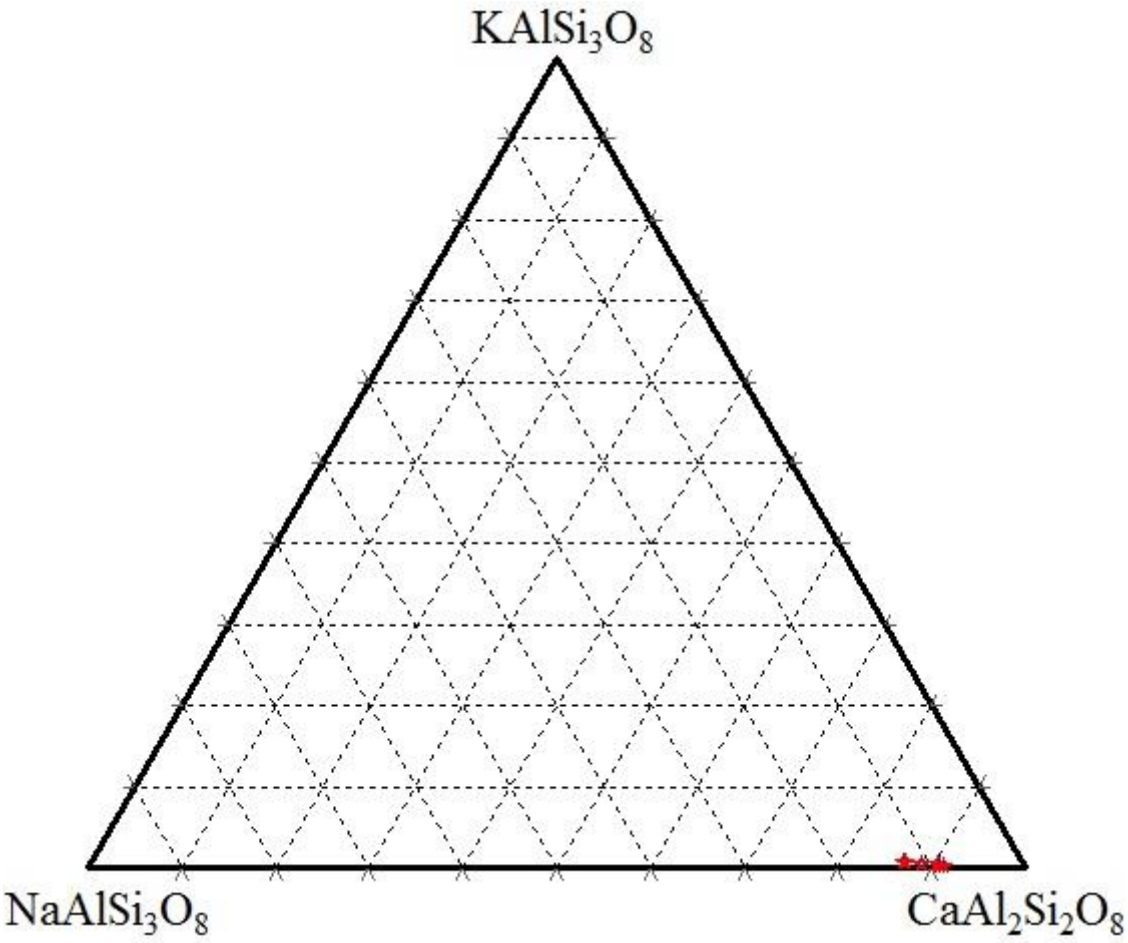

Fig. 2.39 Chemical composition of maskelynite in Padvarninkai.

2.2.5. Y-75011

Y-75011 is an Antarctic meteorite found in Yamato Mountains in 1975. It is a surface eucrite that contains abundant clasts of fine-grained pyroxene, plagioclase and groundmass (Fig. 2.40). The groundmass contains smaller pyroxene, lathy plagioclase grains and some minor minerals such as opaque minerals. The quenched texture shows that Y-75011 had preserved the pristine nature of its initial crystallization. Y-75011 is apparently fragments of lavas that were extruded onto or close to the surface of the parent asteroid putatively 4Vesta (Takeda and Graham, 1991).

Pyroxene shows subhedral to euhedral shapes and I found a variation in size, which reaches up to 2 mm. The lathy plagioclase shape shows that it has experienced a rapid cooling. The plagioclase composition is An_{92-89}, and the FeO abundance is 0.3-0.4 wt% (Table 2.2 and Fig. 2.41).

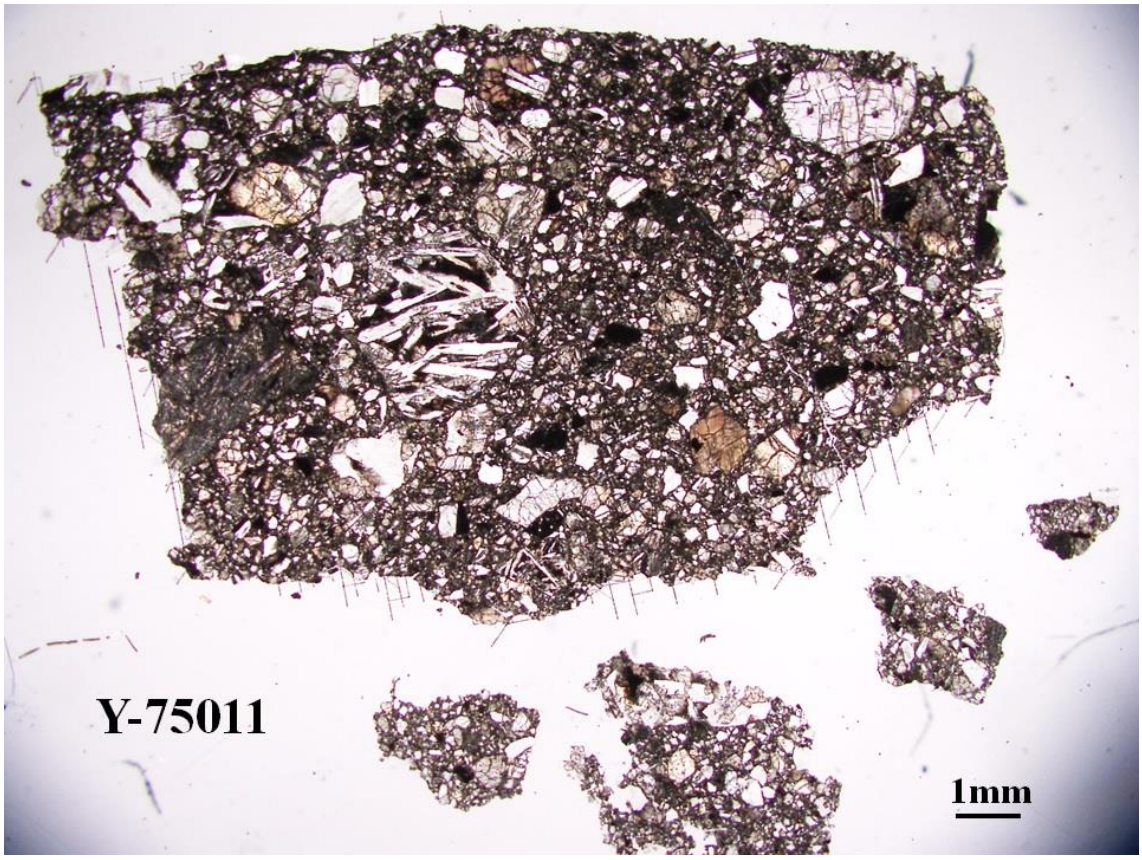

Fig. 2.40 Optical photomicrograph of Y-75011 (plane-polarized light).

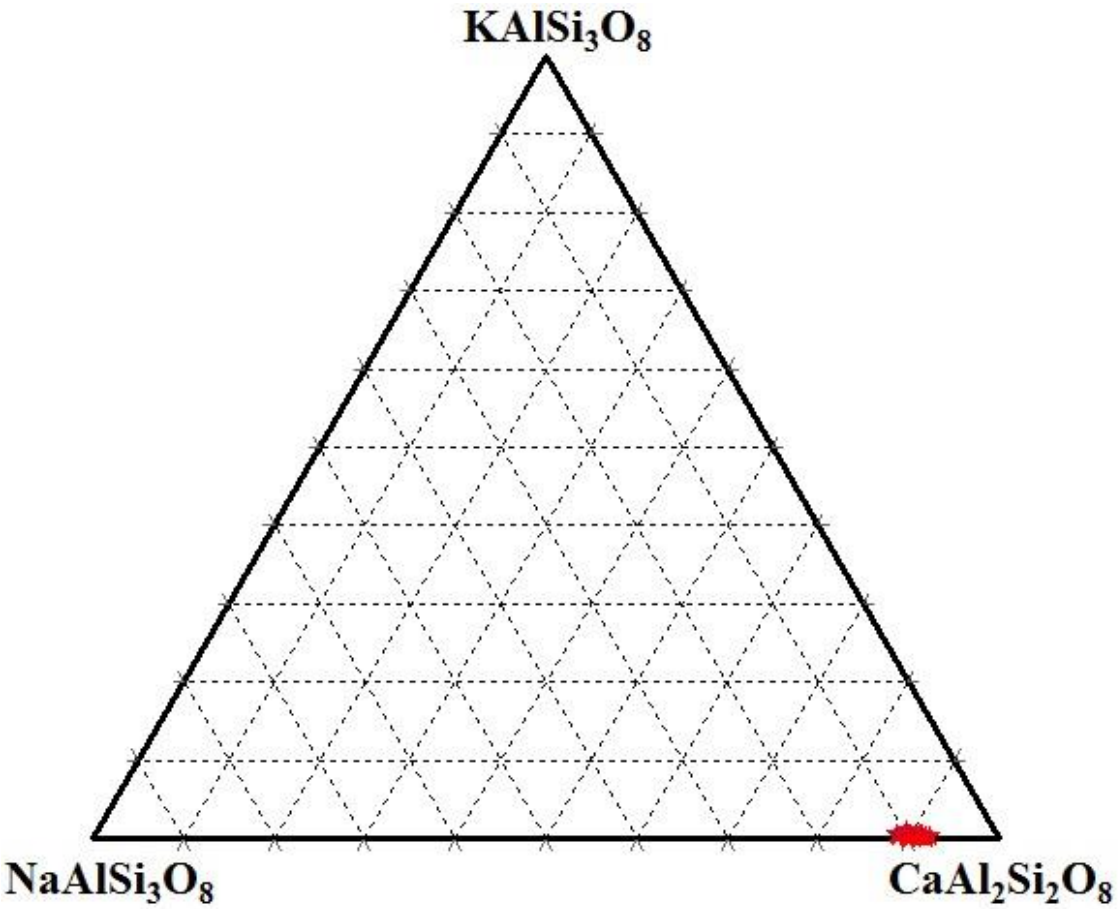

Fig. 2.41 Chemical composition of plagioclase in Y-75011.

2.2.6. EETA 87520

EETA 87520 is an Antarctic meteorite and it was found in Elephant Moraine in 1987. EETA 87520 is an unbrecciated cumulate eucrite showing a coarse-grained texture (Fig. 2.42). As a point to be noted, this meteorite contains pyroxene which is more Mg-rich than other non-cumulate eucrites. The weathering grade of EETA 87520 is B (Grossman 1993).

EETA 87520 is mainly composed of pyroxene and plagioclase with accessories such as ilmenite. Most of the pyroxene is pigeonite and there is a small amount of augite. The chemical compositions of low-Ca and high-Ca pyroxenes are $En_{45}Wo_5$ and $En_{46}Wo_{37}$, respectively. Pigeonite grains show narrow exsolution lamellae (Fig. 2.43). Plagioclase shows subhedral to euhedral shapes and its size is commonly larger than 1 mm. The plagioclase composition is about An_{91-80} and the FeO abundance is lower than 0.05 wt% (Table 2.2 and Fig. 2.44).

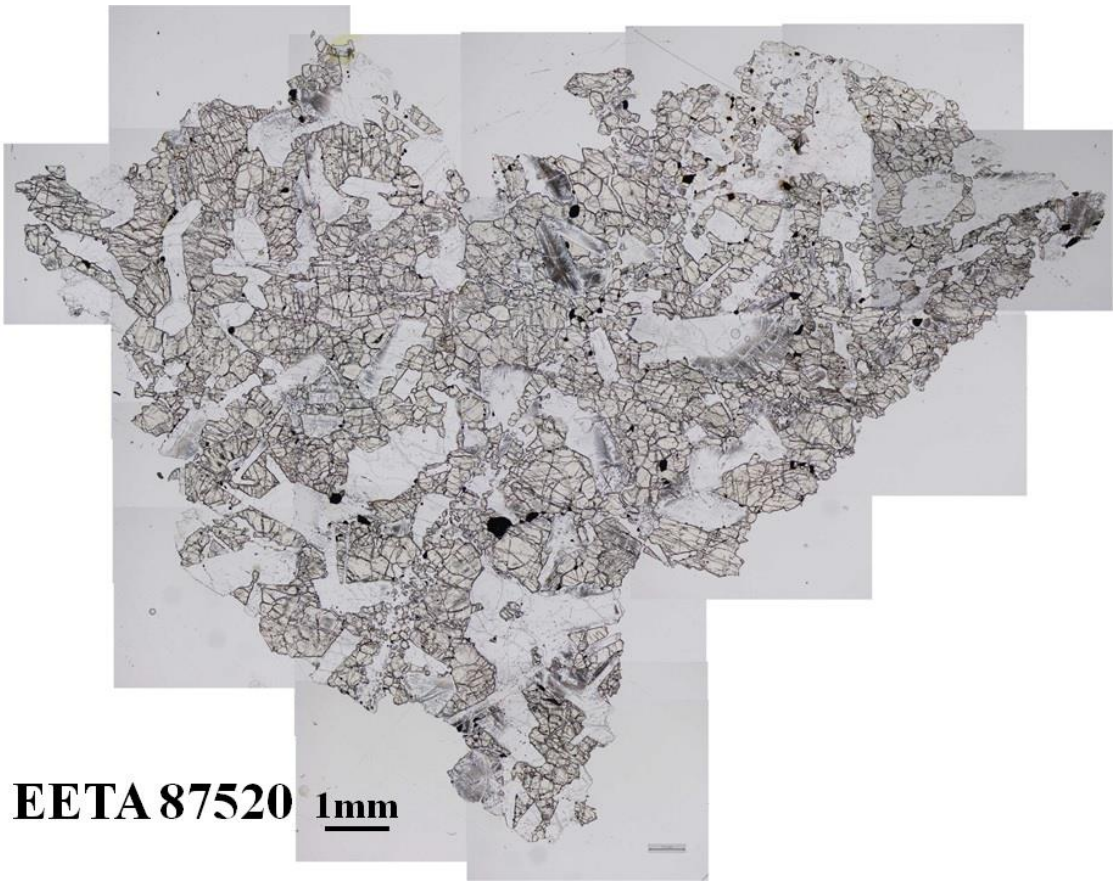

Fig. 2.42 Optical photomicrograph of EETA 87520 (plane-polarized light).

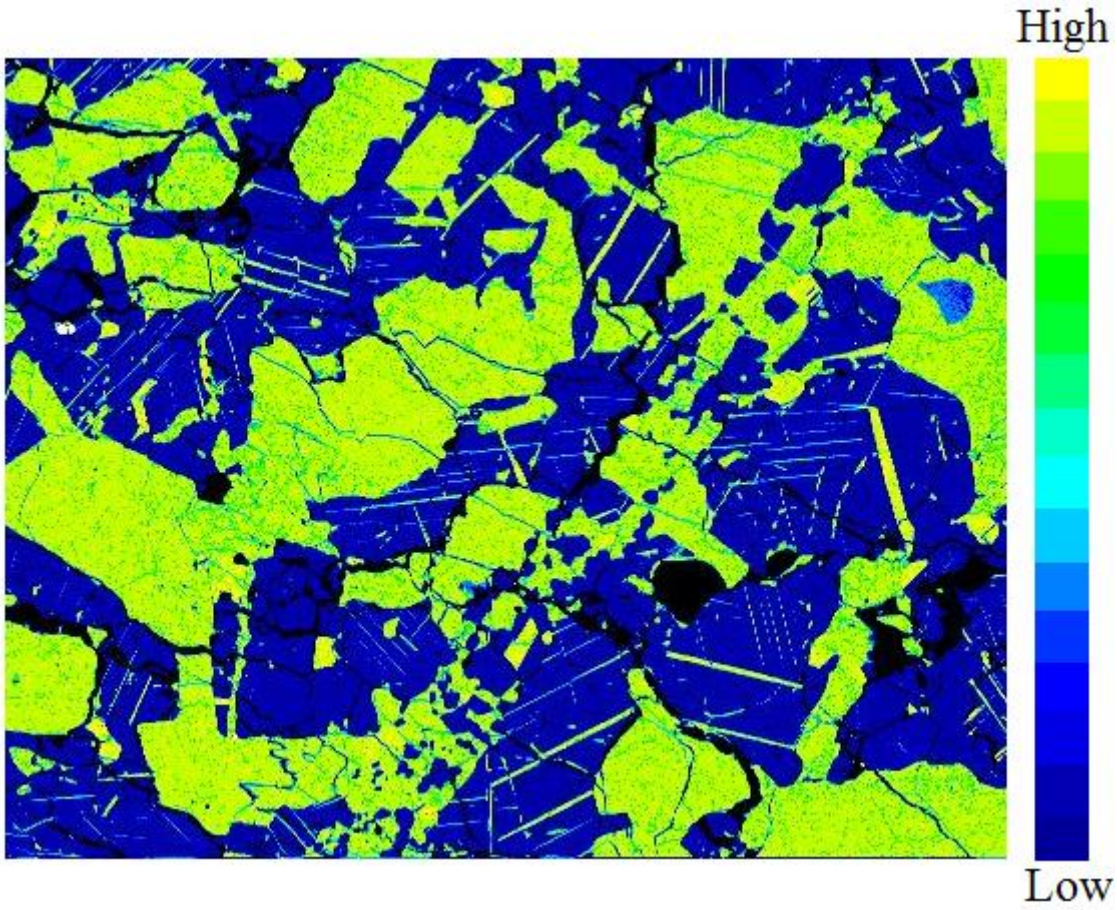

Fig. 2.43 Ca X-ray map of EETA 87520. Yellow-to-green part shows the high-Ca area and blue-colored parts shows the low-Mg area.

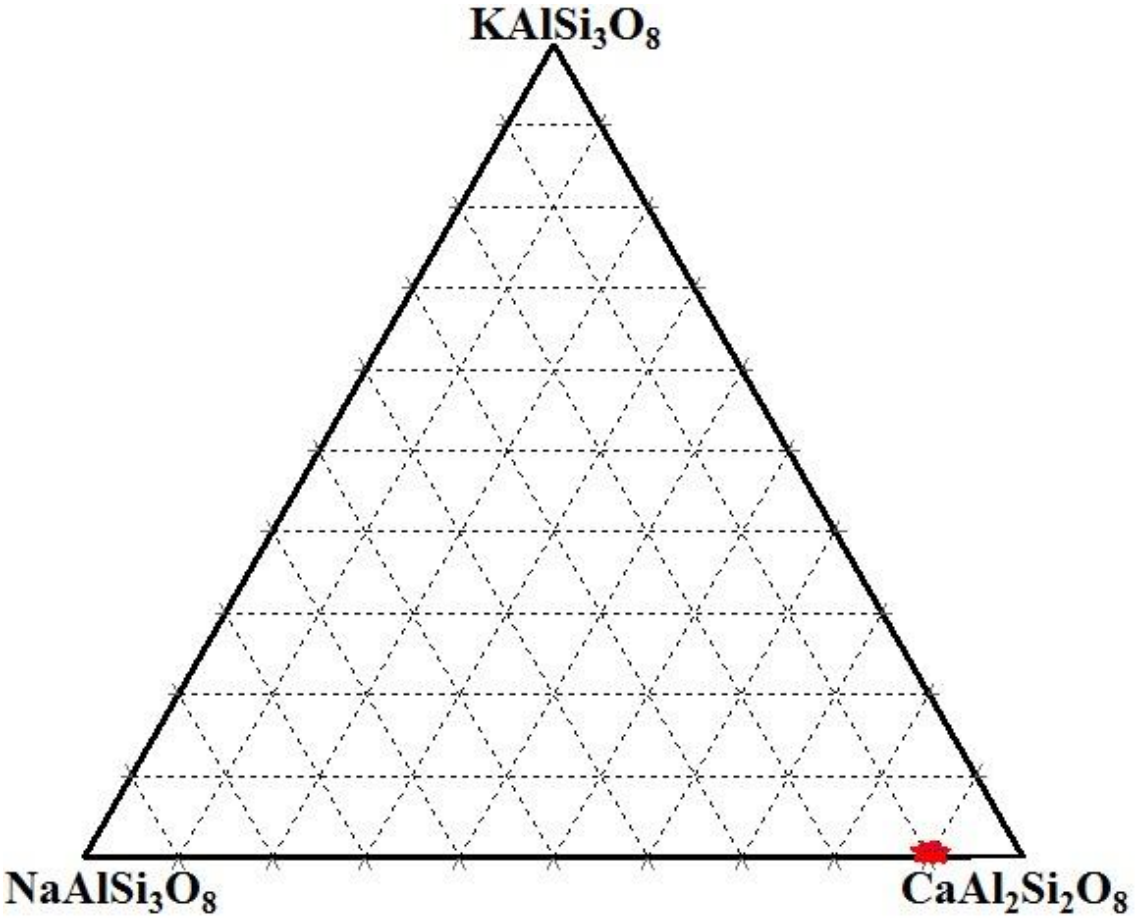

Fig. 2.44 Chemical composition of plagioclase in EETA 87520.

2.2.7. Moore County

Moore County fell in Moore County, North Carolina, USA at 5:00 PM on April 21, 1913. Henderson and Davis (1936) reported that the fusion crust is < 1mm on the front face, which is transparent enough to observe the color of component minerals. Moore County is an unbrecciated cumulate eucrite with an equigranular coarse-grained texture (Fig. 2.45). Hess and Henderson (1949) reported that it is texturally and chemically similar to terrestrial cumulates, including evidence of crystal accumulation at the bottom of a magma chamber. Moore County has experienced two-stage cooling history and the burial depth of this meteorite was about 8-9 km (Miyamoto and Takeda 1994).

The main pyroxene in Moore County is pigonite whose chemical composition is $En_{47}Wo_6$ (Ishii and Takeda 1974). It mainly consists of coarse augite lamellae (100 μm in width) and fine augite lamellae (100 nm) in the host augite (Miyamoto and Takeda 1994). Plagioclase is commonly larger than 1 mm. The plagioclase composition is

An_{90-92}, and the FeO abundance is less than 0.1 wt% (Table 2.2 and Fig. 2.46).

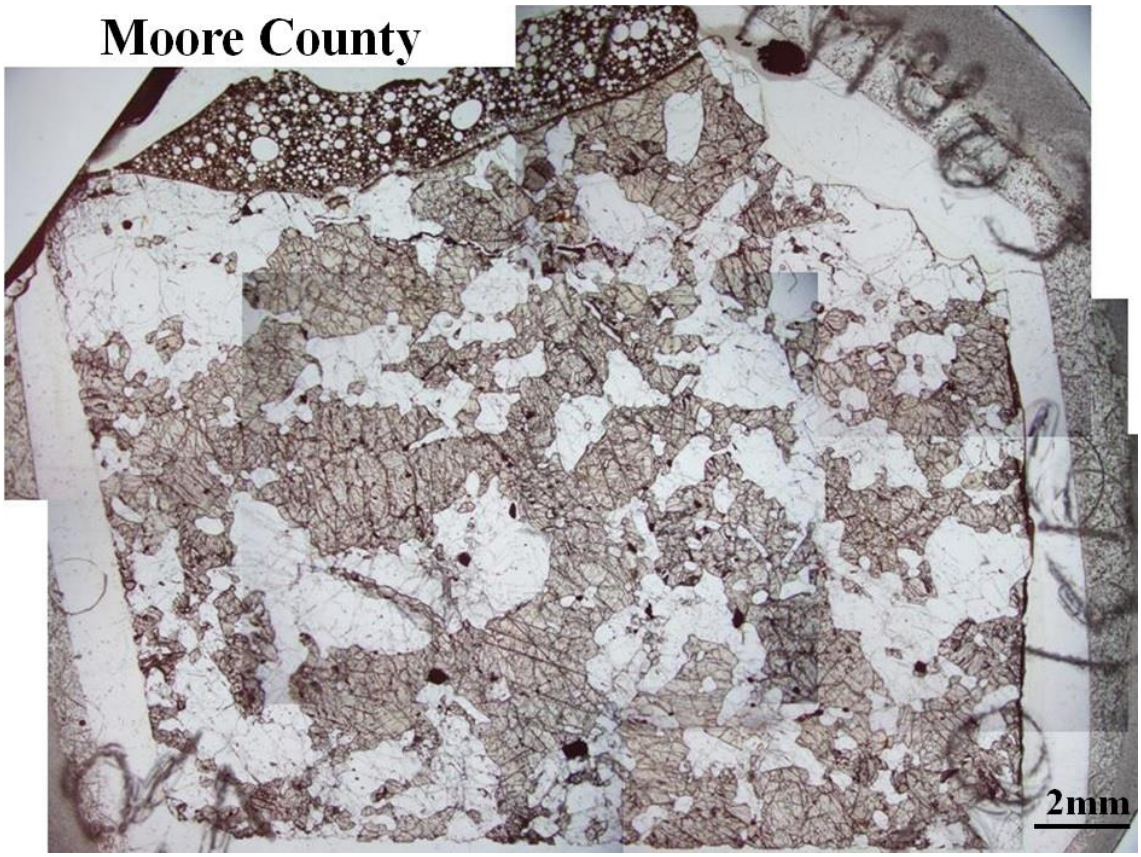

Fig. 2.45 Optical photomicrograph of Moore County (plane-polarized light).

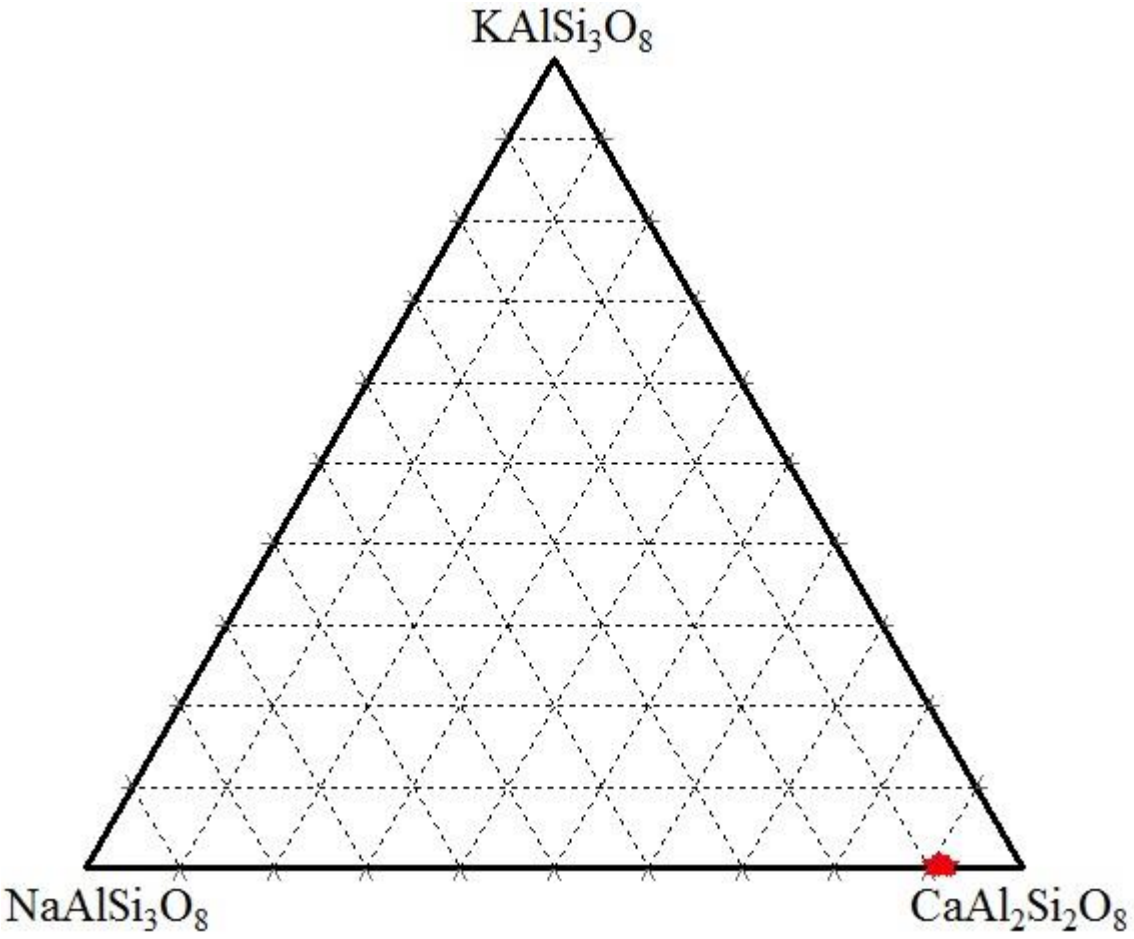

Fig. 2.46 Chemical composition of plagioclase in Moore County.

2.2.8. Y 980433

This meteorite was found in Antarctica in 1998. Y 980433 is a Mg-rich cumulate eucrite showing a coarse-grained texture and it consists of low-Ca pyroxene and plagioclase with accessory opaque minerals (Fig. 2.47). Pyroxene and plagioclase show mosaic extinction due to shock.

Y 980433 has clearly thick exsolution lamella of pyroxene, indicating that this sample formed in slowly cooling magma as in terrestrial layered intrusions (Takeda et al. 2011). The chemical composition of pyroxene is about $En_{51}Wo_2$. Plagioclase is commonly larger than 2 mm and is enclosed in continuous networks of pyroxene grains. The plagioclase composition is $An_{91\text{-}87}$ and the FeO abundance is < 0.1 wt% (Table 2.2 and Fig. 2.48).

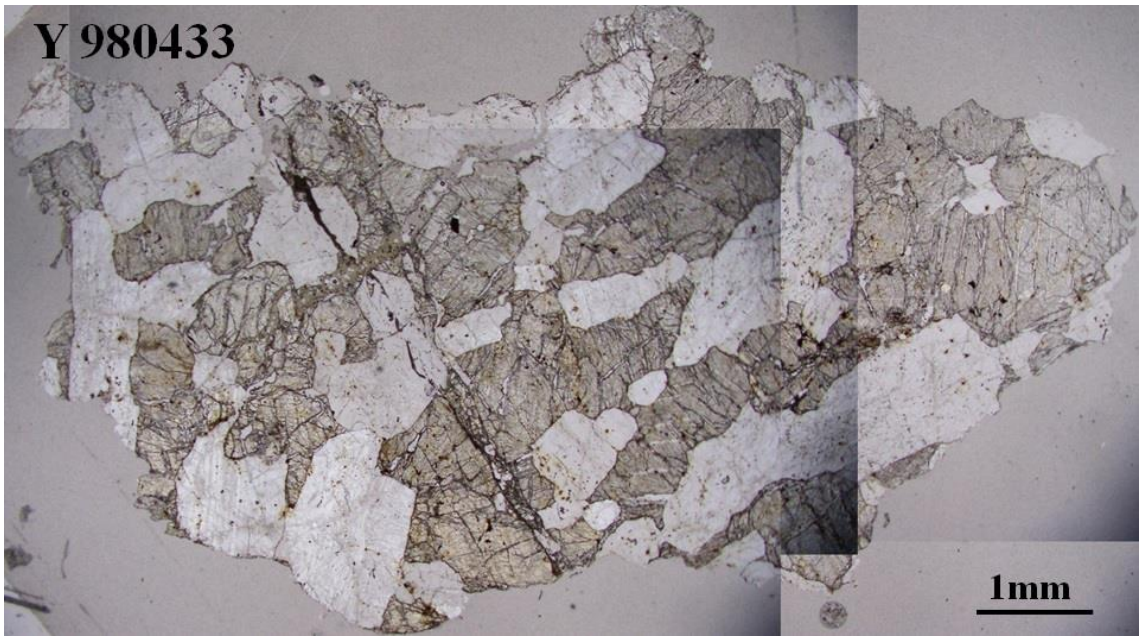

Fig. 2.47 Optical photomicrograph of Y 980433 (plane-polarized light).

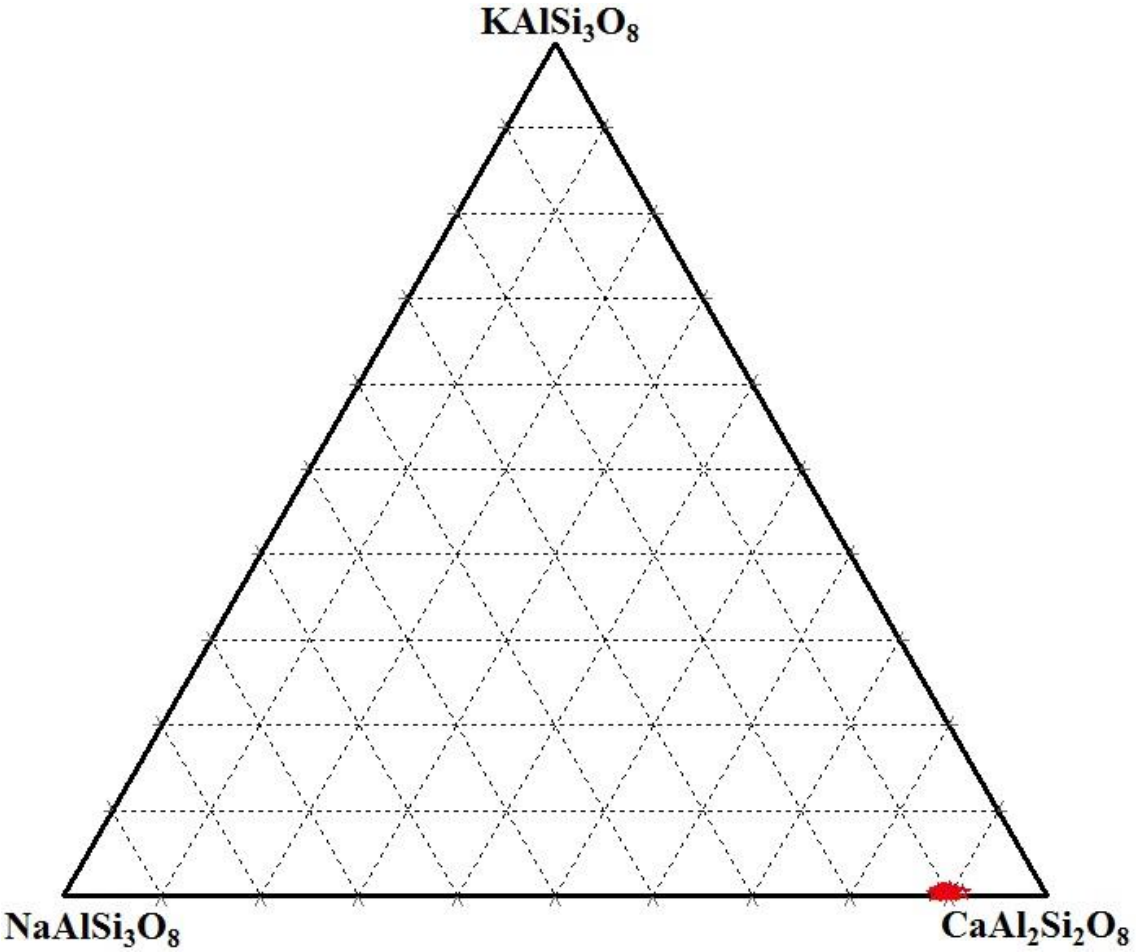

Fig. 2.48 Chemical composition of plagioclase in Y 980433.

2.2.9. Y-75032

Y-75032 is an Antarctic meteorite classified as a ferroan and Ca-rich diogenite. Y-75032 is mainly composed of pyroxene megacrysts and groundmass which consists of small pyroxene and dark glassy matrix. This sample shows a coarse-grained texture and their pyroxene grain size is larger than 1 mm (Fig. 2.49). This meteorite contains plagioclase which is not contained generally in diogenite. The rare plagioclase grain, which shows a fine-grained feather-like texture, probably formed by recrystallization of maskelynite (Mikouchi et al. 2002).

The plagioclase composition is An_{91-87} and the FeO abundance is < 0.1 wt% (Table 2.2 and Fig. 2.50).

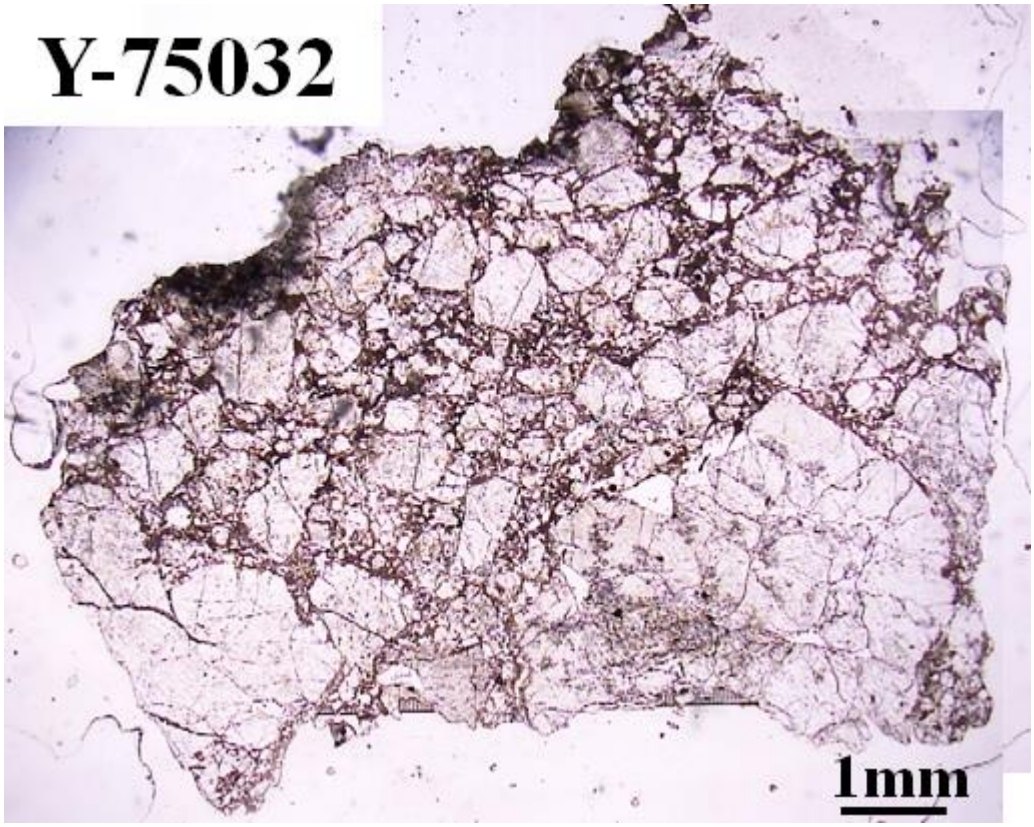

Fig. 2.49 Optical photomicrograph of Y-75032 (plane-polarized light).

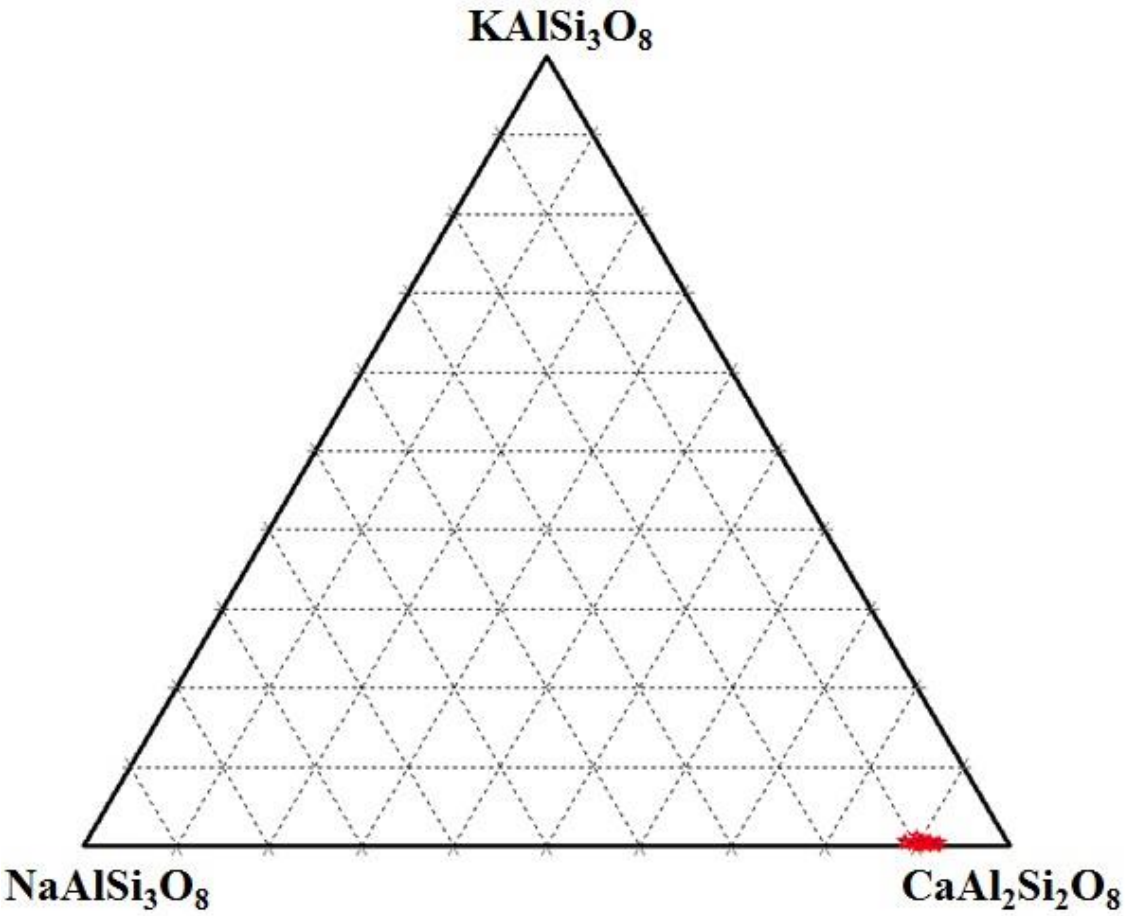

Fig. 2.50 Chemical composition of plagioclase in Y-75032.

Table 2.2

Group, average plagioclase and maskelynite compositions (anorthite and orthoclase contents and FeO* abundance) for studied HED meteorites.

Sample	Group	An	Or	FeO* (FeO* = FeO + Fe_2O_3) (wt%)
ALH 76005	Surface eucrite	92–80	–1	0.2–0.4
Petersburg	Surface eucrite	89–86	–2	0.2–0.4
Piplia Kalan	Surface eucrite	89–87	–1	0.2–0.3
Padvarninkai	Surface eucrite	92–87	–1	0.4
Y-75011	Surface eucrite	92–89	–1	0.3–0.4
EETA 87520	Cumulate eucrite	91–80	–1	~0.05
Moore County	Cumulate eucrite	92–90	–1	~0.1
Y 980433	Cumulate eucrite	91–87	–1	~0.1
Y-75032	Diogenite	91–87	–1	~0.1

2.3. Samples of Shock-loading Experiment

I also studied plagioclase samples of shock-loading experiment by courtesy of Prof. A. Tsuchiyama at Division of Earth and Planetary Science, Graduate School of Science, Kyoto University. Shock-loading experiments were carried out using a propellant gun at Tohoku University with various composition of plagioclase. The analyzed samples are An_{80} (unshocked) (Fig. 2.51), An_{80} shocked at 20 GPa (Fig. 2.52), An_{80} shocked at 30 GPa (Fig. 2.53), An_{80} shocked at 40 GPa (Fig. 2.54), An_{60} (unshocked) (Fig. 2.55), An_{60} shocked at 30 GPa (Fig. 2.56), An_{20} (unshocked) (Fig. 2.57), An_{20} shocked at 20 GPa (Fig. 2.58), An_{20} shocked at 30 GPa (Fig. 2.59) and An_{20} shocked at 40 GPa (Fig. 2.60). All of starting materials are 10 mm in diameter with 2 mm thickness. The recovered specimens were polished for optical microscope observation and subsequent Fe XANES analysis.

An unshocked sample of An_{80} is polycrystalline plagioclase and the samples of An_{60} and An_{20} are both single crystals of plagioclase. They show coarse-grained textures and their sizes are all larger than 1 mm (Fig. 2.51, 55 and 57). Except for the sample of An_{80} shocked at 30 GPa, experimentally-shocked samples show polymorphic fine-grained textures and include shock melt. In addition, experimentally-shocked samples show undulatory and extinction mosaicism due to shock.

Some samples of shock-loading experiment are transformed to isotropic glass (maskelynite) and the details of samples are shown in Table 2.3 by optical microscope analysis and X-ray diffraction (XRD) analysis (Tsukada et al. 1999).

Table 2.3

List of samples, the results of optical microscopy and XRD analysis (Tsukuda et al. 1999). In optical microscopy result, "A" showed that all area is crystalline, "B" showed that very small area is amorphous, "C" showed that almost area is amorphous and "D" showed that all area is amorphous, respectively. In the XRD result, "A" showed that there is no change for the peak, "B" showed that peak is blurred slightly, "C" showed that peak is blurred and "D" showed that there is no peak, respectively.

Sample	Optical microscope	XRD
An_{80} (unshocked)	A	A
An_{80} shocked at 20GPa	B	A
An_{80} shocked at 30GPa	C	B
An_{80} shocked at 40GPa	D	D
An_{60} (unshocked)	A	A
An_{60} shocked at 30GPa	B	B
An_{20} (unshocked)	A	A
An_{20} shocked at 20GPa	C	A
An_{20} shocked at 30GPa	B	B
An_{20} shocked at 40GPa	D	C

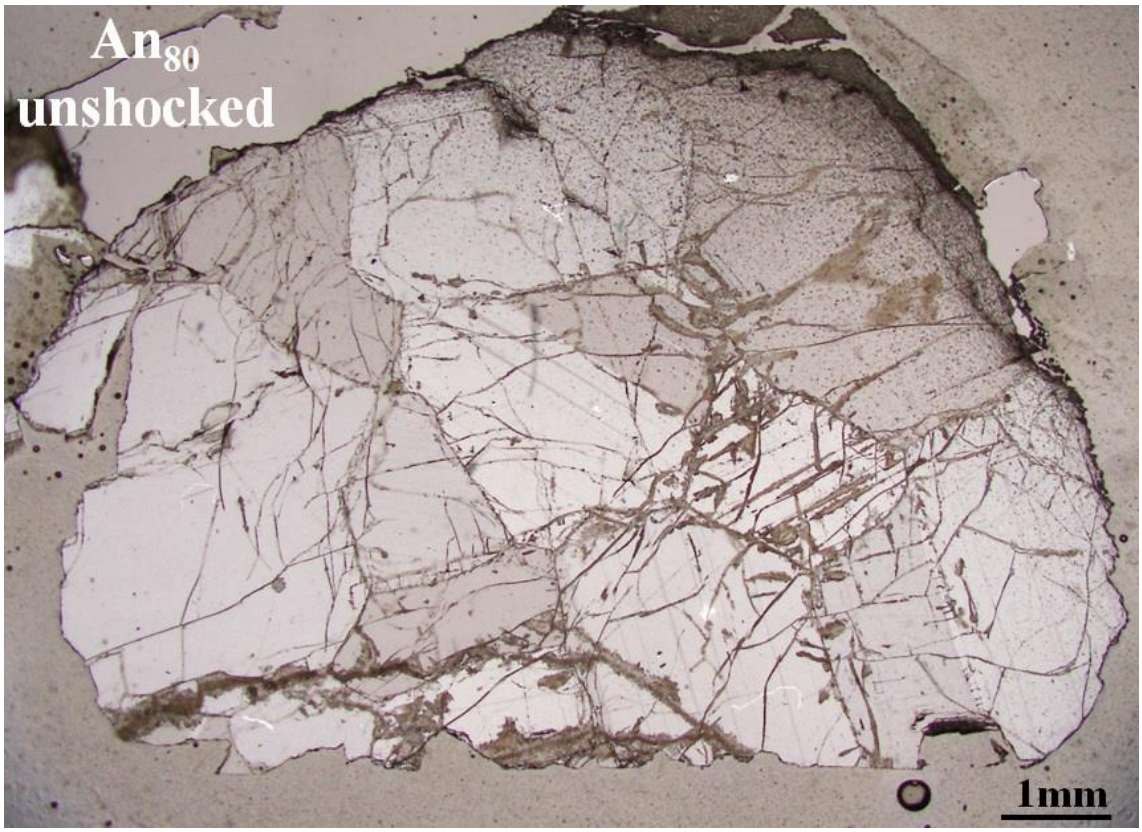

Fig. 2.51 Optical photomicrograph of An_{80} unshocked sample (plane-polarized light).

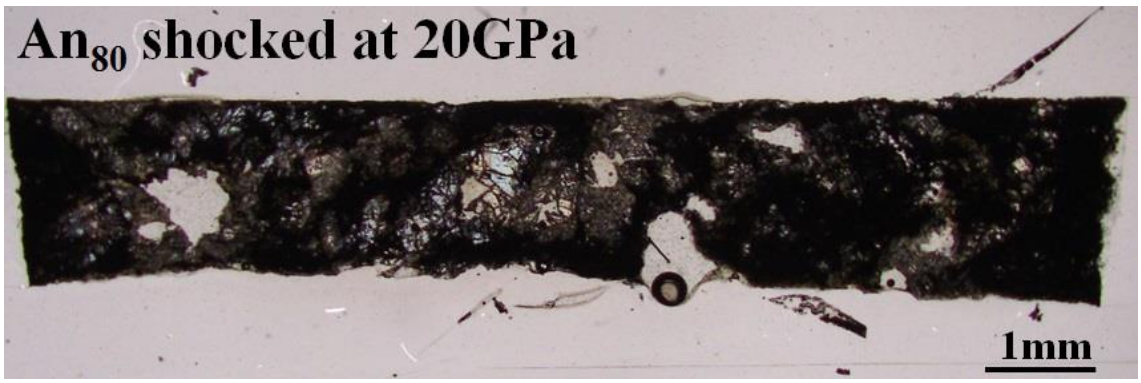

Fig. 2.52 Optical photomicrograph of An_{80} plagioclase shocked at 20 GPa (plane-polarized light).

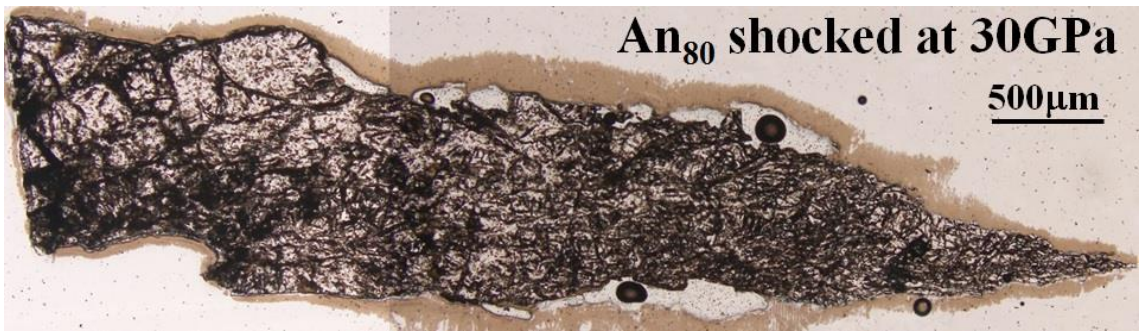

Fig. 2.53 Optical photomicrograph of An_{80} plagioclase shocked at 30 GPa (plane-polarized light).

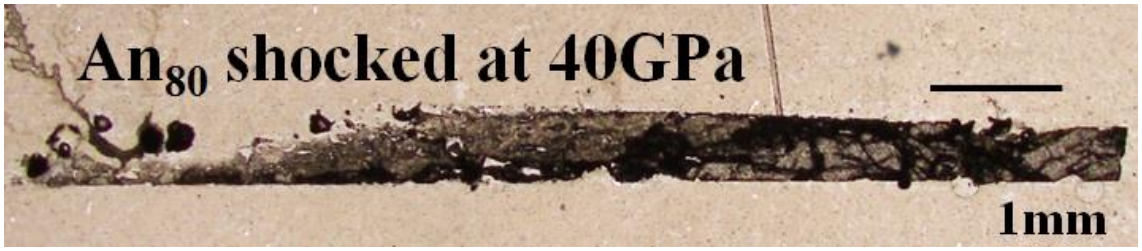

Fig. 2.54 Optical photomicrograph of An_{80} plagioclase shocked at 40 GPa (plane-polarized light).

Fig. 2.55 Optical photomicrograph of An_{60} unshocked sample (plane-polarized light).

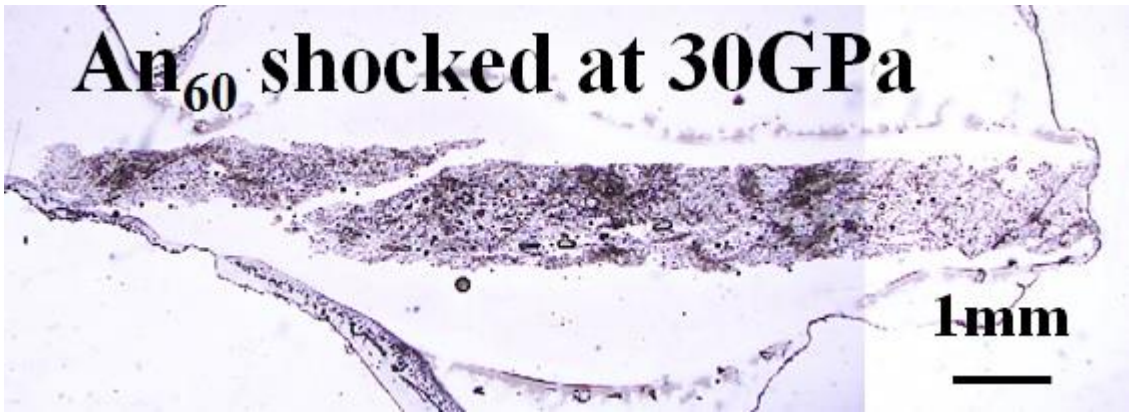

Fig. 2.56 Optical photomicrograph of An_{60} plagioclase shocked at 30 GPa (plane-polarized light).

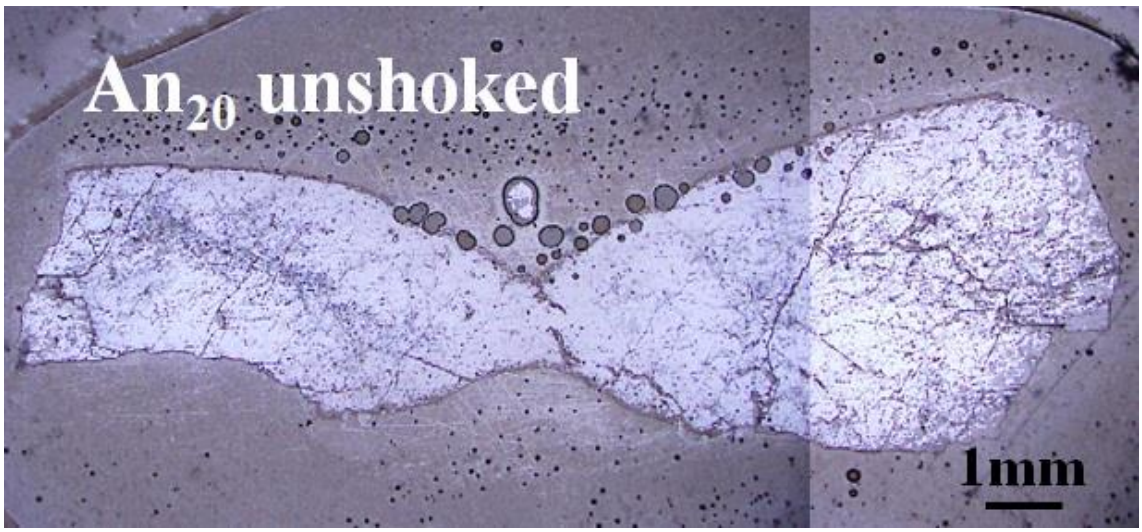

Fig. 2.57 Optical photomicrograph of An_{20} unshocked sample (plane-polarized light).

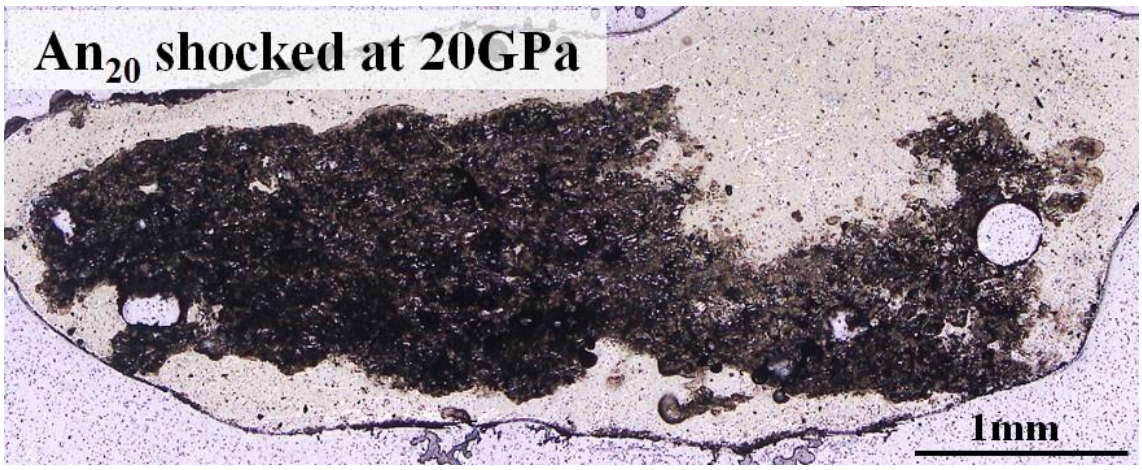

Fig. 2.58 Optical photomicrograph of An_{20} plagioclase shocked at 20 GPa (plane-polarized light).

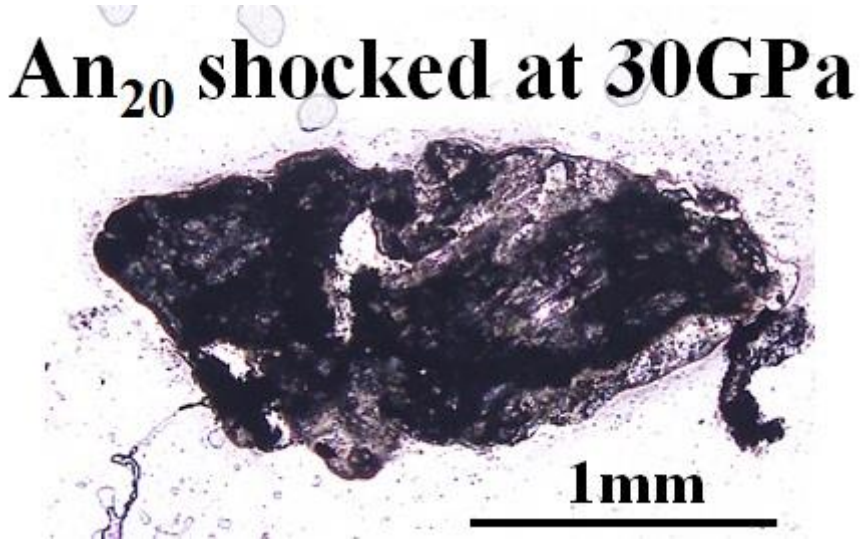

Fig. 2.59 Optical photomicrograph of An_{20} shocked at 30 GPa (plane-polarized light).

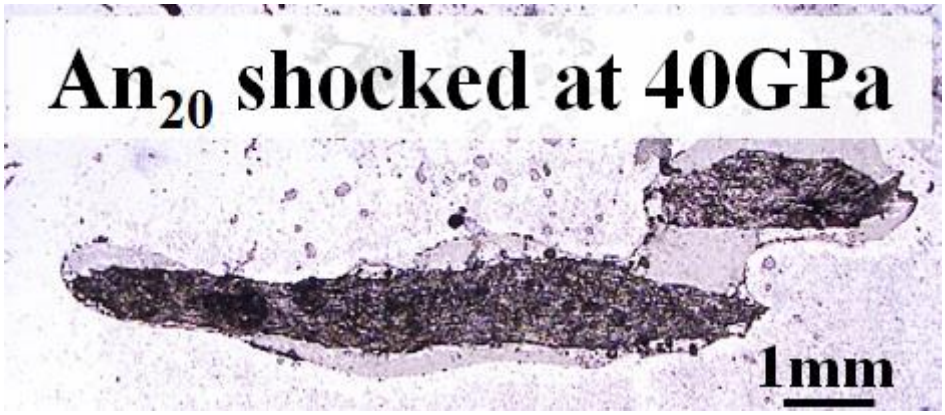

Fig. 2.60 Optical photomicrograph of An_{20} plagioclase shocked at 40 GPa (plane-polarized light).

2.4. Samples of Synthetic Experiment and Terrestrial Plagioclase

I synthesized two basaltic plagioclase samples by crystallization experiment under controlled fO_2 in order to create a calibration curve used for the Fe XANES results. One sample crystalized at log fO_2 = QFM –2 and the other sample crystallized at log fO_2 = QFM. One polished thin section of each sample was analyzed. The thin section sizes are 2x2 mm for both QFM –2 and QFM samples.

Optical microscope observations show that these two samples are mainly composed of glass with plagioclase phenocrysts (Figs. 2.61 and 62). Plagioclase is the liquidus phase in the starting material. I set homogenization temperature to 1260 ^{o}C and only plagioclase crystallized at the temperature. The plagioclase abundance in the QFM–2 sample is higher than that of the QFM sample. Most plagioclase grains in both QFM and QFM –2 samples crystallized near the edge of the charges because of nucleation from the wall. Plagioclase grains in the QFM sample show euhedral shapes. The largest grain size in this sample is about 300 x 200 μm and most of the plagioclase grains are less than 300 μm (Fig. 2.61). In the case of the QFM –2 sample, plagioclase grains show a needle-like lath shape. The largest grain size in the QFM –2 sample is about 1000 x 50 μm (Fig. 2.62). Many fine-grained plagioclases show subhedral shape.

The chemical composition of plagioclase in the QFM -2 sample is An_{63-58} and the FeO abundance is 0.1-0.4 wt% (Fig. 2.63).

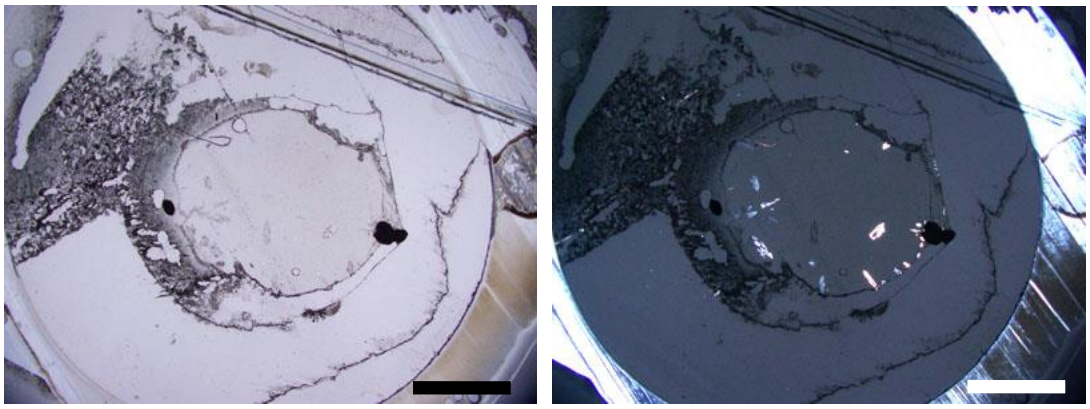

Fig. 2.61 Optical photomicrographs of the QFM sample. The left image is open nicol and the right one is crossed nicols. Black and white bars at the lower right corners of each image are scales of 1 mm.

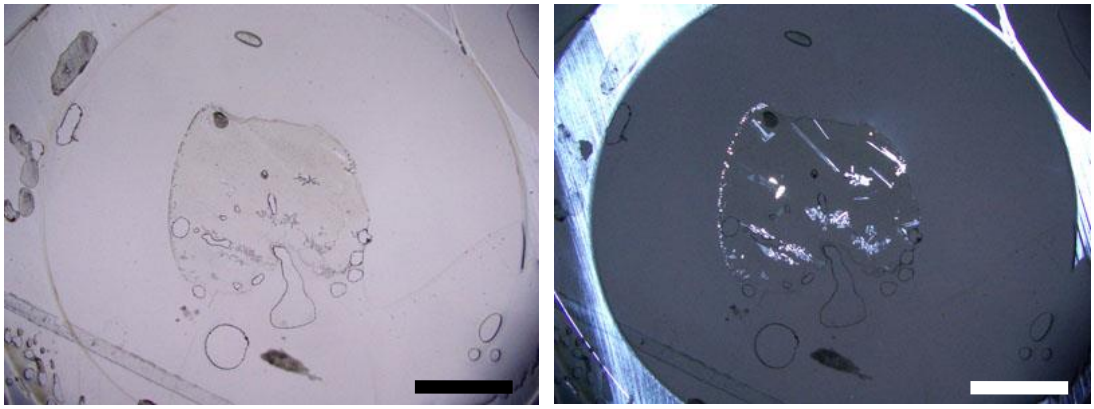

Fig. 2.62 Optical photomicrographs of the QFM–2 sample. The left image is open nicol and the right one is crossed nicols. Black and white bars at the lower right corner of each image are scales of 1 mm.

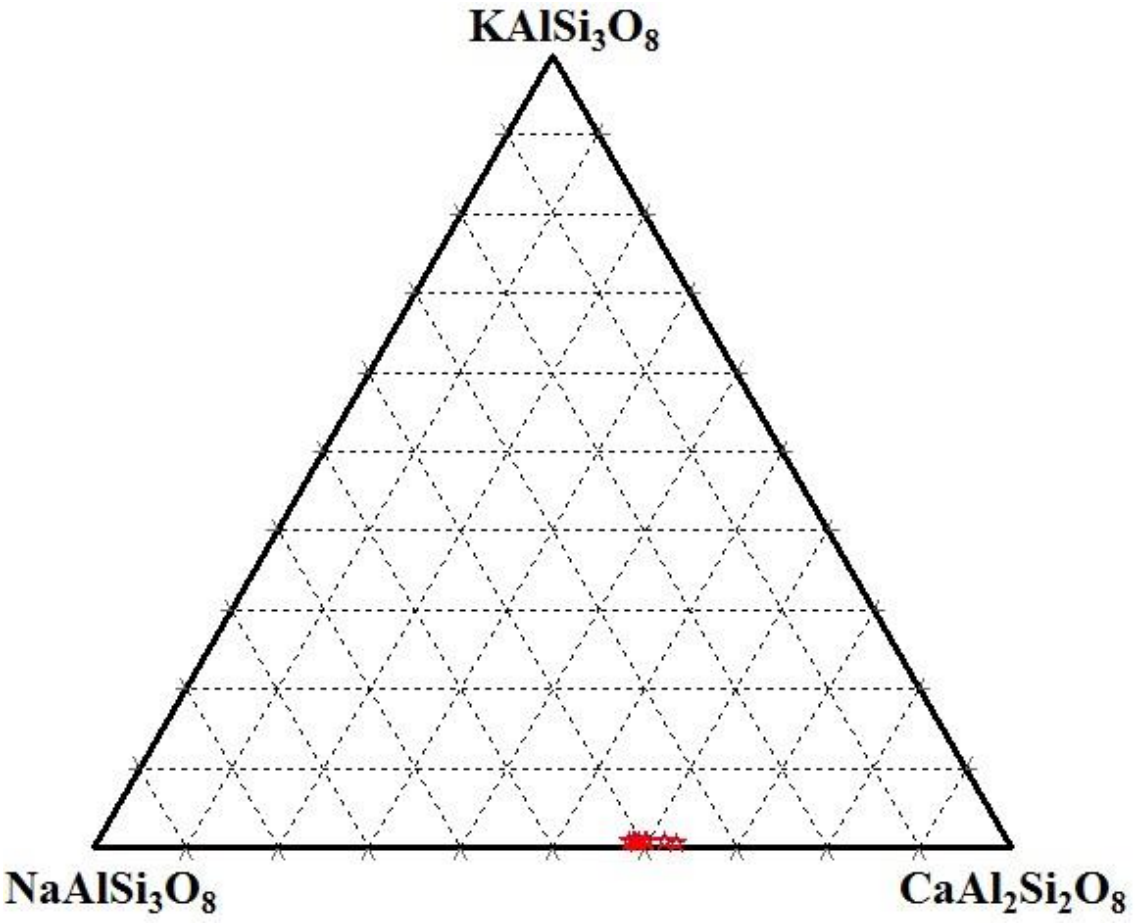

Fig. 2.63 Chemical composition of plagioclase in the QFM–2 sample.

2.5. Terrestrial Plagioclase with Known fO_2

Additionally, I obtained a terrestrial basaltic rock including plagioclase crystals whose oxygen fugacity was estimated by Dr. C. D Herd at Department of Earth and Atmospheric Science, University of Alberta, Canada. This sample is estimated to have crystallized at log fO_2 = QFM –1.5 using the Ol-Sp-Opx oxybarometer. The thin section of 10x10 mm was used for the XANES analysis.

This sample is mainly composed of megacrysts of plagioclase and pyroxene set in the groundmass (Fig. 2.64). Plagioclase megacrysts show euhedral shapes and their sizes are larger than 1 mm. Pyroxene grains are euhedral to subhedral and their sizes are about 700 μm. The groundmass consists of small laths of plagioclase grains showing needle-like shapes. The chemical composition of plagioclase in this sample is $An_{60\text{-}51}$ and the FeO abundance is 0.3-0.5 wt% (Fig. 2.65).

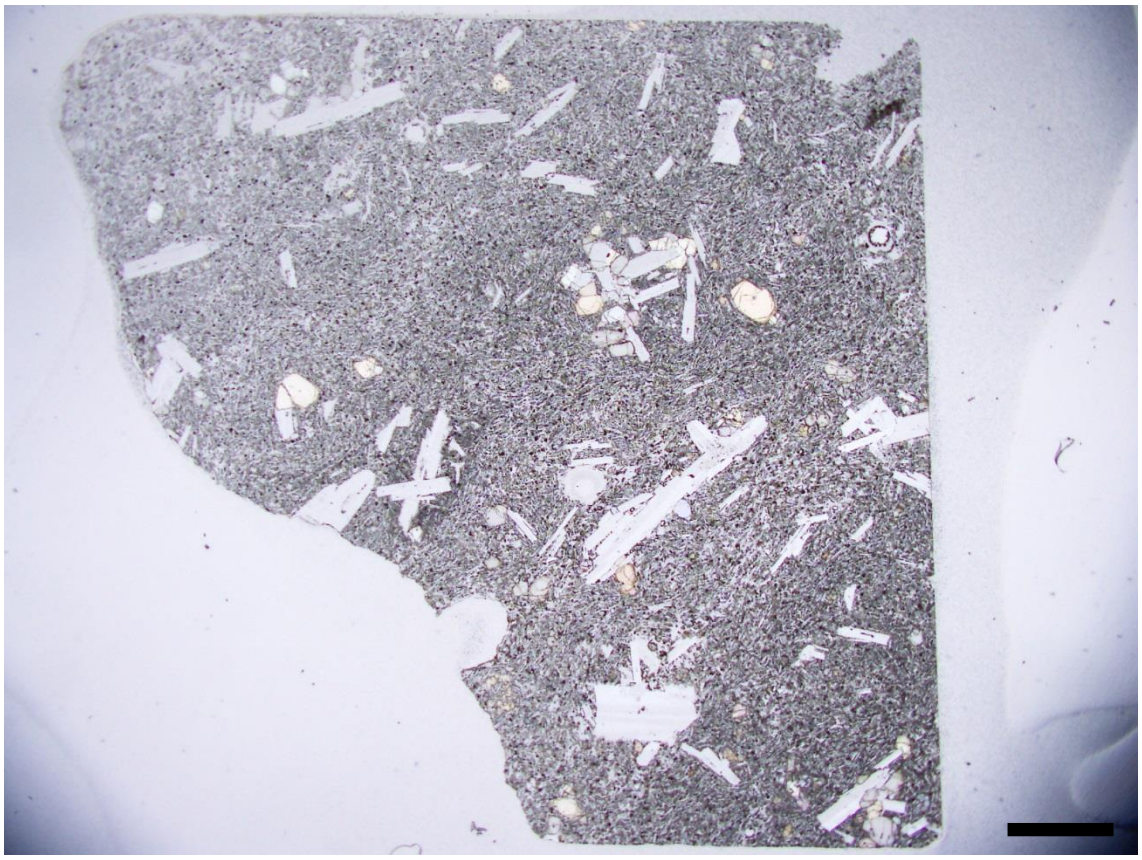

Fig. 2.64 Optical photomicrograph of thin section of the studied terrestrial basaltic rock (plane-polarized light). A black bar at the lower right corner is scale of 1 mm.

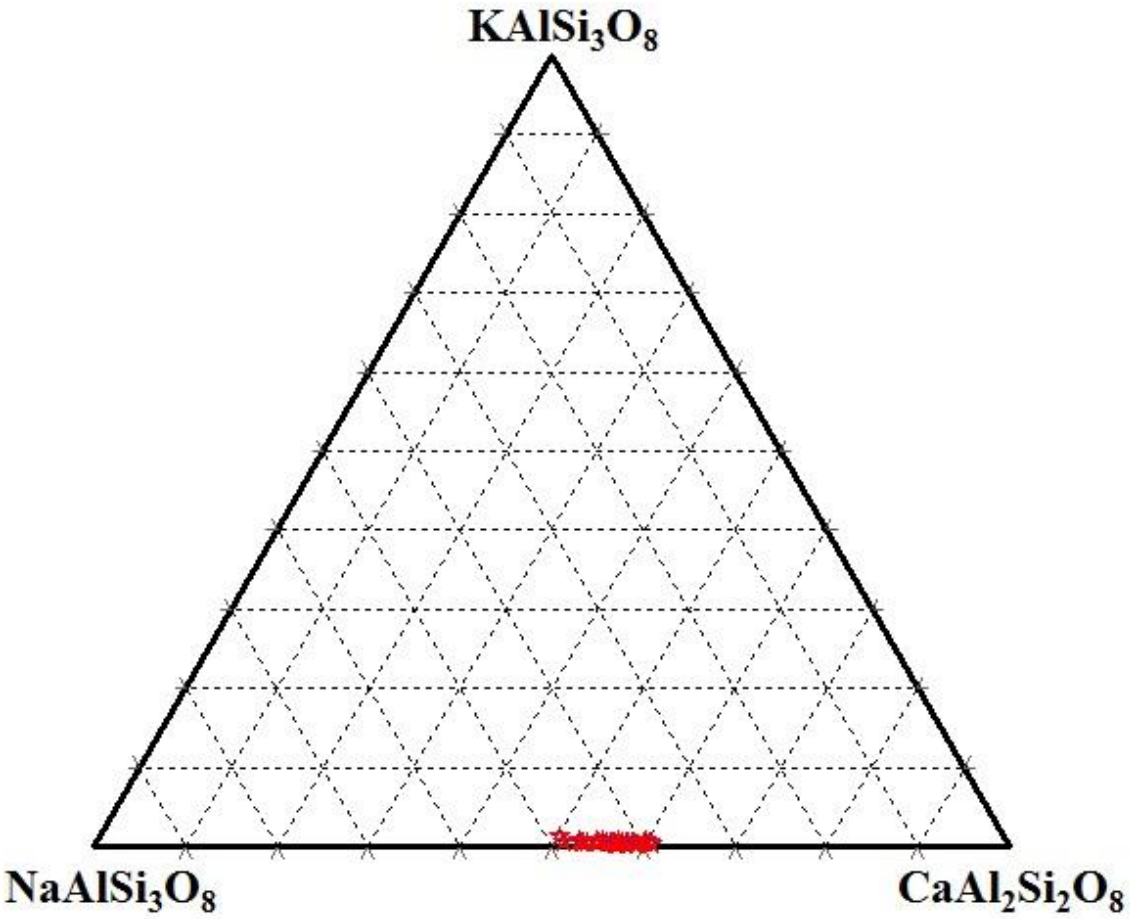

Fig. 2.65 Chemical composition of studied terrestrial plagioclase.

3. Methods

3.1. Optical and Scanning Electron Microscopy

I first observed all thin sections by an optical microscope and then by field emission gun scanning electron microscope (FEG-SEM) (Hitachi S-4500 at Department of Earth and Planetary Science, University of Tokyo) (Fig. 3.1). To clarify minute textures of samples analyzed, high-resolution backscattered electron (BSE) images were obtained with SEM equipped with energy dispersive spectrometer (EDS) and KEVEX SIGMA analysis system. Accelerating voltage of FEG-SEM was 15 kV and the beam current was 15 nA.

Fig. 3.1 FEG-SEM (Hitachi S-4500) at Department of Earth and Planetary Science, University of Tokyo.

3.2 Chemical Analysis with Electron Microprobe

I then analyzed maskelynite and plagioclase in the samples by electron microprobe (JEOL JXA-8900L at Department of Earth and Planetary Science, University of Tokyo) to obtain their chemical compositions. Accelerating voltage was 15 kV with the beam current of 8 nA. The probe diameter was set to be ~5 μm. Short analytical time (6 seconds for peak analysis and 3 seconds for the background) was adopted to minimize volatile loss. I used natural and synthetic minerals for the standards analysis. The ZAF program was employed for correcting experimental data. The principle of the ZAF program is correcting the relative intensity data using atomic number correction,

absorption correction and fluorescence correction (Potts et al. 1995). The thin sections were also analyzed with the chemical map analysis (CMA) software package of the JEOL 8900L for Si, Al, Ti, Fe, Mn, Mg, Ca, Na, K, and P to reveal chemical zoning within each grain of maskelynite and plagioclase.

Fig. 3.2 EPMA (JEOL JXA-8900L) at Department of Earth and Planetary Science, University of Tokyo.

3.3. Micro XANES Analysis

The $Fe^{3+}/\Sigma Fe$ ratios of minerals can be estimated by the energy shift of a pre-edge peak in XANES (X-ray Absorption Near Edge Structure) spectra obtained using the synchrotron radiation (SR) X-ray fluorescence because the pre-edge peak is independent of influence of self-absorption effects (e.g., Bajt et al., 1994). Pre-edge peak is always observed on the low-energy side of K-absorption edges (main-edge) of first-row transition elements.

The region below the absorption edge typically contains a pre-edge peak due to electronic transition from 1*s* to 3*d*. This pre-edge position shifts to higher energy with increasing the $Fe^{3+}/\Sigma Fe$ ratios of the minerals. Bajt et al. (1994) observed a linear relationship between pre-edge peak position and the $Fe^{3+}/\Sigma Fe$ ratio in silicate and oxide minerals by using the shift of pre-edge position. Delaney et al. (1998) reported that the $Fe^{3+}/\Sigma Fe$ ratios estimated by XANES analysis are in good agreement with those estimated by Mössbauer and wet chemical analysis. Some other researchers also discuss

quantitative estimation of the $Fe^{3+}/\Sigma Fe$ ratios in silicate and oxide minerals by using Fe XANES spectroscopy (e.g., Dyar et al. 2001, 2002; Wilke et al. 2001). Dyar et al. (2002) obtained Fe XANES spectra from single crystals of pyroxenes, amphiboles, and micas with the X-ray beam polarized along the X, Y, and Z optical orientations. They showed that pre-edge positions of sheet silicates depend on their crystallographic orientations. They predicted that errors on the use of pre-edge positions for determination of $Fe^{3+}/\Sigma Fe$ ratios in minerals could be better constrained by using crystallographic features.

I performed SR Fe-XANES analysis at BL-4A, Photon Factory (PF), High Energy Accelerator Research Organization (KEK), Tsukuba, Japan to estimate the Fe^{3+}-Fe^{2+} peak-intensity ratios of maskelynite and plagioclase, which is directly related to the $Fe^{3+}/\Sigma Fe$ ratios. The transmitted and fluorescent X-rays were measured by an ionization chamber and a Si (Li) detector, respectively. The angle between the incident beam and the detector was fixed at 90^{o} (Hayakawa et al. 1991) (Fig. 3.3). Kirkpatrick-Baez geometry mirrors were used to focus the beam to about a 5 x 6 μm square on the specimen. I recorded various energy range spectra. The minimum energy is 7087 eV and the maximum energy is 7183 eV, using a 0.11 eV step for the pre-edge and main-edge regions. The energy was calibrated by defining the first derivative peak of Fe foil to be 7111 eV. Each energy interval was counted between 5-40 live seconds for a total XANES spectrum acquisition time of about 0.7-5.0 hours, depending upon the Fe concentration in the sample. Anisotropic crystalline phases have variation in XANES intensity due to different crystal orientations as stated above (e.g., Dyar et al. 2002). In this respect analyzing maskelynite has a merit because of its isotropic nature and I do not need to consider the effect by the sample orientation. When analyzing crystalline plagioclase, I set the elongated dimension (*c* axis) of plagioclase grains studied always horizontally against the synchrotron beam. Then, I consider that I can minimize the orientation effect and can compare each XANES result in the same manner.

In most cases, I experimented with the top-up operation mode of the synchrotron beam. However, the incident beam intensity was not constant, and therefore I first divided the counting rates (cps) of the sample by the incident beam intensity (cps). Then, the obtained values are normalized by dividing them by the maximum count number at the main-edge peak that is present between 7087 to 7183 eV. After obtaining the corrected spectra, I first extracted the pre-edge region with the energy range about 7109-7115 eV from the data obtained.

The data were smoothed with the simple moving average method. Next, I subtracted a baseline, which I defined as a straight line covering the pre-edge region. I compared the

results by using both straight baseline and baseline with damped harmonic oscillator function. The obtained results show only little difference (about 1%) for the Fe^{3+}-Fe^{2+} peak-intensity ratio. Therefore, for simplicity to reduce the data, in this study I drew straight baseline to subtract background for all samples. Then, the obtained pre-edge peaks were deconvoluted into two Gaussian components after the background profiles were removed.

The values of half width of the peak, peak energy and the height of the peak are variable and these values are optimized when the data were fitted, although I set the initial values of half width of the peak and peak energy into the same values. Therefore, the value of half width of the peak has a wide value, although the position is not shifted. The energy positions of the obtained two peaks were almost same even in different samples. The higher energy position corresponds to the Fe^{3+} peak and the lower energy position corresponds to the Fe^{2+} peak, respectively (Wilke et al. 2001).

Thus, from the peak intensity of divalent and trivalent Fe obtained, the Fe^{3+}-Fe^{2+} peak-intensity ratio is defined by the following equation:

$$\text{The } Fe^{3+} - Fe^{2+} \text{peak intensity ratio}: \frac{Fe^{3+} \text{peak intensity}}{Fe^{3+} \text{ peak intensity } + \ Fe^{2+} \text{ peak intensity}}$$

I calculated all the propagation of statistical errors that occurs in the calculation of the normalization and above equation for the Fe^{3+}-Fe^{2+} peak-intensity ratio. Because it was impossible to prepare standard plagioclase samples with known $Fe^{3+}/\Sigma Fe$ ratios, it is not possible to determine the accuracy of this XANES analysis. Thus, in order to define the error of this analysis, I considered that several factors producing errors such as difference of chemical composition, crystal orientation, and mechanical and electrical tolerances of XANES device, statistical error is considered to give the largest error for the current XANES measurement because of low Fe concentration in maskelynite and plagioclase. Since I set the elongated dimension (*c* axis) of plagioclase grains always horizontally against the synchrotron beam, the error due to orientation effect is not significant and especially it is not the issue for maskelynite.

I estimated the influence of crystal orientation of plagioclase using the Y-75011 (Table 3.1). The difference of the obtained Fe^{3+}-Fe^{2+} peak-intensity ratio is only about 1% when the offset of the angle was 30 degrees against the *c* axis. Because I set the orientation of plagioclase with an accuracy of less than 30 degrees, the error due to the orientation effect of plagioclase sample is not significant.

Furthermore, in order to confirm the reproducibility of this analysis, I measured the

same location of maskelynite in Zagami five times. The results show the standard deviation of about 2% (Table 3.2). Another conceivable error factor is deviation of the peak position and the half width of the peak. As I wrote above in this section, the difference of the peak energy is very small as shown in Appendix 1, 2 and 3. The half width of the peak showed a wide range (Appendix 1, 2, and 3) and Fig. 3.4 shows the relationship among counting rates. According to Fig. 3.4, the difference in the half width of the peak is due to counting rates. However, Table 3.3 showed that the value of Fe^{3+}-Fe^{2+} peak-intensity ratio is almost unchanged even if the half width of the peak is changed. In addition, the error caused by the fitting is only about 1% (Appendix 1, 2 and 3).

Thus, among the errors which are considered, counting rate is the largest error for the present XANES analysis. The error was calculated by the statistical error of a counting rate and incident beam intensity by the following formulas:

Error value of counting rates = $\pm\frac{\sqrt{N}\times 100}{N}$ (%) N: signal counts

Error value of incident beam intensity = $\pm\frac{\sqrt{I}\times 100}{I}$ (%) I: incident beam intensity

Furthermore, I calculated the propagation of statistical errors. Generally, the error propagation in addition and division calculations are shown by the following formulas:

$$(A \pm \varepsilon_A) + (B \pm \varepsilon_B) = A + B \pm \sqrt{(\varepsilon_A)^2 + (\varepsilon_B)^2}$$

$$(A \pm \varepsilon_A) \div (B \pm \varepsilon_B) = \frac{A}{B} \pm \frac{A}{B}\sqrt{(\frac{\varepsilon_B}{B})^2 + (\frac{\varepsilon_A}{A})^2}$$

Table.3.1 Influence of crystal orientation

Angle	Fe^{3+}-Fe^{2+} peak-intensity ratio (%)
0^o (Horizontality)	21
30^o	22
60^o	37

Table.3.2 Verification result of reproducibility

Number of times	Fe^{3+}-Fe^{2+} peak-intensity ratio (%)
1	50
2	52
3	53
4	50
5	54
Average	51.8
Standard deviation	1.8

Table 3.3 Relationship between the value of half width of the peak and the Fe^{3+}-Fe^{2+} peak intensity ratio

	The best fit data	Case 1	Case2
Half width of the Fe^{2+} peak (eV)	1.21	1.1	0.66
Half width of the Fe^{3+} peak (eV)	1.65	1.1	0.66
Height of the Fe^{2+} peak	0.015182	0.015212	0.015421
Height of the Fe^{3+} peak	0.012713	0.012974	0.012464
Fe^{3+}-Fe^{2+} peak intensity ratio (%)	45.5	46.0	44.6

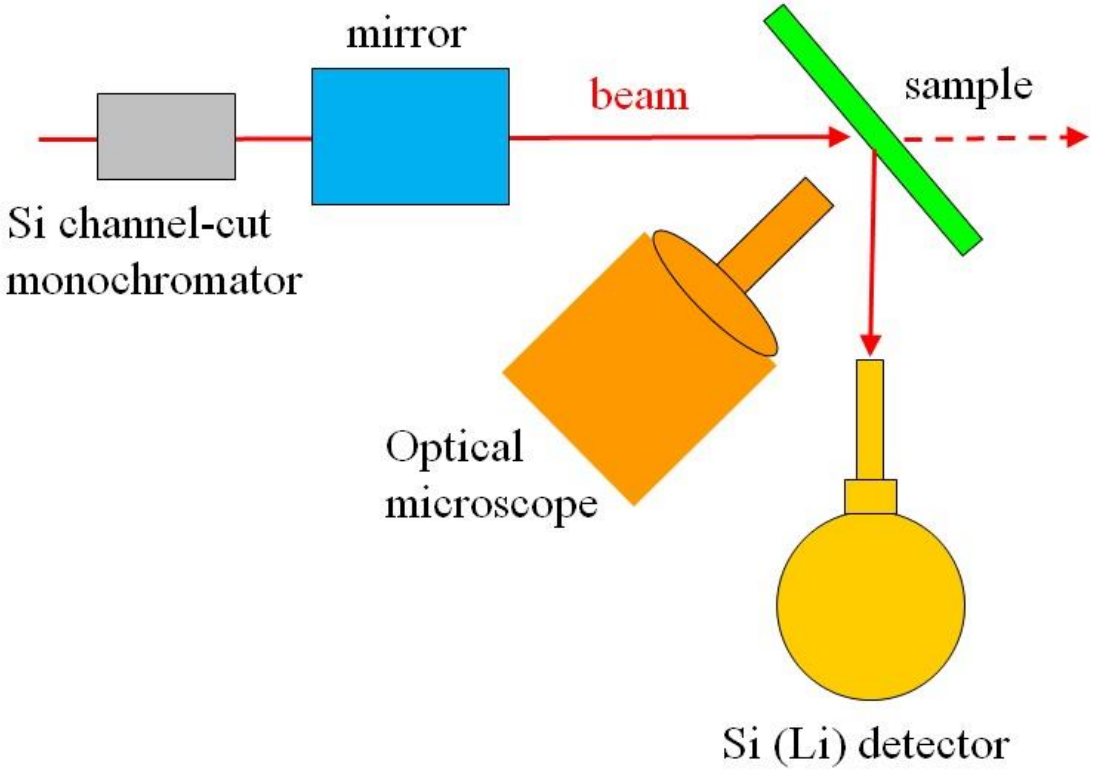

Fig. 3.3 Schematic illustration of a XANES system employed in this study.

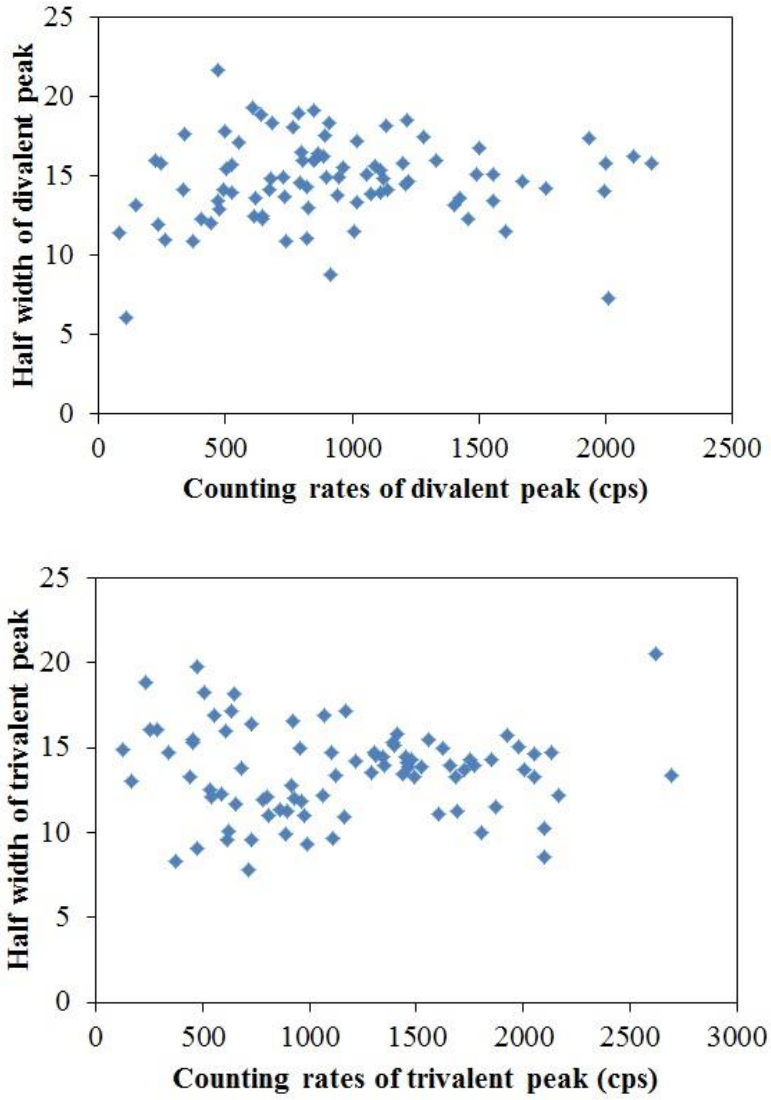

Fig. 3.4 Relationship between number of counts and half width of the peaks in this study. The upper graph shows a relationship of the divalent peak and the lower shows a trivalent peak. As these graphs show, the variations (error) of the half width becomes smaller as counting rates increase.

3.4. Synthetic Experiment of Plagioclase

Crystallization experiments of plagioclase were performed in order to establish an oxybarometer using an iron valence ratio of plagioclase. I employed the experimental procedures used in Jurewicz et al. (1994), McKay et al. (1994) and Miyamoto and Mikouchi (1996). The gabbroic rock from Muroto, Japan in which plagioclase appears

to crystallize as a liquidus phase was used because of apparent high abundance of plagioclase and its euhedral crystal shapes. However, volatile elements (e.g., Na) are very difficult to be kept their amounts during experiments due to the small size of experimental charges. Two pellets were prepared by pressing ~100 mg of the powdered starting material, and they were placed onto Pt wire loops whose diameter was approximately 5 mm (Fig. 3.5). Afterward, they were suspended inside an alumina tube at the hot spot of a SILICONIT vertical 1 atm gas-mixing furnace. These vertical furnaces heat the alumina muffle tube (Fig. 3.6) and experimental temperatures were measured with thermocouples calibrated by using the melting point of gold (1064.4^{o}C). The precision of temperature control is within ±1^{o}C (Miyamoto and Mikouchi, 1996). Gas mixtures of CO_2-H_2 were used to control the oxygen fugacity, and each gas flow rate was monitored by mass flow meter. Oxygen fugacity was measured by an oxygen electrolytic zirconia cell (SIRO$_2$ C700+). The ZrO_2 contains 6 wt% of Y_2O_3, 50wt% of Al_2O_3, 0.03 wt% of SiO_2, 0.02 wt% of Na_2O, and 0.01 wt% of Fe oxide, and was fabricated by Ceramic Oxide Fabriactors Pty. Ltd (Jurewicz et al. 1993). A zirconia cell was introduced into the furnace and the oxygen fugacity was directly measured (Fig. 3.7). Oxygen fugacity was calibrated by the reference air, which is supplied by an air pump through the four-bore alumina insulator tube.

The chemical composition of the starting material is shown in Table 3.4. They were homogenized at 1260 ^{o}C for 48 hours at the target oxygen fugacity. Then, samples were kept in the furnace at 1170 ^{o}C at the same oxygen fugacity as they were homogenized. I chose two different oxygen fugacities for the experiments. The experimental oxygen fugacities were at log fO_2 = QFM and QFM –2.

Table.3.4 The locality, rock type and chemical composition of the starting material.

Starting material	
Locality	Muroto, Japan
Rock type	Gabbro
SiO_2	50.21
TiO_2	1.18
Al_2O_3	17.56
Cr_2O_3	0.05
FeO	10.92
MgO	8.44
CaO	6.82
Na_2O	2.68
K_2O	0.65
P_2O_5	0.03
Total	98.54

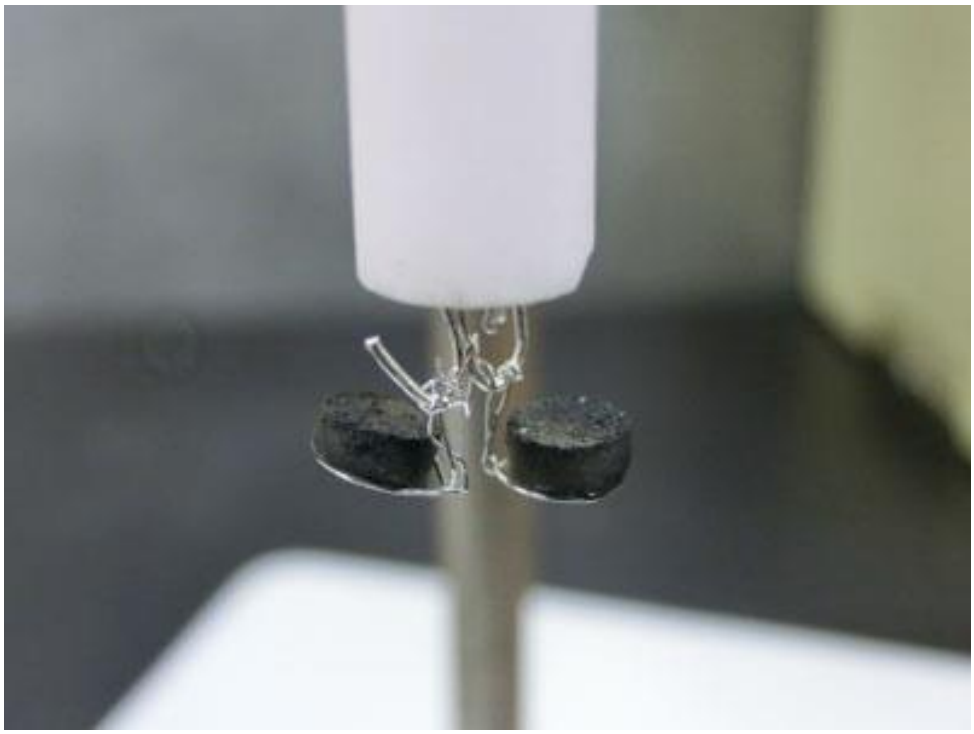

Fig. 3.5 The Pt wire holding two pellets of the starting material.

Fig. 3.6 Photograph of the furnace system. Left: temperature controller. Right: SILICONIT furnace with a gas mixing system.

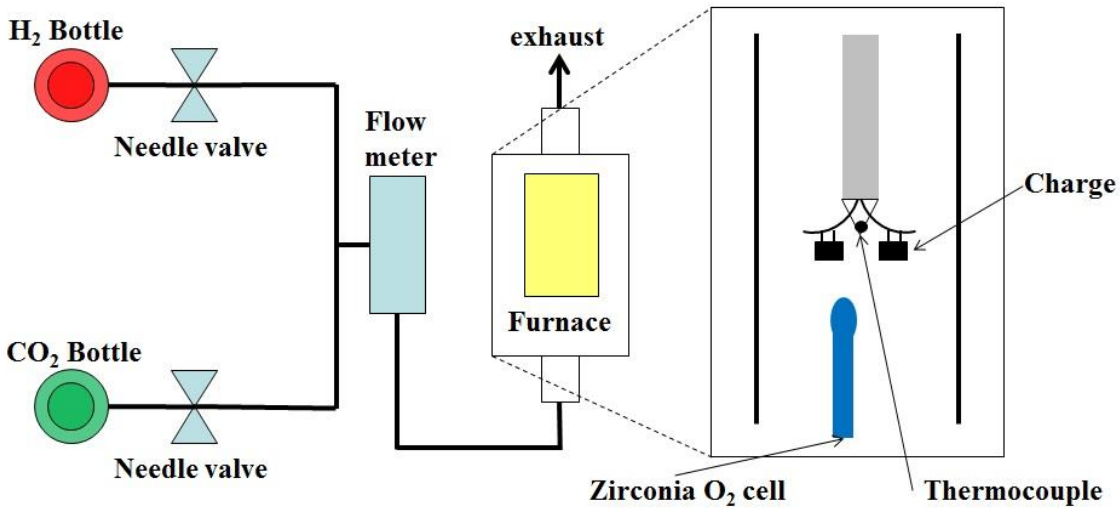

Fig. 3.7 Schematic illustration of the furnace system. The oxygen fugacity is monitored directly in the furnace by the zirconia cell.

3.5. Thermodynamic calculation using MELTS software

MELTS is a software package designed to facilitate thermodynamic modeling of phase equilibria in magmatic system. It provides the ability to compute equilibrium phase relations for igneous systems over the temperature range of 500-2000 ^{o}C and the pressure range of 0-2 GPa. MELTS is based on the work of Ghiorso and Sack (1991) and revised by Asimow and Ghiorso (1998).

Evolution scenarios for magmatic processes can be modeled with MELTS as a series of steps in temperature and pressure (Gibbs energy minimization), temperature and volume (Helmholtz energy minimization), enthalpy and pressure (entropy maximization) or entropy and pressure (enthalpy minimization). Isenthalpic (constant enthalpy), isentropic (constant entropy) or isochoric (constant volume) scenarios can be utilized to explore magmatic processes such as energy constrained assimilation, adiabatic decompression melting, or post-entrapment crystallization in phenocryst melt inclusions. The thermodynamic model for the liquid phase included in the MELTS was fitted largely from low-pressure experimental phase equilibria and an independent set of thermodynamic data/models for mineral phase. MELTS is intended for modeling magmatic phase relations at low pressure (<2 GPa).

I used the MELTS calculation in order to investigate the crystallization history of shergottites studied. Furthermore, I used this calculation to determine the liquidus temperature and crystallization temperature of plagioclase. In this study, MELTS calculation was also used to estimate the mineral compositions that were formed at appropriate temperature and oxygen fugacity under 1 atm total pressure. Based on previous studies estimating oxygen fugacity of several shergottites (Herd et al. 2001, 2002 and 2006; Goodrich et al 2003; Peslier et al. 2010), I employed oxygen fugacity of QFM –3.0, QFM –2.0, QFM –1.0 and QFM for the calculation.

4. XANES Analysis

4.1. Shergottites

4.1.1. Depleted Shergottites

I analyzed two depleted shergottites Dar al Gani 476 and Dhofar 019. Four spots in three maskelynite grains were analyzed for Dar al Gani 476 (Fig. 4.1). The obtained Fe^{3+}-Fe^{2+} peak-intensity ratios of this sample are 0.40-0.49 (Table 4.1).

In the case of Dhofar 019, I analyzed four spots in four grains (Fig. 4.1). The obtained Fe^{3+}-Fe^{2+} peak-intensity ratios are 0.39-0.44 (Table 4.1). Fig. 4.1 shows SR XANES spectra of these two depleted shergottites, exhibiting that the lower energy peaks are clearly higher than higher energy peak (Fig. 4.2).

Furthermore, I analyzed one pyroxene grain in Dhofar 019. The obtained XANES spectrum showed only the lower energy peak and does not have the higher energy peak (Fig. 4.3). Thus, the Fe^{3+}-Fe^{2+} peak-intensity ratios of Dhofar 019 pyroxene is 0.

4.1.2. Intermediate Shergottites

I analyzed four intermediate shergottites ALH 77005, EETA 79001 lithology A, LEW 88516 and NWA 5029.

Three spots of two grains in ALH 77005 were measured (Fig. 4.1). As I wrote above in the section “Description of the samples studied”, ALH 77005 contains small areas showing partial recrystallization of plagioclase. Thus, I selected maskelynite by optical microscope to avoid crystalline areas because I wanted to estimate oxygen fugacity when plagioclase crystallized from the primary melt and eliminate the error due to crystal orientation. The obtained Fe^{3+}-Fe^{2+} peak-intensity ratios of this sample are ranging from 0.13 to 0.29 (Table 4.1), which is clearly lower than those of other intermediate shergottites.

I also analyzed two spots in two grains of EETA 79001 lithology A (Fig. 4.1). The Fe^{3+}-Fe^{2+} peak-intensity ratios of this sample are 0.40 and 0.53 (Table 4.1).

Three spots in three maskelynite grains of LEW 88516 were analyzed (Fig. 4.1) and the obtained Fe^{3+}-Fe^{2+} peak-intensity ratios of this sample are 0.54-0.66 (Table 4.1). These ratios are higher than those of other intermediate shergottites.

In the case of NWA 5029, I analyzed four spots in four grains (Fig. 4.1). The Fe^{3+}-Fe^{2+} peak-intensity ratios of this sample are 0.31-0.46 (Table 4.1).

The obtained XANES spectra of maskelynite in ALH 77005, EETA 79001 lithology A and NWA 5029 showed that the lower energy peaks are higher than higher energy peaks (Fig. 4.2). On the other hand, the obtained XANES spectra of maskelynite in LEW

88516 showed that the higher energy peaks are larger than lower energy peak (Fig. 4.2).

4.1.3. Enriched Shergottites

I analyzed eight enriched shergottites (Dhofar 378, LAR 06319, NWA 856, NWA 1068, NWA 4468, Zagami, RBT 04262 and Shergotty).

Three plagioclase grains of Dhofar 378 were analyzed (Fig. 4.1). As I wrote in the section "Description of the samples studied", plagioclase in Dhofar 378 shows a fibrous fine-grained texture probably by recrystallization from shocked plagioclase melt. I selected large plagioclase domains that exceed the SR beam size. The obtained Fe^{3+}-Fe^{2+} peak-intensity ratios are 0.55-0.69 (Table 4.1).

In the thin section of LAR 06319, four maskelynite grains were selected and one point for each grain was analyzed (Fig. 4.1). The Fe^{3+}-Fe^{2+} peak-intensity ratios of this sample are 0.54-0.59 (Table 4.1). In this sample I analyzed both rim and core of a single maskelynite grain to see whether there is a difference or not. The obtained ratio from the core (LAR 06319-2) is 0.54 and that from the rim (LAR 06319-3) is 0.56 (Table 4.1). Therefore, I did not see any obvious differences in the Fe^{3+}-Fe^{2+} peak-intensity ratio between the core and the rim, suggesting that the redox state was unchanged during the crystallization of the plagioclase.

For NWA 856 I analyzed four spots in four maskelynite grains (Fig. 4.1). The Fe^{3+}-Fe^{2+} peak-intensity ratios of this sample are 0.52-0.59 (Table 4.1).

I analyzed four maskelynite grains of NWA 1068 and one point in each grain was analyzed (Fig. 4.1). The obtained Fe^{3+}-Fe^{2+} peak-intensity ratios are 0.58-0.62 (Table 4.1).

Five spots in four maskelynite grains in NWA 4468 were analyzed (Fig. 4.1). The Fe^{3+}-Fe^{2+} peak-intensity ratios of this sample are 0.63-0.71 (Table 4.1). I also analyzed both rim and core of a single maskelynite grain in the same way as I did for LAR 06319. The obtained ratios from the core (NWA 4468-4) and the rim (NWA 4468-3) are both 0.68 (Table 4.1), again showing that there is no difference between the core and rim.

For Zagami I analyzed three spots in two maskelynite grains (Fig. 4.1). The Fe^{2+}-Fe^{3+} peak intensity ratios of this sample are 0.52- 0.58 (Table 4.1).

Three spots in two maskelynite grains were analyzed for RBT 04262 (Fig. 4.1). The Fe^{3+}-Fe^{2+} peak-intensity ratios of this sample are 0.74-0.81 (Table 4.1), which is the highest among the samples studied. I also analyzed one pyroxene grain in RBT 04262. The obtained XANES spectrum showed only a lower energy peak and does not have the higher energy peak (Fig. 4.3). Thus, the Fe^{3+}-Fe^{2+} peak-intensity ratios of pyroxene in

RBT 04262 is 0 even though this sample appears to have crystallized at the highest fO_2.

I selected four maskelynite grains in Shergotty and analyzed one point in each grain (Fig. 4. 1). The Fe^{3+}-Fe^{2+} peak-intensity ratios of this sample are 0.40-0.59 (Table 4.1), showing slightly larger ranges than other samples.

The obtained XANES spectra of maskelynite in all enriched shergottites showed that the higher energy peaks are clearly larger than lower energy peak (Fig. 4.2), suggesting Fe^{3+}-rich nature of maskelynite.

Table 4.1

Fe^{3+}-Fe^{2+} peak-intensity ratios and corresponding errors for maskelynite in studied shergottites.

Sample	Group	Fe^{3+}-Fe^{2+} peak-intensity ratio (%)	Error
Dar al Gani 476-1	Depleted	40.0	±0.8
Dar al Gani 476-2	Depleted	44.8	±0.6
Dar al Gani 476-3	Depleted	42.2	±0.6
Dar al Gani 476-4	Depleted	49.1	±0.8
Dhofar 019-1	Depleted	43.5	±0.5
Dhofar 019-2	Depleted	42.0	±0.6
Dhofar 019-3	Depleted	40.4	±0.6
Dhofar 019-4	Depleted	39.2	±0.8
ALH 77005-1	Intermediate	12.7	±0.5
ALH 77005-2	Intermediate	28.8	±0.4
ALH 77005-3	Intermediate	24.0	±0.2
EETA 79001 lith. A-1	Intermediate	52.6	±0.7
EETA 79001 lith. A-2	Intermediate	39.9	±0.5
LEW 88516-1	Intermediate	65.8	±1.2
LEW 88516-2	Intermediate	65.3	±1.3
LEW 88516-3	Intermediate	53.8	±1.3
NWA 5029-1	Intermediate	45.6	±0.8
NWA 5029-2	Intermediate	41.2	±0.6
NWA 5029-3	Intermediate	31.4	±0.4
NWA 5029-4	Intermediate	35.7	±0.6
Dhofar 378-1	Enriched	54.9	±0.8

Dhofar 378-2	Enriched	60.8	±1.1
Dhofar 378-3	Enriched	68.6	±1.4
LAR 06319-1	Enriched	53.8	±0.8
LAR 06319-2	Enriched	53.6	±0.4
LAR 06319-3	Enriched	55.6	±0.7
LAR 06319-4	Enriched	59.4	±1.2
NWA 856-1	Enriched	58.8	±1.2
NWA 856-2	Enriched	52.8	±0.6
NWA 856-3	Enriched	56.3	±1.0
NWA 856-4	Enriched	52.3	±1.2
NWA 1068-1	Enriched	62.0	±1.5
NWA 1068-2	Enriched	59.8	±1.1
NWA 1068-3	Enriched	62.3	±0.9
NWA 1068-4	Enriched	58.0	±0.9
NWA 4468-1	Enriched	62.9	±2.4
NWA 4468-2	Enriched	71.3	±1.3
NWA 4468-3	Enriched	68.0	±1.3
NWA 4468-4	Enriched	67.9	±1.5
NWA 4468-5	Enriched	64.8	±1.3
Zagami-1	Enriched	52.0	±0.9
Zagami-2	Enriched	56.8	±0.9
Zagami-3	Enriched	57.8	±1.0
RBT 04262-1	Enriched	80.6	±1.3
RBT 04262-2	Enriched	74.3	±1.5
RBT 04262-3	Enriched	75.2	±1.9
Shergotty-1	Enriched	54.0	±1.3
Shergotty-2	Enriched	58.6	±0.9
Shergotty-3	Enriched	47.1	±1.0
Shergotty-4	Enriched	40.0	±0.7

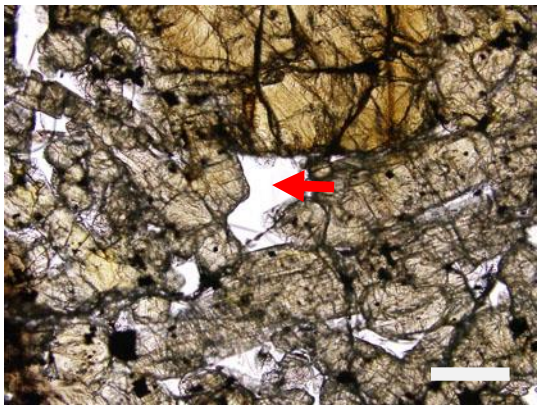

Dar al Gani 476

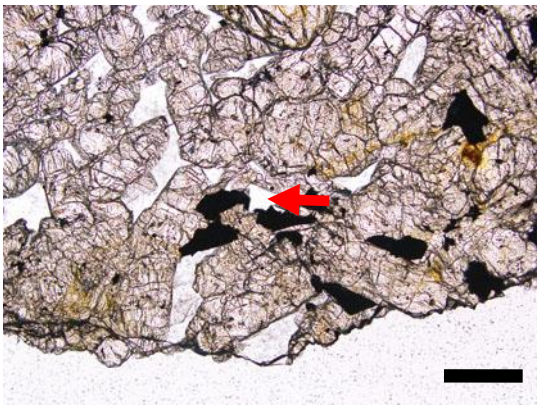

Dhofar 019

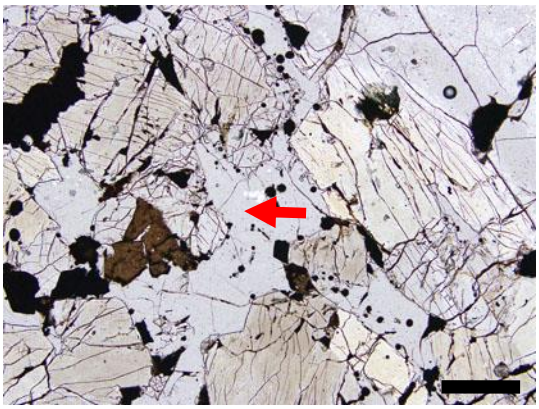

ALH 77005

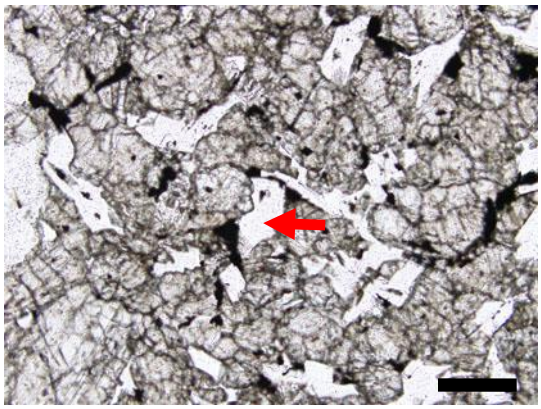

EETA 79001 lithology A.

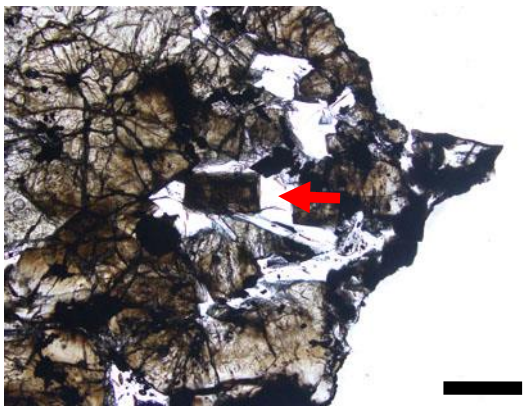

LEW88516

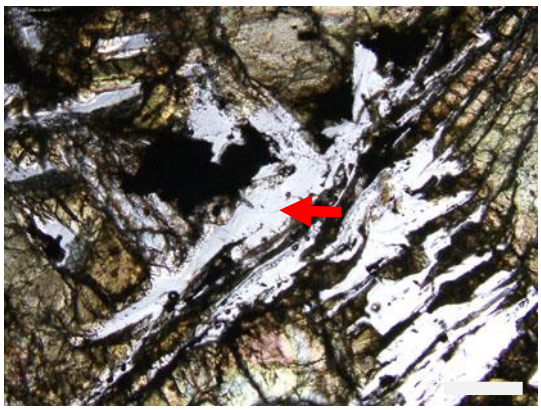

NWA 5029

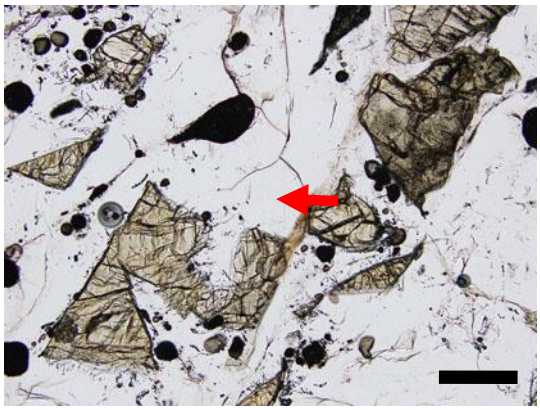

Dhofar 378

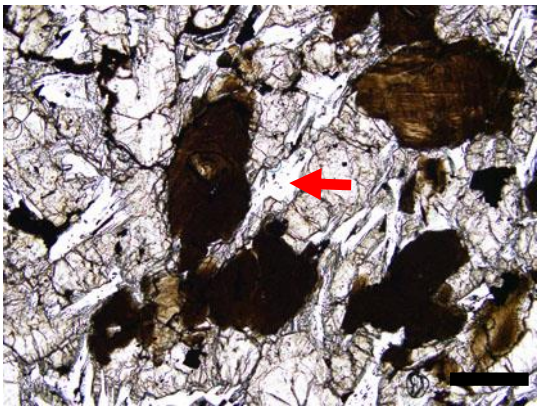

LAR 06319

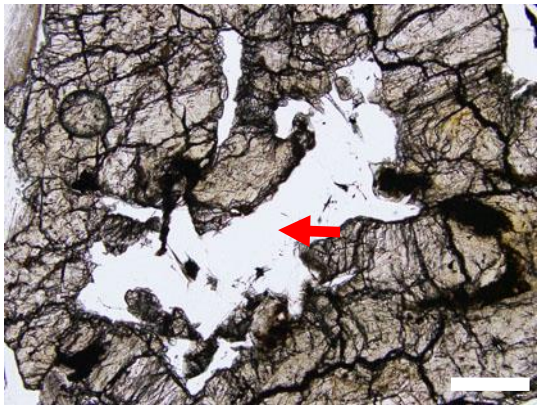

NWA 856

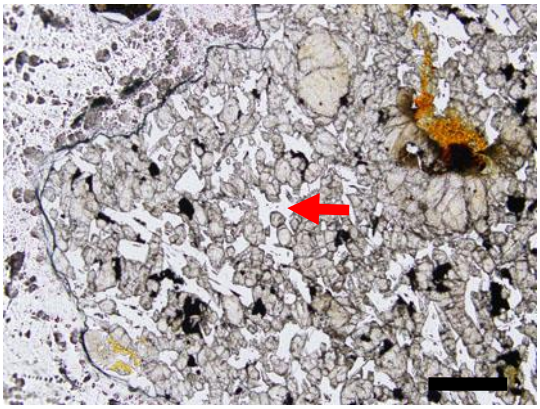

NWA 1068

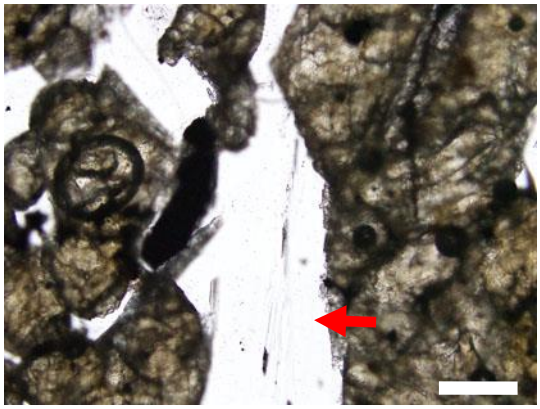

NWA 4468

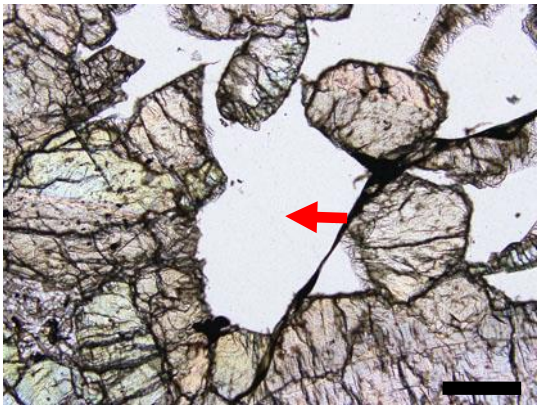

Zagami

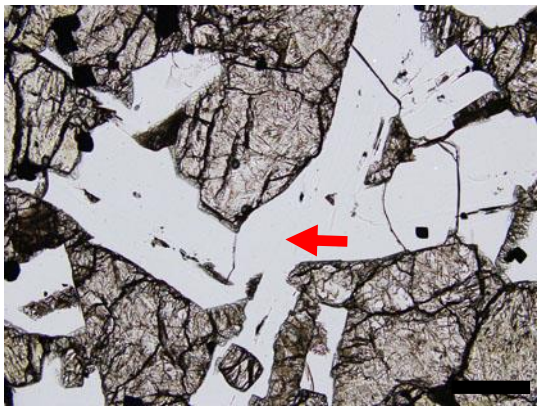

RBT 04262

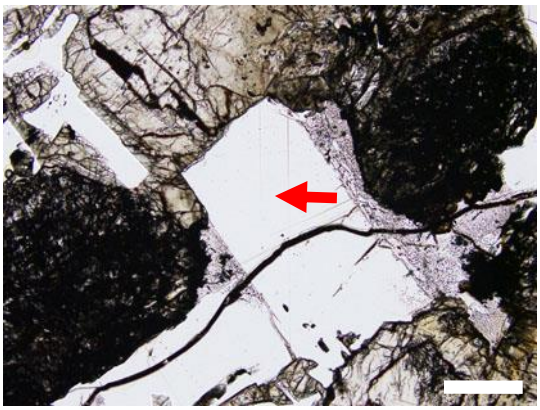

Shergotty

Fig. 4.1 Optical photomicrographs of Dar al Gani 476, Dhofar 019, ALH 77005, EETA 79001 lithology A, LEW 88516, NWA 5029, LAR 06319, NWA 856, NWA 1068, NWA 4468, Zagami, RBT 04262, and Shergotty (plane-polarized light). Red arrows in images indicate points analyzed using SR-XANES. Black and white bars at lower right of the images indicate 200 μm scales.

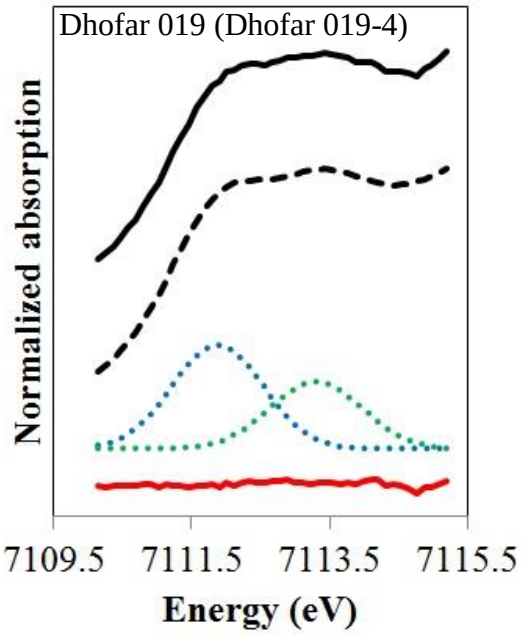
Dhofar 019 (Dhofar 019-4)
Normalized absorption
7109.5
7111.5
7113.5
7115.5
Energy (eV)

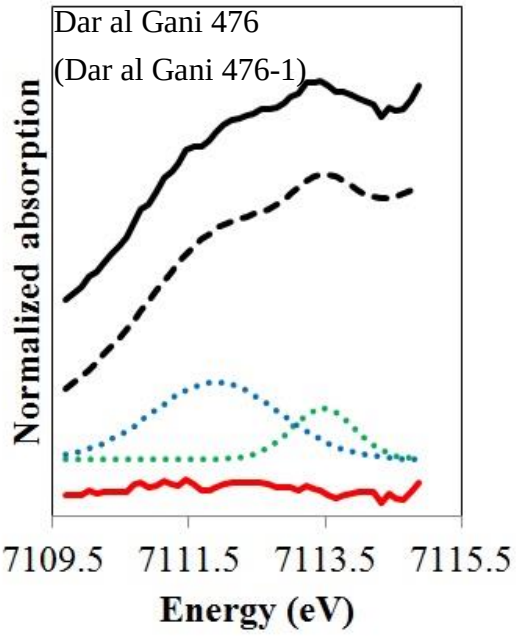
Dar al Gani 476
(Dar al Gani 476-1)
Normalized absorption
7109.5
7111.5
7113.5
7115.5
Energy (eV)

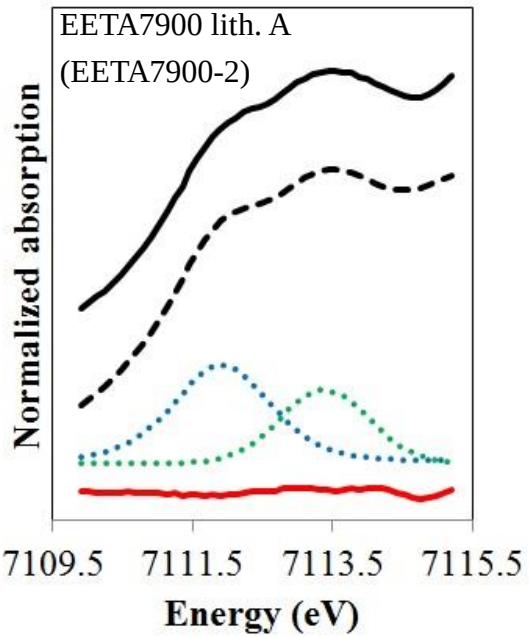
EETA7900 lith. A
(EETA7900-2)
Normalized absorption
7109.5
7111.5
7113.5
7115.5
Energy (eV)

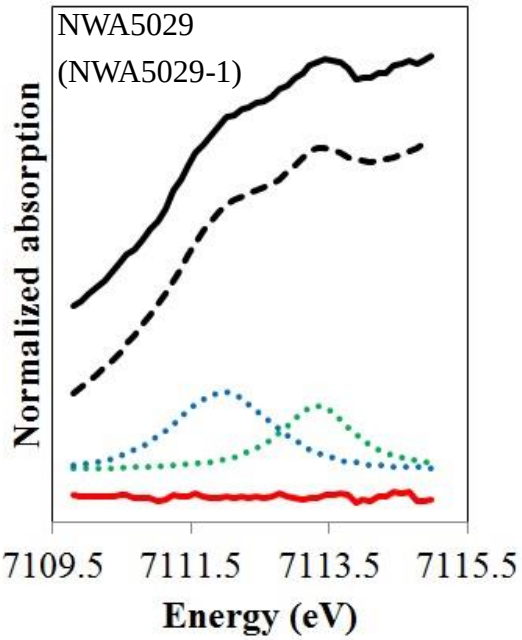
NWA5029
(NWA5029-1)
Normalized absorption
7109.5
7111.5
7113.5
7115.5
Energy (eV)

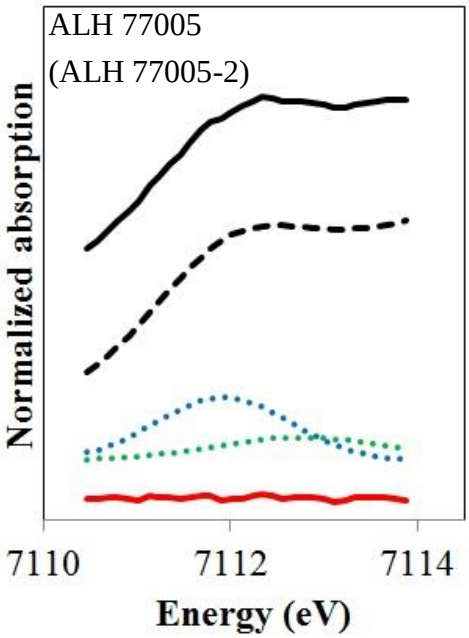
ALH 77005
(ALH 77005-2)
Normalized absorption
7110
7112
7114
Energy (eV)

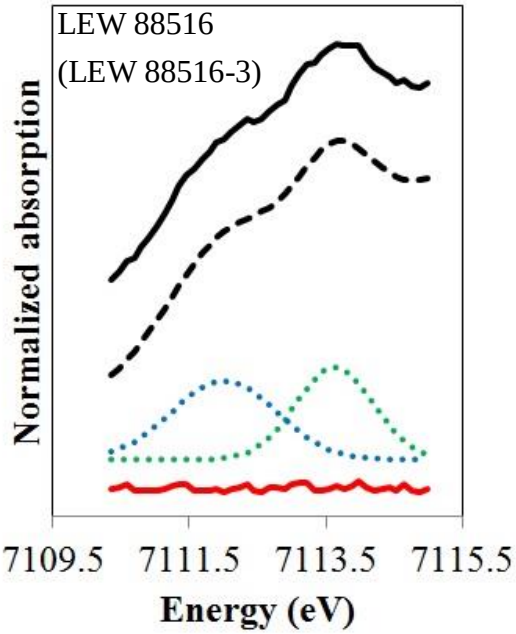
LEW 88516
(LEW 88516-3)
Normalized absorption
7109.5
7111.5
7113.5
7115.5
Energy (eV)

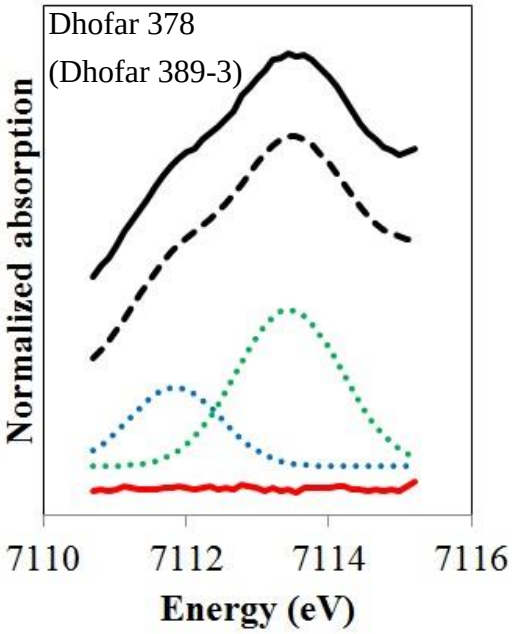
Dhofar 378
(Dhofar 389-3)
Normalized absorption
7110
7112
7114
7116
Energy (eV)

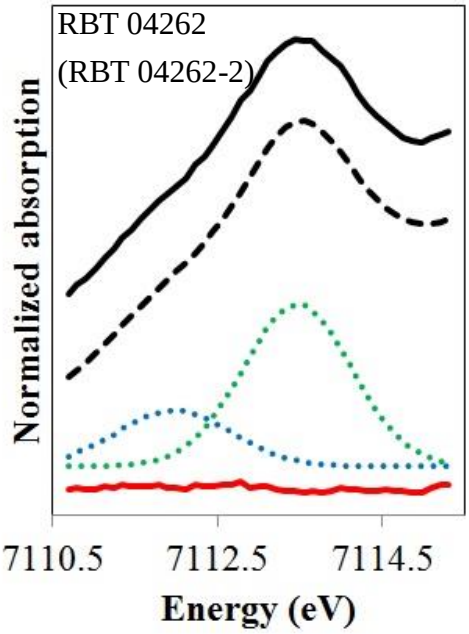
RBT 04262
(RBT 04262-2)
Normalized absorption
7110.5
7112.5
7114.5
Energy (eV)

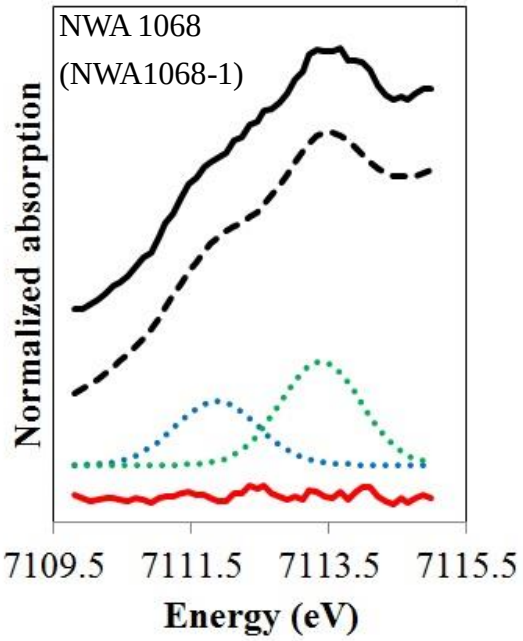
NWA 1068
(NWA1068-1)
Normalized absorption
7109.5
7111.5
7113.5
7115.5
Energy (eV)

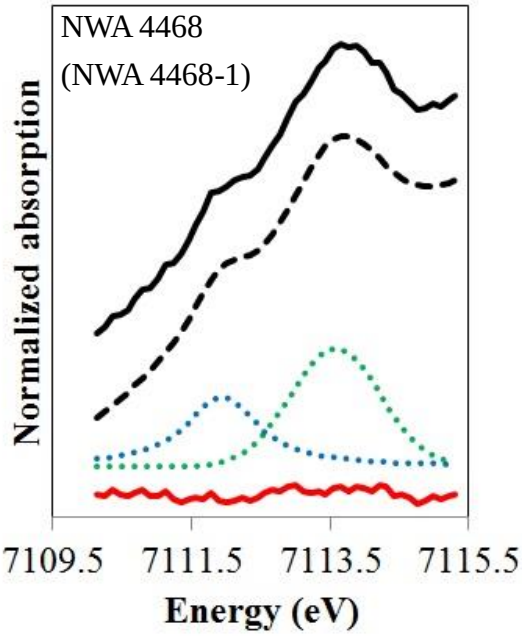
NWA 4468
(NWA 4468-1)
Normalized absorption
7109.5
7111.5
7113.5
7115.5
Energy (eV)

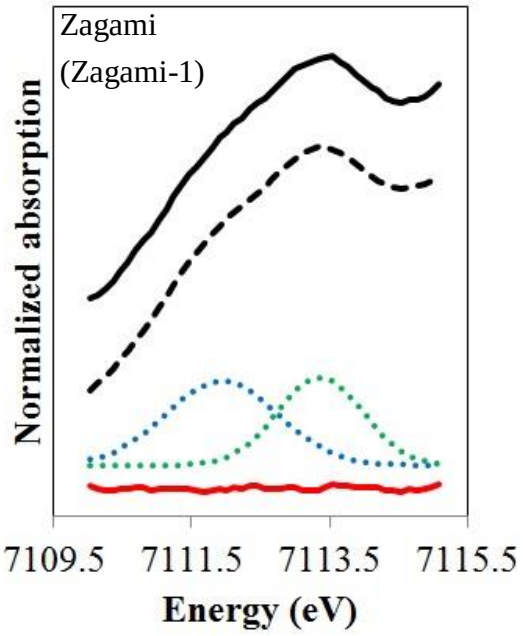
Zagami
(Zagami-1)
Normalized absorption
7109.5
7111.5
7113.5
7115.5
Energy (eV)

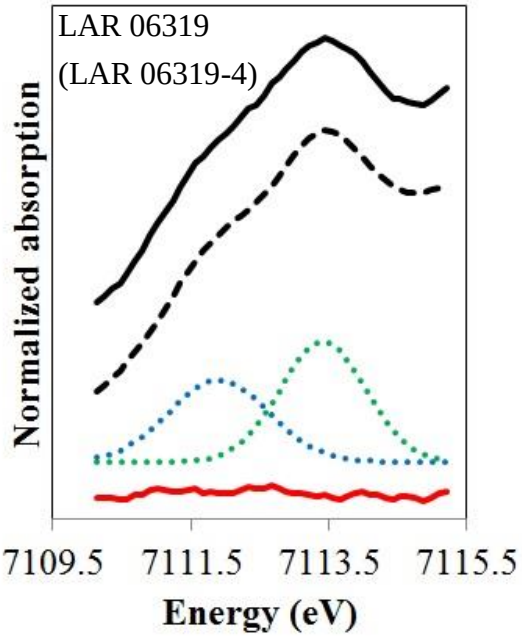
LAR 06319
(LAR 06319-4)
Normalized absorption
7109.5
7111.5
7113.5
7115.5
Energy (eV)

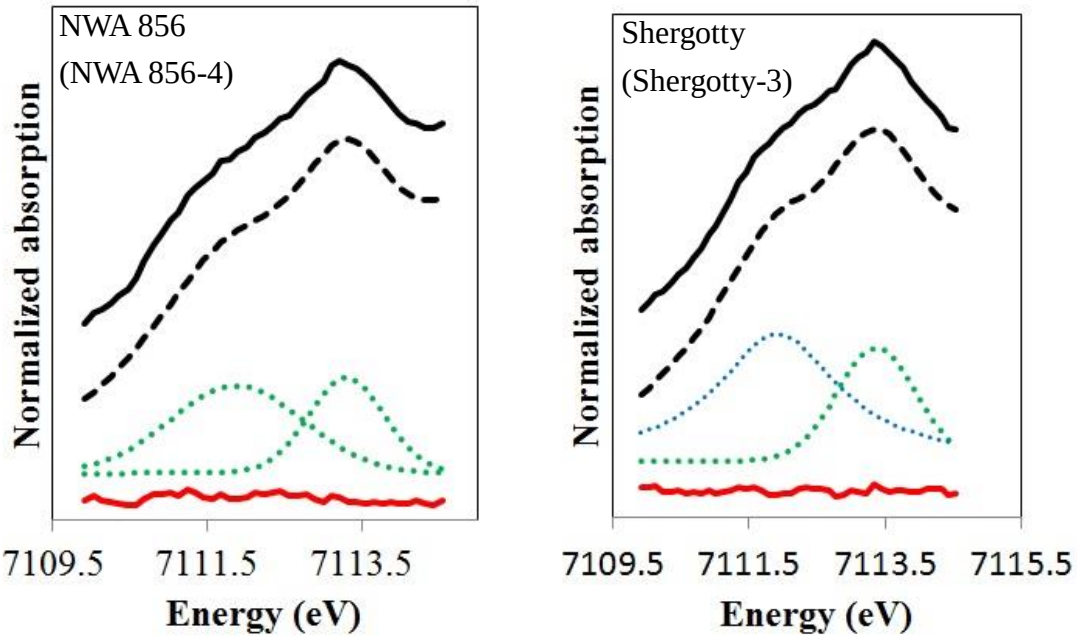

Fig.4.2 SR Fe-XANES pre-edge spectra in the range of about 7109–7116 eV, as obtained from maskelynite and plagioclase in Dhofar 019, ALH77005, NWA 1068, Dhofar 378, NWA 4468, EETA 79001 lithology A, NWA 5029, LAR 06319, NWA 856, Shergotty, LEW 88516 and RBT 04262. Blue and green dots represent deconvoluted peaks of divalent and trivalent Fe, respectively. The raw data are shown by black solid lines, the fitted data are shown by black dashed lines and the residuals of fitting data are shown by red solid lines, respectively. The raw and convoluted spectra are shifted to higher position in vertical axis for ease of comparison.

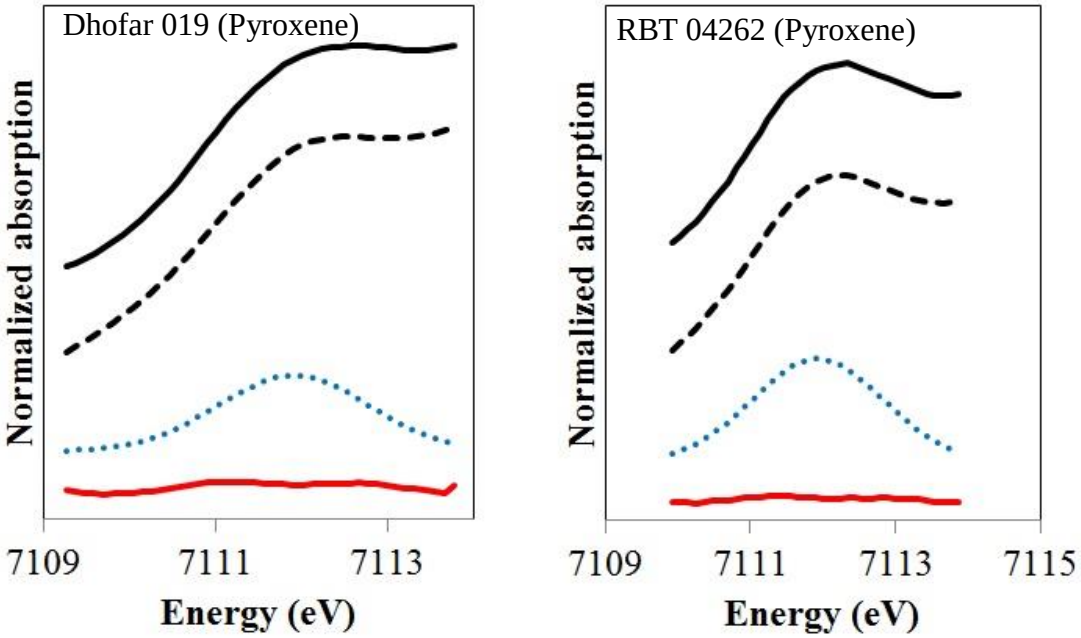

Fig. 4.3 Left: SR Fe-XANES pre-edge spectra in range 7109–7114 eV, as obtained from pyroxene in Dhofar 019. Right: Range 7109–7115 eV obtained from pyroxene in RBT 04262. Blue plots represent peak of divalent iron. The raw data is shown by black solid line, the fitted data is showed by dashed line and the residuals of fitting data are shown by red solid lines, respectively. The raw and convoluted spectra are shifted to higher position in vertical axis for ease of comparison.

4.2. HED Meteorites

4.2.1. ALH 76005

I analyzed three grains of plagioclase in the ALH 76005 eucrite. Because ALH 76005 is a polymict breccia, I selected basaltic clasts showing ophitic textures with lathy plagioclase grains. Grain 1 shows an euhedral shape and its grain size is 200 x 50 μm. Grain 2 is in subhedral shape and grain 3 shows a euhedral shape and their grain sizes are 500 x 100 μm (Fig. 4.4). The Fe^{3+}-Fe^{2+} peak-intensity ratios of grain 1, grain 2 and grain 3 are 0.25, 0.33 and 0.35, respectively (Table 4.2).

The obtained XANES spectra of plagioclase in ALH 76005 showed that there is little difference in the shape of spectra and the lower energy peaks are clearly larger than higher energy peak (Fig. 4.13), suggesting an Fe^{2+}-rich composition.

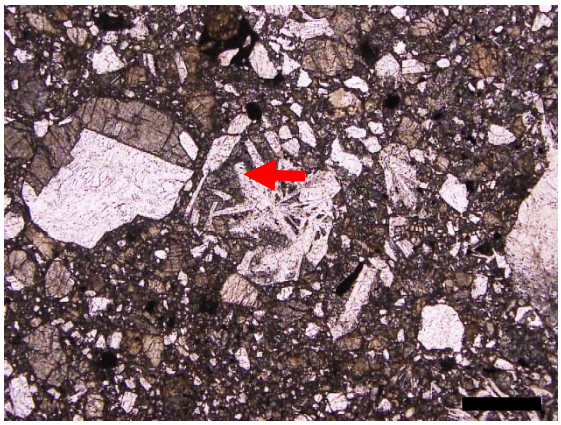

ALH 76005 grain 1

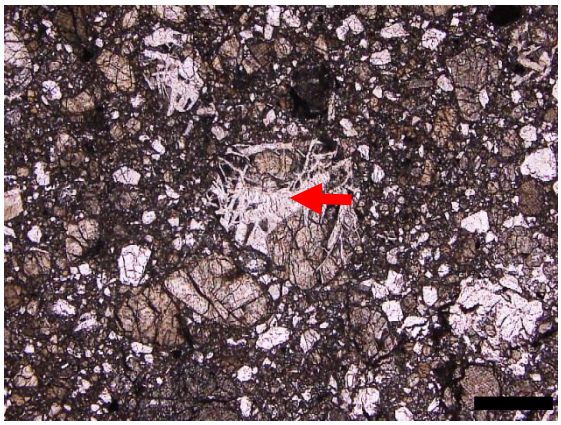

ALH 76005 grain 2

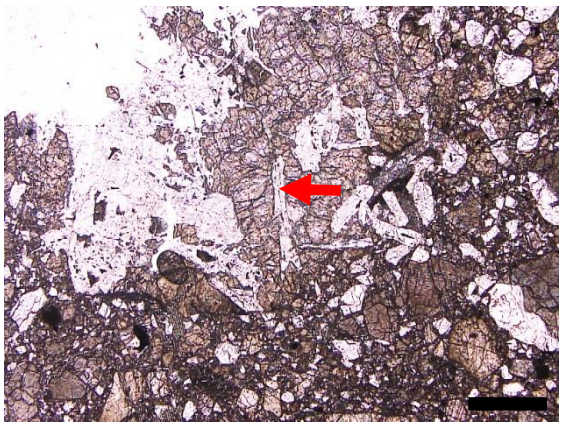

ALH 76005 grain 3

Fig. 4.4 Optical photomicrographs of ALH76005 (plane-polarized light). Red arrows shown in each image are analyzed points by SR-XANES. Black bar at the lower right corner of the images are scales of 500 μm.

4.2.2. Petersburg

I analyzed three plagioclase grains in the Petersburg eucrite. Grain 1 shows a subhedral shape and its grain size is about 1000 x 250 μm. The size of grain 2 is smaller than the other grains whose size is about 500 x 250 μm. Grain 3 is subhedral in shape and its size is about 1000 x 250 μm (Fig. 4.5). The Fe^{3+}-Fe^{2+} peak-intensity ratios of these three plagioclase grains in Petersburg are 0.31, 0.41 and 0.32, respectively (Table 4.2).

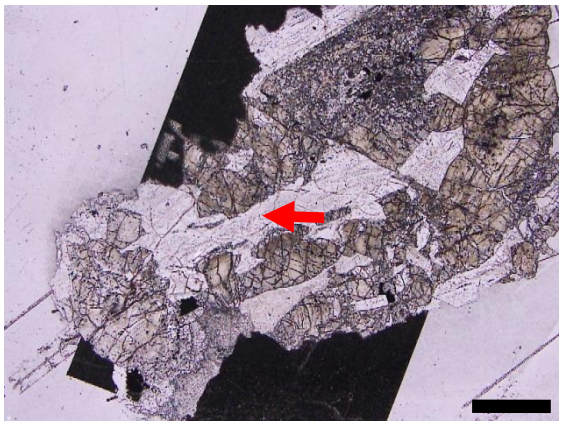

Petersburg grain 1

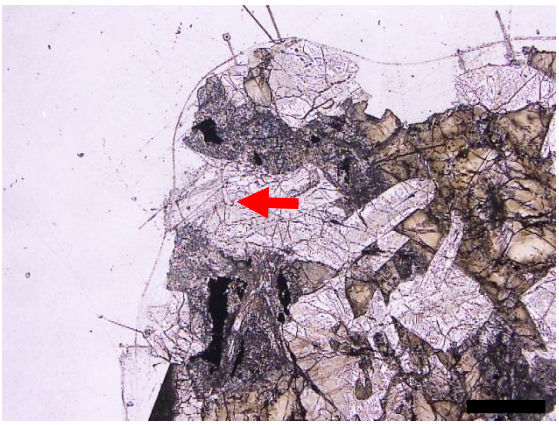

Petersburg grain 2

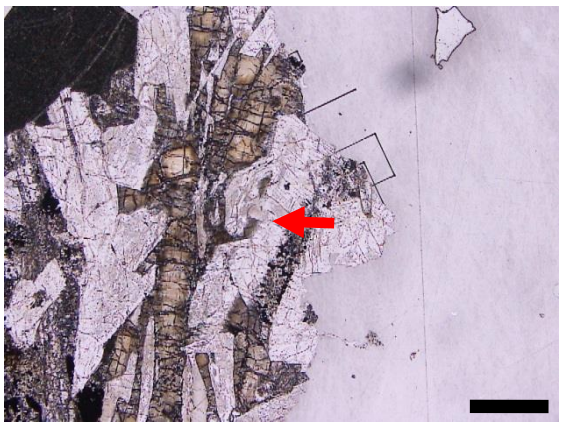

Petersburg grain 3

Fig. 4.5 Optical photomicrographs of Petersburg (plane-polarized light). Red arrows shown in each image are analyzed points by SR-XANES. Black bar at the lower right are scales of 500 μm.

4.2.3. Piplia Kalan

I analyzed two plagioclase grains in the Piplia Kalan eucrite (Fig. 4. 6). I selected two clasts with distinct textures, grain 1 is coarse-grained and its plagioclase size is about 1000 x 250 μm. On the other hand, grain 2 shows a needle-like shape and its plagioclase size is 200 x 50 μm. The Fe^{3+}-Fe^{2+} peak-intensity ratios of this sample are 0.43 and 0.31, respectively (Table 4.2).

The obtained XANES spectra of plagioclase in Piplia Kalan showed that the peak height of trivalent iron in grain 1 is slightly larger than the peak height of grain 2 (Fig. 4.13).

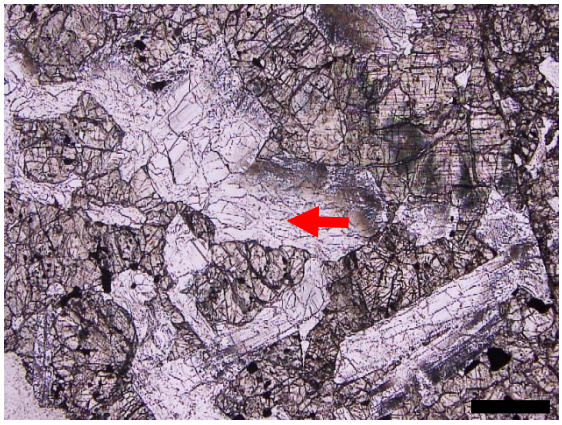

Piplia Kalan grain 1

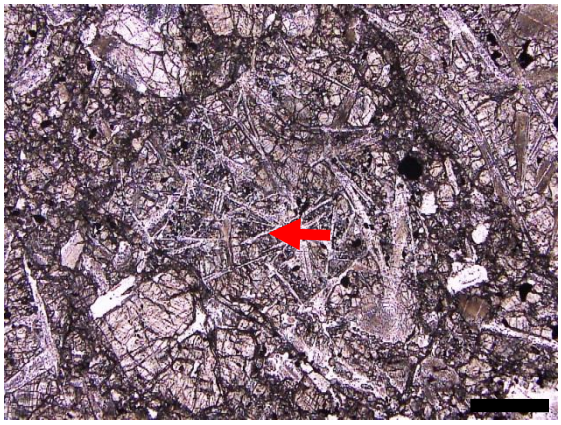

Piplia Kalan grain 2

Fig. 4.6 Optical photomicrographs of Piplia Kalan (plane-polarized light). Red arrows shown in each image are analyzed points by SR-XANES. Black bar at the lower right are scales of 500 μm.

4.2.4. Padvarninkai

As I wrote in the section "Description of the samples studied", Padvarninkai is highly shocked and plagioclase grains are transformed to maskelynite as similar to Martian meteorites. I analyzed two maskelynite grains in Padvarninkai (Fig. 4.7). I selected big maskelynite grains whose sizes are 500 x 300 μm. The Fe^{3+}-Fe^{2+} peak-intensity ratios of this sample are 0.14-0.23 (Table 4.2).

The obtained XANES spectra of maskelynite in Padvarninkai showed that there is little difference in the shape of spectra and the lower energy peaks are clearly higher than the higher energy peak (Fig. 4.13).

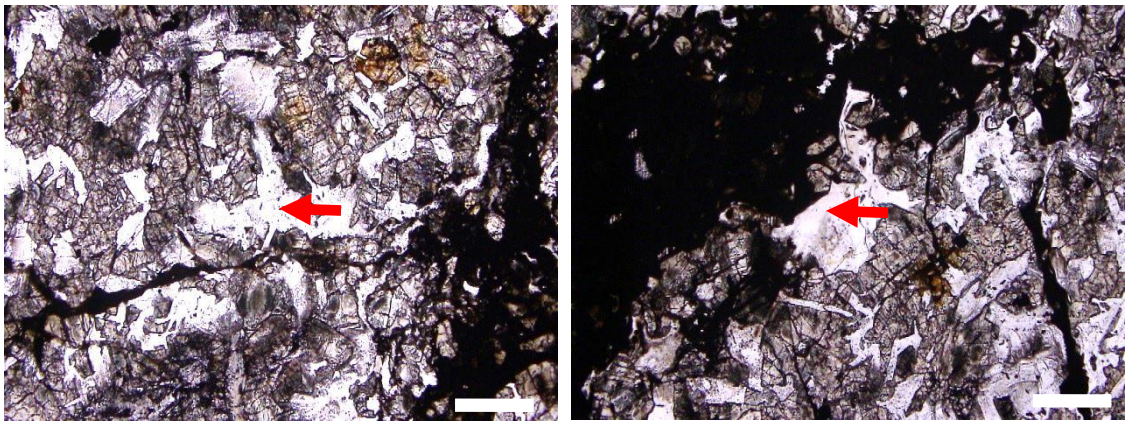

Padvarninkai grain 1　　Padvarninkai grain 2

Fig. 4.7 Optical photomicrographs of Padvarninkai (plane-polarized light). Red arrows shown in each image are analyzed points by SR-XANES. White bars at the lower right corners are scales of 500 μm.

4.2.5. Y-75011

I analyzed two grains of plagioclase in the Y-75011 eucrite. I selected two grains showing euhedral shapes and their grain sizes are 500 x 50 μm (Fig. 4.8). The Fe^{3+}-Fe^{2+} peak-intensity ratios of grain 1 and grain 2 are both 0.22 (Table 4.3).

The obtained XANES spectra of plagioclase in Y-75011 showed that the shape of spectra of grain 1 and 2 are very similar (Fig. 4.13).

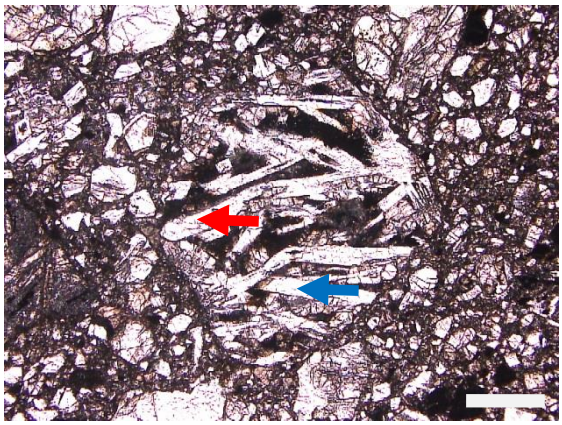

Fig. 4.8 Optical photomicrograph of Padvarninkai (plane-polarized light). Red and blue arrows show the analyzed points of grain 1 and 2 by SR-XANES, respectively. A white bar at the lower right is a scale of 500 μm.

4.2.6. EETA 87520

I analyzed four plagioclase grains in the EETA 87520 cumulate eucrite. EETA 87520 shows a coarse-grained texture and I selected plagioclase larger than 1 mm (Fig. 4.9). For example, the size of grain 1 is 1500 x 800 μm. I confirmed that the analyzed grains show no visible effects of weathering, although the weathering grade of this sample is "B". The Fe^{3+}-Fe^{2+} peak-intensity ratios of this sample ranges from 0.51 to 0.58 (Table 4.2).

The obtained XANES spectra of plagioclase in EETA 87520 showed that there is little difference in the shape of spectra and the higher energy peaks are slightly more intense than the lower energy peaks, suggesting significant amount of Fe^{3+} (Fig. 4.13).

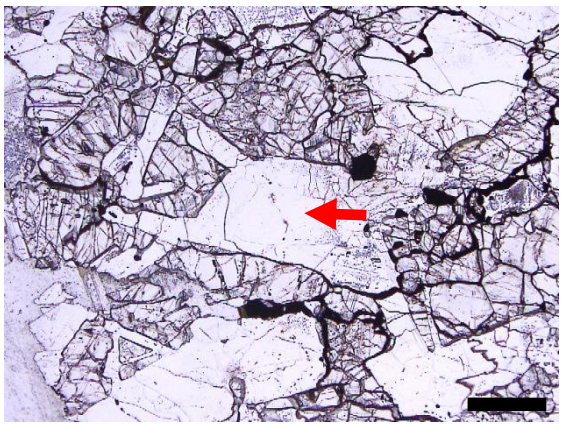

EETA 87520 grain 1

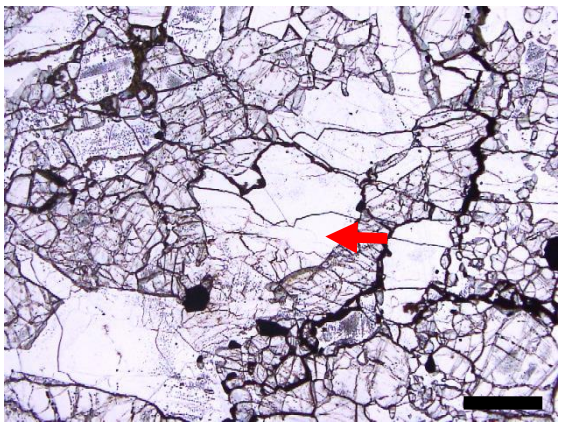

EETA 87520 grain 2

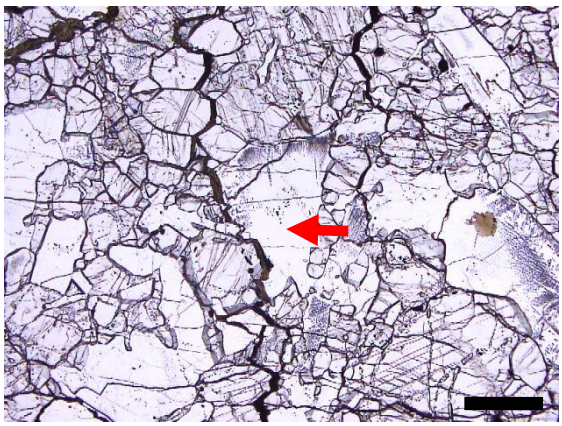

EETA 87520 grain 3

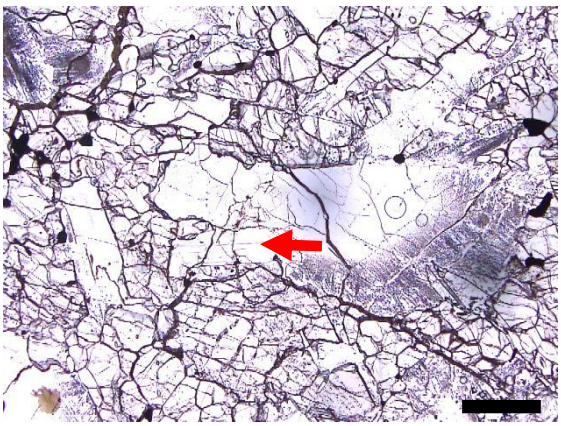

EETA 87520 grain 4

Fig. 4.9 Optical photomicrographs of EETA 87520 (plane-polarized light). Red arrows shown in each image are analyzed points by SR-XANES. Black bars in the lower right are scales of 500 μm.

4.2.7. Moore County

Moore County is another cumulate eucrite showing a coarse-grained texture similar to EETA 87520. I analyzed four plagioclase grains in Moore County (Fig. 4. 10). Selected plagioclase grains are all larger than 1 mm. The Fe^{3+}-Fe^{2+} peak-intensity ratios of this sample are 0.49-0.55 (Table 4.2).

The obtained XANES spectra of plagioclase in Moore County showed that there is little difference in the shape of spectra. Except for grain 3, the higher energy peaks are slightly larger than lower energy peak (Fig. 4.13).

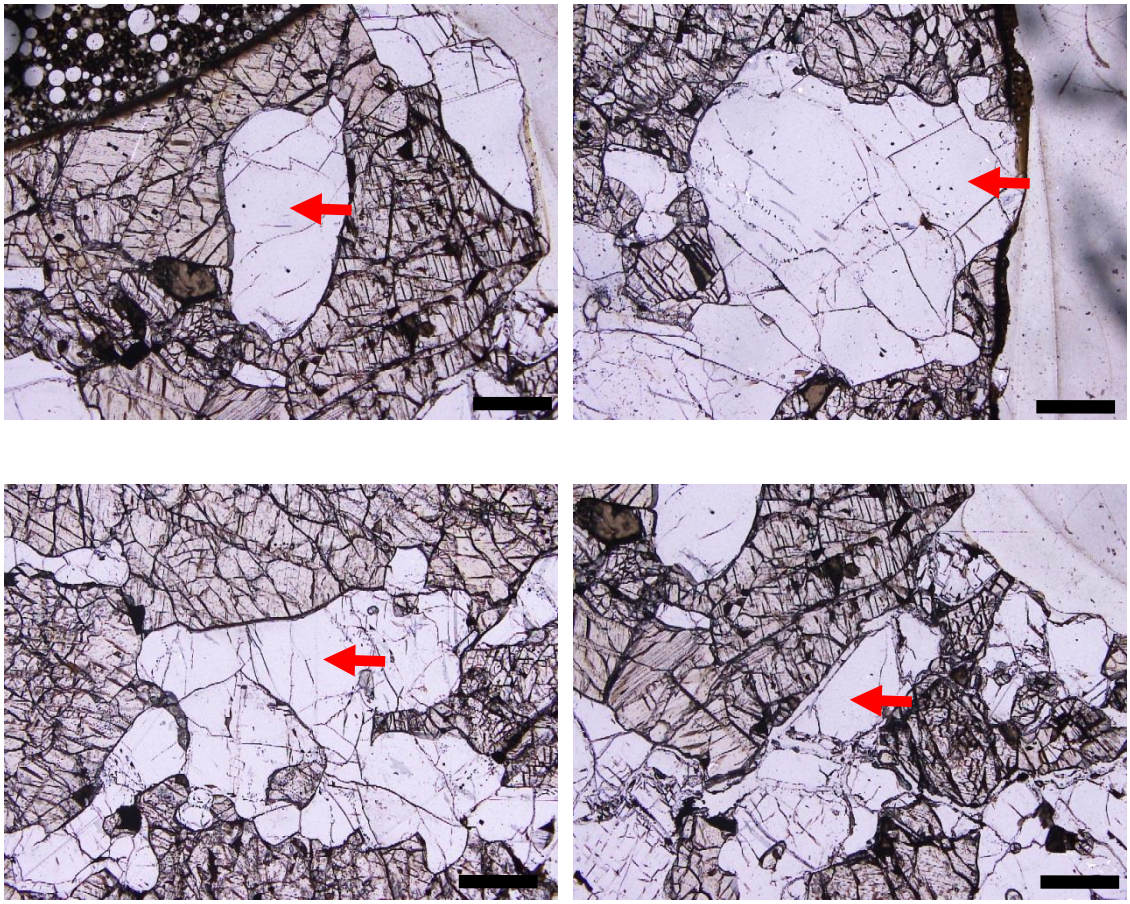

Fig. 4.10 Optical photomicrographs of Moore County (plane-polarized light). Red arrows shown in each image are analyzed points by SR-XANES. Black bars in the lower right are scales of 500 μm.

4.2.8. Y 980433

I analyzed one plagioclase grain in Y 980433 (Fig. 4. 11). Y 980433 is a cumulate eucrite showing a much coarser-grained texture than EETA 87520 and Moore County, and I selected a coarse plagioclase grain whose size reaches 2000 x 1500 μm. The Fe^{3+}-Fe^{2+} peak-intensity ratios of this sample is 0.70 (Table 4.2).

The obtained XANES spectra of plagioclase in Y 980433 showed that the higher energy peaks are clearly higher than lower energy peak (Fig. 4.13).

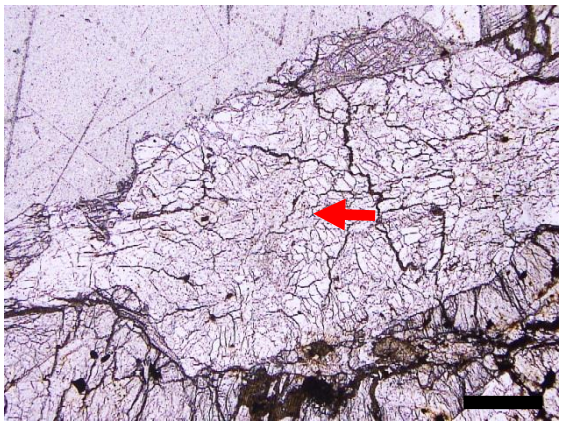

Fig. 4.11 Optical photomicrograph of Y 980433 (plane-polarized light). A red arrow shown in the image shows an analyzed point by SR-XANES. A black bar in the lower right is scale of 500 μm.

4.2.9. Y-75032

Y-75032 is a rare diogenite containing plagioclase. I could find only one plagioclase grain in Y-75032 and analyzed it. The size of analyzed plagioclase is about 500 μm (Fig. 4.12). The obtained XANES spectrum of plagioclase in Y-75032 showed that the height of higher energy peak and lower energy peak are almost same (Fig. 4.13). The obtained Fe^{3+}-Fe^{2+} peak-intensity ratio of this sample is 0.52 (Table 4.2).

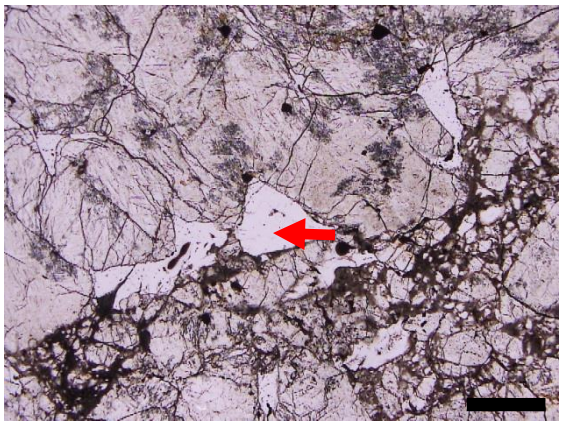

Fig. 4.12 Optical photomicrograph of Y-75032 (plane-polarized light). A red arrow shown in the image is an analyzed point by SR-XANES. A black bar in the lower right is a scale of 500 μm.

Table 4.2 Fe^{3+}-Fe^{2+} peak-intensity ratios of analyzed HED meteorites

Sample	Group	Fe^{3+}-Fe^{2+} peak-intensity ratios (%)	Error
ALH 76005 grain-1	Surface eucrite	25.2	±0.7
ALH 76005 grain-2	Surface eucrite	33.3	±0.9
ALH 76005 grain-3	Surface eucrite	34.9	±0.6
Petersburg grain-1	Surface eucrite	30.9	±0.8
Petersburg grain-2	Surface eucrite	40.6	±0.9
Petersburg grain-3	Surface eucrite	31.6	±0.9
Piplia Kalan grain-1	Surface eucrite	43.4	±1.8
Piplia Kalan grain-2	Surface eucrite	31.4	±0.6
Padvarninkai grain-1	Surface eucrite	23.0	±1.1
Padvarninkai grain-2	Surface eucrite	14.1	±0.6
Y-75011 grain-1	Surface eucrite	21.6	±0.4
Y-75011 grain-2	Surface eucrite	22.1	±0.6
EETA 87520 grain-1	Cumulate eucrite	57.3	±2.0
EETA 87520 grain-2	Cumulate eucrite	58.5	±1.7
EETA 87520 grain-3	Cumulate eucrite	50.9	±1.8
EETA 87520 grain-4	Cumulate eucrite	51.6	±1.8
Moore County grain-1	Cumulate eucrite	51.9	±1.9
Moore County grain-2	Cumulate eucrite	54.1	±2.0
Moore County grain-3	Cumulate eucrite	49.1	±1.8
Moore County grain-4	Cumulate eucrite	55.4	±3.6
Y 980433	Cumulate eucrite	69.6	±3.4
Y-75032	Diogenite	51.8	±2.8

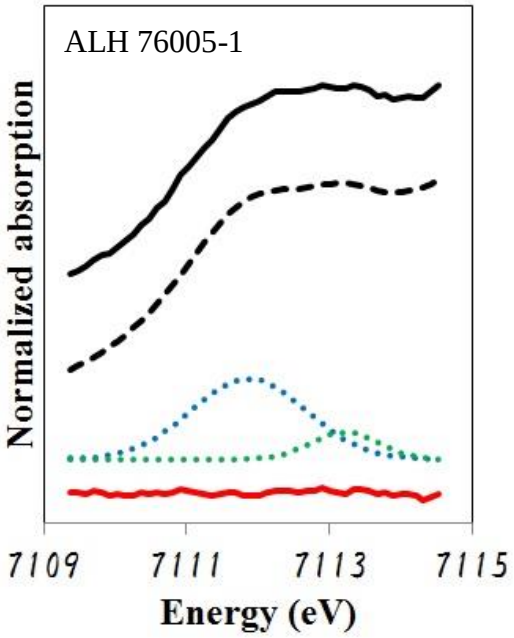
ALH 76005-1
Normalized absorption
7109
7111
7113
7115
Energy (eV)

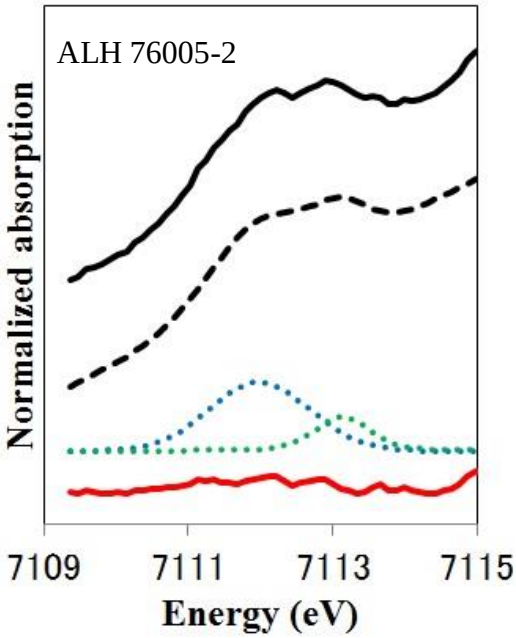
ALH 76005-2
Normalized absorption
7109
7111
7113
7115
Energy (eV)

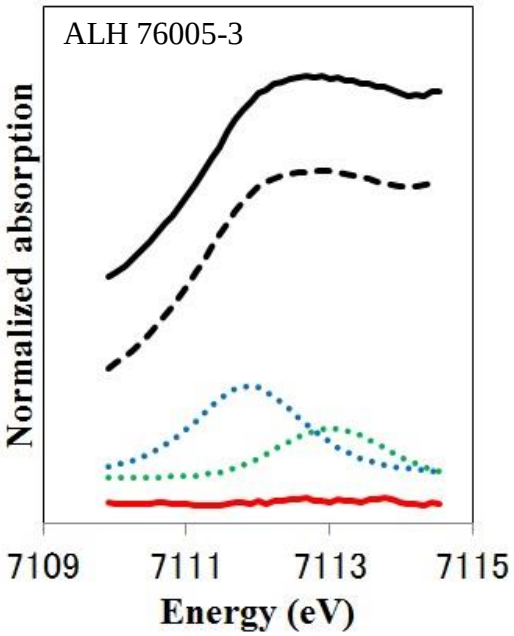
ALH 76005-3
Normalized absorption
7109
7111
7113
7115
Energy (eV)

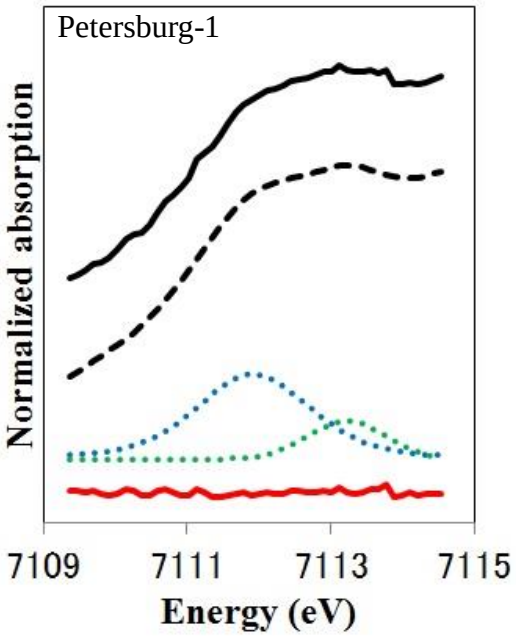
Petersburg-1
Normalized absorption
7109
7111
7113
7115
Energy (eV)

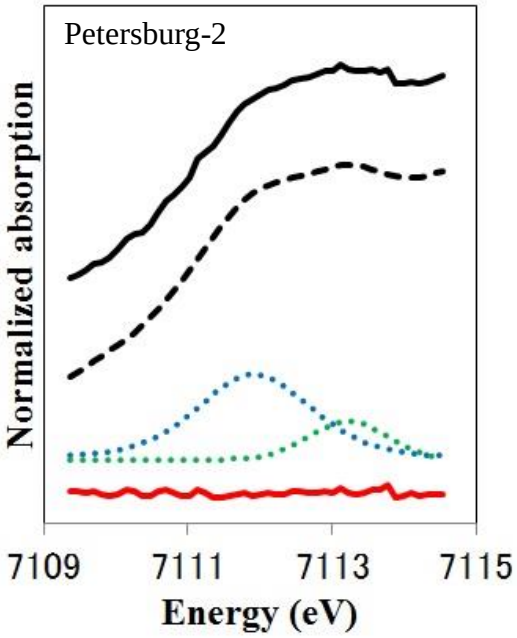
Petersburg-2
Normalized absorption
7109
7111
7113
7115
Energy (eV)

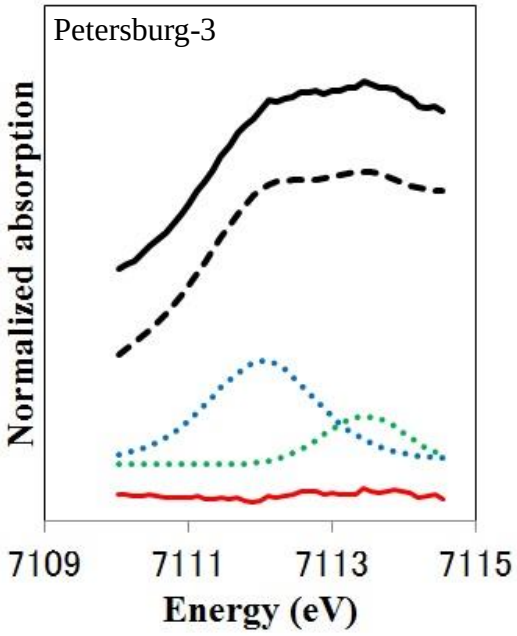
Petersburg-3
Normalized absorption
7109
7111
7113
7115
Energy (eV)

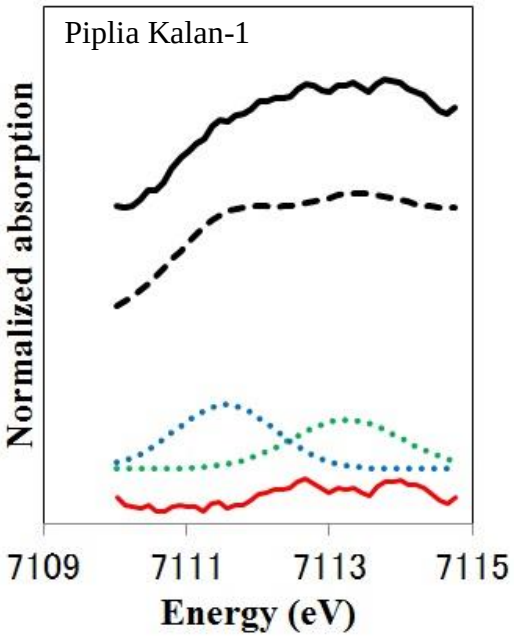
Piplia Kalan-1
Normalized absorption
7109
7111
7113
7115
Energy (eV)

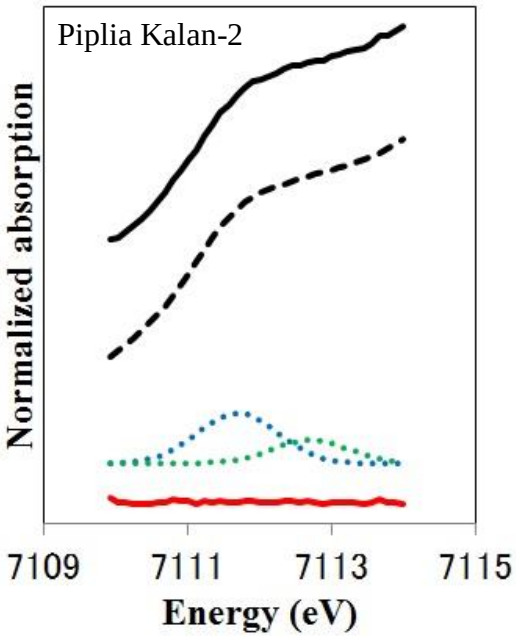
Piplia Kalan-2
Normalized absorption
7109
7111
7113
7115
Energy (eV)

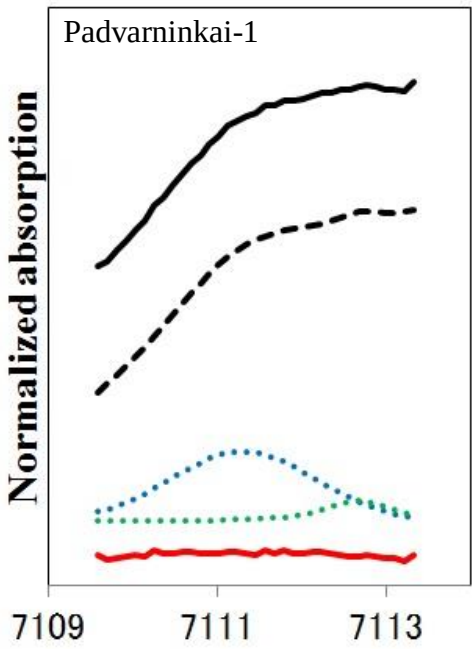
Padvarninkai-1
Normalized absorption
7109
7111
7113

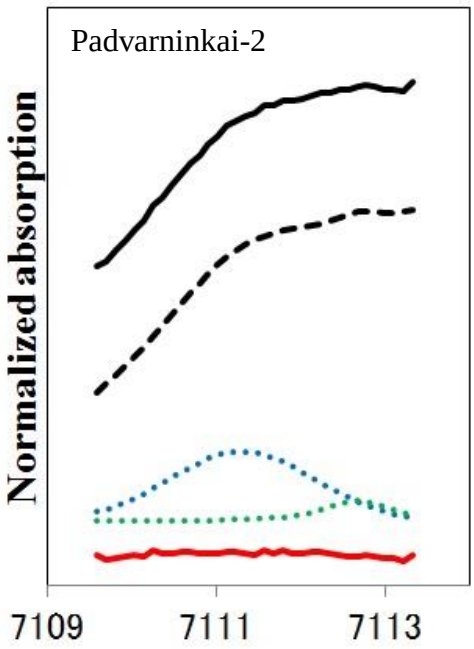
Padvarninkai-2
Normalized absorption
7109
7111
7113

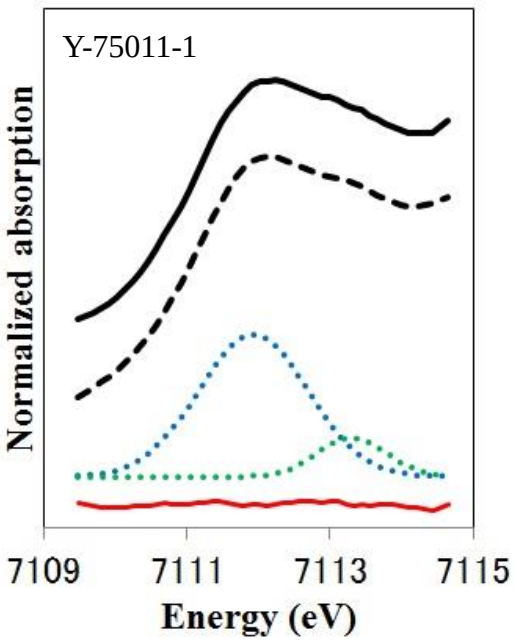
Y-75011-1
Normalized absorption
7109
7111
7113
7115
Energy (eV)

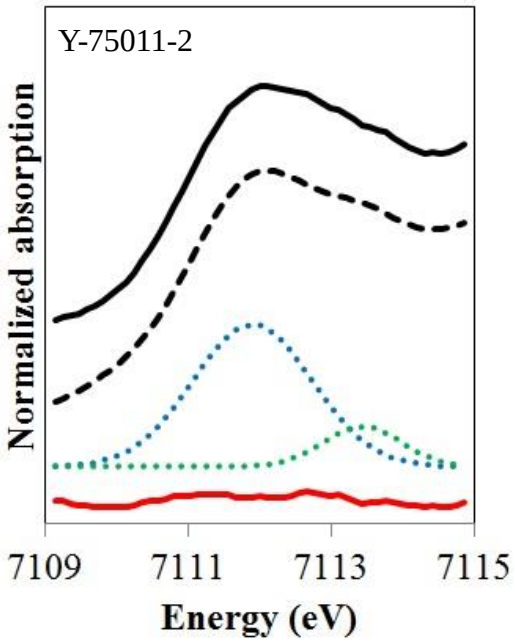
Y-75011-2
Normalized absorption
7109
7111
7113
7115
Energy (eV)

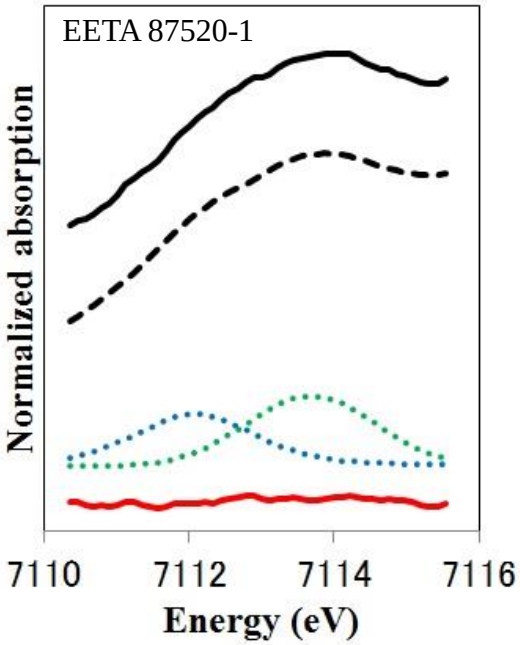
EETA 87520-1
Normalized absorption
7110
7112
7114
7116
Energy (eV)

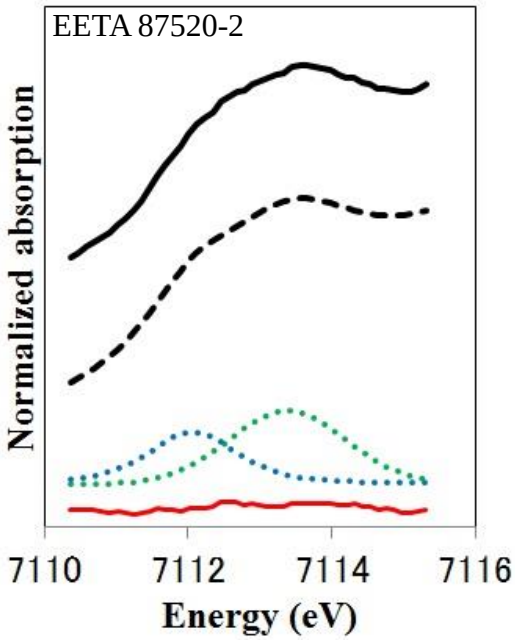
EETA 87520-2
Normalized absorption
7110
7112
7114
7116
Energy (eV)

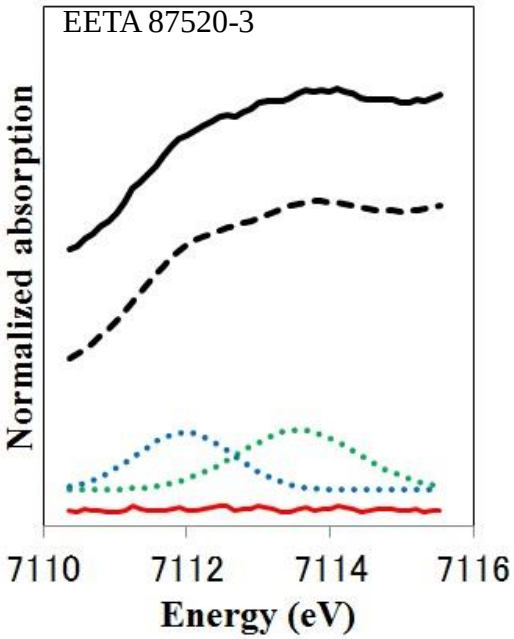
EETA 87520-3
Normalized absorption
7110
7112
7114
7116
Energy (eV)

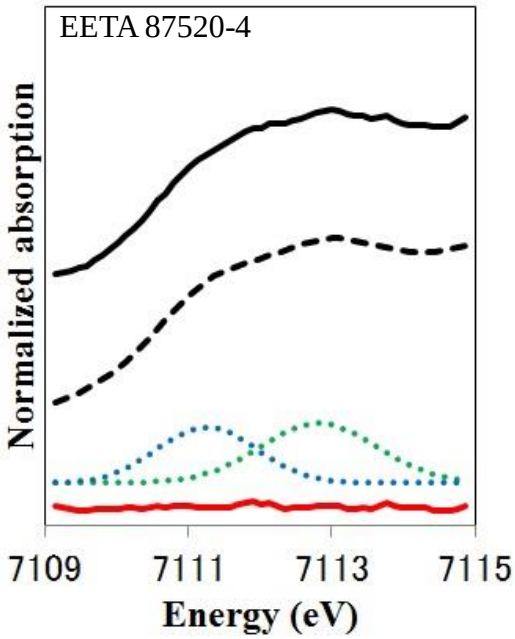
EETA 87520-4
Normalized absorption
7109
7111
7113
7115
Energy (eV)

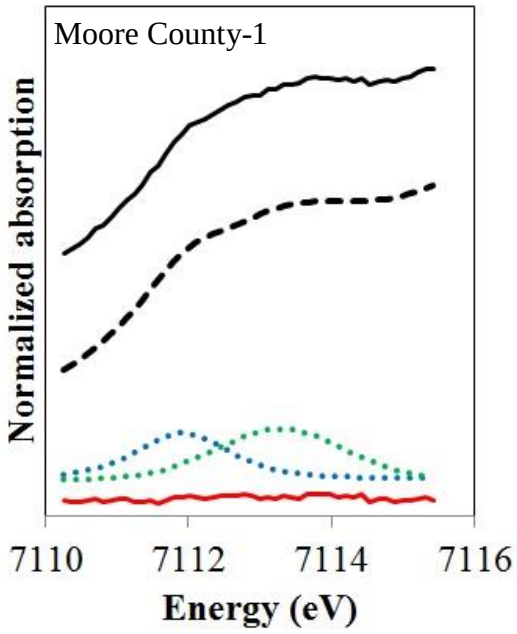
Moore County-1
Normalized absorption
7110
7112
7114
7116
Energy (eV)

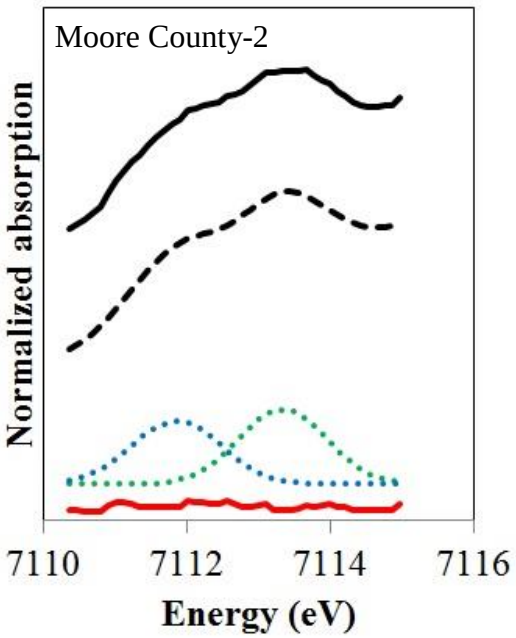
Moore County-2
Normalized absorption
7110
7112
7114
7116
Energy (eV)

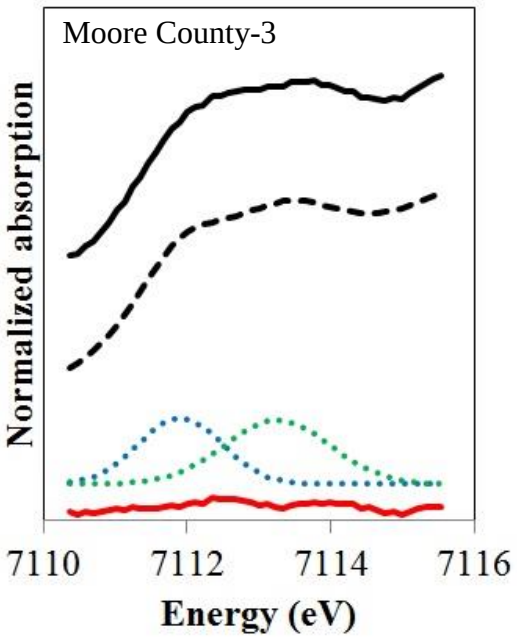
Moore County-3
Normalized absorption
7110
7112
7114
7116
Energy (eV)

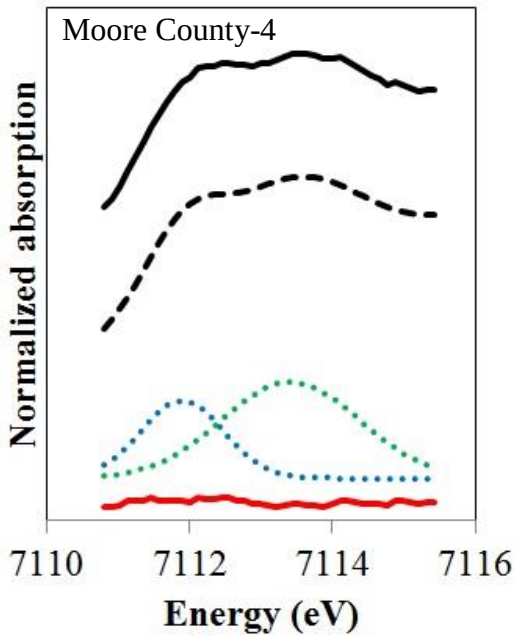
Moore County-4
Normalized absorption
7110
7112
7114
7116
Energy (eV)

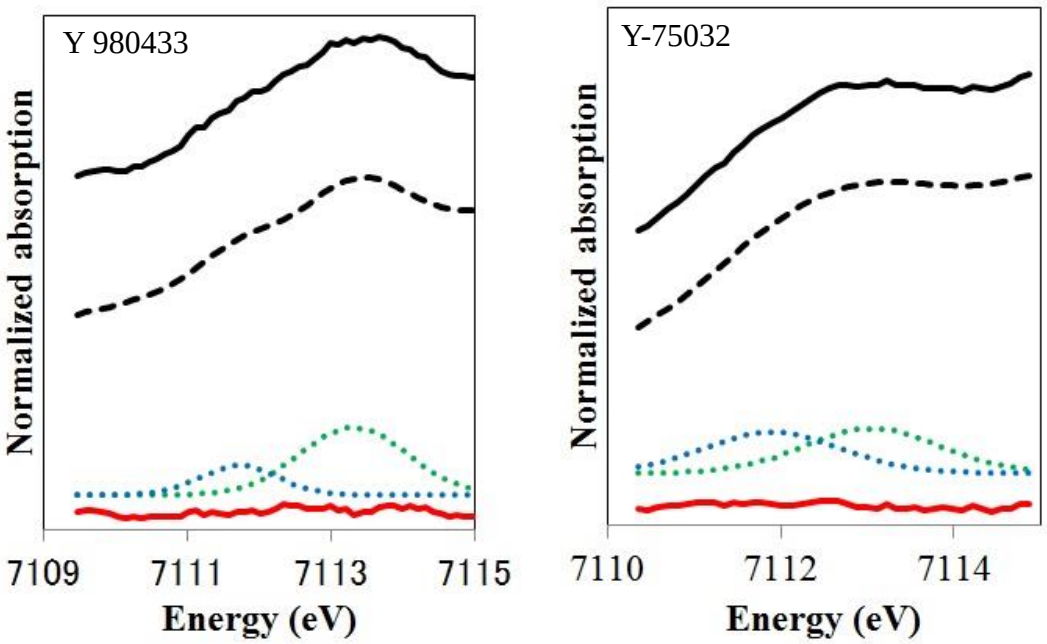

Fig. 4.13 SR Fe-XANES pre-edge spectra in the range of 7109-7116 eV, as obtained from plagioclase and maskelynite in HED meteorites: ALH 76005, Petersburg, Piplia Kalan, Padvarninkai, Y-75011, EETA 87520, Moore County, Y 980433 and Y-75032. Blue and green dots represent deconvoluted peaks of divalent and trivalent Fe, respectively. The raw data are shown by black solid lines, the fitted data are shown by black dashed lines and the residuals of fitting data are shown by red solid lines, respectively. The raw and convoluted spectra are shifted to higher position in vertical axis for ease of comparison.

4.3. The Sample of Shock-loading Experiments

I analyzed one spot in each of ten samples recovered from a shock-loading experiment of plagioclase. As I summarized characteristics of the samples in Fig. 2.3, several samples show partial amorphousization of plagioclase. In these samples I selected amorphous areas by optical microscope and analyzed points in these amorphous areas.

The Fe^{3+}-Fe^{2+} peak-intensity ratios of An_{80} (unshocked), An_{80} shocked at 20 GPa, An_{80} shocked at 30 GPa and An_{80} shocked at 40 GPa samples are 0.80, 0.81, 0.80 and 0.78, respectively (Table 4.3). There is little difference in Fe^{3+}-Fe^{2+} peak-intensity ratios of

the experimentally shocked plagioclase with the An_{80} composition. The obtained SR XANES spectra of these An_{80} samples show that the high energy peaks have higher intensity than lower energy peak and it should be note that the spectrum shape is almost unchanged over wide range of shock pressure (Fig. 4.14).

In the case of An_{60} samples, the Fe^{3+}-Fe^{2+} peak-intensity ratios of An_{60} (unshocked) and An_{60} shocked at 30 GPa samples are 0.74 and 0.73 (Table 4.3). The shape of the SR XANES spectrum is a slightly different and an unshocked An_{60} sample gave significantly low counts (Fig. 4.14). However, the Fe^{3+}-Fe^{2+} peak-intensity ratios of these two samples showed the same value.

In addition, the Fe^{3+}-Fe^{2+} peak-intensity ratios of An_{20} (unshocked), An_{20} shocked at 20 GPa, An_{20} shocked at 30 GPa and An_{20} shocked at 40 GPa samples are 0.67, 0.67, 0.68 and 0.67, respectively (Table 4.3). With the exception of An_{20} shocked at 30 GPa, the shapes of the SR XANES spectra are all similar (Fig. 4.14). The SR XANES spectrum of the An_{20} sample shocked at 30 GPa has the lower counts than other samples.

Thus, there is no change in the Fe^{3+}-Fe^{2+} peak-intensity ratios between unshocked and shocked samples, suggesting that shock metamorphism hardly changes Fe^{3+}-Fe^{2+} peak-intensity ratios even if the samples are shocked up to 40 GPa. It is also noted that plagioclase with variable anorthite contents shows similar XANES spectra.

Table 4.3 Fe^{3+}-Fe^{2+} peak-intensity ratios of unshocked and shocked samples

Sample	Phase	Fe^{3+}-Fe^{2+} peak-intensity ratios (%)	Error
An_{80} (unshocked)	P	80.2	±3.8
An_{80} shocked at 20GPa	P	80.9	±3.4
An_{80} shocked at 30GPa	M	80.3	±4.1
An_{80} shocked at 40GPa	M	78.3	±3.1
An_{60} (unshocked)	P	73.6	±7.8
An_{60} shocked at 30GPa	M	73.4	±6.7
An_{20} (unshocked)	P	66.9	±1.7
An_{20} shocked at 20GPa	P	67.2	±3.3
An_{20} shocked at 30GPa	M	67.8	±8.1
An_{20} shocked at 40GPa	M	66.6	±4.0

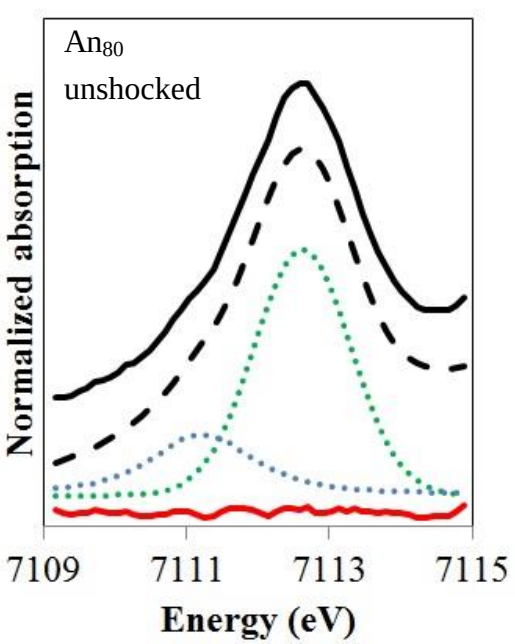
An80
unshocked
Normalized absorption
7109
7111
7113
7115
Energy (eV)

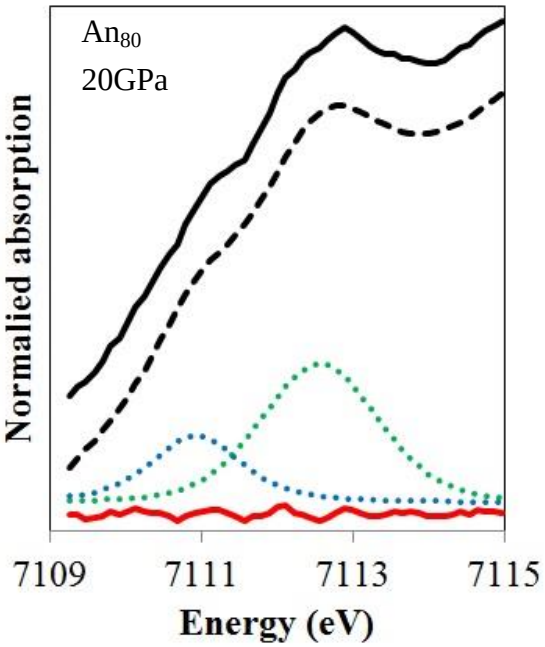
An80
20GPa
Normalied absorption
7109
7111
7113
7115
Energy (eV)

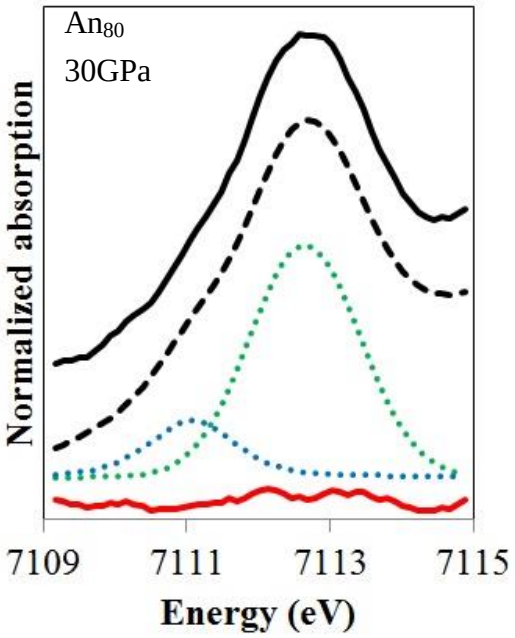
An80
30GPa
Normalized absorption
7109
7111
7113
7115
Energy (eV)

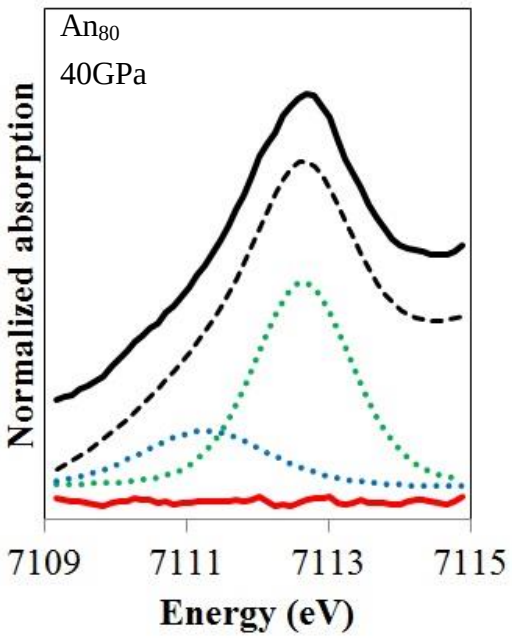
An80
40GPa
Normalized absorption
7109
7111
7113
7115
Energy (eV)

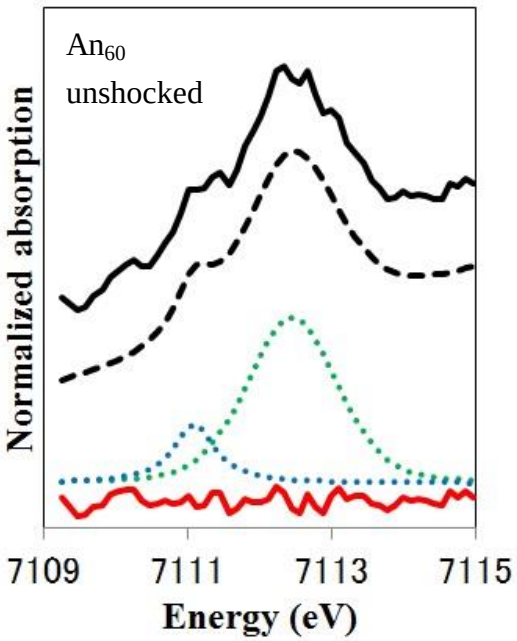
An60
unshocked
Normalized absorption
7109
7111
7113
7115
Energy (eV)

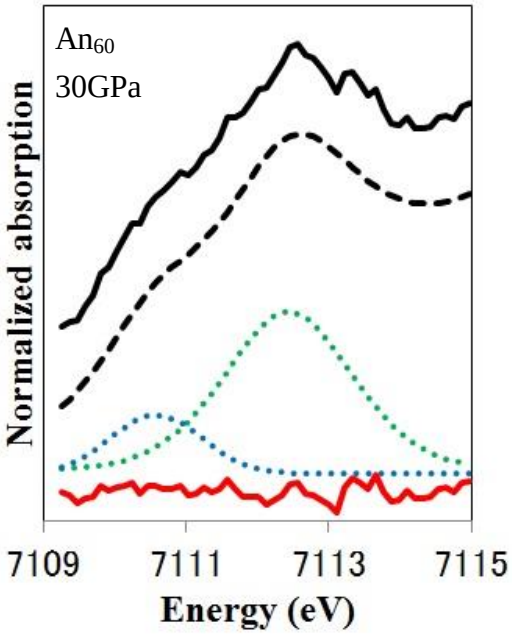
An60
30GPa
Normalized absorption
7109
7111
7113
7115
Energy (eV)

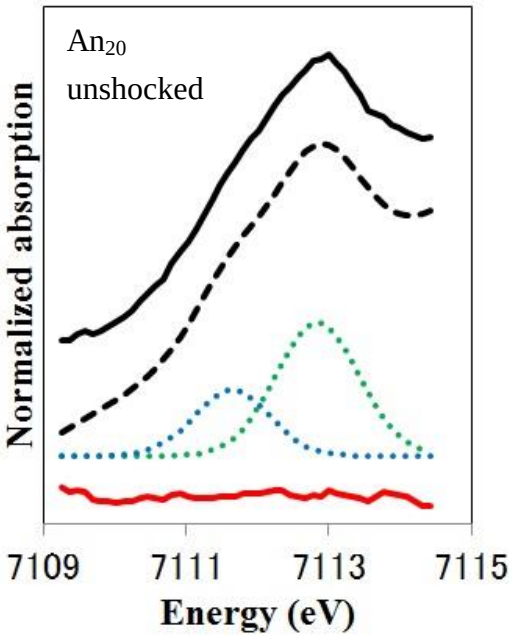
An20
unshocked
Normalized absorption
7109
7111
7113
7115
Energy (eV)

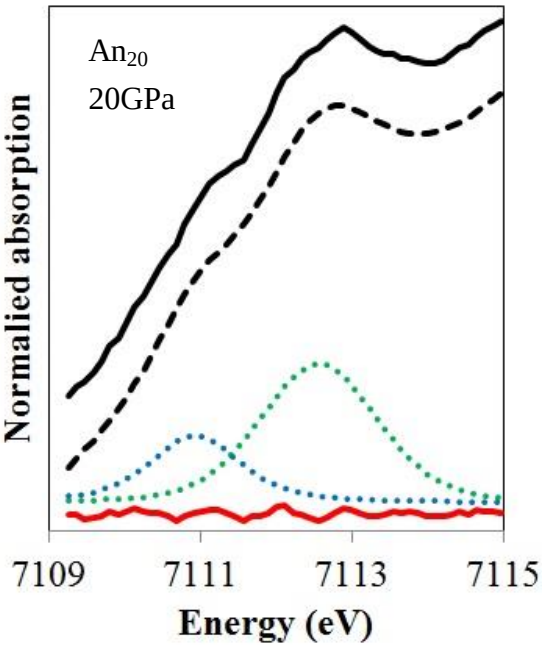
An20
20GPa
Normalied absorption
7109
7111
7113
7115
Energy (eV)

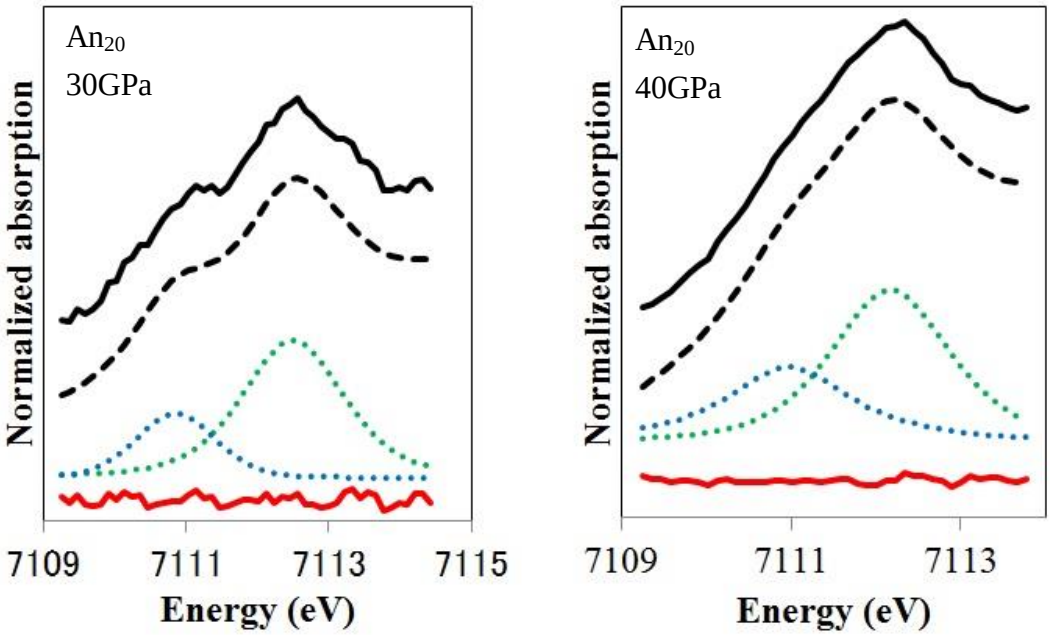

Fig. 4.14 SR Fe-XANES pre-edge spectra in the range of 7109–7115 eV, as obtained from plagioclase and maskelynite in unshocked and experimentally-shocked plagioclase samples: An_{80} (unshocked), An_{80} shocked at 20 GPa, An_{80} shocked at 30 GPa and An_{80} shocked at 40 GPa, An_{60} (unshocked), An_{60} shocked at 30 GPa, An_{20} (unshocked), An_{20} shocked at 30 GPa and An_{20} shocked at 40 GPa. Blue and green dots represent peaks of divalent and trivalent Fe, respectively. The raw data are shown by black solid lines, the fitted data are shown by black dashed lines and the residuals of fitting data are shown by red solid lines, respectively. The raw and convoluted spectra are shifted to higher position in vertical axis for ease of comparison.

4.4. Synthetic Experiment of Plagioclase

As I wrote in the section “Description of the sample studied”, optical microscopic observations show that plagioclases are present in all samples by synthetic experiment. I analyzed clean areas of these phases that are enough far away from surrounding residual glass.

The Fe^{3+}-Fe^{2+} peak-intensity ratios of plagioclase in the QFM –2 and QFM samples are 0.42 and 0.90 (Table 4.4), respectively. From both QFM –2 and QFM samples, the sharp pre-edge spectra of Fe XANES analysis were obtained (Fig. 4.15).

Table 4.4 Fe^{3+}-Fe^{2+} peak-intensity ratios of QFM –2 and QFM samples

Sample	Fe^{3+}-Fe^{2+} peak-intensity ratios (%)	Error
QFM –2	41.8	±1.2
QFM	89.8	±3.3

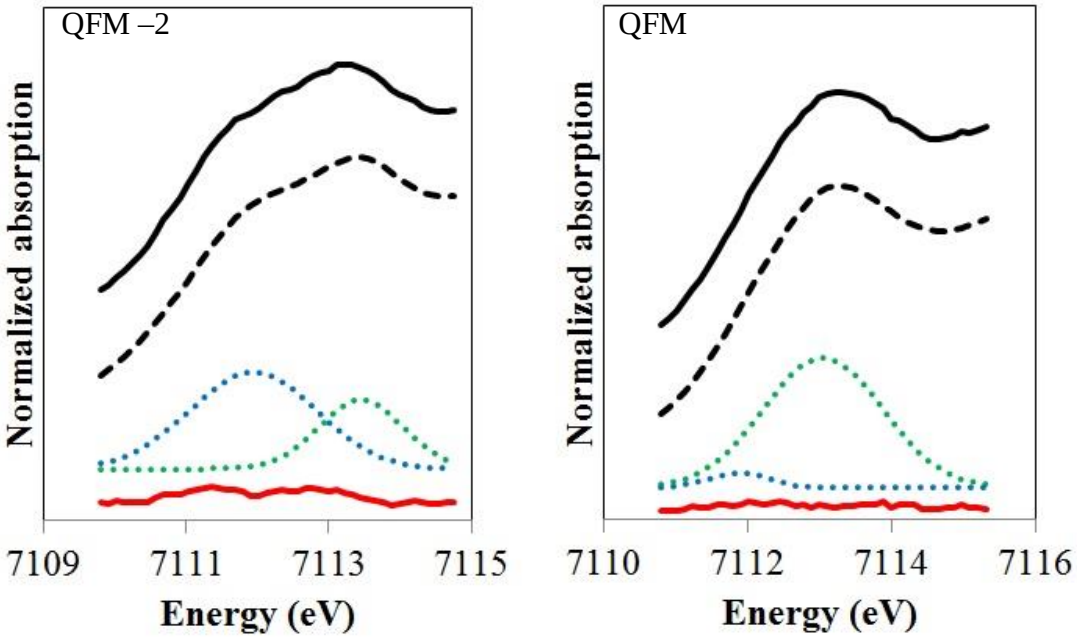

Fig. 4.15 SR Fe-XANES pre-edge spectra of QFM –2 and QFM samples in the range of 7109–7116 eV. Blue and green dots represent peaks of divalent and trivalent Fe, respectively after deconvolution. The raw data are shown by black solid lines, the fitted data are shown by black dashed lines and the residuals of fitting data are shown by red solid lines, respectively. The raw and convoluted spectra are shifted to higher position in vertical axis for ease of comparison.

4.5. Terrestrial Plagioclase with Known fO_2

I analyzed two grains of plagioclase in the terrestrial sample whose fO_2 has been

measured. The estimated fO_2 is log fO_2 = QFM –1.5. I selected two grains showing euhedral shapes and their grain sizes are larger than 1 mm (Fig. 4.16). The Fe^{3+}-Fe^{2+} peak-intensity ratios of grain 1 and grain 2 are 0.75 and 0.76, respectively (Table 4.5).

The obtained XANES spectra of plagioclase in this terrestrial sample showed that the shapes of XANES spectra at the pre-edge regions are very similar between grains 1 and 2 (Fig. 4.17).

Table 4.5 Fe^{3+}-Fe^{2+} peak-intensity ratios of terrestrial plagioclase

Sample	Fe^{3+}-Fe^{2+} peak-intensity ratios (%)	Error
Terrestrial grain-1	75.3	±3.0
Terrestrial grain-2	75.9	±3.7

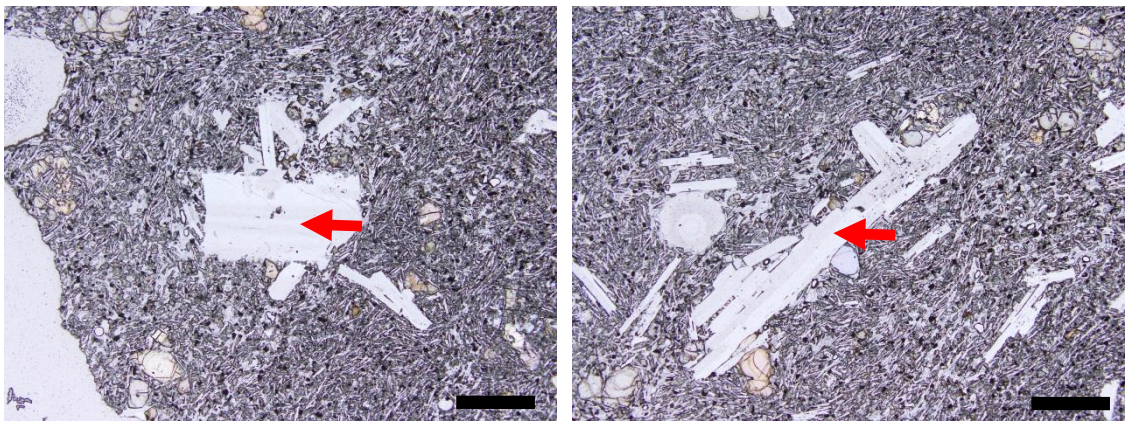

Terrestrial grain-1 Terrestrial grain-2

Fig. 4.16 Optical photomicrographs of the studied terrestrial basaltic sample (plane-polarized light). A red arrow shown in the image is an analyzed point by SR-XANES. Black bars at the lower right corner are scales of 500 μm.

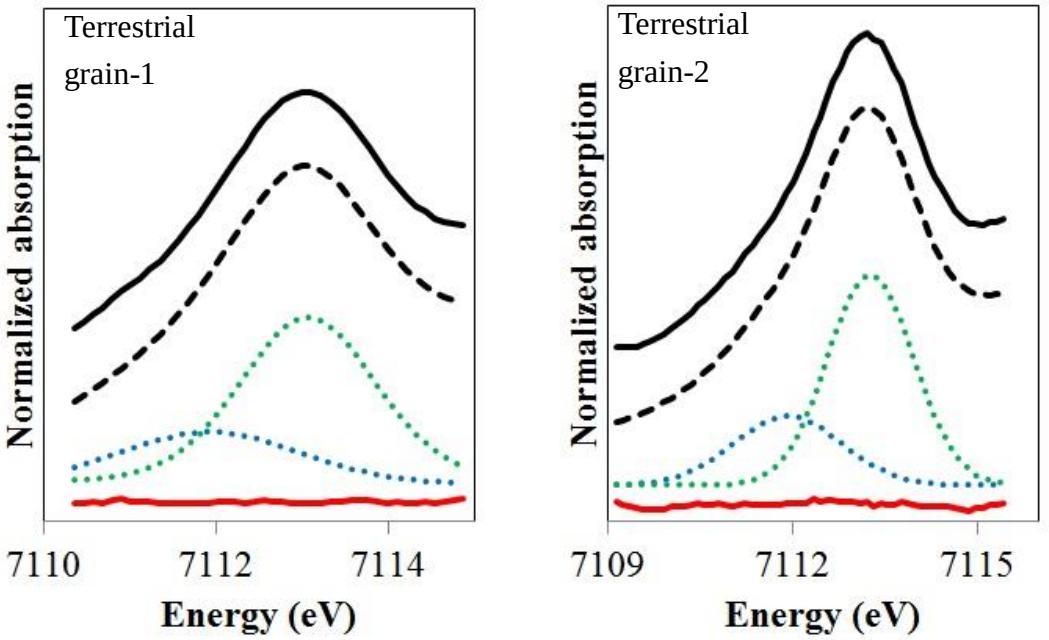

Fig. 4.17 SR Fe-XANES pre-edge spectra of plagioclase from the studied terrestrial basalt with known fO_2 in the range of 7109–7116 eV. Blue and green dots represent peaks of divalent and trivalent Fe, respectively. The raw data are shown by black solid lines, the fitted data are shown by black dashed lines and the residuals of fitting data are shown by red solid lines, respectively. The raw and convoluted spectra are shifted to higher position in vertical axis for ease of comparison.

5. Discussion

5.1 Fe^{3+}-Fe^{2+} Peak Intensity Ratios of Pyroxene

XANES analysis of plagioclase and maskelynite requires long counting time because of low iron abundance in the samples. Therefore, I also attempted to analyze the Fe^{3+}-Fe^{2+} peak intensity ratios of pyroxene by using the same XANES analysis in order to examine the usefulness of the oxybarometer using iron valence differences, because pyroxene contains large amounts of Fe and pyroxene is included in all meteorites analyzed. I did not choose olivine because it is absent in eucrites although Fe abundance in olivine is as high as in pyroxene.

I analyzed pyroxene grains of depleted shergottite Dhofar 019 and enriched shergottite RBT 04262, that are two extreme examples in the redox states suggested from Fe valences in maskelynite (Table 4.1). The obtained XANES spectra of pyroxenes in both Dhofar 019 and RBT 04262 showed only lower energy peaks and do not have the higher energy peak corresponding to Fe^{3+} (Fig. 4.3). This result indicates that pyroxene is not appropriate for estimating relative redox states by using iron valence states. Therefore, it is revealed that pyroxene cannot be used as an oxybarometer for Martian meteorites and eucrites.

5.2 Does the Fe^{3+}-Fe^{2+} Peak Intensity Ratio Change by Shock?

All shergottites and most of HED meteorites have experienced heavy shock and one may be concerned that there is a possibility that the Fe^{3+}-Fe^{2+} peak intensity ratios of plagioclase was changed by the impact. Therefore, I attempted to estimate redox state of various plagioclase samples recovered from shock-loading experiments by XANES analysis.

As I wrote in the section “Sample of shock-loading experiment”, I analyzed the plagioclase samples with three different chemical compositions, An_{20}, An_{60} and An_{80}. The Fe^{3+}-Fe^{2+} peak intensity ratios of shocked samples in all compositional types are almost unchanged after shock even if the plagioclase is transformed to isotropic glass (maskelynite) (Table 4.3).

Thus, there is little difference in the Fe^{3+}-Fe^{2+} peak-intensity ratios between unshocked and shocked samples, suggesting that shock metamorphism would not change Fe^{3+}-Fe^{2+} peak-intensity ratios even if the samples are shocked at up to 40 GPa, which is an estimated shock pressure of most shergottites. Therefore, the relative redox states of these samples can be estimated from maskelynite and plagioclase using Fe^{3+}-Fe^{2+} peak intensity ratios of plagioclase and maskelynite as measured by iron micro-XANES

analysis.

There is a possibility that the Fe^{3+}-Fe^{2+} peak-intensity ratios of plagioclase was changed by thermal metamorphism after the impact. However, I consider that this is not likely because the difference of ionic radii of divalent and trivalent irons are not significant (ionic radius of divalent iron is 0.76 Å and trivalent iron is 0.64 Å), implying similar diffusion coefficients. The charge difference between Fe^{2+} and Fe^{3+} may cause the diffusion rate of these two ions, but it is not clear because there are no literature diffusion data for two different iron ions in plagioclase.

5.3 Redox State Estimated from Fe^{3+}-Fe^{2+} Peak Intensity Ratios of Maskelynite and Plagioclase

The redox states of shergottites and HED meteorites can be relatively compared using the Fe^{3+}-Fe^{2+} peak-intensity ratios of maskelynite and plagioclase. I created a calibration curve relating the Fe^{3+}-Fe^{2+} peak-intensity ratios of maskelynite and plagioclase and oxygen fugacity by applying the result from the crystallization experiment.

As I wrote in the section "Description of the sample studied and XANES analysis", I synthesized the plagioclase specimens under the redox conditions of two different oxygen fugacities, and analyzed the specimens by XANES analysis. In addition, I analyzed plagioclases in the terrestrial sample whose fO_2 has been measured.

Schreiber et al. (1987) reported that there is a relationship of the expression to trivalent ratio of divalent iron and fO_2: (Fig. 5.1)

Fig. 5.1 shows a calibration curve by an approximate curve power approximation of the result of synthetic experiment of plagioclase and terrestrial plagioclase. As a result, from the Fe^{3+}-Fe^{2+} peak-intensity ratio obtained, log fO_2 (⊿QFM) is defined by the following equation:

log fO_2 (⊿QFM) = 0.39 × exp (2.1 × Fe^{3+}-Fe^{2+} peak-intensity ratio) – 3 …(b) (Fig. 5.2)

I substitute the Fe^{3+}-Fe^{2+} peak-intensity ratios of maskelynite and plagioclase in shergottites and HED meteorites obtained this study for this calibration curve, in order to estimate fO_2 of the source of shergottites and Vesta's crust.

Table 5.1 summarizes the estimated fO_2 of shergottites obtained from the calibration curve. It is very important that the obtained log fO_2 values (⊿QFM) are between the estimates by Ol-Px-Sp and Fe-Ti oxides oxybarometers. Each of Ol-Px-Sp and Fe-Ti oxides oxybarometers shows that redox sates when each minerals crystallized.

Therefore, the results are consistent with the crystallization sequence of mineral in the basaltic Martian magma. This result indicates again that maskelynite and plagioclase record initial redox states when plagioclase crystallized from magma. In addition, oxygen fugacity of RBT04262 is log fO_2 = QFM –1.1 ~ –0.9 and NWA 4468 is log fO_2 = QFM –1.5 ~ –1.3, respectively. This is the first report showing that RBT 04262 and NWA 4468 are oxidized samples because no oxybarometer measurements had previously been performed on these meteorites.

Similarly, Table 5.2 shows the redox states of HED meteorites obtained from the calibration curve. As I wrote in the section "Introduction", redox state of Vesta's crust has not been well estimated yet because any oxybarometer measurements have not been performed on these samples. For this reason, this is the first report estimating their oxygen fugacity. The obtained results suggest that HED meteorites crystallized at log fO_2 = QFM –2.4 to 2.0 at near the surface of Vesta and QFM –1.9 to –1.3 at near the bottom of the crust, respectively.

Table 5.1 Oxygen fugacity of shergottites (log fO_2 (⊿QFM)) determined by three different methods.

Sample	Group	Fe-Ti Oxybarometer	This study	Sp-Ol-Px Oxybarometer
Dal al Gani 476	D	–1.5	–2.1 ~ –1.9	–2.3
Dhofar 019	D	-	–2.1 ~ –2.0	–3.8
ALH 77005	I	-	–2.5 ~ –2.3	–2.6
EETA 79001 lithology A	I	–1.7	–2.1 ~ –1.8	–2.8
LEW 88516	I	-	–1.8 ~ –1.4	-
NWA 5029	I	-	–2.2 ~ –2.0	-
Dhofar 378	E	-	–1.8 ~ –1.4	-
LAR 06319	E	0.5	–1.8 ~ –1.6	–2
NWA 856	E	-	–1.8 ~ –1.7	-
NWA 1068	E	–0.5	–1.7 ~ –1.6	–2.5
NWA 4468	E	-	–1.5 ~ –1.3	-
Zagami	E	–1.2	–1.8 ~ –1.7	-
RBT 04262	E	-	–1.1 ~ –0.9	-
Shergotty	E	–1.2	–2.1 ~ –1.7	-

Table 5.2 Oxygen fugacity of HED meteorites estimated in this study.

Sample	Group	log fO_2 (⊿QFM)
ALH 76005	Surface eucrite	–2.3 ~ –2.2
Petersburg	Surface eucrite	–2.3 ~ –2.1
Piplia Kalan	Surface eucrite	–2.2 ~ –2.0
Padvarninkai	Surface eucrite	–2.4
Y-75011	Surface eucrite	–2.4
EETA 87520	Cumulate eucrite	–1.9 ~ –1.7
Moore County	Cumulate eucrite	–1.9 ~ –1.8
Y 980433	Cumulate eucrite	–1.3
Y-75032	Diogenite	–1.8

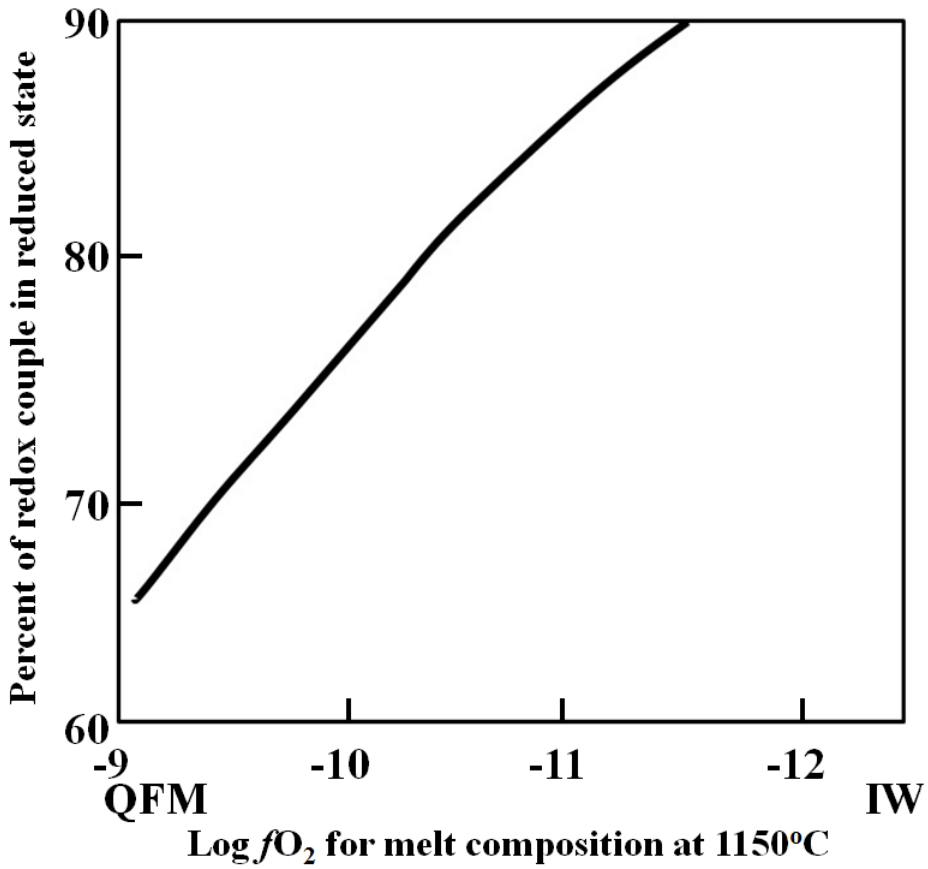

Fig. 5.1 The estimation of redox ion distributions after mutual interactions in a melt of composition SRL-131 which possesses natural basaltic abundances of the multivalent elements at 1150 ^{o}C from Schreiber et al. (1987).

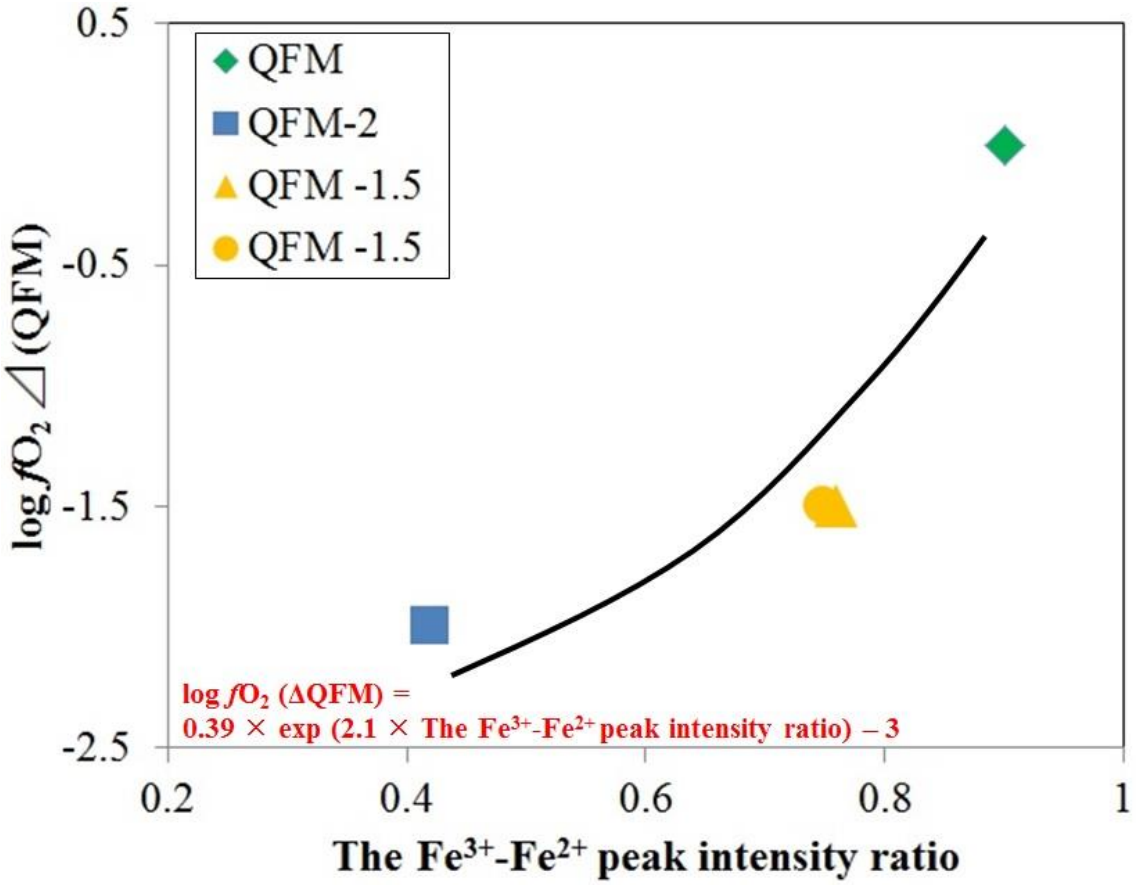

Fig. 5.2 Relation between Fe^{3+}-Fe^{2+} peak-intensity ratios and oxygen fugacity. Calibration line is drawn with a black line.

5.4 What Does the Fe^{3+}-Fe^{2+} Peak Intensity Ratio Indicate?

I assumed that the Fe^{3+}-Fe^{2+} peak-intensity ratios of plagioclase and maskelynite showed the redox states of magma when plagioclase crystallized, although maskelynite was secondary formed during the later shock event. The result of the section 5.2. "Does the Fe^{3+}-Fe^{2+} Peak Intensity Ratio Change by Shock?" indicates that the measured Fe^{3+}-Fe^{2+} peak intensity ratios of plagioclase and maskelynite in shergottites and HED meteorites are preserved, thus recording redox states of their initial crystallization from magma.

In the melt of shergottites and HED meteorites, pyroxene crystallizes before plagioclase. The result of the section "Fe^{3+}-Fe^{2+} peak-intensity ratios of pyroxene" showed that pyroxene preferentially takes divalent iron, and the residual melt when plagioclase crystallized, might not have information for the initial melt.

I calculated the ferric and ferrous ratio in the residual melt when plagioclase

crystallized at different oxygen fugacity by MELTS calculation (Fig. 5.3). It showed that the residual melt is not depleted in divalent iron even if abundant pyroxenes crystallize before plagioclase precipitation. Fig. 5.4 also shows that the residual melt is not depleted in divalent iron and its ferric/ferrous ratio does not significantly change when plagioclase starts crystallizing. This is because spinel crystallized at an early stage (Table 5.3) and most trivalent iron is contained in spinel. Fig. 5.5 showed that there is a positive relationship between Fe^{3+}-Fe^{2+} peak-intensity ratios and oxygen fugacity, and its trend is similar to Fig. 5.3.

As I wrote in the section "Redox sate estimated form Fe^{3+}-Fe^{2+} peak-intensity ratios of maskelynite and plagioclase", obtained Fe^{3+}-Fe^{2+} peak-intensity ratios in maskelynite and plagioclase showed redox states when plagioclase crystallized from magma. I consider that I can discuss the shergottites source, because there is no significant difference in Fe valence ratios between the initial melt and the residual liquid when plagioclase crystallized.

In fact log fO_2 values ($\triangle$QFM) estimated by Fe^{3+}-Fe^{2+} peak-intensity ratios of plagioclase and maskelynite are sandwiched by the estimates obtained from Ol-Px-Sp and Fe-Ti oxides oxybarometers, supporting that the Fe^{3+}-Fe^{2+} peak-intensity ratios of maskelynite and plagioclase reflects the oxygen fugacity when plagioclase crystallized from magma.

One may be concerned that there is a possibility that Ca sites in plagioclase may affect the ability of Fe^{2+} to substitute in its structure. Hoffmeister and Rossman (1984) reported that the $Fe^{2+}/\Sigma Fe$ correlates directly with total Ca contents, implying that the number of Ca sites in feldspar may affect the ability of Fe^{2+} to substitute in its structure. However, Fig. 5.6 and Fig. 5.7 show that there is no correlation between the Fe^{3+}-Fe^{2+} peak-intensity ratios and chemical composition of plagioclase. This result is consistent with Mössbauer spectroscopic study and it suggested that $Fe^{2+}\leftrightarrow$Ca substitution effect is less important than oxygen fugacity and other factors as suggested by Dyar et al. (2001). Thus, there is no correlation between the chemical composition and the variation of the results of measurement of the one sample.

Another consideration matter is the variations of the Fe^{3+}-Fe^{2+} peak-intensity ratios of plagioclase in the same sample (Figs. 5.8 and 9).

In order to determine the cause of this variation, I investigated the influence due to surrounding minerals and the effect of chemical composition of maskelynite and plagioclase. However, the obtained Fe^{3+}-Fe^{2+} peak-intensity ratios have no relationship with the distance from the peripheral minerals (Table 5.4 and Fig.5.10). The distance from the peripheral minerals for HED meteorites (Table 5.5 and Fig.5.11) appears to be

related, since it only shows that large mineral indicates that they are coarse-grained cumulate eucrites.

The obtained Fe^{3+}-Fe^{2+} peak-intensity ratios also have no relationship with the An content (Tables 5.4 and 5, Fig. 5.12) and Fe/Mg ratio of maskelynite and plagioclase (Fig. 5.13). I could not properly estimate the Fe/Mg ratio of plagioclase in HED meteorites because the iron concentration is very low. This result suggested that variations for the Fe^{3+}-Fe^{2+} peak-intensity ratios in the same sample is not due to these factors. Thus, I assumed that it is due to the local heterogeneity of residual liquid because at the late crystallization stage of magma the volume of the residual melt became small and interstitial residual melt has a locally heterogeneous composition. Then, I conclude that the average Fe^{3+}-Fe^{2+} peak-intensity ratios of maskelynite and plagioclase of each sample can be used to discuss the redox states because the variation is not so significant.

If I take the average values for the obtained Fe^{3+}-Fe^{2+} peak-intensity ratios in the same sample, the standard deviation is less than 10% (Table. 5.6). The range of 10% of the Fe^{3+}-Fe^{2+} peak-intensity ratios corresponds to only about $\log fO_2$=0.1 by using a calibration curve obtained in this study. Because the $\log fO_2$ value of plagioclase converted by the calibration curve is sandwiched between the by Ol-Px-Sp oxybarometer and Fe-Ti oxides oxybarometer, I concluded that the obtained Fe^{3+}-Fe^{2+} peak-intensity ratios of plagioclase can be used as an indicator of the redox state.

Table.5.3 Crystallization temperature (^oC) of minerals and the oxygen fugacity calculated by the MELTS program. I used the bulk composition of Yamato 980459 for the melt composition, because it is reported to represent a parent magma composition of depleted shergottites (Mikouchi and Koizumi 2007).

	QFM	QFM-1	QFM-2	QFM-3
Spinel	1480	1460	1440	1430
Olivine	1430	1440	1440	1450
Orthopyroxene	1380	1370	1360	1350
Clinopyroxene	1200	1200	1200	1200
Plagioclase	1150	1150	1150	1160

Table 5.4

Fe^{3+}-Fe^{2+} peak-intensity ratios, An content of plagioclase and distance from the closet mineral of studied shergottites.

Sample	Group	Fe^{3+}-Fe^{2+} peak-intensity ratio (%)	An	Distance (μm)
Dar al Gani 476-1	Depleted	40.0	66	20
Dar al Gani 476-2	Depleted	44.8	65	15
Dar al Gani 476-3	Depleted	42.2	68	20
Dar al Gani 476-4	Depleted	49.1	68	20
Dhofar 019-1	Depleted	43.5	64	40
Dhofar 019-2	Depleted	42.0	58	30
Dhofar 019-3	Depleted	40.4	50	20
Dhofar 019-4	Depleted	39.2	53	5
ALH 77005-1	Intermediate	12.7	48	10
ALH 77005-2	Intermediate	28.8	40	5
ALH 77005-3	Intermediate	24.0	50	10
EETA 79001 lith. A-1	Intermediate	52.6	57	20
EETA 79001 lith. A-2	Intermediate	39.9	56	20
LEW 88516-1	Intermediate	65.8	56	5
LEW 88516-2	Intermediate	65.3	57	45
LEW 88516-3	Intermediate	53.8	56	40
NWA 5029-1	Intermediate	45.6	50	20
NWA 5029-2	Intermediate	41.2	51	15
NWA 5029-3	Intermediate	31.4	49	20
NWA 5029-4	Intermediate	35.7	49	30
Dhofar 378-1	Enriched	54.9	55	40
Dhofar 378-2	Enriched	60.8	55	40
Dhofar 378-3	Enriched	68.6	50	70
LAR 06319-1	Enriched	53.8	55	15
LAR 06319-2	Enriched	53.6	55	20
LAR 06319-3	Enriched	55.6	56	10
LAR 06319-4	Enriched	59.4	55	20
NWA 856-1	Enriched	58.8	53	40

NWA 856-2	Enriched	52.8	56	20
NWA 856-3	Enriched	56.3	56	40
NWA 856-4	Enriched	52.3	55	15
NWA 1068-1	Enriched	62.0	51	25
NWA 1068-2	Enriched	59.8	49	20
NWA 1068-3	Enriched	62.3	51	20
NWA 1068-4	Enriched	58.0	47	4025
NWA 4468-1	Enriched	62.9	53	20
NWA 4468-2	Enriched	71.3	55	20
NWA 4468-3	Enriched	68.0	41	25
NWA 4468-4	Enriched	67.9	54	40
NWA 4468-5	Enriched	64.8	43	30
Zagami-1	Enriched	52.0	48	130
Zagami-2	Enriched	56.8	50	75
Zagami-3	Enriched	57.8	50	75
RBT 04262-1	Enriched	80.6	40	10
RBT 04262-2	Enriched	74.3	55	110
RBT 04262-3	Enriched	75.2	32	30
Shergotty-1	Enriched	54.0	44	55
Shergotty-2	Enriched	58.6	46	55
Shergotty-3	Enriched	47.1	47	85
Shergotty-4	Enriched	40.0	50	20

Table 5.5

Fe^{3+}-Fe^{2+} peak-intensity ratios, An content of plagioclase and distance from the closet mineral of studied HED meteorites.

Sample	Group	Fe^{3+}-Fe^{2+} peak-intensity ratios (%)	An	Distance (μm)
ALH 76005 grain-1	Surface eucrite	25.2	90	40
ALH 76005 grain-2	Surface eucrite	33.3	92	60
ALH 76005 grain-3	Surface eucrite	34.9	92	30
Petersburg grain-1	Surface eucrite	30.9	88	90
Petersburg grain-2	Surface eucrite	40.6	88	240
Petersburg grain-3	Surface eucrite	31.6	88	160
Piplia Kalan grain-1	Surface eucrite	43.4	88	140
Piplia Kalan grain-2	Surface eucrite	31.4	88	5
Padvarninkai grain-1	Surface eucrite	23.0	92	160
Padvarninkai grain-2	Surface eucrite	14.1	92	90
Y-75011 grain-1	Surface eucrite	21.6	90	30
Y-75011 grain-2	Surface eucrite	22.1	90	40
EETA 87520 grain-1	Cumulate eucrite	57.3	95	340
EETA 87520 grain-2	Cumulate eucrite	58.5	95	90
EETA 87520 grain-3	Cumulate eucrite	50.9	95	210
EETA 87520 grain-4	Cumulate eucrite	51.6	95	110
Moore County grain-1	Cumulate eucrite	51.9	92	330
Moore County grain-2	Cumulate eucrite	54.1	92	4430
Moore County grain-3	Cumulate eucrite	49.1	92	310
Moore County grain-4	Cumulate eucrite	55.4	92	230
Y 980433	Cumulate eucrite	69.6	91	860
Y-75032	Diogenite	51.8	90	100

Table 5.6 The average value of the Fe^{3+}-Fe^{2+} peak-intensity ratios of shergottites, standard deviation and number of measurements

Sample	Average of the Fe^{3+}-Fe^{2+} peak-intensity ratios (%)	Standard deviation	Number of measurements
DaG 476	44.0	3.9	4
Dhofar 019	41.3	1.9	4
ALH 77005	21.8	8.3	3
EETA 79001lith.A	46.3	9.0	2
LEW881180	61.6	6.8	3
NWA 5029	38.5	6.2	4
Dhofar 378	61.4	7.0	3
LAR 06319	55.6	2.7	4
NWA 856	55.1	3.1	4
NWA1068	60.5	2.0	4
NWA 4468	67.0	3.2	5
Zagami	55.5	3.1	3
RBT 04262	76.7	3.4	3
Shergotty	49.9	8.1	4

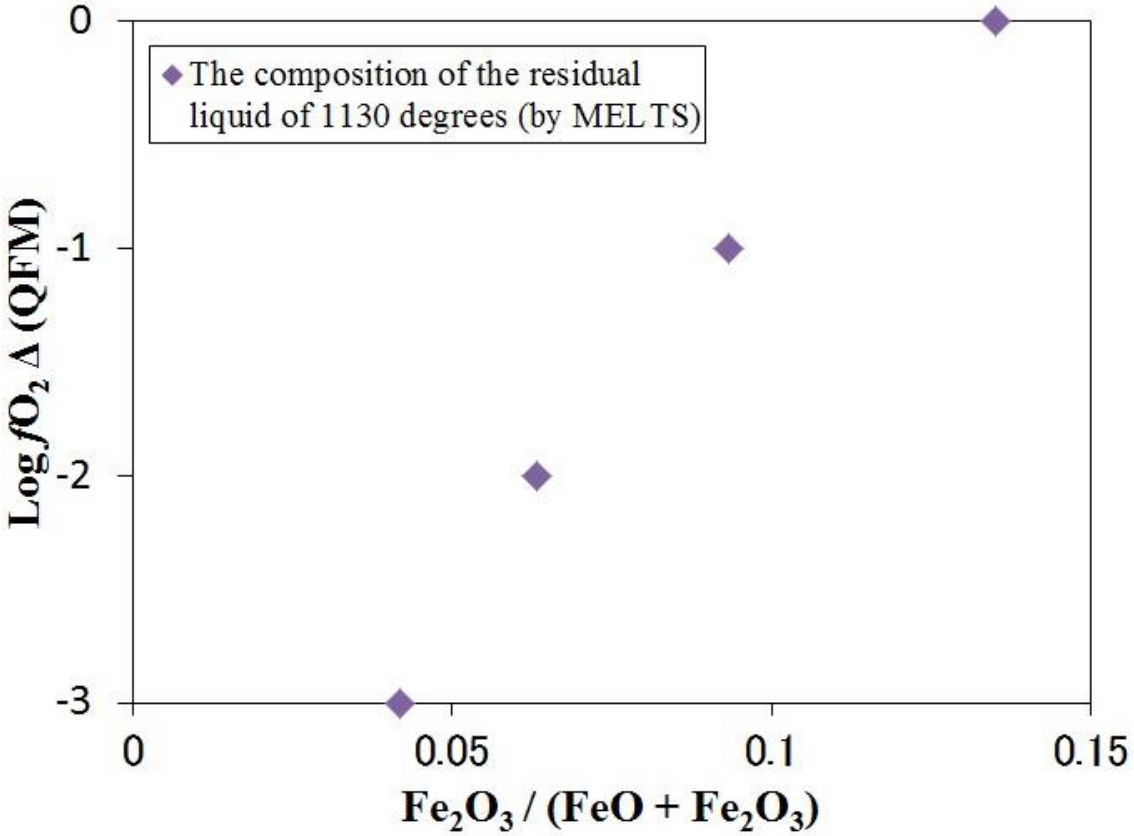

Fig. 5.3 Relationship between ferric/ferrous ratio of residual melt and oxygen fugacity calculated by the MELTS program when plagioclase crystallized. I used the bulk composition of Yamato 980459 for melt composition, because it is reported to represent a parent magma composition of depleted shergottites (Mikouchi and Koizumi 2007).

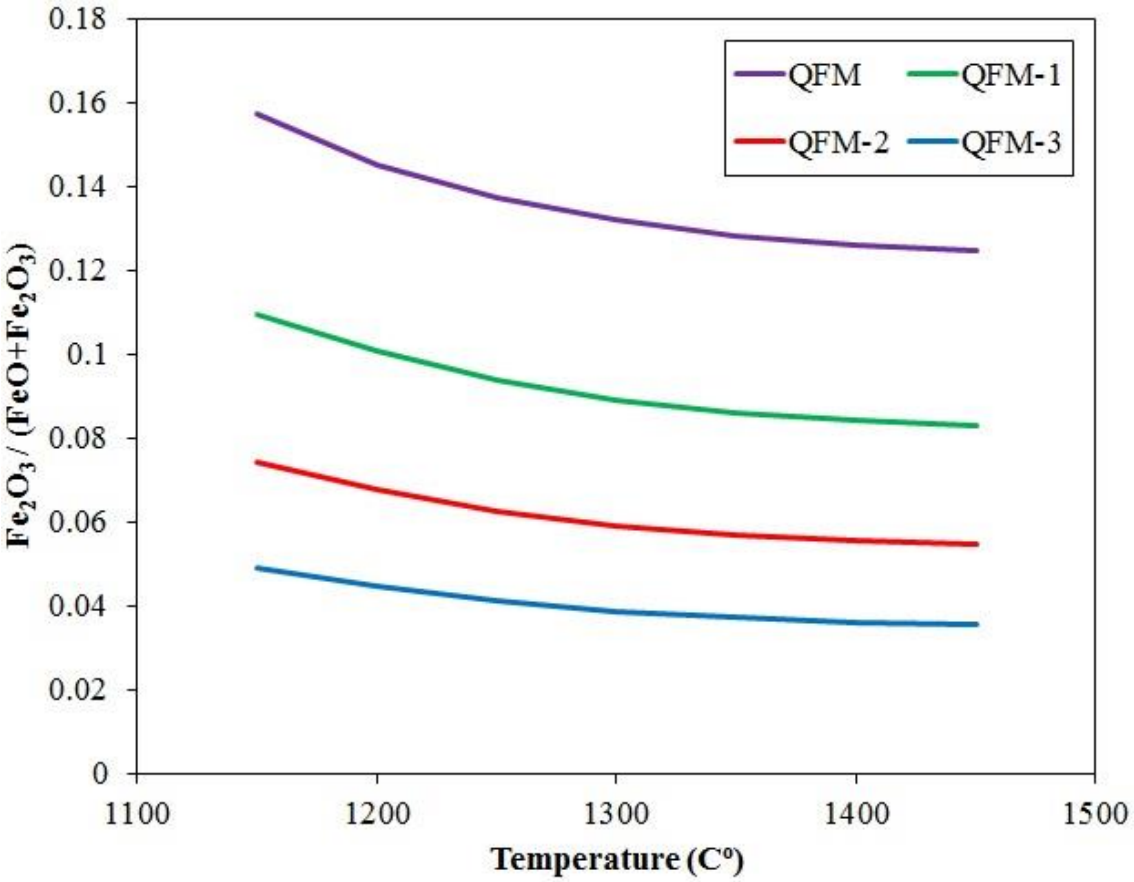

Fig. 5.4 Relationship between ferric/ferrous ratio of residual melt and temperature calculated by the MELTS program when plagioclase crystallizes. I used the bulk composition of Yamato 980459 for the melt composition, because it is reported to represent a parent magma composition of depleted shergottites (Mikouchi and Koizumi 2007).

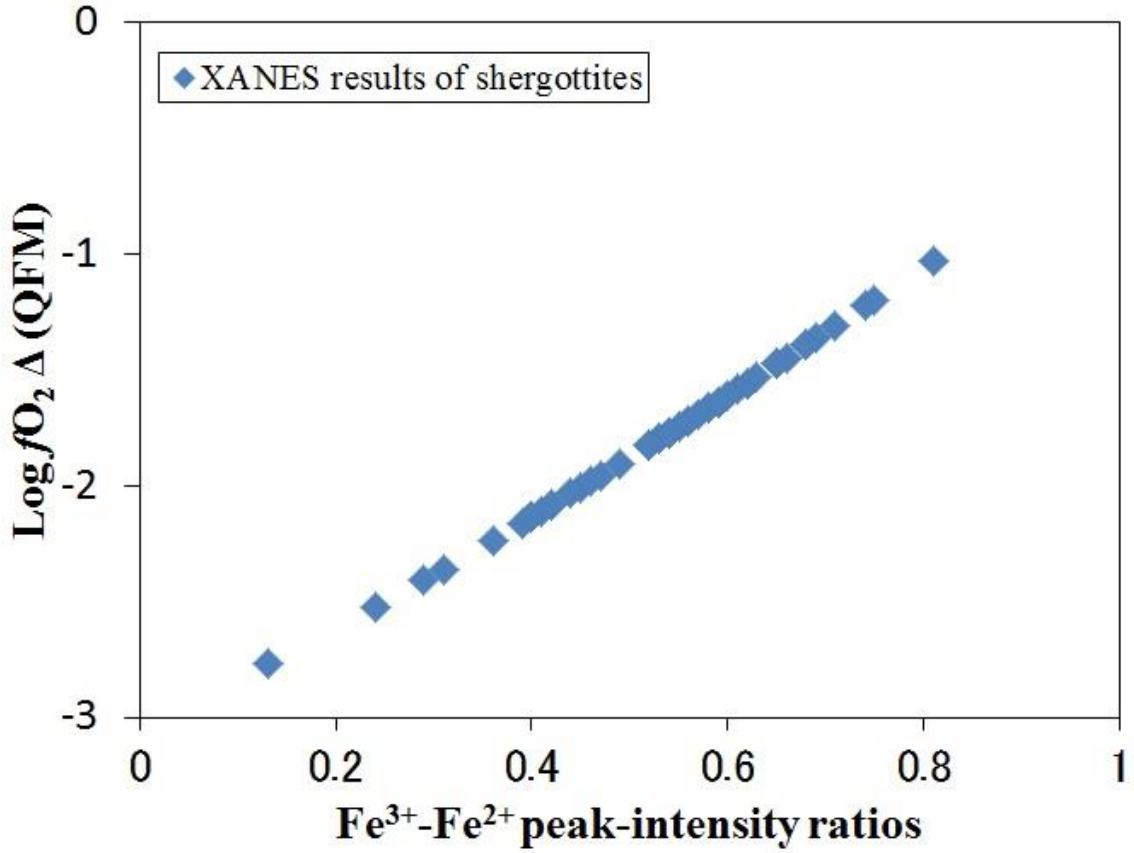

Fig. 5.5 Relationship between the Fe^{3+}-Fe^{2+} peak-intensity ratios and oxygen fugacity calculated by a calibration curve. Oxygen fugacity was calculated by the formula which is written in the section "Redox sate estimated form Fe^{3+}-Fe^{2+} peak-intensity ratios of maskelynite and plagioclase" and obtained data in this study.

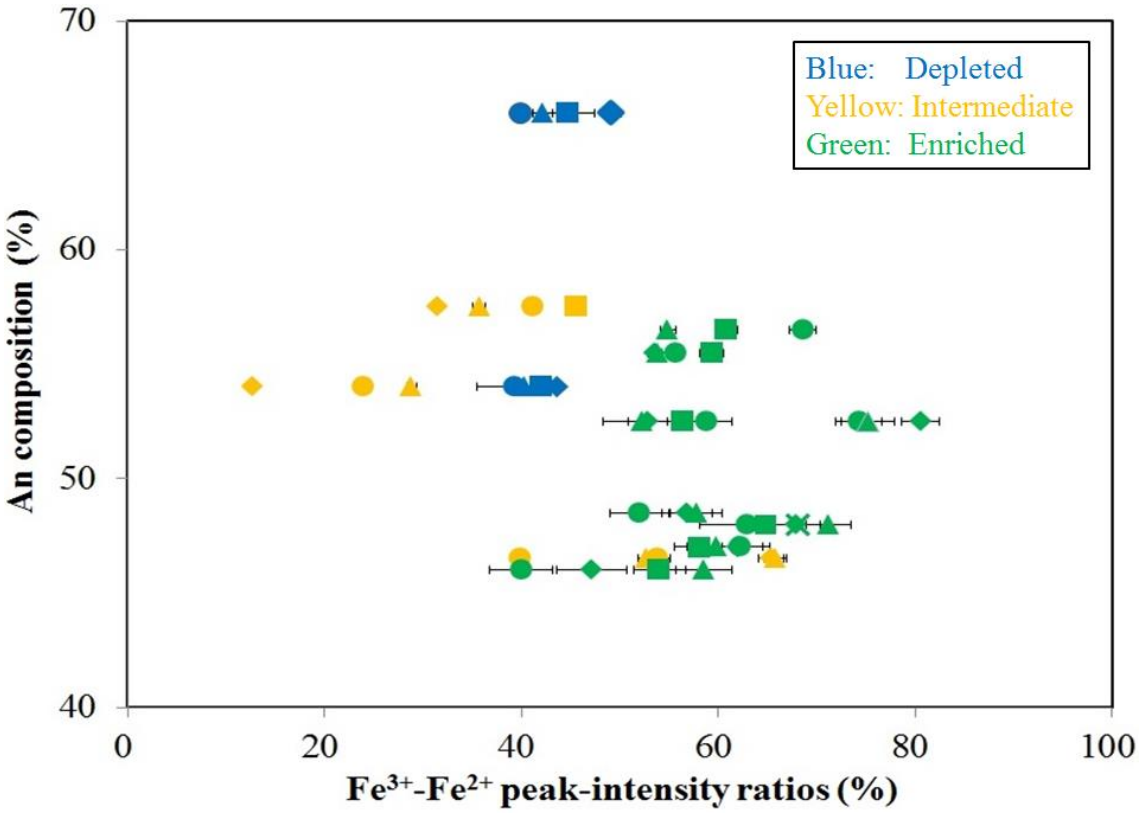

Fig. 5.6 Relation between Fe^{3+}-Fe^{2+} peak-intensity ratios and chemical composition of maskelynite and plagioclase for studied shergottites. Blue, yellow, and green plots represent depleted, intermediate, and enriched shergottites, respectively.

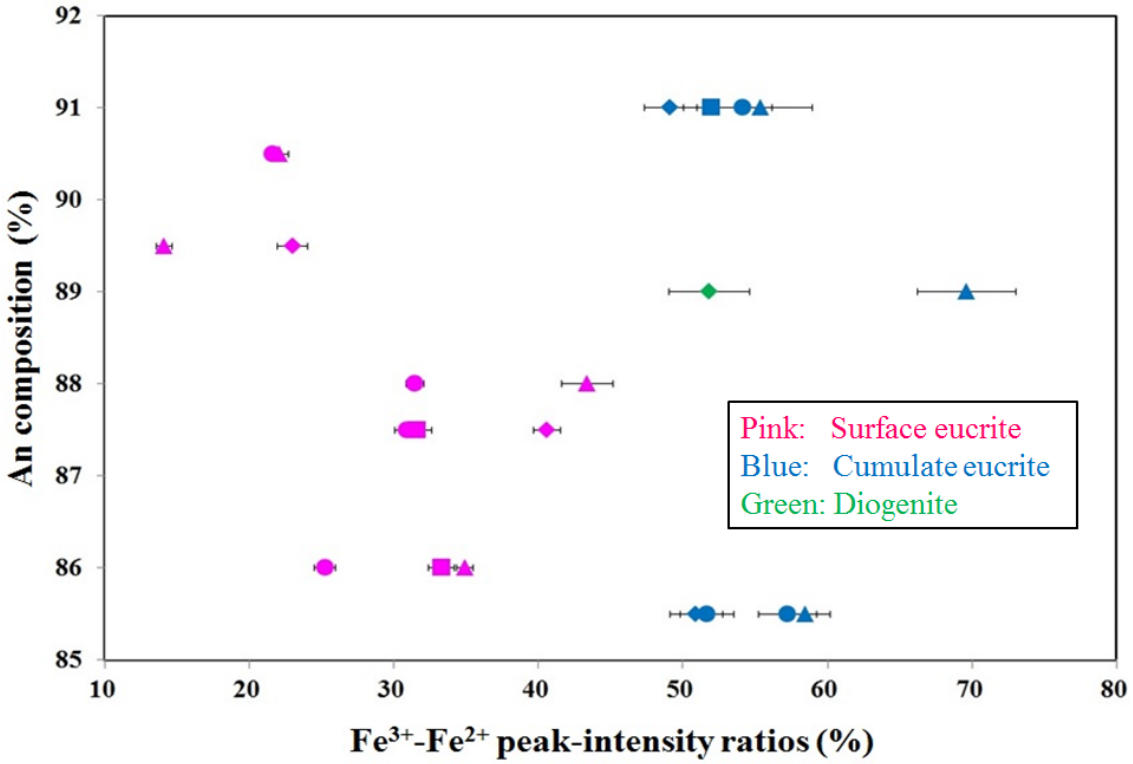

Fig. 5.7 Relation between Fe^{3+}-Fe^{2+} peak-intensity ratios and chemical composition of plagioclase and maskelynite for studied HED meteorites. Pink, blue and green plots represent surface eucrites, cumulate eucrites, and diogenite, respectively.

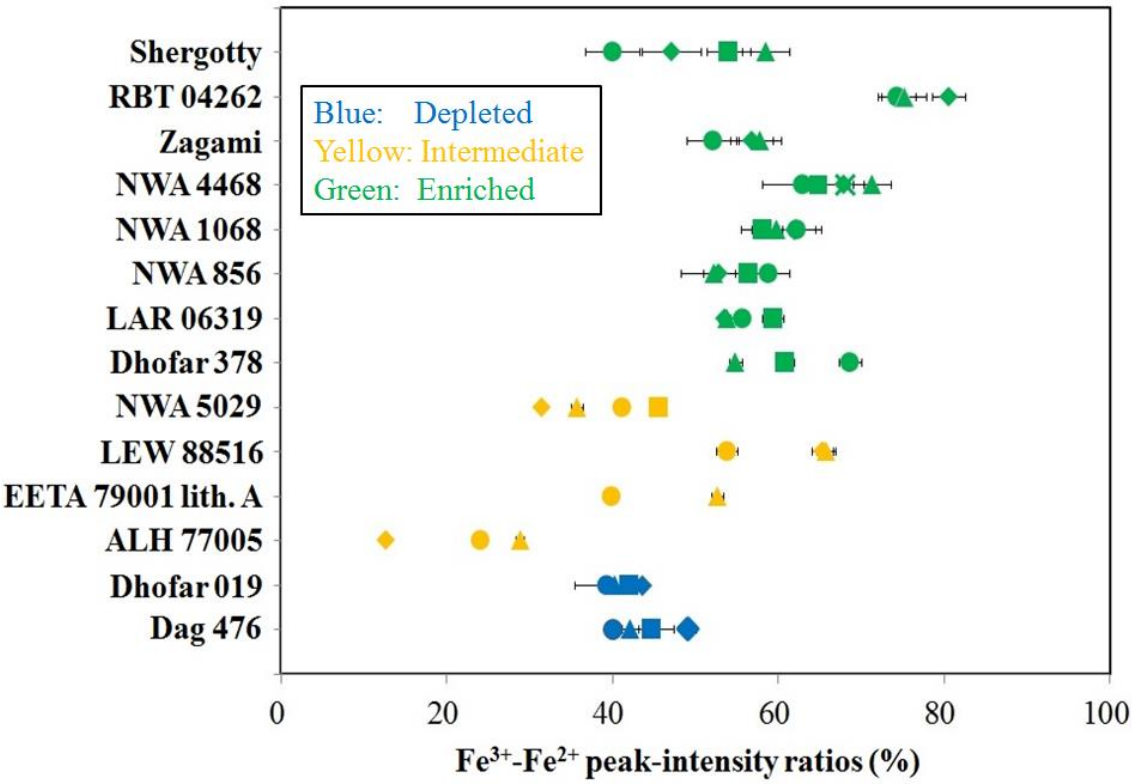

Fig. 5.8 Fe^{3+}-Fe^{2+} peak-intensity ratios of maskelynite and plagioclase for studied shergottites. Blue, yellow, and green plots represent undetermined, depleted, intermediate, and enriched shergottites, respectively.

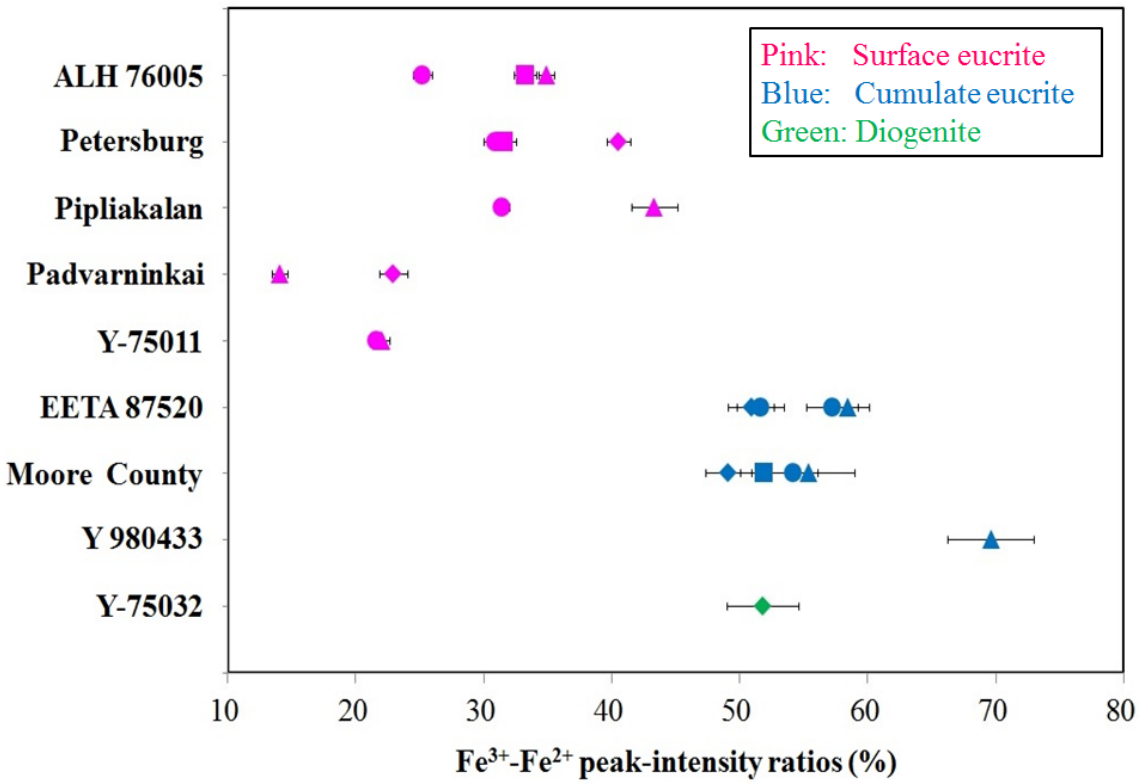

Fig. 5.9 Fe^{3+}-Fe^{2+} peak-intensity ratios of plagioclase and maskelynite from HED meteorites. Pink, blue and green plots represent surface eucrites, cumulate eucrites, and diogenite, respectively.

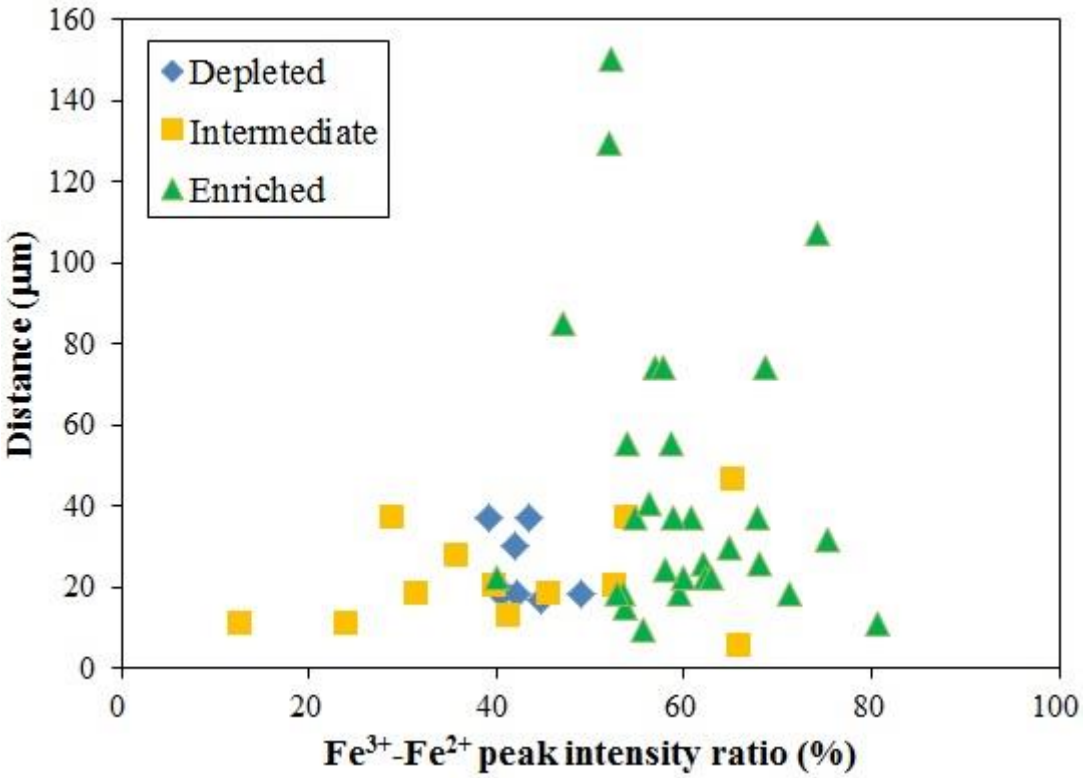

Fig. 5.10 Relationship between the distance from the peripheral minerals for studied shergottites and the Fe^{3+}-Fe^{2+} peak-intensity ratios of maskelynite and plagioclase. Blue, yellow, and green plots represent undetermined, depleted, intermediate, and enriched shergottites, respectively.

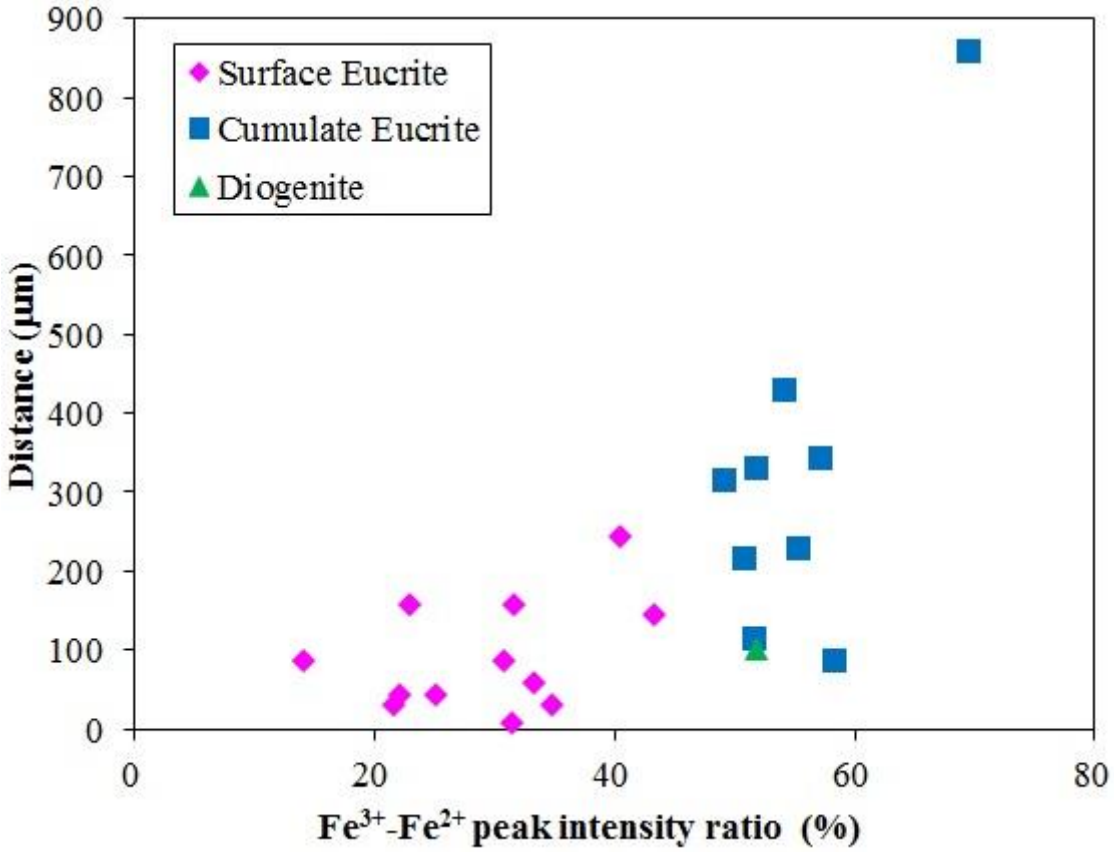

Fig. 5.11 Relationship between the distance from the peripheral minerals for HED meteorites and the Fe^{3+}-Fe^{2+} peak-intensity ratios of plagioclase and maskelynite. Pink, blue and green plots represent surface eucrites, cumulate eucrites, and diogenite, respectively.

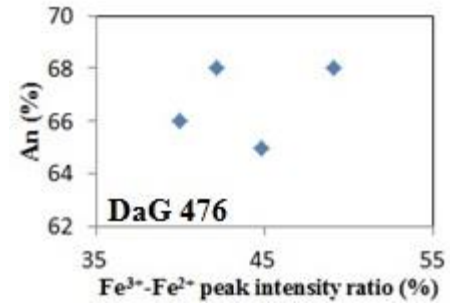
DaG 476
An (%)
Fe3+-Fe2+ peak intensity ratio (%)

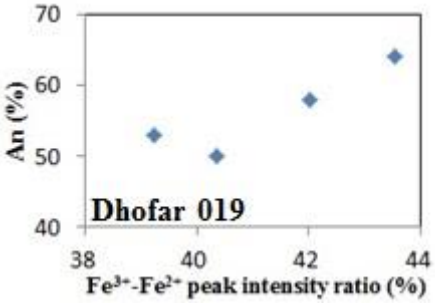
Dhofar 019
An (%)
Fe3+-Fe2+ peak intensity ratio (%)

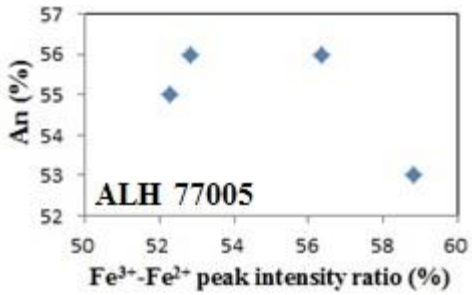
ALH 77005
An (%)
Fe3+-Fe2+ peak intensity ratio (%)

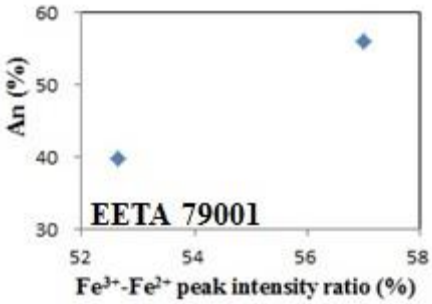
EETA 79001
An (%)
Fe3+-Fe2+ peak intensity ratio (%)

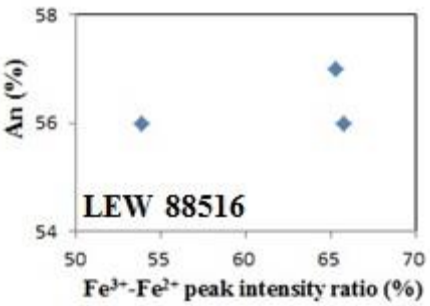
LEW 88516
An (%)
Fe3+-Fe2+ peak intensity ratio (%)

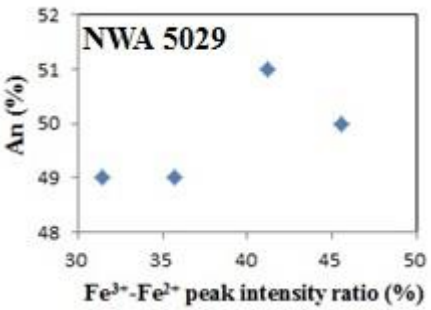
NWA 5029
An (%)
Fe3+-Fe2+ peak intensity ratio (%)

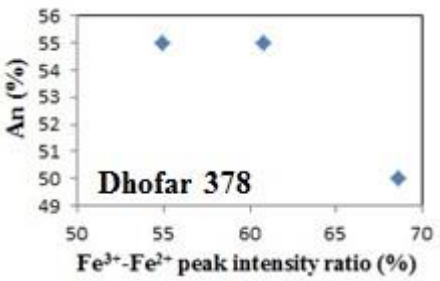
Dhofar 378
An (%)
Fe3+-Fe2+ peak intensity ratio (%)

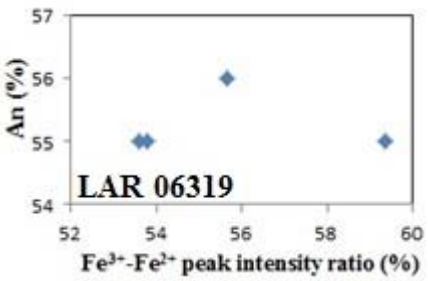
LAR 06319
An (%)
Fe3+-Fe2+ peak intensity ratio (%)

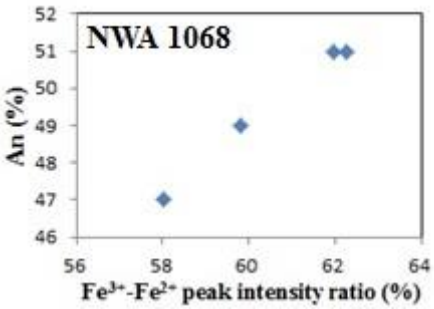
NWA 1068
An (%)
Fe3+-Fe2+ peak intensity ratio (%)

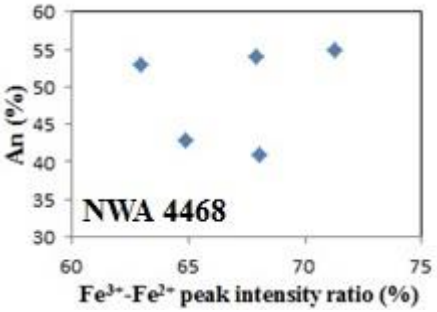
NWA 4468
An (%)
Fe3+-Fe2+ peak intensity ratio (%)

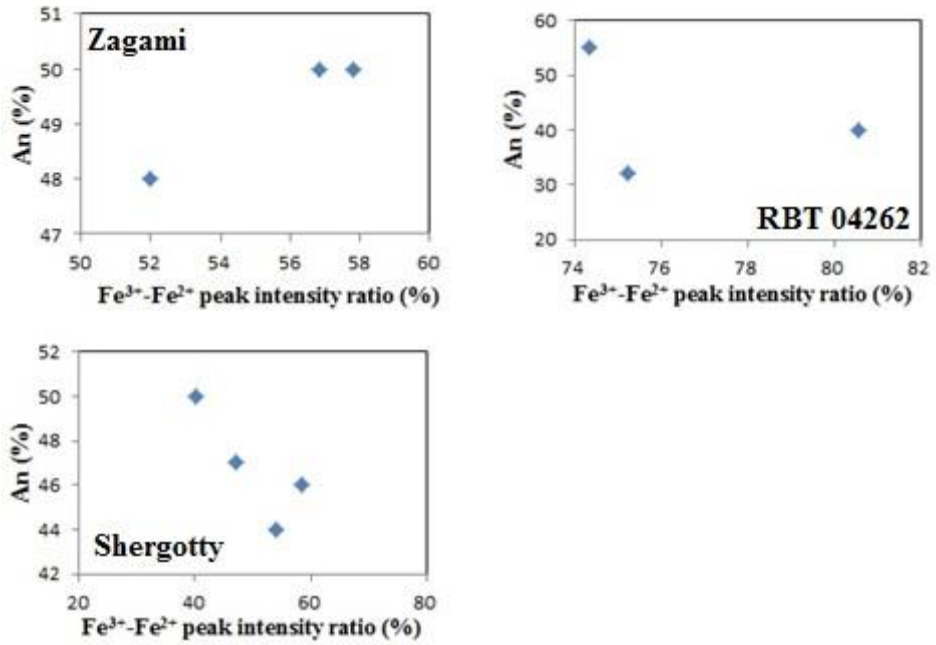

Fig. 5.12 Relation between Fe^{3+}-Fe^{2+} peak-intensity ratios and their anorthite contents in maskelynite and plagioclase for studied shergottites in the same sample.

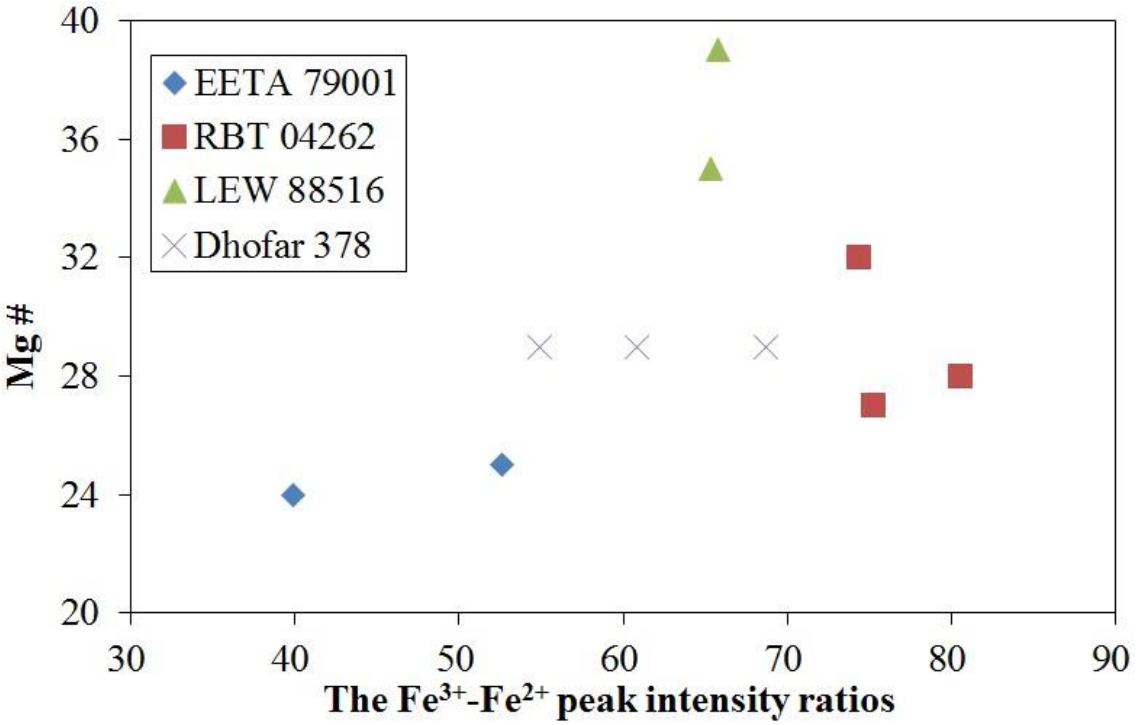

Fig. 5.13 Relation between Fe^{3+}-Fe^{2+} peak-intensity ratios and Mg# (atomic MgO / (MgO + FeO) x 100) of maskelynite and plagioclase for EETA 79001 lithology A, RBT 04262, LEW 88516 and Dhofar 378.

5.5 Fe^{2+}-Fe^{3+} Peak Intensity Ratios of Maskelynite and Plagioclase in Shergottites

The Fe^{3+}-Fe^{2+} peak-intensity ratios for the maskelynite and plagioclase in the analyzed shergottites showed wide ranges from 0.13 to 0.81. Specifically, the Fe^{3+}-Fe^{2+} peak-intensity ratios for the maskelynite and plagioclase in the depleted, intermediate, and enriched shergottites were about 0.39–0.49, 0.13–0.66, and 0.40–0.81, respectively (Table 5.1).

The FeO abundance in the analyzed maskelynite and plagioclase showed some variation ranging from 0.2 to 2.0 wt% (Table 2.1). NWA 1068 and LAR 06139 are reported to show a change in redox state during crystallization (Herd et al. 2006; Peslier et al. 2010; Shearer et al. 2013). To examine this possibility, I analyzed the Fe^{3+}-Fe^{2+} peak-intensity ratios for the core and rim in the same maskelynite grains, which show Fe chemical zoning in LAR 06319, NWA 4468 and ALH 77005 (Fig. 5.14), in order to examine whether there is a difference in the Fe^{3+}-Fe^{2+} peak-intensity ratios for the core and rim. However, I did not find any difference between the Fe^{3+}-Fe^{2+} peak-intensity

ratios for the core and rim of NWA 4468 and LAR 06319 (NWA 4468 core (NWA 4468-4): 0.68, NWA 4468 rim (NWA 4468-3): 0.68, LAR 06319 core (LAR 06319-2): 0.54, and LAR 06319 rim (LAR 06319-3): 0.56) (Table 5.4). The Fe^{3+}-Fe^{2+} peak-intensity ratios for the core and rim of ALH 77005 (ALH 77005 core (ALH 77005-2): 0.29 and ALH 77005 rim (ALH 77005-1):0.13) is slightly different. However, according to the section "What does the Fe^{3+}-Fe^{2+} peak-intensity ratios indicate?", it is not obvious whether this is due to the difference of rim and core, because the standard deviation of ALH 77005 is 0.08 (Table 5.6).

Peslier et al. (2010) reported that fO_2 changed during the crystallization of LAR 06319 because the results obtained using the Ol-Px-Sp and Fe-Ti oxide oxybarometers were clearly different. These two oxybarometers recorded fO_2 at high (~1200 °C) and low (~900 °C) temperatures. Although the plagioclase phase crystallized between these temperatures, the temperature interval might not have been large enough to record a change in the redox state during plagioclase crystallization, suggesting that the redox states of LAR 06319, NWA 4468 and ALH 77005 did not significantly change during plagioclase crystallization.

The Fe^{3+}-Fe^{2+} peak-intensity ratios for the maskelynite in the intermediate shergottites show a very wide range (0.13–0.66), exceeding those obtained for the maskelynite in the depleted and enriched shergottites. In particular, ALH 77005 showed the lowest peak-intensity ratio for maskelynite in all the samples. This result is consistent with those previously obtained using XANES and Mössbauer analysis (Delaney et al. 1998 and Polyak et al. 1999).

Polyak et al. (1999) showed that the $Fe^{3+}/\Sigma Fe$ ratio for maskelynite in ALH 77005 was lower than those for maskelynite in two other intermediate shergottites (EETA 79001 and LEW 88516), although the values of LEW 88516 and EETA 79001 obtained by this study are different those in Polyak et al. (1999) (Fig. 5.15). It is not clear why these values are different because Polyak et al. (1999) did not provide detailed information about the composition, number of samples and the area of the measurement.

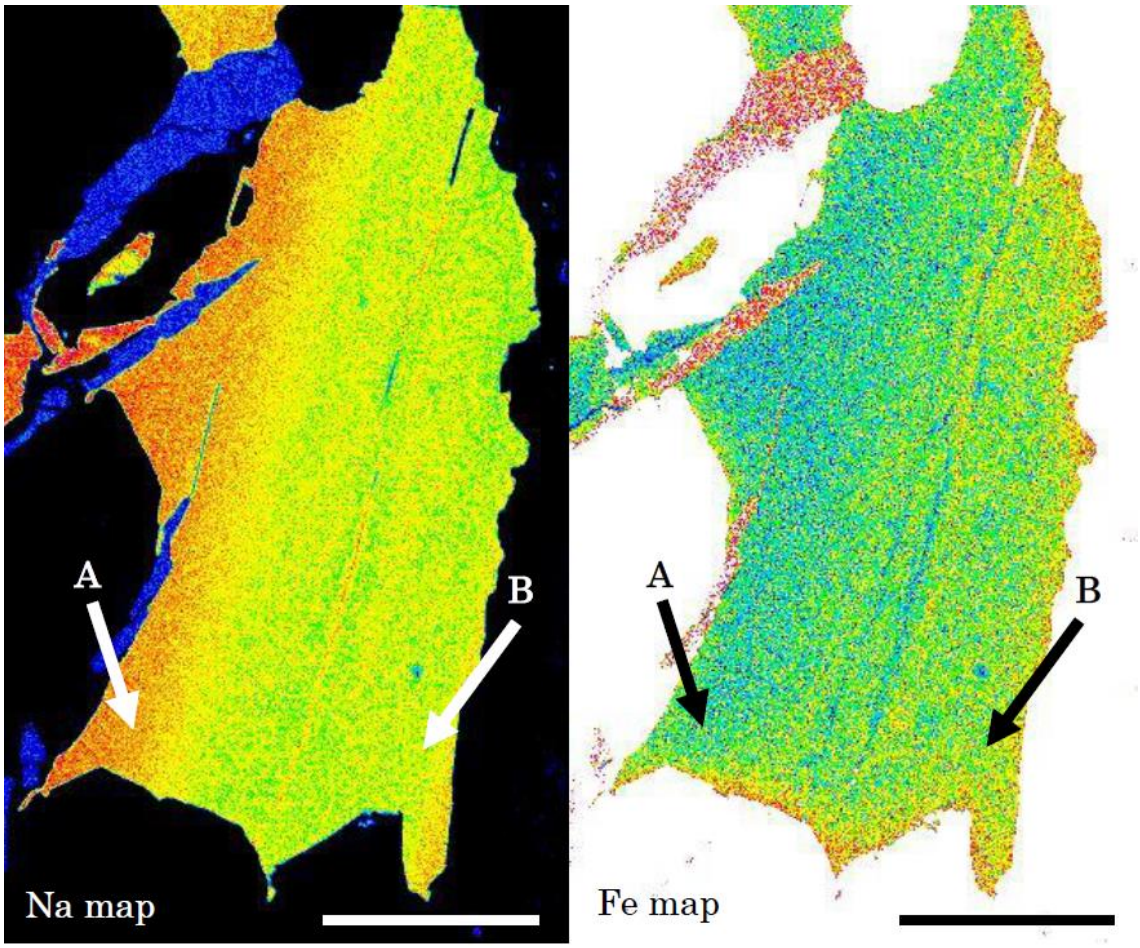

Fig. 5.14 Na and Fe X-ray maps of NWA 4468 maskelynite. Red-to-yellow-colored part (arrow A) shows the area with higher Na and Fe abundance, and blue-colored part (arrow B) shows the area with lower element Na and Fe abundance. A and B arrows shown in these images are analyzed points by SR-XANES. Black and white bars in the lower right corners are scales of 200 μm.

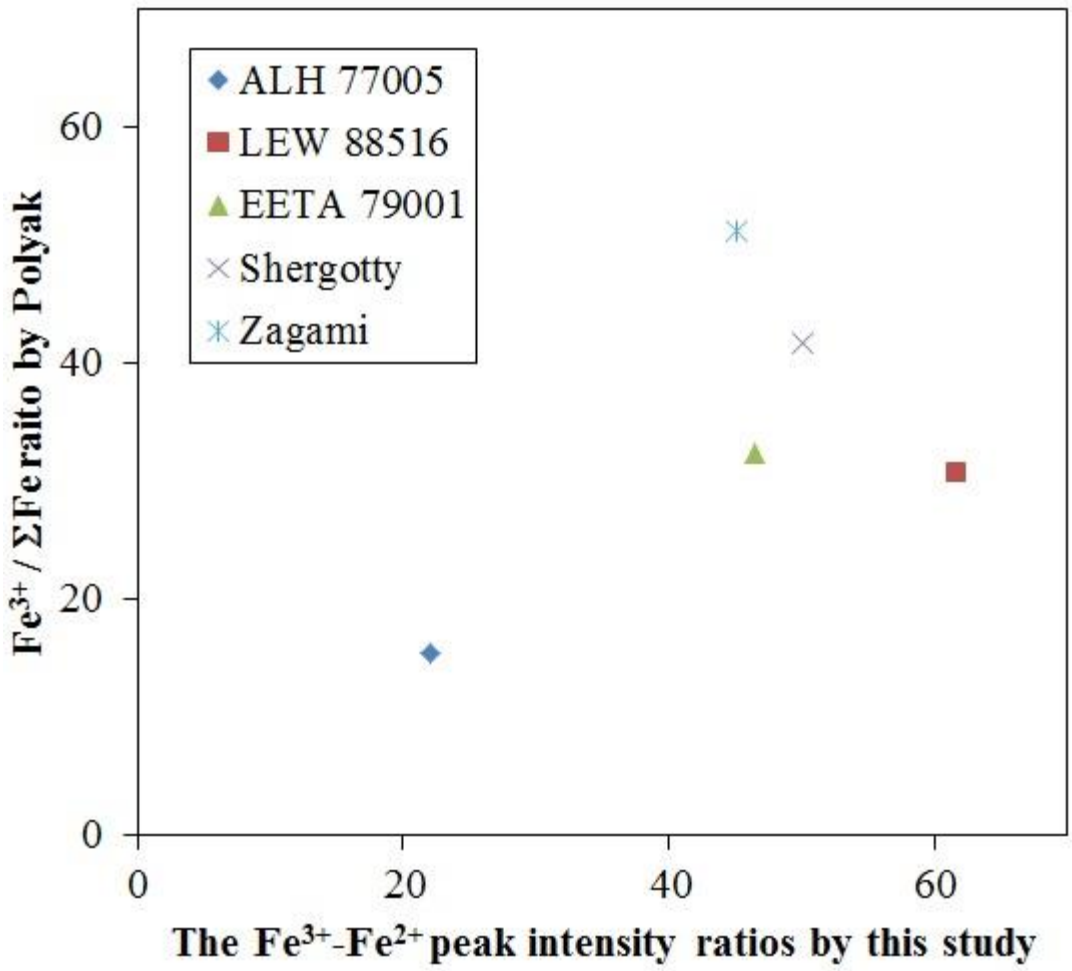

Fig. 5.15 Relation between Fe^{3+}-Fe^{2+} peak-intensity ratios of maskelynite by this study and Polyak et al. (1999).

5.6 Sources for the Shergottites

In this study, I revealed that the Fe^{3+}-Fe^{2+} peak-intensity ratios for maskelynite in intermediate shergottites show a very wide range (0.13–0.66), exceeding the ratios obtained for maskelynite in depleted and enriched shergottites (Table 5.7). Although Herd et al. (2003) reported the oxygen fugacity of ALH 77005, the value is higher than depleted meteorites. Similarly, although Polyak et al. (2001) reported $Fe^{3+}/\Sigma Fe$ ratio of maskelynite in six shergottites, it did not exceed the ratios in depleted and enriched shergottites. Above all, previous studies did not measure many samples by one approach and their discussion is based upon limited data. From this point of view, this study has a much better potential to understand the sources of shergottites because I analyzed fourteen samples by the only one technique.

As I wrote in the section "Mars and Martian meteorites", it is widely known that depleted shergottites crystallized under reduced environment while enriched shergottites crystallized under oxidized environment (Borg and Draper 2003).

However, the analysis of fourteen samples showed that oxygen fugacity has only obscure relationship with light rare earth element abundance (Fig. 5.16) as intermediate shergottites (ALH 77005) show more reducing formation environment than those of two depleted shergottites (Dar al Gani 476 and Dhofar 019).

As I also wrote in the section "Mars and Martian meteorites", there are two models regarding the two geochemical source reservoirs for the shergottites.

I focus on the model that proposes mixing of two distinct mantle reservoirs during melting as stated above (Fig. 1.4) (Symes et al. 2008; Borg and Draper 2003; Treiman et al. 2003). In this models, both geochemical reservoirs resided in the mantle and were formed as a result of either the crystallization of a magma ocean to produce geochemically depleted and enriched domains (Borg and Draper, 2003), or fluid-induced metasomatism to produce mantle heterogeneity (Treiman, 2003).

The εNd for the intermediate shergottites shows an intermediate value between those for the depleted and enriched shergottites (Fig. 5.17). In contrast, the Fe^{3+}-Fe^{2+} peak-intensity ratios for maskelynite in the intermediate shergottites show a wide range. Therefore, the intermediate shergottites could not have been produced through the simple mixing of depleted and enriched mantle reservoirs. In particular, the Fe^{3+}-Fe^{2+} peak-intensity ratios for maskelynite in ALH 77005 and NWA 5029 were lower than those for maskelynite in the depleted shergottites. The wide range of Fe^{3+}-Fe^{2+} peak-intensity ratios obtained for maskelynite in the intermediate and enriched shergottites suggests that a mantle reservoir distinct from the depleted and enriched reservoirs is required for the shergottites to form.

One of the Martian mantle models proposes assimilation of oxidized crust by mantle-derived, reduced magmas (Fig. 1.3) (Herd et al. 2002; Wadhwa et al. 2001). In this model, the assimilated enriched reservoir occurs as domains in the crust, which must be traversed by ascending mantle magmas. The assimilation process of the crust cannot be generated by the reductive mantle source which classified an intermediate group.

There is a concern that the source of intermediate shergottites changed reductively after its initial formation by the mixing of depleted and enriched sources. However, in order to make this process happen, a reducing agent, such as a large amount of carbon must be present in the mantle. This model and the latest model by Papike et al. (2013) are consistent with my result that the Fe^{3+}-Fe^{2+} peak-intensity ratios of enriched

shergottites have a wide range, although the possibility that the presence of the reducing agent is low.

Therefore, I suggest that it is necessary to consider that presence of the reducing intermediate source in either model.

Thus, iron micro-XANES analyses of the maskelynite and plagioclase phases in shergottites is a useful method to compare the redox states of different samples and it can provide useful information about the evolution of the shergottite source.

Table 5.7 Estimated oxygen fugacities (relative to the QFM buffer) and Fe^{3+}-Fe^{2+} peak-intensity ratios for maskelynite and plagioclase. Each Fe^{3+}-Fe^{2+} peak-intensity ratio represents average of data obtained from several areas of each sample and includes previously described statistical error in the section "Micro-XANES Analysis" of the "Methods" chapter. Estimated fO_2 by two oxybarometers (shown as the value relative to the QFM buffer) are from Herd et al. (2001, 2002, and 2006), Goodrich et al. (2003) and Peslier et al. (2010).

Sample	Group	Fe-Ti Oxybarometer	Sp-Ol-Px Oxybarometer	Fe^{3+}-Fe^{2+} peak-intensity ratio (%)
Dar al Gani 476	Depleted	−1.5	−2.3	40.0–49.1
Dhofar 019	Depleted	-	−3.8	39.2–43.5
ALH77 005	Intermediate	-	−2.6	12.7–28.8
EETA 79001 lithology A	Intermediate	−1.7	−2.8	39.9–52.6
LEW 88516	Intermediate	-	-	53.8–65.8
NWA 5029	Intermediate	-	-	31.4–45.6
Dhofar 378	Enriched	-	-	54.9–68.6
LAR 06319	Enriched	0.5	−2.0	53.6–59.4
NWA 856	Enriched	-	-	52.3–58.8
NWA 1068	Enriched	−0.5	−2.5	58.0–62.3
NWA 4468	Enriched	-	-	62.9–71.3
Zagami	Enriched	−1.2	-	52.0–57.8
RBT 04262	Enriched	-	-	74.3–80.6
Shergotty	Enriched	−1.2	-	40.0–58.6

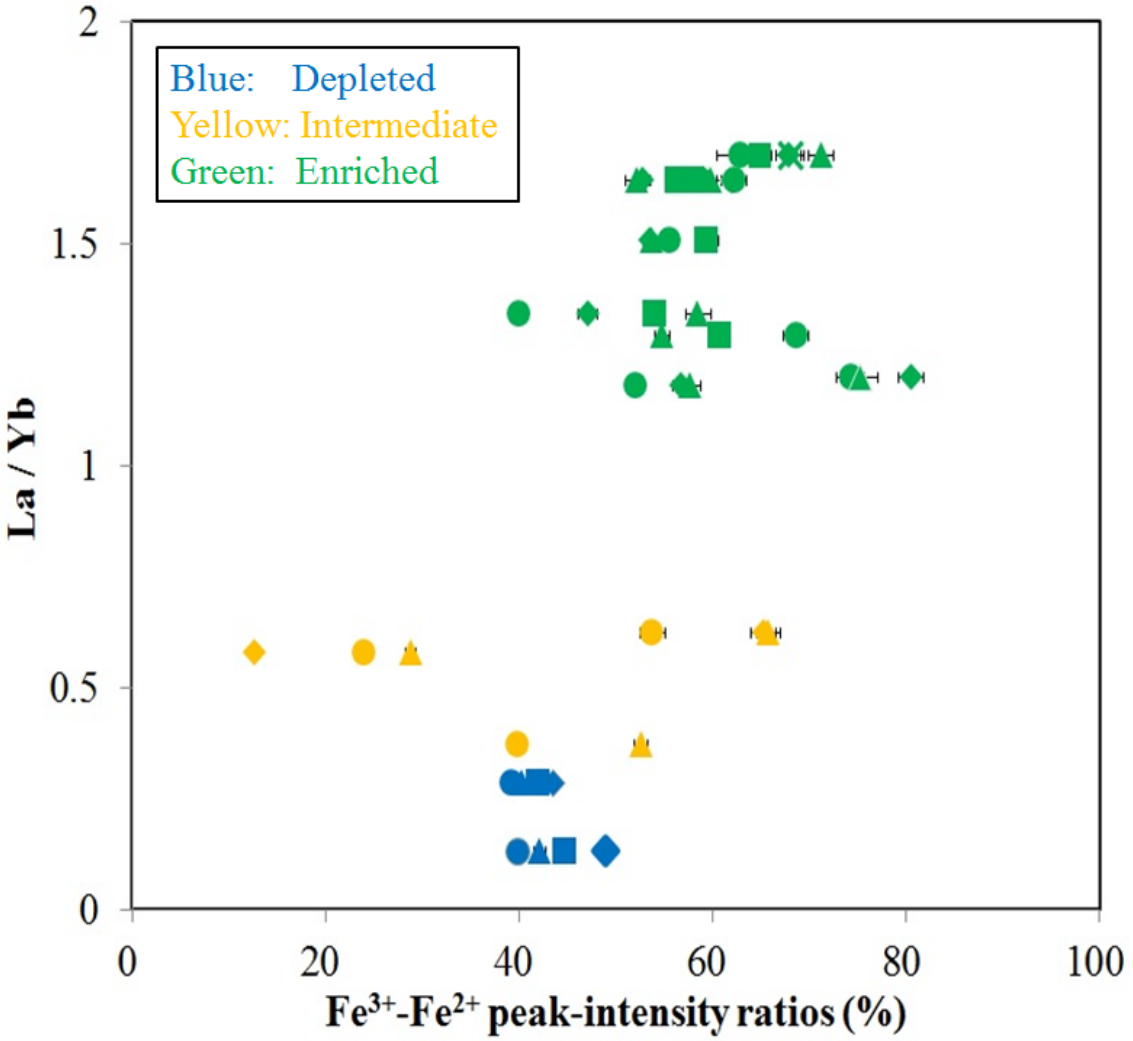

Fig. 5.16 Relation between Fe^{3+}-Fe^{2+} peak-intensity ratios of maskelynite and plagioclase and light rare earth element pattern (La / Yb) reported for studied shergottites. Blue, yellow, and green plots represent depleted, intermediate, and enriched shergottites, respectively.

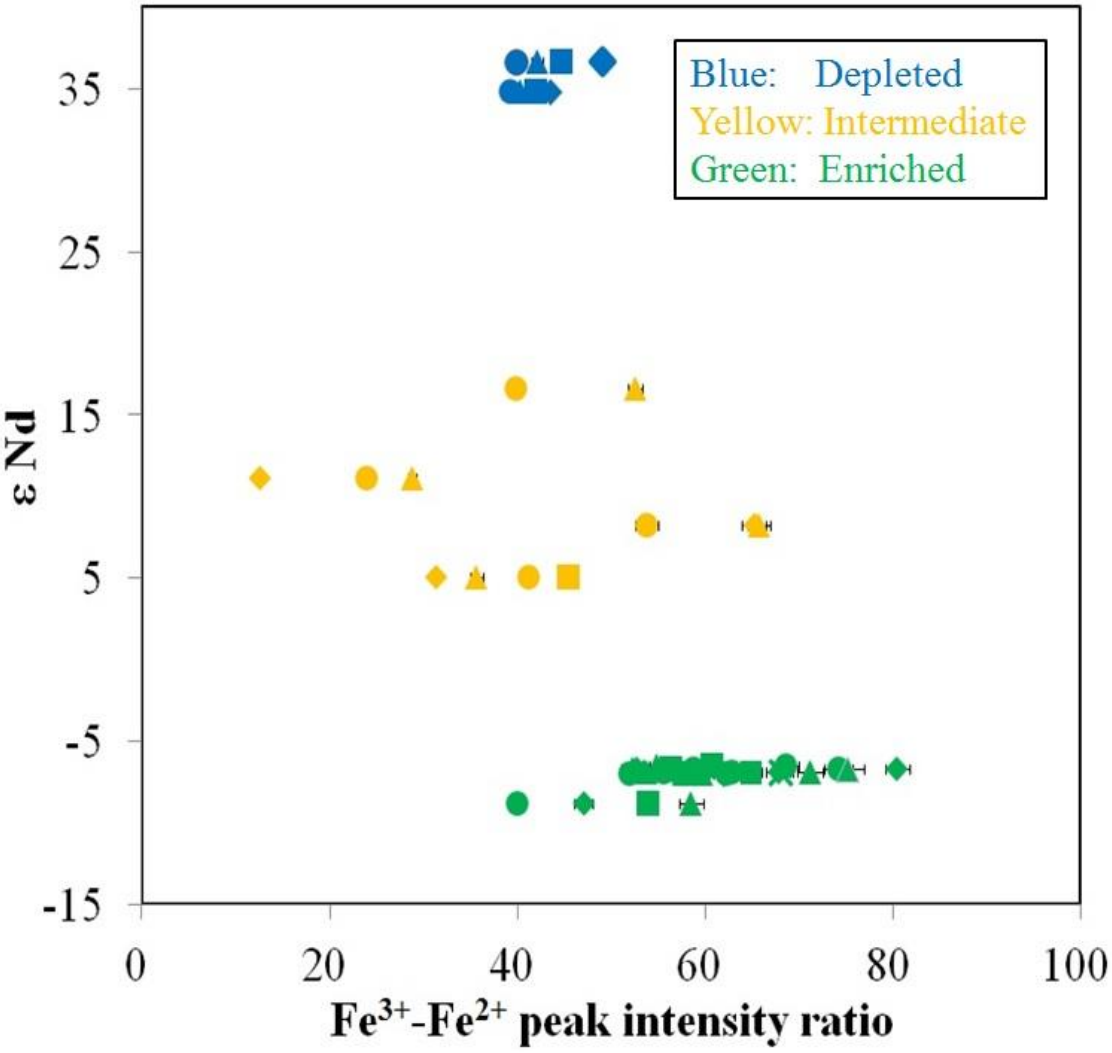

Fig. 5.17 Relation between Fe^{3+}-Fe^{2+} peak-intensity ratios of maskelynite and plagioclase and εNd reported for studied shergottites. Each Fe^{3+}-Fe^{2+} peak-intensity ratio represents average of data obtained from several areas in each sample and includes previously described statistical error in the section "Micro-XANES Analysis" of the "Methods" chapter. Blue, yellow, and green plots represent depleted, intermediate, and enriched shergottites, respectively. εNd are from following references. Dar al Gani 476: Borg et al. (2000), Dhofar 019: Borg et al. (2001), ALH 77005: Borg et al. (2002), LEW 88516: Borg et al. (2002), LAR 06319: Shin et al. (2009), NWA 856: Brandon et al. (2004), NWA 1068: Shih et al. (2003), NWA 4468: Borg et al. (2008), Zagami: Nyquist et al. (1995), RBT 04262: Shih et al. (2009), and Shergotty: Nyquist et al. (2001).

5.7 Redox State of Vesta

The obtained Fe^{3+}-Fe^{2+} peak-intensity ratios of plagioclase and maskelynite in HED meteorites are shown in Fig. 5.9 and it indicates that the Fe^{3+}-Fe^{2+} peak-intensity ratios of surface eucrites are clearly lower than those of cumulate eucrites and diogenite.

Most of HED meteorites have experienced annealing with differing degrees (e.g., Takeda and Graham, 1991), and the iron valence states of plagioclase may have been disturbed by this annealing event(s). Among a lot of HED meteorites, Y-75011 and Y 980433 are known that they have never experienced annealing (Takeda et al. 1997; Takeda et al. 2011). The Fe^{3+}-Fe^{2+} peak-intensity ratio of plagioclase in the Y-75011 surface eucrite is not different from those of other surface eucrites (Padvarninkai, ALH 76005, Piplia Kalan and Petersburg) in its low Fe^{3+}-Fe^{2+} peak-intensity ratio. Similarly, the Fe^{3+}-Fe^{2+} peak-intensity ratio of plagioclase in the Y 980433 cumulate eucrite is similar to those of other cumulate eucrites (EETA 87520 and Moore County). According to these results, it is concluded that the Fe^{3+}-Fe^{2+} peak-intensity ratios of plagioclase from surface and cumulate eucrites have not been affected by later thermal metamorphism and they reflect the redox states of original crystallization environment.

The data of this study showed that the Fe^{3+}-Fe^{2+} peak-intensity ratios of plagioclase in cumulate eucrites are clearly higher than those of surface eucrites (Fig. 5.9). This result implies that the Vesta's deep crust had a global oxidized environment. Thus, this study suggests that there was a heterogeneous redox environment in the Vesta's crust possibly with the depth from the surface, and deep areas were more oxidized than the surface. As the grain size of HED meteorites is partly relevant to crystallization depth, there is a relationship between the Fe^{3+}-Fe^{2+} peak-intensity ratios and grain size (Fig. 5.18)

There may be a possibility that the solar wind lowered the Fe^{3+}-Fe^{2+} peak-intensity ratio of plagioclase in surface eucrites. However, the possibility is low, because all surface eucrites were not exposed on the surface of the Vesta and some samples were located slightly below the surface where there was no affect by the solar wind, but still show low Fe^{3+}-Fe^{2+} peak-intensity ratios. The difference of diffusion coefficient between trivalent and divalent irons may cause difference of the Fe^{3+}-Fe^{2+} peak-intensity ratios between surface and cumulate eucrites and diogenite. However, I consider that this is not likely because the difference of ionic radii of divalent and trivalent irons are not significant (ionic radius of divalent iron is 0.76 Å and trivalent iron is 0.64 Å), implying similar diffusion coefficients. The charge difference between Fe^{2+} and Fe^{3+} may cause the diffusion rate of these two ions, but it is not clear because there are no literature diffusion data for two different iron ions in plagioclase.

One possibility is that the oxidizing environment of Vesta's deep crust was caused by

water in the Vesta's interior. Treiman et al. (2004) reported that Serra de Mage cumulate eucrite contains quartz veins, suggesting the presence of liquid water. I did not analyze Serra de Mage, but Moore County had a very similar cooling history to that of Serra de Mage. Serra de Mage is estimated to have crystallized at 8 km depth, and it is similar to the burial depth of Moore County (Miyamoto et al. 1994). The water is considered as secondary origin as brought by comet (Treiman et al. 2004). However, water may have been present from an early crystallization stage since my XANES study shows significant Fe^{3+} in igneous plagioclase of cumulate eucrites. In either case, there is a relatively more oxidized environment in the deep crust of Vesta.

The other possibility is that the presence of Fe^{3+} is originally related to the formation process of the Vestan crust. As I wrote in the section "HED meteorites", there are two general models for the formation of Vesta. In the residual melt model by Ikeda and Takeda (1985), I considered that the difference of surface and cumulate eucrites is affected by the degassed oxygen during differentiation process. The surface of Vesta temporarily formed a thin layer in early differentiation (Righter et al. 1997). Eventually, oxygen was lost from lava when exposed on the Vesta surface without atmosphere, however, would be retained if it was under pressure in the deep environment. A thin surface layer could prevent oxygen from degassing. The remaining oxygen reacted hydrogen, as a result, water was produced. The melt became oxidized by the reaction which is expressed by the following equation:

$$2FeO + H_2O \Leftrightarrow H_2 + Fe_2O_3$$

Therefore, cumulate eucrites crystallized under oxidized environment. After the cumulate eucrites had cumulated, remelting of the surface and subsequent resolidification formed surface eucrites under more reduced environment.

In the case of the residual partial melt model by Stolper (1977), I considered that it is difficult to have oxidizing environment by this formation process because it is not possible that oxygen remains in the deep crust of Vesta. However, partial melt might become oxidative when parental melts of diogenites have intruded into the eucritic crust (Barrat et al. 2010). At the time, cumulate eucrites become oxidized by water and/or ice as its presence has been suggested by Treiman et al. (2004). A recent model provided by Mandler et al. (2013) suggests the presence of many shallow magma chambers to explain the variation of cumulate eucrites. In this model, it is difficult to have global oxidizing environment for all cumulate eucrites, and from the redox point of view, this model is not able to explain the global oxidizing environment for all cumulate eucrites.

After all, it is not possible to determine which model (partial melting vs. fractional crystallization) is more likely at present and it is not clear whether the difference of surface and cumulate eucrites is due to the formation process, effect of water, or both. However, this study at least reveals Vesta's deep crust shows a global oxidized environment.

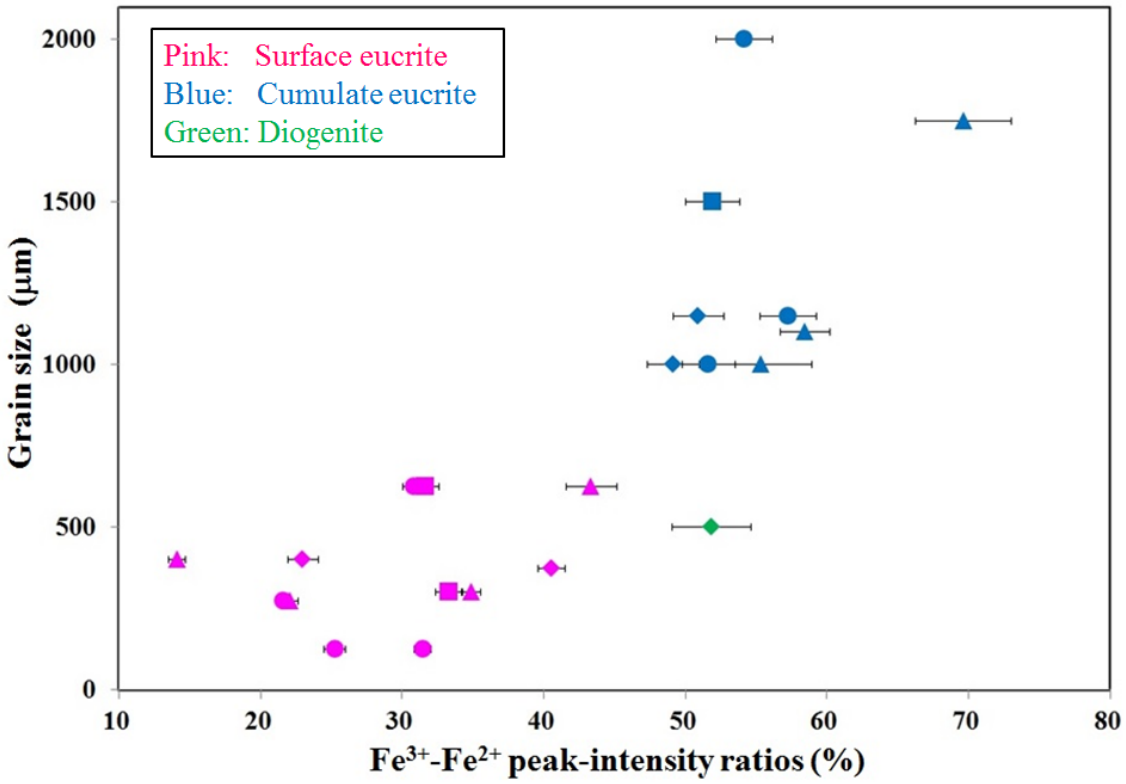

Fig. 5.18 Relation between Fe^{3+}-Fe^{2+} peak-intensity ratios of plagioclase in HED meteorites and grain size. Pink, blue and green plots represent surface eucrites, cumulate eucrites, and diogenite, respectively.

6. Conclusions

Followings are conclusions drawn from this study.

(1) The XANES spectra of pyroxene in depleted and enriched shergottites showed only lower energy peaks and did not have the higher energy peak at pre-edges, suggesting that all iron is present as Fe^{2+}. Although the Fe abundance in pyroxene is much higher than those in plagioclase and maskelynite, pyroxene is not appropriate for estimating relative redox states by using iron valence states. Therefore, it is revealed that pyroxene cannot be used as a potential oxybarometer for Martian meteorites and HED meteorites.

(2) I estimated redox states of various plagioclase samples recovered from shock-loading experiments by XANES analysis. As the result, there is little difference in the Fe^{3+}-Fe^{2+} peak-intensity ratios between unshocked and shocked samples even if the plagioclase is transformed to isotropic glass (maskelynite), suggesting that shock metamorphism little changes Fe^{3+}-Fe^{2+} peak-intensity ratios of plagioclase even shocked up to 40 GPa. It is indicated that the relative redox states of these samples can be estimated from maskelynite and plagioclase using their Fe^{3+}-Fe^{2+} peak intensity ratios as measured by iron micro-XANES analysis.

(3) I created a calibration line relating the Fe^{3+}-Fe^{2+} peak-intensity ratios of plagioclase and oxygen fugacity by applying the result from the crystallization experiment at controlled oxygen fugacities. From the Fe^{3+}-Fe^{2+} peak-intensity ratio obtained, log fO_2 ($\triangle$QFM) is defined by the following equation:

$$\log fO_2\ (\triangle \mathrm{QFM}) = 0.39 \times \exp\ (2.1 \times Fe^{3+}\text{-}Fe^{2+}\ \text{peak-intensity ratio}) - 3 \quad \ldots(a)$$

The estimated redox states of shergottites obtained from the calibration line are between the estimates by Ol-Px-Sp and Fe-Ti oxides oxybarometers. This is consistent with the suggestion that fO_2 changed during the crystallization in parent magma of shergottites. Furthermore, oxygen fugacity of RBT04262 is –1.1 ~ –0.9 and NWA 4468 is –1.5 ~ –1.3, respectively and it is the first report showing that oxygen fugacities of RBT 04262 and NWA 4468. The redox states of HED meteorites obtained from the calibration line showed that HED meteorites were crystallized at log fO_2 = QFM –2.4 to –2.0 at near the surface of Vesta and QFM –1.9 to –1.3 at near the bottom of the Vesta's crust, respectively. This is the first report estimating the oxygen fugacity of Vesta's crust.

(4) I assumed that the Fe^{3+}-Fe^{2+} peak-intensity ratios of maskelynite and plagioclase showed the redox states of magma when plagioclase crystallized. The variation of Fe^{3+}-Fe^{2+} peak-intensity ratios in the same sample is perhaps due to the local heterogeneity of residual liquid.

(5) The Fe^{3+}-Fe^{2+} peak-intensity ratios of the maskelynite and plagioclase in the analyzed shergottites showed a wide range from 0.13 to 0.81. Specifically, the Fe^{3+}-Fe^{2+} peak-intensity ratios for the maskelynite and plagioclase in the depleted, intermediate, and enriched shergottites were about 0.39–0.49, 0.13–0.66, and 0.40–0.81, respectively. This result suggests that oxygen fugacity shows little relationship with light rare earth element abundance.

(6) I revealed for the first time the Fe^{3+}-Fe^{2+} peak-intensity ratios for the maskelynite in the intermediate shergottites show a very wide range (0.13–0.66), exceeding those obtained for the maskelynite in the depleted and enriched shergottites. This result may suggest that a mantle reservoir distinct from the depleted and enriched reservoirs is required to form intermediate shergottites.

(7) The Fe^{3+}-Fe^{2+} peak-intensity ratios of plagioclase and maskelynite in surface eucrites are lower than those of cumulate eucrites and diogenite, suggesting that there was a heterogeneous redox environment in the Vesta's crust and deep areas were more oxidized than the surface. To explain this difference, the model that the surface of Vesta temporarily formed a thin layer in early differentiation and / or the presence of water in the crust is considered.

(8) Iron micro-XANES analyses of the maskelynite and plagioclase phases in Martian and HED meteorite showed that it is a useful method to compare the redox states of extraterrestrial samples whose redox states cannot be estimated using regular oxybarometers such as Fe-Ti oxides and orthopyroxene-olivine-spinel. It is possible to obtain useful information that will be discussed by the result obtained from this method with other oxybarometer such as Fe-Ti oxides and orthopyroxene-olivine-spinel.

7. Acknowledgement

I express very much gratitude to Dr. T. Mikouchi for guidance throughout my thesis, gave me many pieces of helpful advice, valuable discussions, supports and encouragement all through this study. I am also grateful to Prof. M. Miyamoto who supported and encouraged me at every opportunity and gave me many pieces of advice. I express very much gratitude to Prof. A. Iida for his support during the synchrotron-radiation-based micro-XANES analysis performed at The High Energy Accelerator Research Organization. This work was performed under the approval of the Photon Factory Program Advisory Committee (Proposal No. 2010G534). Mr. H. Yoshida kindly supported my analyses when I used the scanning electron microscope and electron microprobe at The Department of Earth and Planetary Science at The University of Tokyo. I also greatly thank Prof. H. Kagi, Dr. P. H. Buchanan, Dr. T. Iizuka, Prof. K. Ozawa, Prof. H. Nagahara and Prof. N. Sugiura for valuable advice.

I also thank Dr. K. Righter, Dr. C. Herd, Dr. L. Nyquist, Prof. A. Tsuchiyama and Prof. H. Kojima for providing samples. I also greatly thank Dr. T. Niihara for much invaluable advice and help. I also thank Yuya Aoyagi for the appropriate help.

Finally, I express my special graduate to my family and Ms. Iseko Kawasaki for many encouragements and supports.

This research was financially supported by a grant from the Global Centers of Excellence (COE) Program, From the Earth to “Earths” from the Ministry of Education, Culture, Sports, Science, and Technology of Japan.

References

Anand, M., James, S., Greenwood, R. C., Johnson, D., Franchi, I. A. and Grady, M. M. (2008) Mineralogy and geochemistry of shergottite RBT 04262 (abstract) *LPSC XXXIX*, #2173.

Asimow, D. P. and Ghiorso, S. M. (1998) Algorithmic modifications extending MELTS to calculate subsolidus phase relations: *Am. Min. 83*, 1127-1132.

Bajt, S., Sutton, S. R., and Delaney, J. S. (1994) X-ray microprobe analysis of iron oxidation sates in silicates and oxides using X-ray absorption near edge structure (XANES): *GCA.* 58, 5209-5214.

Barrat, J. A., Blichert-Toft, J., Nesbitt, R. W. and Keller, F. (2001) Bulk chemistry of Saharan shergottite Dar al Gani 476: *Meteoritics & Planet. Sci.* 36, 23-29.

Barrat, J. A., Yamaguchi, A., Greenwood, C. R., Bohn, M., Cotten, J., Benoit, M. and Franchi, A. I. (2007) The Stannern trend eucrites: Contamination of main group eucritic magma by crustal partial melts: *GCA*, 71: 4108-4124.

Barrat, J. A., Yamaguchi, A., Zanda, B., Bollinger, C. and Bohn, M. (2010) Relative chronology of crust formation on asteroid Vesta: Insights from the geochemistry of diogenites: *GCA*, 74. 6218-6231.

Barrat, J. A., Jambon, A., Bohn, M., Gillet, Ph., Sautter, V., Göpel, C., Lesourd, M. and Keller, F. (2002) Petrology and chemistry of the picritic Shergottite North West Africa 1068 (NWA 1068): *GCA.* 66:3505-3518.

Becker, R. H. and Pepin, R. O. (1984) The case for a Martian origin of the shergottites - Nitrogen and noble gases in EETA 79001: *EPSL*. 69, 225-242.

B´ezos, A. and Humler, E. (2005) The $Fe^{3+}/\Sigma Fe$ ratios of MORB glasses and their implications for mantle melting: *GCA.* 69, 711-725.

Bischoff, A. and Stoeffler, D (1992) Shock metamorphism as a fundamental process in the evolution of planetary bodies: information from meteorites: *EJM*. 4, 707-755.

Bogard, D. D. and Johnson, P. (1983) martian gases in an Antarctic meteorite?: *Science*, 221. 651-654.

Borg, L. E., Nyquist, L. E., Taylor, L. A., Wiesmann, H. and Shih, C. Y. (1997) Constraints on Martian differentiation processes from Rb-Sr and Sm-Nd isotopic analyses of the basaltic shergottite QUE 94201: *GCA.* 61, 4915-4931.

Borg, L. E., Nyquist, L. E., Wisemann, H., Reese, Y. and Papike, J. J. (2000) Sr-Nd isotopic systematic of Martian meteorite DaG 476 (abstract) *LPSC XXXI*, #1036.

Borg, L. E., Nyquist, L. E., Reese, Y., Wisemann, H., Shih, C. Y., Ivanova M., Nazarov, M. and Taylor, L. A. (2001) The age of Dhofar 019 and its relationship to the other

Martian meteorites (abstract) *LPSC XXXII*, #1144.

Borg, L. E., Nyquist, L. E., Wisemann, H., and Y. and Reese, Y. (2002) Constraints on the petrogenesis of Martian meteorites from Rb-Sr and Sm-Nd isotopic systematic of the lherzolitic shergottites ALH 77005 and LEW 88516: *GCA*. 66, 2037-2053.

Borg, L.E. and Draper, D. S. (2003) A petrogenic model for the origin and compositional variation of the Martian basaltic meteorites: *Meteoritics & Planet. Sci*. 38, 1713-1731.

Borg, L. E., Gaffney A. M. and DePaolo, D. (2008) Preliminary age of Martian meteorite Northwest Africa 4468 and its relationship to the other incompatible element-enriched shergottites (abstract) *LPSC XXXIX*, #1851

Brandon, A. D., Draper and D. S. (1996) Constraints on the origin of the oxidation state of mantle overlying subduction zones: an example from Simcoe, Washington, USA: *GCA* 60, 1739-49.

Brandon, A. D., Nyquist, L. E., Shih, C. Y. and Wiesmann, H. (2004) Rb-Sr and Sm-Nd isotope systematic of shergottite NWA 856: crystallization age and implications for alteration of hot desert SNC meteorites (abstract) *LPSC XXXV*, #1931.

Bryndzia, L. T. and Wood, B. J. (1990) Oxygen thermobarometry of abyssal spinel peridotites: the redox state and C-O-H volatile composition of the Earth's suboceanic mantle: *Am. J. Sci.* 290:1093-116.

Buchanan, P. C. and Reid, A. (1996) M.Petrology of the polymic eucrite Petersburg: *GCA*. 60, 135-146.

Canil, D., Virgo, D. and Scarfe, C. M. (1990) Oxidation state of mantle xenoliths from British Columbia, Canada: *Contrib. Mineral. Petrol.* 104:453-62.

Cassidy, W. A. and Rancitelli, L. A. (1982) Antarctic meteorites: *Am. Sci.*70, 156-164.

Cottrell, E., Kelley, K. A., Lanzirotti, A. and Fischer, R. A. (2009) High-precision determination of iron oxidation state in silicate glasses using XANES: *Chemical Geology* 268, 167-179.

Debaille, V., Brandon, A. D., Yin, Q. Z. and Jacobsen, B. (2007) Coupled ^{142}Nd-^{143}Nd evidence for a protracted magma ocean in Mars: *Nature*. 450, 525-528.

Delaney, J. S., Dyar, M. D., Sutton, S. R. and Bajt, S. (1998) Redox ratios with relevant resolution: Solving an old problem by using the synchrotron micro-XANES probe: *Geology* 26, 139-142.

Delaney, J. S., Sutton, S. R. and Dyar, M. D. (1998) Variable oxidation states of iron in Martian meteorites (abstract) *LPSC* XXIX, #1241.

Delaney, J. S., Dyar., M. D., Horz, F., and Johnson., J. R (2003) Evidence for coordination and redox changes of iron shocked feldspar from synchrotoron micro

XANES (abstract) *LPSC XXXIV*, #1417

Dyar, M. D., Delaney, J. S. and Sutton S. R. (2001) Fe XANES spectra of iron-rich micas: *Eur. Jour. Mineral.* 13, 1079-1098.

Dyar, M. D., Gunter, M. E., Delaney, J. S., Lanzarotti, A. and Sutton S. R. (2002) Systematics in the structure and XANES spectra of pyroxene, amphiboles, and micas as derived from oriented single crystals: *Can. Min.* 40, 1375-1393.

Eugster, O., Weigel, A. and Polnau, A. (1996) Two Different Ejection Events for Basaltic Shergottites QUE94201, Zagami and Shergotty (2.6 MA Ago) and Lherzolitic Shergottites LEW88516 and ALH77005 (3.5 MA Ago): *Lunar and Planetary Science 27*, 345.

Folco, L., Franchi, I. A., Scherer, P., Schultz, L. and Pillinger, C. T. (1999) Dar al Gani 489 basaltic shergottite: A new find from the Sahara likely paired with Dar al Gani 476: *Meteoritics & Planet. Sci.* 34, Supplement A36.

Frost, J. D., and McCammon A. C. (2008) The redox state of Earth's mantle: *Annu. Rev. Earth Planet. Sci*, 36, 389-420.

Ghiorso, M. S., and Sack, R.O. (1991) Fe-Ti oxide geothermometry: thermodynamic formulation and the estimation of intensive variables in silicic magmas: *CMP*, 108, 485-510.

Gleason, J. D., Kring, D.A., Hill, D.H. and Boynton, W.V. (1997) Petrography and bulk chemistry of Martian Lherzolite LEW88516: *GCA.* 61, 4007-4014.

Goodrich, C. A., Herd, C. D. K., and Taylor, L. A. (2003) Spinels and oxygen fugacity in olivine-phyric and lherzolitic shergottites: *Meteoritics & Planet. Sci.* 38, 1773-1792.

Graham, A. L., Beva, A. W. R. and Hutchinson, R. (1985) Catalogue of meteorites. With special reference to those represented in the collection of the British Museum (Natural History): *London British Museum*, 4th ed.

Grossman, N. J (1994) The meteoritical bulletin, No. 76, 1994 January: The U.S. antarctic meteorite collection: *Meteoritics*. 29, 100-143.

Hayakawa, S., Gohshi, Y., Iida, A., Aoki, S. and Sato, K. (1991) Fluorescence x-ray absorption fine structure measurements using a synchrotoron radiation x-ray microprobe: *Rev. Sci. Instrum.* 62, 2545-2549.

Herd, C. D. K., Papike, J. J. and Brearley, A.J. (2001) Oxygen fugacity of Martian basalts from electron microprobe oxygen and TEM-EELS analyses of Fe-Ti oxides: *Am. Min.* 86, 1015-1024.

Herd, C. D. K., Borg, L. E., Jones, J. H. and Papike, J. J. (2002) Oxygen fugacity and geochemical variations in the Martian basalts: implications for Martian basalt

petrogenesis and the oxidation state of the upper mantle of Mars: *GCA.* 66, 2025-2036.

Herd, C. D. K. (2003) The oxygen fugacity of olivine-phyric Martian basalts and the components within the mantle and crust of Mars: *Meteoritics & Planet. Sci.* 38, 1793-1805.

Herd, C. D. K. (2006) Insights into the redox history of the NWA 1068/1110 Martian basalt from mineral equilibria and vanadium oxybarometry: *Am. Min.* 91, 1616-1627.

Hewins, H. R. (1984) Intrinsic oxygen fugacities of diogenites and mesosiderite clasts: *GCA.* 48, 1555-1560.

Hofmeister, A. M. and Rossman G.R. (1984) Determination of Fe3+ and Fe2+ concentrations in feldspar by optical absorption and EPR spectroscopy: *Phys. Chem. Mins.* 11, 213-224.

Ikeda, Y. and Takeda, H. (1985) A model for the origin of basaltic achondrites based on the Yamato 7308 howardite: *JGR.*90, C649-C663.

Ikeda, Y. (1994) Petrography and petrology of the ALH-77005 shergottite: *Proc. NIPR Symp. Antarct. Meteorites.* 7th, 9-29.

Ikeda, Y., Takeda, H., Kimura, M. and Suzuki, A. (2002) A new shergottite Oman, Dhofar 378 (abstract) *LPSC XXXIII*, #1434.

Irving, A. J., Kuehner, S., Korotev, R. L. and Hupe, G. M. (2007) Petrology and Bulk Composition of Primitive Enriched Olivine Basaltic Shergottite Northwest Africa 4468 (abstract) *LPSC XXXVIII*, #1526.

Jambon, A., Battat, J. A., Sautter, V., Gillet, Ph., Gopel, C. Javoy, M., Joron, J. L. and Lesourd M. (2002) The basaltic shergottite Northwest Africa 856: Petrology and chemistry: *Meteoritics & Planet. Sci.* 37, 1147-1164.

Jurewicz, Stephen, R. and Jones, J. H. (1994) Preliminary results of sulfide melt/silicate wetting experiments in a partially melted ordinary chondrite: (abstract) *LPSC XXV*, 653-654.

Jurewicz, Stephen, R. and Jones, J. H. (1993) Experimental partitioning of Zr, Ti, and Nb between silicate liquid and a complex noble metal alloy and the partitioning of TI between perovskite and platinum metal: (abstract) *LPSC XXIV*, 741.

Kress, V. C. and Carmichael, I. S. E. (1991) The compressibility of silicate liquids containing Fe2O3 and the effect of composition, temperature, oxygen fugacity and pressure on their redox states: *Contrib. Miner. Petrol.* 108, 82-92.

Laul, J. C. and Smith, M. R. (1986) Chemical systematics of the Shergotty meteorite and the composition of its parent body (Mars): *GCA.* 50:909-926.

Lodders, K. (1998) A survey of shergottite, nakhlite and chassigny meteorites whole-rock compositions: *Meteoritics & Planet. Sci.* 33, A183-A190.

Marti, K., Kim, J. ., Thakur, A. N., McCoy, T. J. and Keil, K. (1995) Signatures of the Martian atmosphere in Glass of the Zagami meteorite: *Science*. 267, 1981-1984.

Masson, B. (1962) *Meteorites*. Wiley.

Mandler, E. B. and Elkins-Tanton, T. L. (2013) The origin of eucrites, diogenites, and olivinediogenites: Magma ocean crystallization and shallow magma chamber processes on Vesta: *Meteoritics & Planet. Sci.* 48, 2333-2349.

McCanta, C. M., Dyar, D. M., Rutherford, J. Malcom. (2004) Iron partitioning between basaltic melts and clinopyroxene as a function of oxygen fugacity: *Am. Min.* 89, 1685-1693.

McCarthy, T. S., Erlank, A. J. and Willis, J. P. (1973) On the origin of eucrites and diogenite: *EPSL*. 18, 433-442.

McCord, B., Adams, B. J. and Johnson, T. V. (1970) Asteroid Vesta: Spectral Reflectivity and Compositional Implications: *Science*. 168, 1445-1447.

McCoy,T. J and Lofgren G. E. (1999) Crystallization of the Zagami shergottite: an experimental study: *EPSL*. 173, 397-411.

McKay, G., Le, L., Wagstaff, J. and Crozaz, G. (1994) Experimental partitioning of rare earth elements and strontium: Constraints on petrogenesis and redox conditions during crystallization of Antarctic angrite Lewis Cliff 86010: *GCA*. 58, 2911-2919.

McSween, H. Y. and Stoffler, D. (1980) Shock Metamorphic Features in Allan Hills 77005 Meteorite: (abstract) *LPSC XI*, 717-719.

McSween, H. Y. (2002) The rocks of Mars, from far and near: *Meteoritics & Planet. Sci.* 37, 7-25.

McInnes, B. I. A., Gregoire, M., Binns, R. A., Herzig P.M. and Hannington, M. D (2001) Hydrous metasomatism of oceanic subarc mantle, Lihir, Papua New Guinea: petrology and geochemistry of fluid-metasomatised mantle wedge xenoliths: *EPSL*. 188, 169-83.

Mikouchi, T. and Miyamoto, M. (1997) Major and minor element distributions in pyroxene and maskelynite from martian meteorite Y-793605 and other lherzolitic shergottites: Clues to their crystallization histories: *Proc. NIPR Symp. Antarct. Meteorites.* 22nd, 109-112.

Mikouchi, T., Miyamoto, M., and McKay, G. (1999) The role of undercooling in producing igneous zoning trends in pyroxenes and maskelynites among basaltic Martian meteorites: *EPSL*. 173, 235-256.

Mikouchi, T., Miyamoto, M. and Mckay, G. (2001) Mineralogy and petrology of the Dar al Gani 476 martian meteorite: Implications for its cooling history and relationship to other shergottites: *Meteoritics & Planet. Sci*. 36, 531-548.

Mikouchi, T. and Miyamoto, M. (2001) Dhofar 019 Shergottite: Mineralogy and Petrology of a New Member of the Basaltic Martian Meteorites (abstract) *LPSC XXXII*, #1644.

Mikouchi, T., Miyamoto, M., Koizumi, E., Monkawa, A. and McKay, G. (2002) Maskelynite recrystallization: Implication for shock and reheating histories of several achondrites: *Meteoritics & Planet. Sci.* 37, Supplement A100.

Mikouchi, T., McKay, G. and Koizumi, E. (2006) Post-shock cooling history of Dhofar 378 shergottite (abstract) *LPSC XXXXI*, #5289.

Mikouchi, T. and Koizumi, E. (2007) Theoretical crystallization of a reduced shergottite: Applying MELTS to Y980459: *Meteoritics & Planet. Sci.* 42, 5294.

Mikouchi, T., Kurihara, T. and Miyamoto M (2008) Petrology and Mineralogy of RBT 04262: Implications for Stratigraphy of the Lherzolitic Shergottite Igneous Block (abstract) *LPSC XXXIX*, #2403.

Mikouchi, T. and Barrat, A. (2009) NWA 5029 basaltic shergottite: A clone of NWA 480 / 1460?: *Meteoritics & Planet. Sci.* 41, Supplement, A143.

Miyamoto, M. and Takeda, H. (1977) Evaluation of a crust model of achondrites from the width of exsolved pyroxenes and their pyroxene crystallization trend: *Meteoritics.*12, 312.

Miyamoto, M, Takeda, H., Yanai, K. and Haramura, M (1979) Mineralogical examination of the Allan Hills no. Meteorite: *Proc. NIPR Symp. Antarct. Meteorites.* 3rd, 59-71.

Miyamoto, M. and Mikouchi, T. (1996) Platinum catalytic effect on oxygen fugacity of $CO_2 \cdot H_2$ gas mixtures measured with ZrO_2 oxygen sensor at 105 Pa from 1300 to 700^{o}C: *GCA.*60, 2917-2920.

Miyamoto, M. and Takeda, H. (1994) Evidence for excavation of deep crustal material of a Vesta-like body from Ca compositional gradients in pyroxene: *EPSL.*122, 343-350.

Monkawa, A., Mikouchi, T., Koizumi, E., Sugiyama, K., and Miyamoto M. (2006) Determination of the Fe oxidation state of the Chassigny kaersutite: A micro XANES spectroscopic study: *Meteoritics & Planet. Sci.* 41, 1321-1329.

Neal, C. R., Taylor, L. A., Ely, J. C., Jain, J. C. and Nazarov, M. A. (2001) Detailed Geochemistry of New Shergottite, Dhofar 019 (abstract) *LPSC XXXII*, #1671.

Nyquist, L.E., Bogard, D. D., Bansal, B., Wisemann, H. and Shin, C.Y. (1995)

"Martains" young and old: Zagami and ALH 84001 (abstract) *LPSC XXVI*, #1065.

Nyquist, L.E., Bogard, D. D., Shin, C.Y., Greshake A., Stoffler, D., and Eugster, O. (2001) Ages and geologic histories of Martian Meteorites: *Space Sci. Rev.* 96, 105-164.

Ott, U. and Begemann, F. (1985) Are all the "Martian" meteorites from Mars?: *Nature*. 317, 509-512.

Papike, J. J., Burger, P.V., Shearer, C. K. and McCubbin F. M. (2013) Experimental and crystal chemical study of the basalt-eclogite transition in Mars and implications for martian magmatism: *GCA*. 104, 358-376.

Park, D., Bogard, D. D., Mikouchi, T. and McKay, G. A. (2008) Dhofar 378 shergottite: Evidence of early shock melting: *JGR*. 113, E08007, doi:10.1029/2007JE003035.

Parkinson, I. J., Arculus, R. J. and Eggins, S. M. (2003) Peridotite xenoliths from Grenada, Lesser Antilles Island Arc: *Contrib. Miner. Petrol.* 146, 241-62.

Peslier, A. H., Hnatyshin, D., Herd, C.D.K., Walton, E.L., Brandon, A.D., Lapen, T.J., Shafer, J. T. (2010) Crystallization, melt inclusion, and redox history of Martian meteorite: Olivine-phyric shergottite Larkman Nunatak 06319: *GCA.* 74:4543-4576.

Polyak, D. E., Dyar, M. D., Delaney, J. S. and Tegnar, C. (1999) Mineralogical $Fe^{3+}/\Sigma Fe$ measurements as proxies of volatile budgets: V. Crystal chemistry of Fe in plagioclase from four heavenly bodies (abstract) *LPSC* XXX, #1911.

Potts, P. J., Bowles, F. J., Reed, S. J. and Cave R. (1995) *Microprobe techniques in the earth sciences*: Springer.

Pringle, A. E., Savage, S. P., Badro, J., Barrat, J. and Moynier, F. (2013) Redox state during core formation on asteroid 4-Vesta: *EPSL*, 373, 75-82.

Righter, K. and Drake, M. J. (1997) A magma ocean on Vesta: Core formation and petrogenesis of eucrites and diogenites: *Meteoritics & Planet. Sci.* 32, 929-944.

Russel, C. T., Raymond, A. C., Coradini, A., McSween, H. Y., Zuber, M. T., Nathues, A., Sanctis, A. C. D., Jaumann, R., Konopliv, A. S., Preusker, F., Asmar, S. W., Park, R. S., Gaskell, R., Keller, D. E., Mottola, S., Roatsch, T., Scully, J. E. C., Smith, D. E., Tricarico, P., Toplis, M. J., Christensen U. R., Feldman, W. C., Lawrence, D. J., McCoy, T. J., Prettyman, T. H., Reedy, R.C., Sykes, M. E. and Titus, T. N. (2012) Dawn at Vesta: Testing the protoplanetary paradigm: *Science*. 336, 684-686.

Sanctis, A. C. D., Ammannito, E., Caprial, M. T., Tosil, F., Capaccioni, F., Zambon, F., Carrarol, F., Fontel, S., Frigeril, A., Jaumann, R., Magni, G., Marchi, S., McCord, T. B., McFadden, L. A., McSeen, H. Y., Mittlefehldt, D. W., Nathues, A.,

Palombal, E. Pieters, C. M., Raymond, C. A., Russell, C. T., Toplis, M. J. and Turrini, D. (2012) Spectroscopic characterization of mineralogy and its diversity across Vesta: *Science*. 336, 697-700.

Sarbadhikan, A. B., Day, J. M. D., Liu, Y., Rumble, D and Taylor, L. A. (2009) Petrogenesis of olivine-phyric shergottite Larkman Nunatak 06319: Implications for enriched components in Martian basalts: *GCA.* 73:2190-2214.

Satake, W., Mikouchi, T. and Miyamoto, M. (2009) Comparison of redox states between geochemically-intermediate and enriched lherzolitic shergottites (abstract) *LPSC XL*, #1717.

Satake, W., Mikouchi, T., and Miyamoto, M. (2010 a) Iron micro-XANES measurement of maskelynite in shergottites: an update (abstract) *LPSC. XLI*, #1902.

Satake, W., Mikouchi, T., and Miyamoto, M. (2010 b) Petrogenetic relationship of geochemically-enriched shergottites as inferred from MELTS calculation (abstract): *Antarct Meteorites XXXIII*, 68-69.

Satake, W., Mikouchi, T., and Miyamoto, M. (2011) Redox states of geochemically-enriched shergottites as inferred from Fe Micro-XANES of maskelynite and plagioclase (abstract): *Antarct Meteorites XXXIV*, 76-77.

Schreiber, D. H., Merkel, C. R., Schreiber, L. V. and Balazs, B. G. (1987) Mutual interactions of redox couples via electron exchange in silicate melts: models for geochemical melt systems: *JGR*, 92. 9233-9245.

Shearer, K. C., Aaron, M. P., Burger, V. P., Guan, Y., Bell, S. A. and Papike, J. J. (2013) Petrogenetic linkages among fO_2 isotopic enrichments-depletions and crystallization history in Martian basalts. Evidence from the distribution of phosphorus in olivine megacrysts: *GCA*. 120, 17-38.

Shih, C.Y., Wooden, J. L., Bansal, B. M., Wiesmann, H., Nyquist, L. E., Bogard, D. D. and McKay, G. A. (1982) Chronology and petrogenesis of young achondrites, Shergotty, Zagami, and ALHA77005 - Late magmatism on a geologically active planet*: GCA.* 46, 2323-2344.

Shih, C.Y., Nyquist, L. A., Wiesmann, H., and Barrat, J. A. (2003) Age and petrogenesis of picritic shergottite NWA1068: Sm-Nd and Rb-Sr Isotopic studies (abstract): *LPSC* XXXIX, #1439.

Shih, C.Y., Nyquist, L. A. and Reese, Y. (2009) Rb-Sr and Sm-Nd studies of olivine-pyric Shergottites RBT04262 and LAR06319: Isotopic evidence for relationship to enriched basaltic Shergottites (abstract). *LPSC XL*, #1360.

Shukla, A. D., Shukla, P. N,. Suthar, K. M., Bhandari, N, Vaya, V. K, Sisodia, M.S., Sinha, R. S., Rao, K. N. and Rajawat, R. S. (1997) Piplia Kalan eucrite : Fall,

petrography and chemical characterization: *Meteoritics*. 32, 611-615.

Smith, J. V. and Hervig, R. L. (1979) Shergotty Meteorite: Mineralogy, Petrography and Minor Elements: *Meteoritics*. 14, 121.

Smith, M. R., Laul, J. C., Ma, M. S., Huston, T., Verkoutern, R. M. Lipschutz, M.E and Schmitt, R. A. (1984) Petrogenesis of the SNC (shergottites, nakhlites, chassignites) meteorites: implication for their origin from a large dynamic planet, possibly Mars: *JGR*. 89, B612-B630.

Spray, J. G. and Boonsue, S (2011) Shock-induced melt pocket formation in NWA 4468: Evidence for phase transformation-induced implosion: *74th Annual Meeting of the Meteoritical Society*, Supplement, id 5201.

Steele, I. M and Smith, J, V (1982) Petrography and mineralogy of two basalts and olivine-pyroxene-spinel fragments in achondrite EETA79001 (abstract) *LPSC XIII*, A375-A384.

Stolper, E. (1977) Experimental petrology of eucritic meteorites: *GCA*. 41, 587-611.

Stolper, E. and McSween, H. Y. (1979) Petrology and origin of the shergottite meteorites: *GCA*. 43, 1475-1477, 1479-1483, 1485-1498.

Stolper, D., Ostertag, R., Jammes, C., Pfannschmidt, G., SenGupta, P. R., Simon, S. B., Papike, J. J. and Beauchamp, R. H. (1986) Shock metamorphism and petrography of the Shergotty achondrite (abstract): *LPSC XVI*, 889-903.

Symes, S. J. K., Borg, L. E., Shearer, C. K. and Irving, A. J. (2008) The age of the Martian meteorite Northwest Africa 1195 and the differentiation history of the shergottites: *GCA*. 69, 17-38.

Takeda, H. and Yanai, K. (1982) Mineralogical examination of the Yamato-79 achodrites polymict eucrites and ureilites: *Proc. NIPR Symp. Antarct. Meteorites*. 7th, 97-123.

Takeda, H. and Mori, H. (1985) The diogenite-eucrite links and the crystallization history of a crust of their parent body: *JGR*. 90, C636-C648.

Takeda, H. and Graham, A. L. (1991) Degree of equilibration of eucritic pyroxenes and thermal metamorphism of the earliest planetary crust: *Meteoritics*, 26. 129-134.

Takeda, H. (1997) Mineralogical records of early planetary processes on the howardite, eucrite, diogenite parent body with reference to Vesta: *EPSL*. 219, 189-199.

Takeda, H., Miyamoto, M., Duke, M. and Ishii, T. (1978) Crystallization of pyroxene in lunar KREEP basalt 15386 and meteoritic basalts: *Proc. 9th Lunar Planet Sci. Conf.*, 1157-1171.

Takeda, H., Yamaguchi, A., Hiroi, T., Nyzuist, L. E., Shih, C.Y., Ohtake, M., Karouji, Y. and Kobayashi, S. (2011) Comparisons of mineralogy between cumulate

eucrites and lunar meteorites possibly from the farside anorthositic crust (abstract) *LPSC XXXXII*, #1632.

Taylor, L. A., Nazarov, M. A., Shearer, C. K., McSween Jr., H. Y., Cahill, J., Neal, C. R., Ivanova, M. A., Barsukova, L. D., Lentz, R. C., Clayton, R. N. and Mayeda, T. K. (2002) Martian meteorite Dhofar 019: A new Shergottite: *Meteoritics & Planet. Sci.* 37, 1107-1128.

Treiman, A. H., Lindstrom, D. J. and Martinez, R. R. (1994) The parent magma of xenoliths in shergottite EETA79001: Bulk and trace element composition inferred from magmatic inclusions (abstract) *LPSC XXV*, #1417.

Treiman, A. H. (2003) Chemical compositions of Martian basalts (shergottites): Some inferences on basalt formation, mantle metasomatism, and differentiation in Mars: *Meteoritics & Planet. Sci.* 38, 1849-1864.

Treiman, A. H., Lanzirotti, A and Xirouchakis, D. (2004) Ancient water on asteroid 4 Vesta: evidence from a quartz veinlet in the Serra de Mage eucrite meteorite: *EPSL*. 219, 189-199.

Trinquier, A., Birck, L. J, Allegre, J. C., Gopel, C. and Ulfbeck, D. (2008) ^{53}Mn-^{53}Cr systematics of the early solar system revisited: *GCA*. 72, 5146-5163.

Tuskada A. (1999) Application to shock pressure gauge of meteorite and attenuation of the characteristic X-ray of Na of plagioclase during in electron beam irradiation (in Japanese): Master Thesis, Department of Earth and Space Science, Graduate school of Science, Osaka University.

Usui, T., Sanborn, M., Wadhwa, and M., McSween, H. Y. (2010) Petrology and trace element geochemistry of Robert Massif 04261 and 04262 meteorites, the first examples of geochemically enriched lherzolitic shergottites: *GCA*. 74, 7283-7306.

Wadhwa, M. (2001) Redox state of Mars upper mantle and crust from Eu anomalies in shergottite: *Science*. 291, 1527-1530.

Wadhwa, M. (2008) Redox conditions on small bodies, the Moon and Mars: *Rev. in Min.* 68, 493-510.

Wilke, M, Farges, F., Petit, P. M., Brown, G. E., Jr. and Martin, F. (2001) Oxidation state and coordination of Fe in minerals: An Fe K-XANES spectroscopic study: *Am. Min*. 86, 714-730.

Wilke, M., Partzsch, G. M., Bernhardt, R. and Lattard, D. (2005) Determination of the iron oxidation state in basaltic glasses using XANES at the K-edge: Chemical Geology. 220 143-161.

Wood, B. J. and Virgo, D. (1989) Upper mantle oxidation state: ferric iron contents of Lherzolite spinels by ^{57}Fe M¨ossbauer spectroscopy and resultant oxygen

fugacities: *Geochim. Cosmochim. Acta.* 53:1227–91.

Zipfel, J., Scherer, P., Spettel, B., Dreibus, G. and Schultz, L. (2000) Petrology and chemistry of the new shergottite Dar al Gani 476: *Meteoritics & Planet. Sci.* 35, 95-106.

Yanai, K., Funaki, M., Cassidy, W. A. and Glass, B. P. (1978) Meteorite recoveries in Antarctica during field season 1977-78 *LPSC IX* 977-987.

Appendix

Appendix 1. The information of XANES analysis of Shergottites.

Sample	Fe^{2+} peak (eV)	Fe^{3+} peak (eV)	Fe^{2+} half width (eV)	Fe^{3+} half width (eV)	Count max	The peak value of Fe^{2+}	The peak value of Fe^{3+}	Residual of the fitting※	Baseline (eV)
DaG476-1	7112.45	7113.96	2.13	1.05	8415	0.0136819	0.00910445	0.017	7109.7-7114.87
DaG476-2	7112.34	7113.69	1.75	1.52	20084	0.015161	0.0122891	0.013	7110.25-7114.87
DaG476-3	7112.34	7113.69	1.73	1.56	19517	0.0145197	0.0105979	0.020	7110.25-7114.87
DaG476-4	7112.23	7113.69	1.66	1.60	16949	0.0163967	0.0158128	0.012	7110.36-7114.98
Dhofar 019-1	7112.23	7113.48	1.54	1.34	27013	0.0161002	0.0124104	0.011	7110.36-7114.87
Dhofar 019-2	7112.23	7113.48	1.45	1.22	21443	0.017058	0.0123677	0.019	7110.36-7114.98
Dhofar 019-3	7112.12	7113.25	1.26	1.07	15094	0.00931128	0.00629911	0.011	7110.25-7114.76
Dhofar 019-4	7112.23	7113.61	1.49	1.52	10711	0.0153477	0.00991457	0.007	7110.14-7115.2
ALH 77005-1	7112.01	7113.52	1.84	1.13	39213	0.011234	0.00163056	0.012	7109.81-7114.32
ALH 77005-2	7112.12	7113.56	1.76	1.24	12274	0.0123215	0.00499573	0.004	7110.47-7113.88
ALH 77005-3	7112.12	7113.24	2.02	1.02	17084	0.00749804	0.00236843	0.010	7109.7-7114.43
EETA 79001lith.A-1	7112.01	7113.25	1.35	1.54	23994	0.0126226	0.014028	0.075	7110.58-7115.2
EETA 79001lith.A-2	7112.34	7113.58	1.66	1.54	23853	0.0134412	0.00892208	0.007	7109.92-7115.2
LEW881180-1	7112.23	7113.80	1.63	1.65	17931	0.0134501	0.02586	0.013	7109.92-7115.53

LEW881180-2	7112.12	7113.80	1.51	1.66	15444	0.0141387	0.026646	0.009	7110.47-7115.42
LEW881180-3	7112.01	7113.57	1.73	1.29	8490	0.0139185	0.0162316	0.008	7110.36-7114.98
NWA 5029-1	7112.34	7113.65	1.64	1.21	11187	0.0151817	0.0127128	0.006	7109.81-7114.98
NWA 5029-2	7112.45	7113.89	1.49	1.27	19975	0.016066	0.0112656	0.016	7109.92-7115.09
NWA 5029-3	7112.56	7113.95	1.91	0.94	23986	0.0150387	0.00689622	0.008	7109.81-7114.32
NWA 5029-4	7112.12	7113.64	1.60	1.09	10871	0.0187472	0.0104246	0.016	7110.14-7114.76
Dhofar 378-1	7112.23	7113.75	1.66	1.51	20202	0.0275024	0.0334281	0.008	7110.03-7115.09
Dhofar 378-2	7112.12	7113.67	1.71	1.62	14327	0.0191795	0.0297437	0.007	7110.69-7115.2
Dhofar 378-3	7112.23	7113.72	1.72	1.57	14237	0.023417	0.0512603	0.012	7110.03-7115.09
LAR 06319-1	7112.12	7113.51	1.61	1.53	18690	0.0141142	0.0164304	0.018	7110.14-7115.2
LAR 06319-2	7112.01	7113.57	1.56	1.61	23228	0.0123723	0.0142788	0.019	7110.25-7115.31
LAR 06319-3	7112.23	7113.72	1.62	1.46	23921	0.0153585	0.0192633	0.019	7110.03-7115.09
LAR 06319-4	7112.23	7113.69	1.64	1.41	11489	0.0144039	0.0210531	0.013	7110.36-7115.2
NWA 856-1	7112.34	7113.76	1.68	1.46	17756	0.0135268	0.0193118	0.002	7109.92-7114.98
NWA 856-2	7112.34	7113.66	1.73	1.47	34347	0.0122544	0.0137332	0.017	7109.92-7114.98
NWA 856-3	7112.23	7113.78	1.55	1.64	10830	0.020628	0.0266149	0.013	7110.03-7115.09
NWA 856-4	7112.34	7113.71	1.96	1.11	6754	0.018786	0.0206048	0.014	7109.92-7114.54
NWA1068-1	7112.23	7113.69	1.37	1.32	11183	0.0111108	0.0181071	0.017	7109.81-7114.98
NWA1068-2	7112.23	7113.80	1.93	1.47	13900	0.00867596	0.0129123	0.008	7110.14-7115.31
NWA1068-3	7112.23	7113.48	1.48	1.62	27852	0.00866333	0.0143061	0.010	7110.36-7114.98
NWA1068-4	7112.45	7113.80	2.04	1.46	20680	0.0115778	0.0159998	0.007	7110.14-7114.76
NWA 4468-1	7112.01	7113.59	1.21	1.46	4804	0.0136267	0.0231368	0.016	7110.14-7115.31

NWA 4468-2	7111.90	7113.61	1.92	1.73	19679	0.0111952	0.0277674	0.014	7110.47-7115.42
NWA 4468-3	7112.12	7113.61	1.22	1.62	10771	0.0132042	0.028097	0.008	7110.25-7115.42
NWA 4468-4	7112.45	7113.83	2.00	1.51	17344	0.0146757	0.0310264	0.013	7109.92-7115.09
NWA 4468-5	7112.34	7113.72	1.64	1.49	12887	0.0117459	0.0216561	0.013	7110.03-7115.2
Zagami-1	7112.45	7113.82	1.78	1.20	13129	0.0166804	0.0180525	0.007	7110.03-7115.09
Zagami-2	7112.23	7113.69	1.56	1.70	18887	0.0153681	0.020234	0.011	7110.25-7115.2
Zagami-3	7112.34	7113.80	1.47	1.59	17185	0.017552	0.0240403	0.013	7110.25-7115.42
RBT 04262-1	7111.78	7113.45	0.80	2.25	36505	0.00130414	0.00540348	0.014	7109.81-7114.32
RBT 04262-2	7112.89	7114.27	1.59	1.57	18816	0.0107101	0.0309875	0.010	7109.48-7115.2
RBT 04262-3	7112.23	7113.80	1.77	1.68	14380	0.0108086	0.032791	0.010	7110.69-7115.31
Shergotty-1	7112.23	7113.74	1.53	1.48	15705	0.0197477	0.0231851	0.012	7110.03-7115.09
Shergotty-2	7112.01	7113.58	1.37	1.82	9952	0.0152081	0.0214929	0.015	7110.25-7115.31
Shergotty-3	7112.45	7113.84	2.08	1.31	8743	0.00228094	0.00203485	0.009	7109.92-7114.54
Shergotty-4	7112.34	7113.87	2.09	1.30	11549	0.0234738	0.0156562	0.007	7109.92-7114.54

Residual of the fitting※ : $\sqrt{\frac{(The\ actual\ value - Value\ of\ the\ fitting)^2}{(The\ actual\ value)^2}}$

Appendix 2. The information of XANES analysis of HED meteorites.

Sample	Fe^{2+} peak (eV)	Fe^{3+} peak (eV)	Fe^{2+} half width (eV)	Fe^{3+} half width (eV)	Count max	The peak value of Fe^{2+}	The peak value of Fe^{3+}	Residual of the fitting※	Baseline (eV)
ALH 76005 grain-1	7112.23	7113.53	1.81	1.06	12724	0.0124615	0.00420739	0.007	7109.37-7114.54
ALH 76005 grain-2	7112.34	7113.45	1.58	0.86	15394	0.00928603	0.00463497	0.017	7109.37-7115.53
ALH 76005 grain-3	7112.23	7113.33	1.78	1.66	22625	0.0193699	0.0103895	0.007	7109.92-7114.54
Petersburg grain-1	7112.34	7113.60	1.81	1.21	12551	0.0132197	0.00590581	0.008	7109.37-7114.54
Petersburg grain-2	7112.23	7113.57	1.53	1.34	22666	0.00951974	0.00649808	0.012	7109.92-7114.54
Petersburg grain-3	7112.45	7113.82	1.76	1.34	11232	0.0181057	0.00838201	0.011	7110.03-7114.54
Piplia Kalan grain-1	7111.90	7113.54	1.56	1.76	3330	0.0148957	0.0114067	0.029	7110.03-7114.76
Piplia Kalan grain-2	7112.12	7113.09	1.26	1.24	28033	0.00663208	0.00304241	0.004	7109.92-7113.99
Padvarninkai grain-1	7112.34	7113.66	1.94	0.92	5076	0.0109422	0.00326599	0.006	7110..36-7113.99
Padvarninkai grain-2	7112.12	7113.59	1.70	1.00	5866	0.0160943	0.00264499	0.009	7109.59-7114.10

Y-75011 grain-1	7112.23	7113.56	1.74	1.10	24850	0.0273421	0.00755311	0.009	7109.48-7114.65
Y-75011 grain-2	7112.12	7113.61	1.89	1.25	14014	0.0247725	0.00702411	0.023	7109.15-7114.87
EETA 87520 grain-1	7112.23	7113.77	1.88	2.00	5037	0.00159413	0.00213502	0.011	7110.36-7115.53
EETA 87520 grain-2	7112.23	7113.50	1.43	1.86	10955	0.00120148	0.0016909	0.011	7110.36-7115.53
EETA 87520 grain-3	7112.12	7113.65	1.53	1.89	5280	0.0154325	0.0160138	0.005	7110.36-7115.53
EETA 87520 grain-4	7112.12	7113.619	1.56	1.86	5709	0.0129326	0.0138109	0.010	7109.15-7114.87
Moore County grain-1	7112.12	7113.42	1.48	2.01	4107	0.0128479	0.0138861	0.007	7110.25-7115.42
Moore County grain-2	7112.34	7113.76	1.42	1.38	4251	0.0173081	0.0204391	0.012	7110.36-7114.98
Moore County grain-3	7112.01	7113.30	1.32	1.69	4081	0.0181006	0.0174898	0.015	7110.367115.53
Moore county grain-4	7112.12	7113.57	1.31	2.17	4283	0.018103	0.0224694	0.009	7110.80-7115.42
Y 980433	7112.01	7113.54	1.20	1.70	2158	0.0122266	0.0280496	0.015	7109.48-7115.2
Y-75032 grain-1	7112.12	7113.23	1.76	1.77	3359	0.00617135	0.00664351	0.007	7110.36-7114.87

Residual of the fitting※ : $\sqrt{\frac{(The\ actual\ value - Value\ of\ the\ fitting)^2}{(The\ actual\ value)^2}}$

Appendix 3. The information of XANES analysis of samples of shock-loading experiments, synthetic experiment of plagioclase and terrestrial plagioclase.

Sample	Fe^{2+} peak (eV)	Fe^{3+} peak (eV)	Fe^{2+} half width (eV)	Fe^{3+} half width (eV)	Count max	The peak value of Fe^{3+}	The peak value of Fe^{3+}	Residual of the fitting※	Baseline (eV)
An80 (unshocked)	7112.23	7113.58	1.63	1.53	9516	0.0191773	0.0775584	0.013	7109.17-7114.89
An80 GPa20	7112.23	7113.59	1.51	1.57	8834	0.0188069	0.0795567	0.012	7109.17-7114.89
An80 GPa30	7112.12	7113.64	1.35	1.73	10102	0.0132975	0.0542147	0.026	7109.17-7114.89
An80 GPa40	7112.23	7113.56	2.10	1.58	10932	0.017854	0.0645156	0.013	7109.17-7114.89
An60 (unschoked)	7112.45	7113.76	0.66	1.43	1152	0.0182775	0.0510207	0.025	7109.26-7114.98
An60 GPa30	7112.12	7113.91	1.45	2.07	1833	0.0160011	0.0440493	0.019	7109.26-7114.98
An20 (unschoked)	7112.23	7113.39	1.20	1.33	11462	0.00951898	0.0192032	0.029	7109.26-7114.43
An20 GPa20	7112.34	7113.91	1.36	1.76	3264	0.0245897	0.0504269	0.012	7109.26-7114.98
An20 GPa30	7112.23	7113.81	1.26	1.64	1199	0.0153224	0.0322613	0.017	7109.26-7114.43
An20 GPa40	7112.23	7113.38	1.74	1.62	3911	0.0106922	0.0212832	0.008	7109.26-7113.77
QFM	7112.23	7113.35	0.97	1.88	8441	0.00460531	0.0403884	0.009	7111.08-7115.31
QFM −2	7112.45	7113.91	2.02	1.35	7978	0.0190705	0.0136991	0.017	7109.81-7114.76

Herd-1	7112.34	7113.64	1.99	1.59	100000	0.0187055	0.0570151	0.010	7109.15-7115.42
Herd-2	7112.12	7113.21	2.38	1.80	6020	0.0145976	0.0459143	0.006	7110.36-7114..87

Residual of the fitting※ : $\sqrt{\frac{(The\ actual\ value - Value\ of\ the\ fitting)^2}{(The\ actual\ value)^2}}$